Order and excitations near the spin-density-wave masked ferromagnetic quantum critical point in $Nb_{1-y}Fe_{2+y}$

Marijn Thomas Lucas

Royal Holloway
University of London

Supervisor: Dr. Philipp Niklowitz

Date: 2019/12/20

Declaration of Authorship

I, Marijn Lucas, hereby declare that this thesis and the work presented in it is entirely my own. Where I have consulted the work of others, this is always clearly stated.

Signed:

Date:

Abstract

Many experimental and theoretical studies suggest that it is difficult to approach ferromagnetic (FM) quantum critical point (QCP) in real materials. Instead, a variety of escape routes have been observed, notably the occurrence of a first order transition or superconductivity. The bulk properties of the C14 Laves phase $Nb_{1-y}Fe_{2+y}$ present a third scenario: marginal Fermi liquid behaviour as expected of a ferromagnetic quantum critical point (FM QCP) [1], but also masking of the FM QCP itself by a spin density wave (SDW) order [2].

Polarised neutron diffraction measurements in the FM state have shown that the direction of the magnetic moment is along $\boldsymbol{c}$.

The ordering wave vector $\boldsymbol{Q}_{\mathbf{SDW}}$ of the SDW as well as the temperature T and composition dependence y of $\boldsymbol{Q}_{\mathbf{SDW}}$ have been directly observed by elastic unpolarised neutron scattering on several single-crystalline samples [3].

We also collected and analysed comprehensive inelastic neutron scattering data which reveals the position in the reciprocal space q, T and y dependence of low-energy excitations in a range covering the paramagnetic (PM), the SDW and the FM states. Those results show softening of the low energy magnetic excitations in a broad q range and a divergence of the inverse linewidth in energy in a considerable region of the phase diagram near the SDW phase. The observed excitation pattern reflects the simultaneous proximity of the $Nb_{1-y}Fe_{2+y}$ system to two types of magnetic order, which makes this a candidate system for SDW order emerging from a FM QCP. We use the models given by the spin fluctuation theory to discuss our observations.

Acknowledgements

I start my acknowledgements by thanking Dr. Philipp Niklowitz, who supervised my thesis, introduced me to the fascinating domain of neutron scattering and explained, re-explained and sometimes even re-re-explained theoretical concepts without loosing his patience and his good mood. I am very grateful to him for the opportunity that I was given to learn about different neutron scattering techniques and to get involved in many experiments. I would also like to thank Dr. Sordi for letting me attend to his excellent quantum mechanics lectures as well as Dr. Montiel for his assistance when I struggled with complicated equations and for proofreading parts of my thesis.

The days at the office would not have been as nice without my office mates. Thank you to Xavier R. for remembering me that it is not all about work. I will remember our countless chess games in Holland Park or while drinking a pint (or three) in so many different pubs. Thank you Xavier M. for distracting me with your endless references to french TV-shows. Thank you Uthay for the curry evenings that we had at your place, I can handle spices now.

A big thank you to my family and especially to my parents, who supported me during this entire PhD. Thanks to you, the eternal student will now stop being a student.

Finally, I am immensely grateful to my partner Nicola, who did so much for me and who cheered me up when I needed it. I will never forget how, despite all the work you have, you found time and energy to be on my side, to make my life so enjoyable, cosy and exciting. Thank you also to Teddy, to whom I owe my sanity during the long hours spent on my writing.

Contents

List of Tables

List of Figures

Abbreviations

AFM anti-ferromagnetic

DAD double axis diffractometer

DFT Density Functional Theory

DHO damped harmonic oscillator

$\mathbf{E_i}$ incident energy

FM ferromagnetic

FM QCP ferromagnetic quantum critical point

FWHM full-width half-maximum

HWHM half-width half-maximum

MCS multi-choppers spectrometer

NFL non-Fermi liquid

NMR nuclear-magnetic resonance

ODHO over-damped harmonic oscillator

PM paramagnetic

QCEP quantum critical end point

QCP quantum critical point

QTCP quantum tricritical point

SDW spin density wave

SNP spherical neutron polarimetry

SODHO soft over-damped harmonic oscillator

TAS triple axis spectrometer

TCP tricritical point

TOF time of flight spectrometer

TS2 target station two

Symbols

Q amplitude of a reciprocal space vector

$\boldsymbol{Q_{\mathbf{FM}}}$ ferromagnetic ordering wave vector

$\boldsymbol{Q_{\mathbf{SDW}}}$ spin density wave ordering wave vector

$\boldsymbol{Q}$ a vector in the reciprocal space

$\boldsymbol{k_{\mathbf{f}}}$ scattered neutrons wave-vector

$\boldsymbol{k_{\mathbf{i}}}$ incident neutrons wave-vector

h_{SDW} component along h of the spin density wave ordering wave vector

k_{f} amplitude of the scattered neutrons wave-vector

k_{i} amplitude of the incident neutrons wave-vector

l_{FM} component along l of the ferromagnetic ordering wave vector

l_{SDW} component along l of the spin density wave ordering wave vector

T_{C} Curie temperature

T_{N} Néel temperature

T_{base} Base temperature for neutron scattering measurements

Chapter 1

Introduction

1.1 Quantum criticality

Since Thomas Andrews observed critical opalescence in carbon dioxide, interest in continuous phase transitions increased significantly over the last century and is, still today, a main research topic in condensed matter physics. Continuous phase transitions are observed in many systems, including the universe itself. Moreover, the theory of continuous phase transitions is ubiquitous and is observed in various areas, such as string theory, transition to chaos in dynamical systems [5], and also in biology with transitions between coordinated biological motions [6] or the swarm model predicting the behaviour of systems with collective intelligence [7]. Therefore continuous phase transitions are present, not only in condensed matter physics, but in science in general.

During the last decades, research interest focused on a particular type of continuous phase transitions: *quantum critical* phase transitions. The latter are observed at 0 K, as illustrated in Figure 1.1, where transitions are driven by quantum fluctuations, rather than thermal fluctuations. Near a QCP, physics of continuous phase transitions combine with quantum mechanics and give rise to exotic behaviour, such as unconventional superconductivity, non-Fermi-liquid behaviour or anti-ferromagnetism. Unconventional superconductivity, was, for instance, observed in $CePd_2Si_2$ and $CeIn_3$ (Figure 1.2a) when tuning the system towards an anti-ferromagnetic (AFM) QCP with pressure [8] or in $BaFe_2(As_{1-x}P_x)_2$ (Figure 1.2b) when tuning the system towards a spin density wave (SDW) QCP with chemical substitution of As with P [9]. Non-Fermi-liquid behaviour, was recorded, for instance, in the pressure [10] or magnetic field [11] tuned $YbRh_2Si_2$ (Figure 1.2c), in doped Ni_xPd_{1-x} [12] or in $CeCu_{5.9}Au_{0.1}$

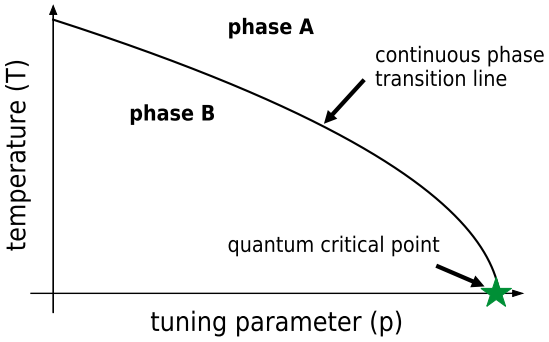

Figure 1.1: Representation of a generic tuning parameter (p)-Temperature (T) phase diagram. When $T > 0\,\mathrm{K}$, the continuous transition between Phase A and Phase B is driven by a change of temperature. At $T = 0\,\mathrm{K}$, the transition line ends in a QCP (green star); at this point the phase transition is driven by quantum fluctuations rather than thermal fluctuations.

at zero magnetic field [13] (Figure 1.2d).

1.2 Ferromagnetic quantum phase transition

The ferromagnetic (FM)-paramagnetic (PM) transition, the classic example of magnetic continuous phase transitions, has been intensively studied and experimental results suggest that FM QCPs are key to understand new phases such as magnetically mediated superconductivity (see the review [14] for examples). However, the FM QCPs themselves are very hard to observe in real materials; experiments have shown how nature avoids these points with alternative scenarios, which are illustrated in Figure 1.3.

In one scenario, the second order phase transition turns into first order with wing splitting at a TCP ending in a quantum critical end point (QCEP) as shown in Figure 1.3a. This has been observed, for instance, in MnSi [15], in $Sr_3Ru_2O_7$ [16], in $ZrZn_2$ [17] or in UGe_2 [18]. For UGe_2 Figure 1.4a shows how the continuous (second order) PM-FM transition becomes first order at the TCP as the system is tuned with pressure towards a FM QCP. At the TCP, the continuous FM-PM splits in two wings, each ending in a QCEP. First order transitions and wing-splitting tri-critical points have been predicted by the Belitz et al. [19, 20].

Another scenario is the emergence of a superconducting dome covering the FM QCP as

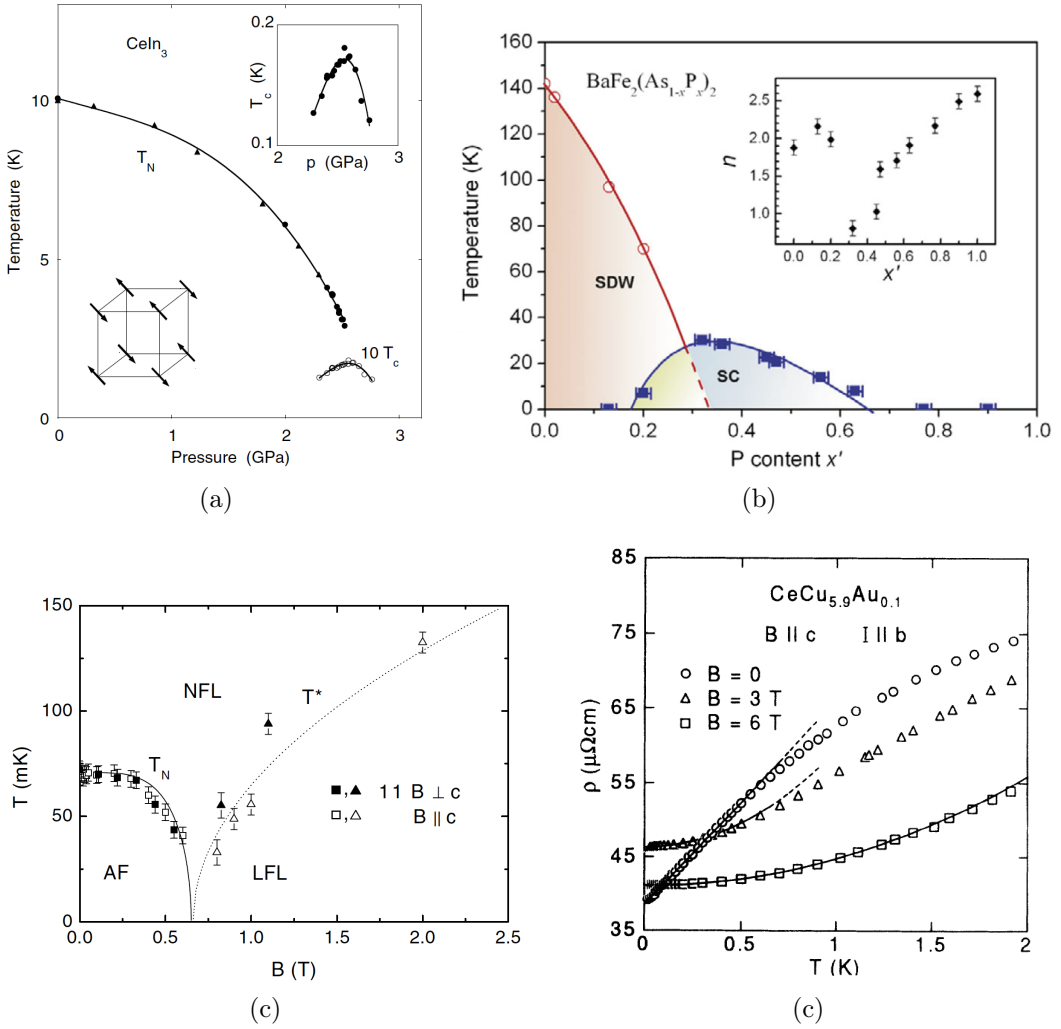

Figure 1.2: (**a**) pressure-temperature phase diagram of $CeIn_3$ featuring unconventional superconductivity, where T_N is the AFM transition temperature and T_C is the superconducting transition temperature (figure from [8]). (**b**) composition (x')-temperature phase diagram of $BaFe_2(As_{1-x'}P_{x'})_2$ featuring superconductivity, where *SDW* denotes spin-density-wave, *SC* denotes superconductivity and n is the fitted temperature exponent of the resistivity (figure from [9]). (**c**) magnetic field (B)-temperature (T) phase diagram of $YbRh_2Si_2$ featuring non-Fermi-liquid (NFL) and Landau-Fermi-liquid (LFL) behaviour, where *AF* is the anti-ferromagnetic phase, T_N is the Neél temperature and T^* is the upper temperature limit of the T^2 behaviour of the electrical resistivity (figure from [11]). (**d**) electrical resistivity measurements of $CeCu_{5.9}Au_{0.1}$ with different applied magnetic field along the c axis (figure from [13]).

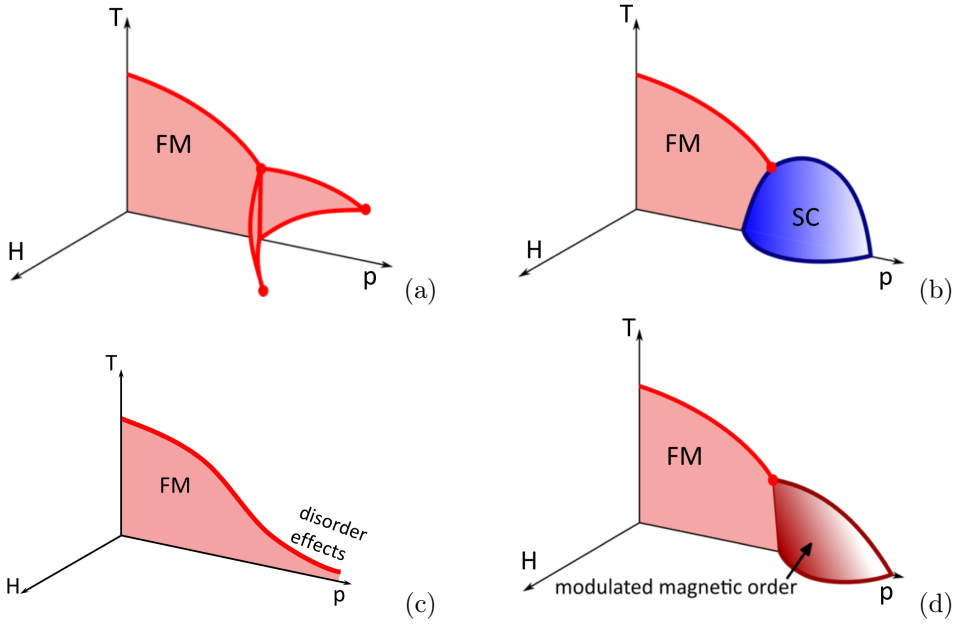

Figure 1.3: Illustration of how nature avoids FM QCPs in temperature (T)-magnetic field (H)-tuning parameter (p) phase diagrams. **(a)** the second order phase transition becomes first order at a TCP, with in-field splitting of wings that end in QCEPs. **(b)** emergence of a superconducting dome masking the FM QCP. **(c)** in a disordered FM system crossover to a spin-glass in the tail of the phase diagram at high p. **(d)** emergence of modulated magnetic ordered phase in place of the QCP. Figure adapted from [14].

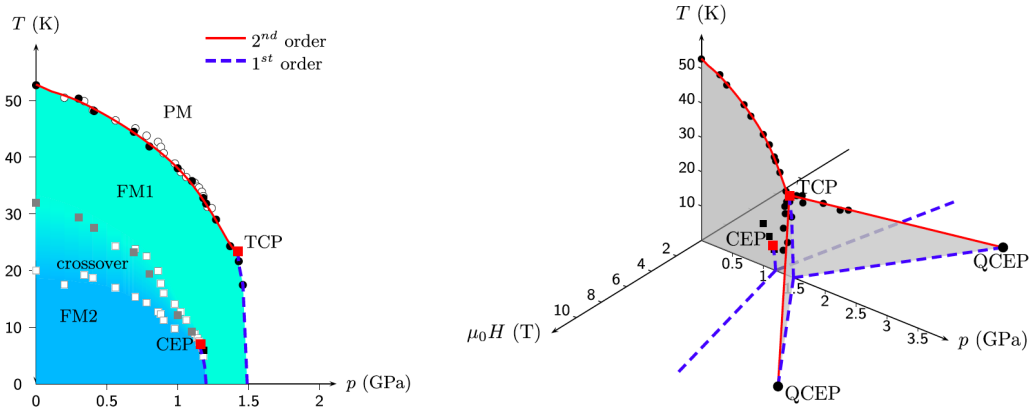

Figure 1.4: Example of UGe_2, where a continuous phase transition becomes first order at a tri-critical point (**a**) with a wing-splitting ended by two QCEPs (**b**). Figures from [18].

illustrated in Figure 1.3b. Examples of this have been observed in UGe_2 [21] or in UCoGe [22]. Furthermore, in view of the Meissner effect, it was believed that superconductivity and ferromagnetism could not coexist. However, experimental results, e.g., on UGe_2 under pressure showed the contrary. Figure 1.5 shows a superconducting phase coexisting with the FM phase in the *d*-electron system UGe_2.

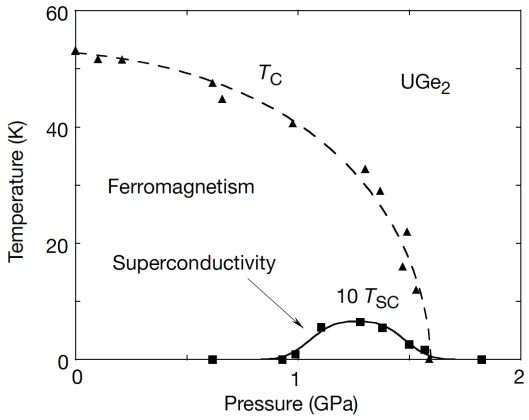

Figure 1.5: Pressure (p)-temperature (T) phase diagram of UGe_2 where superconductivity coexists with FM and how both phases are suppressed at 1.6 GPa as the system is tuned with pressure towards the FM QCP. T_C denotes the Curie temperature and T_{SC} is the superconducting transition temperature. Figure from [21].

The third scenario, generally observed in highly disordered systems and illustrated in Figure 1.3c, consists in a freezing spin-glass at the approach of the FM QCP, which results in a tail in the phase diagram and a non-Fermi-liquid behaviour above this tail [14]. Spin-glass freezing was mainly observed after doping FM metallic systems such as $U_{1-x}Th_xNiSi_2$ [23] or $Ni_{1-x}V_x$ [24]. Figure 1.6 shows how the dilution of the magnetic sublattice in $U_{1-x}Th_xNiSi_2$, by increasing the doping concentration, reduces the ordering temperature and destroys the long range order at the critical concentration x_c. The disappearance of the long range magnetic order creates this tail observed in the phase diagram in place of the FM QCP [23].

The improvement of the experimental techniques and the huge amount of compounds studied over the past decades showed that the standard model of metals does not describe correctly second-order FM-PM phase transitions at low temperatures in itinerant ferromagnets. Hertz, in 1976 [25], with Moriya in 1985 [26] and Millis in 1993 [27], developed a theory —the HMM theory—, based on the generalised Landau-Ginzburg-Wilson functional, to describe QCP in

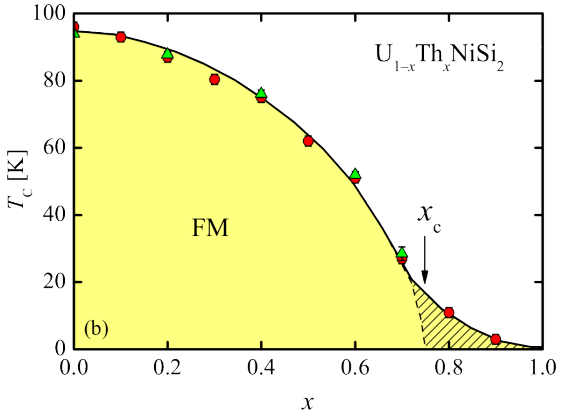

Figure 1.6: Doping concentration (x)-temperature (T) phase diagram of $U_{1-x}Th_xNiSi_2$ from magnetic susceptibility and heat capacity measurements [23]. x_c indicates the critical concentration above which the long range magnetic order disappears. Figure from [23].

itinerant ferromagnets. The HMM theory, which builds on two key assumptions[1], and several other proposed theories [29, 28, 30], are proven correct in many situations, but in more recent studies these assumptions may not be valid [31]. To describe states near a FM QCP more accurately, non-analytical contributions of the order parameter to the free energy functional should be considered [28, 32]; this approach is referred to as *order by disorder*. The latter theory suggests that on the approach a FM QCP, the Fermi surface deforms, which brings new possibilities for low-energy fluctuations and leads to a phase transition that turns first order or to the emergence of new modulated magnetic ordered phases [32]. Thus a fourth scenario is suggested: a new modulated magnetic order that masks the FM QCP [28, 32] as illustrated in Figure 1.3d. $Sr_3Ru_2O_7$ [33], PrPtAl [34], MnP [35] or $NbFe_2$ [36] are examples where new modulated magnetic order has been observed.

The proximity to FM quantum criticality seems to be a common factor between numerous systems featuring exotic behaviour. Pursuing the investigation of such systems could be a reasonable bet for discovering more exciting physics and possibly finding long sought answers to questions centering, e.g., around magnetically mediated superconductivity. In the framework of this thesis we investigate magnetic order and excitations at the border of itinerant ferromagnetism in $Nb_{1-y}Fe_{2+y}$. The FM phase is suppressed by chemical substitution, but the FM QCP seems to be masked by an emerging SDW phase as shown in Figure 1.7 [36].

[1]The two assumptions are, first, non-singular coefficients in the expression of the action, and, second, a q^2 momentum dependence of the static susceptibility [28]

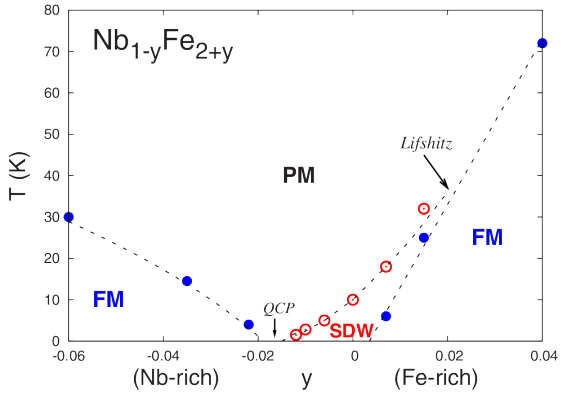

Figure 1.7: Doping concentration (y)-temperature (T) phase diagram of $Nb_{1-y}Fe_{2+y}$, which features a suspected SDW phase masking a FM QCP. Figure from [36].

1.3 Thesis outline

In Chapter 2, we present the key concepts and the theory that are used throughout this research project. We begin with an introduction to phase transitions, with particular focus on the ferromagnetic phase transition and FM quantum criticality. The second section of this chapter is a general presentation of the damped harmonic oscillator system and its adaptation to our neutron scattering results. The third and last section of this chapter presents the spin fluctuation theory, that we use to discuss our main results and we show how this theory predicts that an over-damped harmonic oscillator can describe our results.

Chapter 3 is the review of the $NbFe_2$ compound. We present the crystal and the magnetic structure of $NbFe_2$, as well as a summary of studies of the doping concentration-temperature phase diagram of $Nb_{1-y}Fe_{2+y}$.

Chapter 4 focuses on the experimental aspect of project. We start with the presentation of the samples that were measured. We then cover the theory of neutron scattering, including unpolarised elastic and inelastic scattering as well as polarised neutron diffraction. We end this chapter with a section on the instrumentation that was used for the measurements. This includes the two TASs, 4F2 and Panda, the multi-choppers spectrometer (MCS), LET, and the double axis diffractometer (DAD), POLI, for polarised neutrons measurements.

The next three chapters present the results, which are divided in three parts: polarised neutron diffraction in Chapter 5, elastic scattering with unpolarised neutrons in Chapter 6 and inelastic scattering with unpolarised neutrons in Chapter 7. In Chapter 5 we present polarised neutron diffraction results, which show that the FM state is built of collinear spins pointing along

the $\boldsymbol{c}$ axis, which is also the easy magnetic axis. Chapter 6 describes unpolarised elastic neutron scattering results that establish the SDW ordering wave vector and its composition (y) and temperature (T) dependence. Chapter 7 presents the results of the inelastic unpolarised neutron scattering measurements, which show the temperature-, composition- and q- dependence of the magnetic excitations in the FM, the SDW and the PM phase.

Chapter 8 is the closing chapter of this thesis and summarises the main results and findings. It also provides suggestions for further development of the project or potential improvement of some results.

Chapter 2

Theoretical concepts

2.1 Phase transitions

Phase transitions are central in condensed matter physics and there are numerous examples in everyday life. We can think of ice melting into liquid or a ferromagnet that becomes paramagnetic when temperature increases. The first example is a structural phase transition and involves a change in the crystalline structure. The second example, on the other hand, is a magnetic phase transition; the magnetic structure changes, but the crystalline structure remains unchanged. There exist many other phase transitions (e.g. superconducting transitions, ferroelectric transitions or crystal structure transitions) and what characterise those, is that a tiny variation of a parameter (such as temperature, pressure or magnetic field) provokes qualitative changes in the system.

Although phase transitions can be very different, we also notice huge similarities between them, such as the method applied to study those transitions or the universality of their properties. Based on these similarities, Ehrenfest assumed that the phase transitions can be reduced into two types: first order phase transitions or second order phase transitions [37].

2.1.1 Ehrenfest classification of phase transitions

The Ehrenfest classification of phase transitions relies on the analysis of the singularity of the thermodynamic potential. A phase transition is of first order when physical quantities, which are linked to the *first* order derivative of the thermodynamic potential (e.g. entropy), are discontinuous [37]. A phase transition is of second order when physical quantities, which

are linked to the *second* order derivative of the thermodynamic potential (heat capacity), are discontinuous [37].

Since the Ehrenfest classification is based on thermodynamic properties of the system it becomes irrelevant in the absence of thermal fluctuations. An alternative approach was taken by L. D. Landau, who considered the symmetries in the system to propose an other classification for the phase transitions.

2.1.2 Landau classification of phase transitions

2.1.2.1 The order parameter

L. D. Landau noticed that phase transitions generally involve symmetry breaking in the system, and that the symmetry group of the low-symmetry phase, usually the low temperature phase, is strictly included in the symmetry group of the high symmetry phase [37]. Based on this observation, Landau introduced a new classification for the phase transitions [38].

To describe the less symmetrical phase, Landau introduced a new variable, called the *order parameter* (m). The latter is extensive, temperature dependent and non-zero only in the low-symmetry phase [37]. When the order parameter evolves discontinuously (e.g. with the melting of ice), the transition is *first order*, and when the order parameter evolves continuously (e.g. with the paramagnetic (PM)-ferromagnetic (FM) transition), the transition is *second order* [39].

2.1.2.2 The Landau model

Within the different phases the energy, promoting order, competes with entropy, which promotes disorder. The stable phase observed at thermodynamic equilibrium is the one with the lowest Helmholtz free energy $F = U - TS$, where U is the energy, T is the temperature and S is the entropy of the system. From Landau we know that the free energy is a functional of the order parameter, which is analytical at the transition (when $m = 0$) and it can be developed as a Taylor expansion of the order parameter near the transitions [39, 37]. The functional must have the same symmetries as the most symmetrical phase, which is usually the high-temperature phase.

When temperature decreases, the system experiences a spontaneous phase transition from a low-symmetry phase to a high-symmetry phase; the transition involves a spontaneous symmetry breaking [37]. In the case of the PM-FM phase transition, spontaneous magnetisation appears along one direction in the FM phase and the global rotation symmetry, observed in the PM

phase, is broken. The broken symmetry is caused by the interactions between the particles. An important property in the Landau model of phase transitions is that symmetries are not broken continuously: either a symmetry is present or it is broken, but it cannot be both at the same time [37].

Landau phenomenological mean field theory requires the order parameter to be small and it is, therefore, more suitable to study second order phase transitions [39].

The purpose of this project is to investigate the PM-FM phase transition in the low temperature limit. At 0 K there are no thermal fluctuations to move the system between the *high* and *low* temperature phases any more, instead the transition is driven by quantum fluctuations. In this quantum regime, the Ehrenfest classification is not relevant and the Landau classification is used instead. Future references to *first* or *second* order transitions refer to the definitions given by the Landau classification.

2.1.3 Ferromagnetic phase transition

In the FM phase, the global rotation symmetry of the electron spins is broken. More spins point along one direction than along the other and a magnetisation M appears:

$$M = \mu_{\mathrm{B}}(n_{\uparrow} - n_{\downarrow}), \tag{2.1.1}$$

where μ_{B} is the Bohr magneton, $n_{\uparrow}$ is the number of spins up and $n_{\downarrow}$ is the number of spins down. This spontaneous magnetisation is used as the order parameter for the PM-FM phase transition. Near the latter, the free energy functional is [40]

$$F\left[M(T)\right] = F_0 + \frac{1}{2}a(T - T_c)M(T)^2 + \frac{1}{4}bM(T)^4 - HM(T), \tag{2.1.2}$$

where F_0, a and b are positive phenomenological constants, T_c is the transition temperature and H is the applied magnetic excitation.

2.1.3.1 Ferromagnetism in zero magnetic field ($H = 0$)

In the absence of external magnetic excitation, the expression of the free energy in Equation 2.1.2, only contains even terms in M, because systems with up or down spins are symmetrical and so must be the functional $F[M]$ (M is temperature dependent).

The stable phase at thermodynamic equilibrium minimises the free energy. We see in Fig-

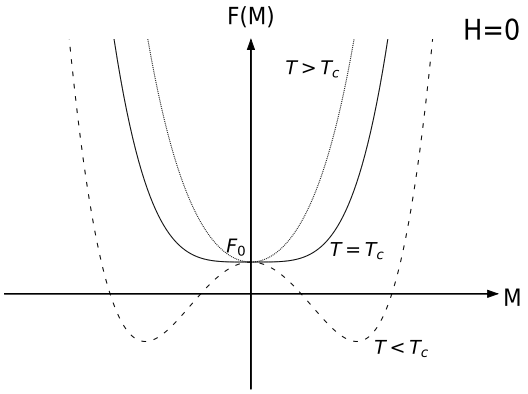

Figure 2.1: Helmholtz free energy of Landau model of ferromagnetism above, below and at transition temperature T_c with zero external magnetic field.

ure 2.1, that, above $\mathrm{T_C}$, there is only one minimum for $F[M]$ at $M = 0$, whereas below T_c, two values for M minimise the free energy. These minima are given by

$$\frac{\delta F}{\delta M} = M\left[a(T - T_c) + bM^2\right] = 0. \tag{2.1.3}$$

Thus the functions $M(T)$ that minimise the free energy are

$$\begin{cases} M &= 0 \quad \text{for} \quad T \geq T_c \\ M &= \pm\sqrt{\frac{a(T_c - T)}{b}} \quad \text{for} \quad T < T_c. \end{cases} \tag{2.1.4}$$

We see that $M(T)$ is continuous at T_c and thus the FM phase transition is of second order.

2.1.3.2 Ferromagnetism in non-zero magnetic field ($H \neq 0$)

If we now apply a magnetic excitation H, the symmetry is broken and the degeneracy of the minimum energy is lifted as illustrated in Figure 2.2. The expression to minimise the thermodynamic potential given in Equation 2.1.3 becomes

$$\frac{\delta F}{\delta M} = M\left[a(T - T_c) + bM^2\right] - H = 0, \tag{2.1.5}$$

and there is a unique value for M that minimises the free energy.

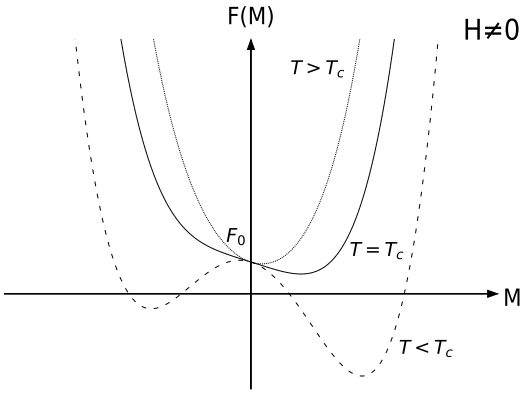

Figure 2.2: Helmholtz free energy of Landau model of ferromagnetism above, below and at transition temperature T_c with non-zero external magnetic field.

2.1.3.3 Magnetic susceptibility

The magnetic susceptibility at constant temperature is defined as

$$\chi_T = \left.\frac{\partial M}{\partial H}\right|_T, \tag{2.1.6}$$

and differentiating Equation 2.1.5 with H gives

$$a(T - T_c)\chi_T + 3bM^2\chi_T - 1 = 0. \tag{2.1.7}$$

Thus near the transition in the PM state, where $M = 0$,

$$\chi_T = \frac{1}{a(T - T_c)}, \tag{2.1.8}$$

and near the transition in the ordered phase, where $M = \pm\sqrt{\frac{a(T_c - T)}{b}}$,

$$\chi_T = \frac{1}{2a(T_c - T)}. \tag{2.1.9}$$

We saw that the magnetisation varies at $M \propto (T_c - T)^\beta$, with $\beta = 1/2$, and the susceptibility varies as $\chi \propto (T - T_c)^{-\gamma}$, with $\gamma = 1$. β and γ are called the *critical exponents*, and more similar critical exponents can be defined to describe continuous phase transitions. However, the critical exponents given by the Landau model ($\beta = \frac{1}{2}$ for M and $\gamma = 1$ for χ_T) deviate from experimental results. This model, based on mean-field theory, does not properly describe

continuous phase transitions at T_c for dimensions $d < 4$ [40]. An important hypothesis about these critical exponents, based on their experimental measurements and known as the hypothesis of *universality*, is that they are independent of the type of phase transition, as long as the latter is continuous. In the static case (no consideration of time), these critical exponents only depend on the dimensionality d of the system, the symmetry D of the order parameter and the range (long or short) of the interactions [40]. Thus to characterise a continuous phase transition, one needs to identify to which *universal class* the system belongs.

2.1.4 Ferromagnetic quantum critical point

In the previous description, the PM-FM phase transition occurs at a finite temperature T_c and the quantum fluctuations in the system are neglected. This makes sense when the thermal energy $k_{\mathrm{B}}T$ is much higher than the energy of the excitations $\hbar\omega$. Now lets imagine a system in which the PM-FM transition parameter is not the temperature, but a non thermal parameter p, such a pressure, doping or a magnetic field. The phase diagram of such a system will look like the illustration in Figure 2.3. The line, which represents the T and p dependent PM-FM phase transitions, is suppressed at $p = p_0$ and $T = 0$K. At this suppression point, called a quantum critical point (QCP), the transition is driven by quantum fluctuations and becomes a *quantum* phase transition.

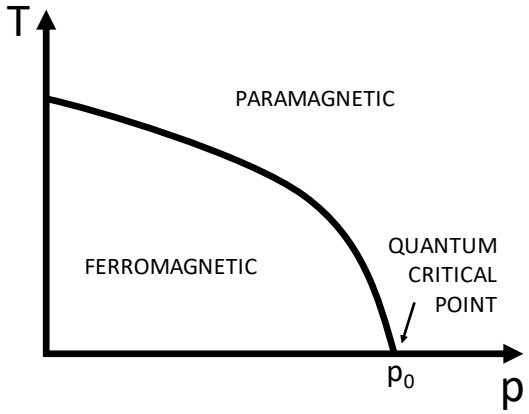

Figure 2.3: Schematic representation of a second order PM-FM phase transition that ends with a quantum critical point at 0K. T is the temperature and p is a non-thermal tuning parameter.

Around the FM QCP the energies of the fluctuating modes are not negligible compared to the thermal energy and static properties cannot be separated from dynamic properties anymore.

Hertz generalised the Landau-Ginzburg-Wilson model to describe quantum critical phenomena by considering imaginary times to account for the dynamic aspects of the phase transition [25]. Later Millis in [27], uses effective bosonic field theory to describe the fluctuations of the ordering field at a 0K continuous phase transition.

The second order QCP have attracted huge attention over the past years because possibly responsible for the emergence of many new exotic quantum phases in itinerant electron systems, such as non-Fermi liquid behaviour or magnetically induced superconductivity. Many different systems have been experimentally studied and, near the QCP, all showed a deviation from the standard behaviour of a second order phase transition [17].

2.2 Damped harmonic oscillator

2.2.1 General equation

The general differential equation of a damped harmonic oscillator system with observable u is:

$$\frac{1}{\omega_0^2}\frac{\mathrm{d}^2u}{\mathrm{d}t^2} + \frac{2\zeta}{\omega_0}\frac{\mathrm{d}u}{\mathrm{d}t} + u = \chi_0 f, \tag{2.2.1}$$

where ω_0 is the undamped angular frequency of the oscillator, ζ is the damping factor, f is the driving force and χ_0 is the static gain. To compute the response of the system, we can use the Laplace transform, which is defined as:

$$\mathcal{L}[u(t)] = \underline{U}(p) = \int_0^\infty u(t)\exp(-pt)\mathrm{d}t, \tag{2.2.2}$$

with p a complex number. Equation 2.2.1 then becomes:

$$\frac{\underline{U}(p)}{\omega_0^2}(\omega_0^2 + 2\zeta\omega_0 p + p^2) = \chi_0\underline{F}(p), \tag{2.2.3}$$

where $\underline{U}(p)$ is the Laplace transform of the observable of the system and $\underline{F}(p)$ is the Laplace transform of the driving force. Equation 2.2.3 can be written as $\underline{U}(p) = \underline{\chi}(p)\underline{F}(p)$, with

$$\underline{\chi}(p) = \frac{\chi_0\omega_0^2}{\omega_0^2 + 2\zeta\omega_0 p + p^2}, \tag{2.2.4}$$

the susceptibility of the system.

2.2.2 Response to an impulse

Since $\mathcal{L}[\delta(t)] = 1$, we can directly measure the susceptibility of a system by exciting the latter with an impulse. With $\underline{F}(p) = \mathcal{L}[F_0\delta(t)] = F_0$, Equation 2.2.4 gives:

$$\underline{U}(p) = \frac{\chi_0 F_0 \omega_0^2}{\omega_0^2 + 2\zeta\omega_0 p + p^2}. \tag{2.2.5}$$

When solving the equation $\omega_0^2 + 2\zeta\omega_0 p + p^2 = 0$ to find the singularities, p_1 and p_2, of $\underline{U}(p)$, we identify three regimes:

$$\begin{aligned}
&\Delta = 4\omega_0^2(\zeta^2 - 1) \\
&\zeta > 1 \quad \text{(over-damped regime):} \quad p_1 = -\omega_0(\zeta + \sqrt{\zeta^2 - 1}) \quad p_2 = -\omega_0(\zeta - \sqrt{\zeta^2 - 1}) \\
&\zeta = 1 \quad \text{(critical regime):} \quad p_1 = p_2 = -\omega_0 \\
&\zeta < 1 \quad \text{(under-damped regime):} \quad p_1 = -\omega_0(\zeta + i\sqrt{1 - \zeta^2}) \quad p_2 = -\omega_0(\zeta - i\sqrt{1 - \zeta^2}),
\end{aligned} \tag{2.2.6}$$

2.2.2.1 Over-damped regime ($\zeta > 1$)

A system is in the over-damped regime when it does not oscillate around its equilibrium state and approaches the latter from one direction only.

Equation 2.2.5 has two real singularity points, which are given in Equation 2.2.6 ($\zeta > 1$). We define $T_1 = -1/p_1$ and $T_2 = -1/p_2$ and we can write Equation 2.2.5:

$$\underline{U}(p) = \frac{\chi_0 F_0}{(1 + T_1 p)(1 + T_2 p)} \quad \text{with} \quad T_1 = \frac{1}{\omega_0(\zeta + \sqrt{\zeta^2 - 1})} \quad T_2 = \frac{1}{\omega_0(\zeta - \sqrt{\zeta^2 - 1})}. \tag{2.2.7}$$

After a decomposition in simple elements and reverse Laplace transform, we find the temporal solution $u(t)$:

$$\begin{aligned}
u(t) &= \frac{\chi_0 F_0}{T_2 - T_1}\left(e^{-t/T_2} - e^{-t/T_1}\right) \\
u(t) &= \frac{\chi_0 F_0 \omega_0}{2\sqrt{\zeta^2 - 1}} e^{-t/\tau_o}\left(1 - e^{-2\omega_0 t\sqrt{\zeta^2 - 1}}\right) \quad \text{with} \quad \tau_o = \frac{1}{\omega_0(\zeta - \sqrt{\zeta^2 - 1})}.
\end{aligned} \tag{2.2.8}$$

τ_o is the time *constant* for an exponential decay of the system towards equilibrium in the over-damped regime.

The yellow line in Figure 2.4a illustrates the response of the over-damped oscillator with $\zeta = 2$. In the strongly over-damped regime ($\zeta >> 1$), the expression of τ_o in Equation 2.2.8

simplifies and we have

$$\tau_o(\zeta) \approx \frac{2\zeta}{\omega_0}. \tag{2.2.9}$$

2.2.2.2 Critical regime ($\zeta = 1$)

The critical regime is the transition between over-damped to under-damped regimes. This regime corresponds the shortest time for the system to go back to equilibrium without pseudo-oscillations.

When $\zeta = 1$, we have $\Delta = 4\omega_0^2(\zeta^2 - 1) = 0$ in Equation 2.2.6 and Equation 2.2.5 has a double real singularity point $p_0 = -\omega_0$. We define $T_0 = -1/p_0 = 1/\omega_0$, which is the time *constant* for an exponential decay of the system towards equilibrium, and Equation 2.2.5 becomes

$$\underline{U}(p) = \frac{\chi_0 F_0}{(1 + T_0 p)^2} \quad \text{with} \quad T_0 = \frac{1}{\omega_0}, \tag{2.2.10}$$

which gives the temporal solution

$$\begin{aligned} u(t) &= \mathcal{L}^{-1}[\underline{U}(p)] \\ u(t) &= \chi_0 F_0 \omega_0^2 t e^{-t/\tau_c} \quad \text{with} \quad \tau_c = \frac{1}{\omega_0}. \end{aligned} \tag{2.2.11}$$

The brown line in Figure 2.4a illustrates the response of the critical oscillator ($\zeta = 1$). τ_c is the time *constant* for an exponential decay of the system towards equilibrium in the critical regime.

2.2.2.3 Under-damped regime ($\zeta < 1$)

A system in the under-damped regime pseudo-oscillates around its equilibrium state and as it approaches the latter. If $\zeta = 0$, the system oscillates indefinitely at angular frequency ω_0.

In the under-damped regime, equation2.2.5 has two complex singularity points, p_1 and p_2 in Equation 2.2.6 ($\zeta < 1$). We can rewrite Equation 2.2.5

$$\begin{aligned} \underline{U}(p) &= \frac{\chi_0 F_0 \omega_0^2}{(p + \zeta\omega_0)^2 + \Omega^2} \quad \text{with} \quad \Omega = \omega_0\sqrt{1 - \zeta^2} \\ &= \frac{\chi_0 F_0 \omega_0}{\sqrt{1 - \zeta^2}} \frac{\Omega}{(p + \zeta\omega_0)^2 + \Omega^2} \\ &= \frac{\chi_0 F_0 \omega_0}{\sqrt{1 - \zeta^2}} \mathcal{L}\left[e^{-\zeta\omega_0 t} \sin \Omega t\right], \end{aligned} \tag{2.2.12}$$

and thus

$$u(t) = \frac{\chi_0 F_0 \omega_0}{\sqrt{1-\zeta^2}} e^{-t/\tau_u} \sin \Omega t \quad \text{with} \quad \tau_u = \frac{1}{\zeta \omega_0}. \tag{2.2.13}$$

Ω is the angular frequency of the pseudo-oscillations.

The blue line in Figure 2.4a illustrates the response of the under-damped oscillator with $\zeta = 0.4$. τ_u is the time *constant* for an exponential decay of the system towards equilibrium in the under-damped regime.

2.2.2.4 Discussion

A damped harmonic oscillators has three working regimes: the under-damped ($\zeta < 1$), the critical ($\zeta = 1$) and the over-damped regime ($\zeta > 1$). In the under-damped regime, the temporal evolution of an observable $u(t)$ oscillates around its equilibrium value, whereas in the critical and over-damped regimes, $u(t)$ exponentially decays towards its equilibrium value (Figure 2.4a).

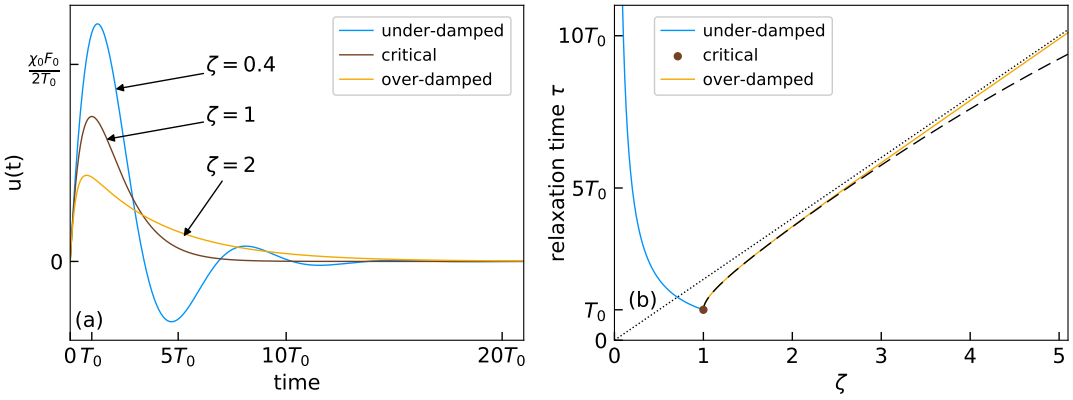

Figure 2.4: **(a)** represents the time evolution in the under-damped ($\zeta < 1$), the critical ($\zeta = 1$) and the over-damped ($\zeta > 1$) regime of a damped harmonic oscillator, which has been excited with an impulse ($f(t) = F_0 \delta(t)$). T_0 on the horizontal axis is the oscillating period at zero damping (i.e. $\zeta = 0$), χ_0 is the static gain and F_0 is the weight of excitation. **(b)** shows ζ-dependence of the relaxation time of the system in the different regimes. The dotted line of equation $\tau_{a1} = 2\zeta T_0$ is the asymptote of the over-damped relaxation time when $\zeta \to \infty$. The dashed curve of equation $\tau_{a2} = T_0 \left[\zeta + \sqrt{2}(\zeta-1)^{\frac{1}{2}} + \frac{\sqrt{2}}{4}(\zeta-1)^{\frac{3}{2}} - \frac{\sqrt{2}}{32}(\zeta-1)^{\frac{5}{2}}\right]$ is an approximation of the over-damped τ when $\zeta \to 1$.

The relaxation time τ is the time *constant* for an exponential decay of the system towards equilibrium. We saw that τ depends on the damping rate ζ and thus on the regime. In Figure 2.4b, which shows the ζ-dependence of τ, we see that the relaxation time in the under-

and over-damped regimes converge to a minimum value τ_0 at $\zeta = 1$ (the critical regime). For $\zeta \to 0$ and $\zeta \to \infty$, on the other hand, $\tau \to \infty$. This means that with zero or infinite damping, the system will never reach its equilibrium position (in the first case the system will oscillate indefinitely, whereas in the second case it will remain immobile). The strongly-damped side of Figure 2.4b shows the linear limit of the relaxation time, $\tau(\zeta) = 2\zeta/\omega_0$, given in Equation 2.2.9. We can see that it is a good approximation when $\zeta \geq 3$: Equation 2.2.8 gives $\tau_o\,(3) \approx \frac{5.83}{\omega_0}$ and Equation 2.2.9 gives $\tau_o\,(3) = \frac{6}{\omega_0}$.

2.2.3 Permanent regime with harmonic driving force

2.2.3.1 General equation

A harmonic driving force means that $f(t)$ is sinusoïdal:

$$f(t) = F_0 \cos(\omega t + \phi_0) = \mathrm{Re}\Big\{F_0 e^{i(\omega t+\phi_0)}\Big\} = \mathrm{Re}\big\{\underline{f}(t)\big\}, \tag{2.2.14}$$

where $\underline{f}(t)$ is the complex form of $f(t)$. To simplify, we take $\phi_0 = 0$. We are interested in the harmonic response of the system and therefore we are looking at the response with the form:

$$u(t) = U\cos(\omega t + \phi) = \mathrm{Re}\Big\{U e^{i(\omega t+\phi)}\Big\} = \mathrm{Re}\Big\{\underline{U} e^{i(\omega t)}\Big\} \quad \text{with} \quad \underline{U} = U e^{i\phi}. \tag{2.2.15}$$

The susceptibility is given by Equation 2.2.4 with $p = i\omega$:

$$\begin{aligned}
\underline{\chi}(\omega) = \frac{\underline{U}(\omega)\cancel{e^{i\omega t}}}{F_0\cancel{e^{i\omega t}}} &= \frac{\chi_0\omega_0^2}{\omega_0^2 - \omega^2 + 2i\zeta\omega_0\omega} \\
&= \frac{\chi_0\omega_0^2(\omega_0^2 - \omega^2 - 2i\zeta\omega_0\omega)}{(\omega_0^2 - \omega^2 + 2i\zeta\omega_0\omega)(\omega_0^2 - \omega^2 - 2i\zeta\omega_0\omega)} \\
&= \frac{\chi_0\omega_0^2(\omega_0^2 - \omega^2 - 2i\zeta\omega_0\omega)}{(\omega_0^2 - \omega^2)^2 + 4\zeta^2\omega_0^2\omega^2} \\
&= \chi'(\omega) - i\chi''(\omega),
\end{aligned} \tag{2.2.16}$$

$$\text{with} \quad \chi'(\omega) = \frac{\chi_0\omega_0^2(\omega_0^2 - \omega^2)}{(\omega_0^2 - \omega^2)^2 + 4\zeta^2\omega_0^2\omega^2} \tag{2.2.17}$$

$$\text{and} \quad \chi''(\omega) = \frac{2\chi_0\zeta\omega_0^3\omega}{(\omega_0^2 - \omega^2)^2 + 4\zeta^2\omega_0^2\omega^2}. \tag{2.2.18}$$

To study the system we look at its harmonic response, i.e. the frequency dependence of $\underline{\chi}(\omega)$. The latter is defined by its amplitude and its phase:

$$\chi(\omega) = |\underline{\chi}(\omega)| = \sqrt{\underline{\chi}(\omega)\underline{\chi}(\omega)^*} = \frac{\chi_0\omega_0^2}{\sqrt{(\omega_0^2-\omega^2)^2+4\zeta^2\omega_0^2\omega^2}} \tag{2.2.19}$$

$$\Phi(\omega) = \arg(\underline{\chi}(\omega)) = -\arctan\left(\frac{2\zeta\omega_0\omega}{\omega_0^2-\omega^2}\right) \tag{2.2.20}$$

2.2.3.2 Application to the neutron scattering measurements

The intensity of neutrons scattered by the system during a neutron experiment is proportional to the dissipative part of the susceptibility. This is a direct manifestation of the *fluctuation-disspation* theorem presented in Appendix A.1. The dissipated energy is contained in the imaginary part of the admittance ($\chi''(\omega)$). If we multiply $\chi''(\omega)$ with $\frac{\hbar^4}{\hbar^4}$, then Equation 2.2.18 becomes a function of energies. With $E = \hbar\omega$ (the energy transfer), $E_0 = \hbar\omega_0$ (the resonance energy of the undamped oscillator) and $D = 2\zeta E_0$, Equation 2.2.18 becomes

$$\chi''(E) = \frac{\chi_0 D E_0^2 E}{(E_0^2-E^2)^2+D^2E^2}. \tag{2.2.21}$$

We see that D is inversely proportional to the under-damped relaxation $\tau_\mathrm{u} = 1/(\zeta\omega_0)$ (Equation 2.2.13):

$$D = \frac{2\hbar}{\tau_\mathrm{u}}. \tag{2.2.22}$$

It is also interesting to rewrite Equation 2.2.21 with $\Gamma = \frac{E_0^2}{D}$ and $A = \chi_0\Gamma$:

$$\chi''(\omega) = \frac{AE}{(\frac{E^2}{D}-\Gamma)^2+E^2}, \tag{2.2.23}$$

where Γ is inversely proportional to the strongly over-damped relaxation time $\tau_\mathrm{o} \approx 2\zeta/\omega_0$ (Equation 2.2.9):

$$\Gamma = \frac{\hbar}{\tau_\mathrm{o}}. \tag{2.2.24}$$

2.2.3.3 Asymptotic behaviour

During an energy scan with a triple axis spectrometer (TAS), we have access to a limited energy range ($0.2\mathrm{meV} \leq \Delta E \leq 5\mathrm{meV}$ for our inelastic neutron scattering experiments, on the energy loss side). Therefore the energy of the magnetic excitations, that we are measuring can be lower of higher than this range, and we only observe the head or the tail of these *out of range* signals.

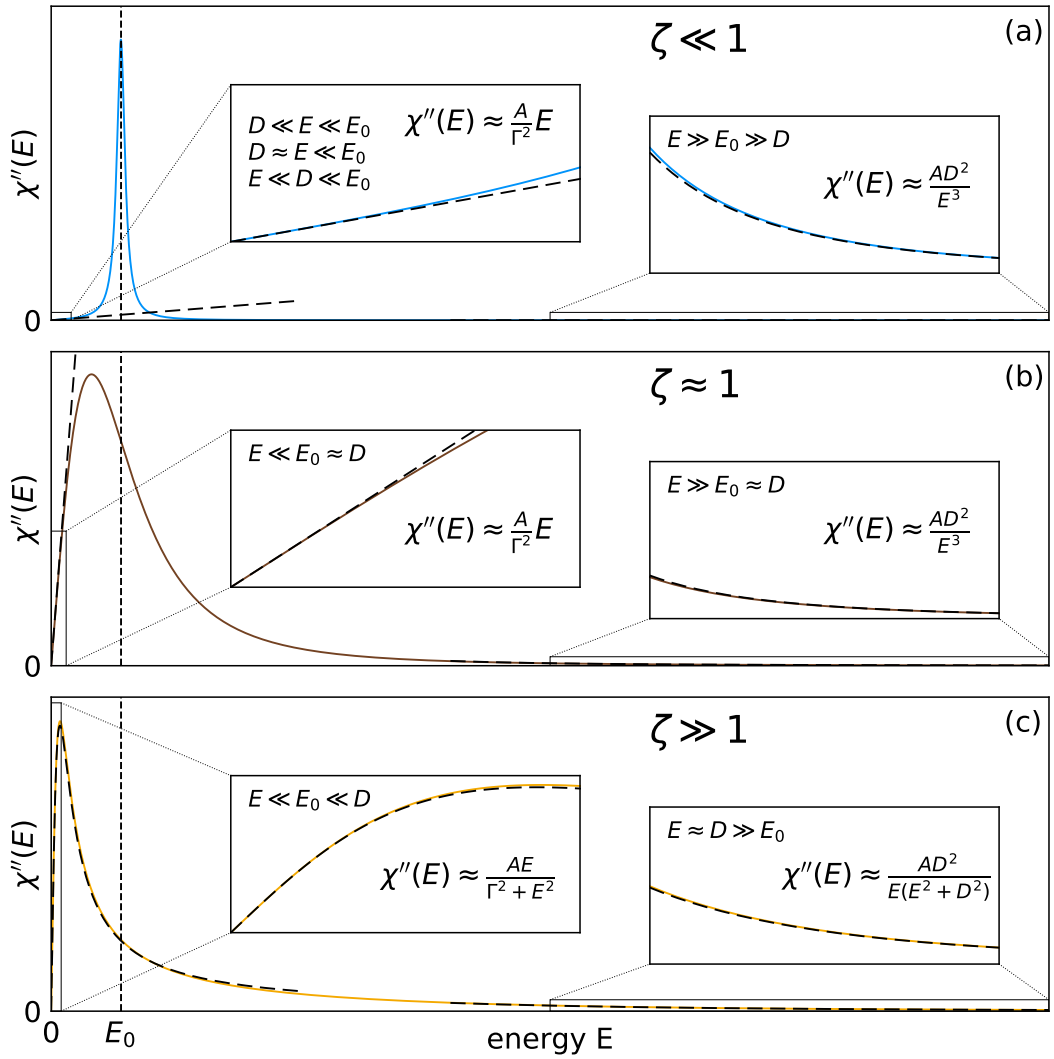

Figure 2.5: This figure shows the asymptotic behaviour of a damped harmonic oscillator $\chi''(\hbar\omega)$ in the strongly under-damped regime, around the critical regime and in the strongly over-damped regime. The small dashes vertical line is the position of the resonance energy E_0. **(a)** shows $\chi''(\hbar\omega)$ in the weakly-damped regime (blue curve) and its asymptotic behaviours (big dashes curves). **(b)** shows $\chi''(\hbar\omega)$ around the critical regime (brown curve) and its asymptotic behaviours (big dashes curves). **(c)** shows $\chi''(\hbar\omega)$ in the strongly-damped regime (yellow curve) and its asymptotic behaviours (big dashes curves).The left and right insets are zoomed-in portions of the head and the tail of χ'', respectively. The right side of the equation in the insets are the approximation functions for χ'' and the inequalities give the validity domains of those approximations.

Figure 2.5 shows the asymptotic behaviours of χ'', the dissipative part of the general damped harmonic oscillator (DHO), where the magnified areas depicted by thin lined black boxes represent the energy range that is available for the measurement.

***E* ≪ *E*$_0$:** the excitation is at higher energies than the scanned energy range and we measure its *head*. This is represented by the left zooming boxes in Figure 2.5. The most suitable function to fit the signal depends on the damping regime of the excitation.

i strongly under-damped regime ($\zeta \ll 1$): $\chi''(E) \approx \frac{AE}{\Gamma}$ represented in Figure 2.5a, where $A = \chi_0\Gamma$.

ii critically-damped regime ($\zeta \approx 1$): $\chi''(E) \approx \frac{AE}{\Gamma}$ represented in Figure 2.5b.

iii strongly over-damped regime ($\zeta \gg 1$):

$$\chi''(E) \approx \frac{AE}{\Gamma^2 + E^2} \tag{2.2.25}$$

represented in Figure 2.5c.

***E* ≫ *E*$_0$:** the excitation is within the resolution of the instrument; the signal is part of the quasi-elastic scattering and we measure its *tail*. This is represented by the right zooming boxes in Figure 2.5. Again, the most suitable function to fit the signal depends on the damping regime of the excitation.

i strongly under-damped regime ($\zeta \ll 1$): $\chi''(E) \approx \frac{AD^2}{E^3}$ represented in Figure 2.5a.

ii critically-damped regime ($\zeta \approx 1$): $\chi''(E) \approx \frac{AD^2}{E^3}$ represented in Figure 2.5b.

iii strongly over-damped regime ($\zeta \gg 1$):

$$\chi''(E) \approx \frac{AD^2}{E\left(E^2 + D^2\right)} \tag{2.2.26}$$

represented in Figure 2.5c.

***E* ≈ *E*$_0$:** when the energy of the measured excitation is within the accessible energy range, we use use the general form of χ'' given in Equation 2.2.21.

2.3 Spin fluctuation theory

At zero temperature, there are no thermal fluctuations and therefore the phase transitions are driven by fluctuations of other non-thermal degrees of freedom. The spin fluctuation theory

suggests that the phase transitions is caused by the fluctuation of spins. This model explains the emergence of new *hidden* magnetic ordered phases at a quantum phase transition. Here we present the theory as presented by G.G. Lonzarich in *The Magnetic Electron* [41].

2.3.1 The limits of the model

In a conductor, electrons can move freely and usually at considerably high velocity, whereas the spin alignment happens locally due to the Coulomb interaction. In a 'hidden' magnetic ordered phase the spin alignment is not static, but it fluctuates slowly and with large amplitudes, whereas in a conventional magnetic ordered state such as FM or anti-ferromagnetic (AFM), the fluctuations have static wave-vectors and amplitude. At 0K, the transition from the magnetic ordered phase to 'hidden' magnetic ordered phase happens without any increase of the entropy and therefore the latter cannot be qualified as disordered state. An intuitive representation of the phase transition between ordered and 'hidden' ordered phases is that the ordered phase is 'melting' to become the 'hidden' magnetic ordered phase. This transition is not driven by temperature change, instead it happens at constant temperature and is provoked by tuning a non-thermal parameter (e.g. doping [3] or magnetic field [42]).

The goal of the spin fluctuation theory presented here is to find a model for the interaction field between the spins of the electrons. The main assumption is that the moments $\boldsymbol{\mu}$ carried by the electrons are coupled by a potential $-\boldsymbol{\mu} \cdot \boldsymbol{h_m}$, where $\boldsymbol{h_m} = \lambda \boldsymbol{m}$ is the exchange field and λ the phenomenological exchange field parameter.

We consider a homogeneous and isotropic system with cubic lattices and states with no symmetry-breaking transitions. For simplicity reasons, we consider only low energy ($\omega < \omega_c$) and small wave-vector ($\boldsymbol{q} < \boldsymbol{q_c}$) fluctuations, with ω_c small compared to the Fermi energy and $\boldsymbol{q_c}$ small compared to the dimension of the Brillouin zone.

2.3.2 The scalar dynamical field

We consider an electron interacting with another through a scattering process with exchange of a boson with the interaction field. An electron can also interact with itself, by first emitting and then recapturing a boson. The electrons, which become quasi-particles, are characterised by their renormalised mass and cross section. The latter can be considered as the size of the quasi-particle. This model gives a linear temperature dependence for the heat capacity C and a quadratical temperature dependence for the resistivity ρ, in the paramagnetic regime.

This is known as the *Fermi liquid theory* and the renormalised quasi-particle's mass and cross section (size) may be represented by the constants C/T and ρ/T^2 respectively. Near the phase transition, the Fermi liquid theory does not correctly describe the physical properties anymore and instead $C \propto T\log(T)$ (observed in $NbFe_2$ for instance [1]) and $\rho \propto T^{5/3}$. The effective mass and size of the quasi-particles then become proportional to $C/T \propto \log(T)$ and $\rho/T^2 \propto T^{-1/3}$, respectively, and become infinite at 0K. This divergence can be interpreted as a long range interaction between quasi-particles.

The objective is to find the average magnetisation as a function of space and time $M(\boldsymbol{r}, t)$ when an external magnetic field $H_{\text{ext}}(\boldsymbol{r}, t)$ is applied. To derive the scalar dynamical field, we start with the static scalar field with a static and uniform applied magnetic field $H_{\text{ext}}(r, t) = H_{\text{ext}}$. The magnetisation $M(r, t)$ is given by the Taylor expansion of H as a function of the order parameter M. In this case the magnetisation is static and uniform and $M(r, t) = M$. H is an odd function and

$$H = a_0 M + b_0 M^3, \tag{2.3.1}$$

where $1/a_0$ is the Pauli susceptibility and b_0 is the anharmonicity parameter. Equation 2.3.1 gives the magnetisation induced by the application of the external field H_{ext} with no consideration of the feedback from the exchange field λM. Now if we also include the latter, Equation 2.3.1 becomes

$$H = aM + bM^3, \tag{2.3.2}$$

where $1/a = 1/(a_0 - \lambda) = \chi^{-1}$ is the enhanced susceptibility (if $a > 0$), $b = b_0$ and supposed positive.

Now we consider non-uniform, but static external field $H_{\text{ext}}(\boldsymbol{r})$. This induces a space-dependent magnetisation $M(\boldsymbol{r})$ in the system and H is now a functional of $M(\boldsymbol{r})$. The induced magnetisation is given by Ginzburg-Landau equation

$$H(\boldsymbol{r}) = H[M] = aM + bM^3 - c\nabla^2 M, \tag{2.3.3}$$

where $M = M(\boldsymbol{r})$ is space dependent and c is a parameter that gives the resistance against spatial modulations. For a FM system, $c > 0$.

We define an effective field which represents the 'distance' of the system to its equilibrium state:

$$H_{\text{eff}} = H - H[M]. \tag{2.3.4}$$

At equilibrium, Equation 2.3.3 is verified and $H_{\text{eff}} = 0$.

We now include the dynamic aspect by considering the time evolution of the system. In the paramagnetic state, we expect that the relaxation of the magnetisation $M(\boldsymbol{r}, t)$ towards equilibrium $H_{\text{eff}} = 0$ satisfies

$$\dot{M}(\boldsymbol{r}, t) = \gamma(\boldsymbol{r}) * H_{\text{eff}}(\boldsymbol{r}, t), \tag{2.3.5}$$

where $\dot{M}$ is the temporal derivative of M, γ is the relaxation function and $*$ is the spatial convolution.

From now on, we look at the scalar dynamical field in leading order in M. This means that we consider only the terms linear in M and Equation 2.3.3 becomes

$$H[M(\boldsymbol{r}, t)] = aM(\boldsymbol{r}, t) - c\nabla^2 M(\boldsymbol{r}, t). \tag{2.3.6}$$

Using equations 2.3.4 and 2.3.6 in Equation 2.3.5 yields

$$\dot{M}(\boldsymbol{r}, t) = \gamma(\boldsymbol{r}) * \left[H_{\text{ext}}(\boldsymbol{r}, t) - \left(aM(\boldsymbol{r}, t) - c\nabla^2 M(\boldsymbol{r}, t)\right)\right]. \tag{2.3.7}$$

With no external field, taking the spatial Fourier transform[1] of this equation and developing the convolution[2] product gives

$$\dot{M}_q(t) = -\int_{-\infty}^{\infty} e^{-i\boldsymbol{q}\cdot\boldsymbol{r}} \int_{-\infty}^{\infty} \gamma(\boldsymbol{r} - \boldsymbol{u}) \left[aM(\boldsymbol{u}, t) - c\nabla^2 M(\boldsymbol{u}, t)\right] \mathrm{d}\boldsymbol{u}\mathrm{d}\boldsymbol{r} \tag{2.3.8}$$

$$= -\int_{-\infty}^{\infty} e^{-i\boldsymbol{q}\cdot(\boldsymbol{r}-\boldsymbol{u})} e^{-i\boldsymbol{q}\cdot\boldsymbol{u}} \int_{-\infty}^{\infty} \gamma(\boldsymbol{r} - \boldsymbol{u}) \left[aM(\boldsymbol{u}, t) - c\nabla^2 M(\boldsymbol{u}, t)\right] \mathrm{d}\boldsymbol{u}\mathrm{d}\boldsymbol{r} \tag{2.3.9}$$

$$= -\gamma_q \int_{-\infty}^{\infty} \left[aM(\boldsymbol{u}, t) - c\nabla^2 M(\boldsymbol{u}, t)\right] e^{-i\boldsymbol{q}\cdot\boldsymbol{u}} \mathrm{d}\boldsymbol{u} \tag{2.3.10}$$

$$= -\gamma_q \left(a + cq^2\right) M_q(t), \tag{2.3.11}$$

where γ_q and $M_q(t)$ are the components of the spatial Fourier transform of $\gamma(\boldsymbol{r})$ and $M(\boldsymbol{r}, t)$. $\chi_q^{-1} = a + cq^2$ is the inverse of the static susceptibility. Solving the first order differential Equation 2.3.11 gives

$$M_q(t) = M_0 e^{-\Gamma_q t}, \tag{2.3.12}$$

[1] $\hat{f}(q) = \int_{-\infty}^{\infty} f(r) e^{-iqr} \mathrm{d}r$

[2] $f * g(x) = \int_{\infty}^{\infty} f(x - u) q(u) \mathrm{d}u$

where $\Gamma_q = \gamma_q/\chi_q$ is the relaxation rate of the moment to equilibrium without external field. Thus in zero magnetic field and in leading order in M, the Fourier components of the magnetisation have an exponential time-relaxation.

We now consider a non-zero external magnetic field that varies in time and space and thus $H(\boldsymbol{r}, t) \neq 0$. Equation 2.3.11 becomes

$$\dot{M}_q(t) = \gamma_q \left[H_q(t) - (a + cq^2)M_q(t)\right]. \tag{2.3.13}$$

And finally, the temporal Fourier transform[3] of the latter equation gives

$$\dot{M}_{q,\omega} = -i\omega M_{q,\omega} \tag{2.3.14}$$

$$= \gamma_q \left[H_{q,\omega} - (a + cq^2)M_{q,\omega}\right], \tag{2.3.15}$$

where $H_{q,\omega}$ and $M_{q,\omega}$ are the Fourier components of, respectively, the equilibrium field and the magnetisation. The general linearised susceptibility $\chi_{q,\omega}$ is defined as

$$H_{q,\omega} = \chi^{-1}_{q,\omega} M_{q,\omega}, \tag{2.3.16}$$

and from Equation 2.3.14

$$\chi^{-1}_{q,\omega} = \chi^{-1}_q \left(1 - i\frac{\omega}{\Gamma_q}\right) \tag{2.3.17}$$

$$\chi^{-1}_q = \chi^{-1} + cq^2 \tag{2.3.18}$$

$$\Gamma_q = \gamma_q \chi^{-1}_q. \tag{2.3.19}$$

$\chi_{q,\omega}$ is the general susceptibility, χ_q it the susceptibility at $\omega = 0$ and χ is the susceptibility at $\omega = 0$ and $q = 0$. γ_q are the Fourier components of the relaxation function introduced in Equation 2.3.7. If the exchange field does not depend on $\dot{M}$, then

$$\gamma_q = \gamma q^n, \tag{2.3.20}$$

where γ is a constant and usually $n = 1$ for small q. In homogeneous and non-interacting Fermi-systems, the electron moves almost freely and has a ballistic trajectory. Hence, when the

[3] $\hat{f}(\omega) = \int_{-\infty}^{\infty} f(t)e^{i\omega t}\mathrm{d}t$

electrons' mean free path is of the order of the magnetic wavelength λ_e, we have

$$\gamma_q \propto \tau^{-1}, \tag{2.3.21}$$

where τ is the time it takes for the ballistic electron to cover a distance $\lambda_e = 2\pi/q$ (the wavelength of a magnetic excitation) at Fermi velocity v_F:

$$\tau = \frac{2\pi}{v_F q}. \tag{2.3.22}$$

Thus we find that

$$\gamma_q \propto \frac{v_F q}{2\pi} \tag{2.3.23}$$

and

$$\Gamma_q \propto q \quad \text{(n=1)} \quad . \tag{2.3.24}$$

This is the *Landau damping* and it is observed in paramagnetic systems for instance.

If now the wavelength of the excitations grows and become much bigger than the electrons' mean free path, the motion becomes diffusive and $\tau \propto \lambda_e^2$. Thus, near the critical point, the fluctuations slow down and $\Gamma_q \propto q^2$ (n=2) .

If we now go back to the generalised linear susceptibility in Equation 2.3.17, it can be written as

$$\chi_{q,\omega} = \left[\chi_q^{-1}\left(1 - i\frac{\omega}{\Gamma_q}\right)\right]^{-1} \tag{2.3.25}$$

$$= \frac{\Gamma_q \chi_q}{\Gamma_q - i\omega} \tag{2.3.26}$$

$$= \frac{\Gamma_q \chi_q}{\Gamma_q - i\omega} \times \frac{\Gamma_q + i\omega}{\Gamma_q + i\omega} \tag{2.3.27}$$

$$= \frac{\Gamma_q^2 \chi_q}{\Gamma_q^2 + \omega^2} + i\frac{\Gamma_q \chi_q \omega}{\Gamma_q^2 + \omega^2}. \tag{2.3.28}$$

We recognise in Equation 2.3.28 a DHO in the over-damped regime (Equation 2.2.25 in section 2.2.3.3). Thus, in the paramagnetic state, near a ferromagnetic quantum critical point, we expect the dissipation of the magnetic excitations, which is given by the imaginary part of generalised linear susceptibility, to behave like a DHO with infinite damping.

2.3.3 Temperature dependence

We can define a dimensionless function for the thermal populations of the different modes. In the limit of the infinitely damped DHO limit obtained in Equation 2.3.28, the dimensionless thermal population of the different modes is given by

$$n_q(\Gamma/T) = \frac{2}{\pi}\int_0^\infty n_\omega \frac{\omega}{\omega^2+\Gamma_q^2}\mathrm{d}\omega \tag{2.3.29}$$

$$\approx \frac{T}{\Gamma_q\left(1+\frac{3\Gamma_q}{\pi T}\right)}, \tag{2.3.30}$$

where $n_\omega = \frac{1}{e^{\hbar\omega/(\mathrm{k_B}T)}-1}$ is the Bose function. Γ_q represents the characteristic energy of the mode q.

Assuming that each modes are statistically independent and that the characteristic energy Γ_q of each mode depends on the thermal populations n_q of all the other modes, the thermal correction Δa (or $\Delta\chi^{-1}$) of the 0K coefficient a in Equation 2.3.7 is

$$\begin{aligned}\Delta a &= 5b\widehat{\sum_q}\gamma_q n_q(\frac{\Gamma_q}{T}) \\ &= 5b\widehat{\sum_q}\gamma_q n_q\left(\frac{\gamma_q}{T}(a+\Delta a+cq^2)\right),\end{aligned} \tag{2.3.31}$$

where $\widehat{\ }$ indicates the sum over the modes per unit volume and a, b are the 0K parameters in Equation 2.3.2. From Equation 2.3.30, we see that $n_q \propto T^2/\Gamma_q^2$ in the low temperature limit, and $n_q \propto T/\Gamma_q$ in the high temperature limit. Thus, from Equation 2.3.31, away from the critical point, we expect $\Delta\chi^{-1} \propto T^2$ at low temperatures and $\Delta\chi^{-1} \propto T$ at high temperatures. From Equation 2.3.19, we expect the same for Γ_q.

The temperature dependence in Equation 2.3.31 is given by $\widehat{\sum}_q \gamma_q n_q$, which, in the general case, becomes

$$\sum_q q^n n_q \propto T^s \int_0^{x_c} \frac{x^{s-2}}{1+x}\mathrm{d}x, \tag{2.3.32}$$

where $x_c \propto T^{-1}$ is a cut-off and

$$\begin{cases} s &= \frac{d+n}{n} \quad \text{away from the critical point} \\ s &= \frac{d+n}{n+2} \quad \text{near the critical point} \quad , \end{cases} \tag{2.3.33}$$

where d is the dimension of the system and n is the coefficient in Equation 2.3.20. Equa-

tion 2.3.32 gives the asymptotic temperature dependence of the susceptibility in the PM state at low temperatures. Away the critical point, usually $s > 2$ and evaluating Equation 2.3.32 in leading order in T gives T^2, independently of the dimension, as expected from the Fermi liquid theory. If we now look near the critical point, usually $s < 2$, and Equation 2.3.32 varies as T^s. For example, a three dimensional system, $d = 3$, with Landau damping, $n = 1$, gives $s = 4/3$ and thus $\chi^{-1} \propto T^{\frac{4}{3}}$.

Chapter 3

Properties of the $Nb_{1-y}Fe_{2+y}$ system

3.1 The $NbFe_2$ compound

The C14 Laves phase $Nb_{1-y}Fe_{2+y}$, an itinerant d-electron ferromagnet, is an ideal study case of the theoretically predicted scenario in which a ferromagnetic quantum critical point (FM QCP) becomes masked by modulated magnetic order. The system undergoes a continuous paramagnetic (PM)-ferromagnetic (FM) phase transition that can be suppressed with substitution of Fe by Nb. However, a magnetic phase with zero net magnetisation replaces the PM-FM transition at lower temperatures. The break down of the Fermi liquid behaviour near stoichiometric concentrations [1] indicate a masked FM QCP at zero magnetic field and at ambient pressure.

3.1.1 Structure of $NbFe_2$

Stoichiometric $NbFe_2$ forms as a hexagonal C14 Laves structure with lattice parameters of $a = b = 4.8401(2)$Å and $c = 7.8963(6)$Å [36] and belongs to the space group $P6_3/mmc$. The unit cell, represented in Figure 3.1, contains four $NbFe_2$ units formula and is thus composed of eight Fe atoms and four Nb atoms.

The Fe atoms are distributed on two different sites, with six atoms on the $6h$ sites and two atoms on the $2a$ sites as shown in Figure 3.1a [43]. Four Nb atoms occupy the $4f$ sites, which are located between the Fe layers [43].

Table 3.1 gives the nearest neighbour distances for each atom site in the unit cell and we can see that those distances are very similar. As a consequence, dopant sites are more likely to be determined by the bonding network between Fe atoms [43]. Density Functional Theory (DFT)

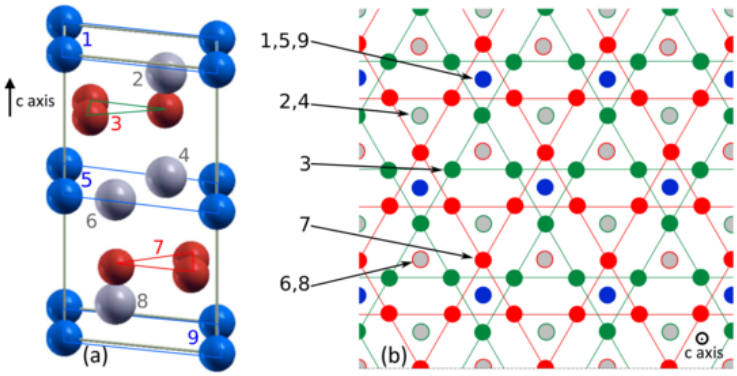

Figure 3.1: **(a)** shows the crystal structure of $NbFe_2$ with six Fe atoms on *6h* sites (red) and two Fe atoms on *2a* sites (blue). **(b)** represents the view along the c axis of the structure, which reveals the stacked Kagome layers. The *6h* sites are on the two opposed Kagome layers and the *2a* sites are on the principal axes of the hexagonal structure. Four Nb atoms (grey) on *4f* sites labeled 2, 4, 6, and 8, are located between the five layers of Fe-atoms labeled 1, 3, 5, 7 and 9 in (a). The image is from [43].

Table 3.1 Distance of the nearest neighbour for each atomic site in stoichiometric $NbFe_2$. Values from [43].

sites	**distance (Å)**
Fe($6h$)-Fe($2a$)	2.42
Fe($6h$)-Fe($6h$)	2.37
Fe($2a$)-Fe($2a$)	3.95
Nb-Fe($2a$)	2.84
Nb-Fe($6h$)	2.81
Nb-Nb	2.89

calculations, using the generalised-gradient approximation with the Perdew-Burke-Ernzerhof correlation functional in the Stoner framework, suggest that for Nb doping with $NbFe_2$ the substitution of Fe($6h$) sites is energetically more favourable than the substitution of Fe($2a$) sites [43].

3.1.2 Characterisation of the magnetic phases in $Nb_{1-y}Fe_{2+y}$

In early measurements, Yamada et al. observed the coexistence of ferromagnetism and anti-ferromagnetism in $(Zr_{1-y}Nb_y)Fe_2$ [44]. Several years later, Yamada and Sakata performed Nb nuclear-magnetic resonance (NMR) and magnetisation measurements in several samples of $Nb_{1-y}Fe_{2+y}$ at different concentrations y and reported an anti-ferromagnetic (AFM) phase near

stoichiometric concentration [45]. Figure 3.2a shows the phase diagram made by the authors. With increase of the Nb concentration, the Néel temperature of the AFM-PM phase transition was observed to quickly decrease to 0K and only the PM phase to survive below $y \approx -0.006$ [45]. Shiga and Nakamura also measured a weak FM phase in off-stoichiometric samples when Nb or Fe are significantly in excess [46]. These results lead to the initial temperature-doping concentration phase diagram shown in Figure 3.2a.

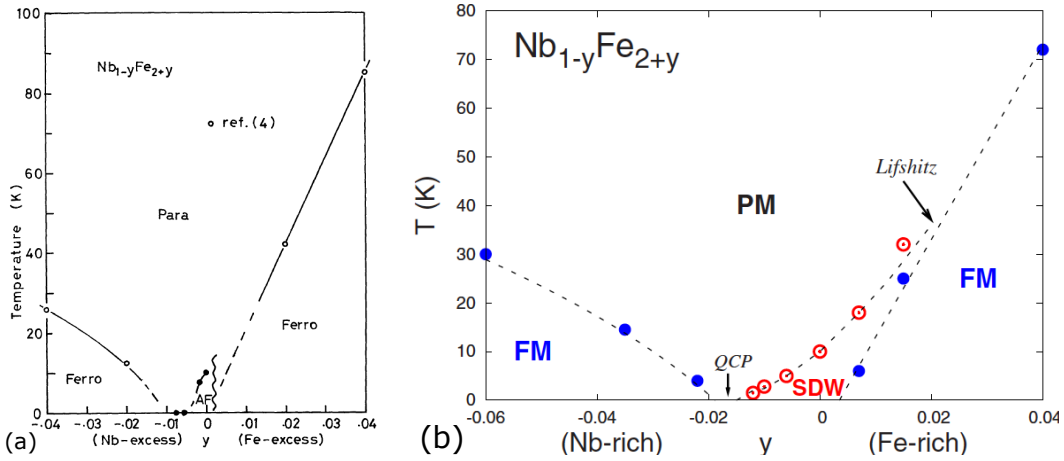

Figure 3.2: **(a)** represents the phase diagram of the temperature against the Fe concentration in $Nb_{1-y}Fe_{2+y}$ as observed by Yamada and Sakata in [45] and Shiga and Nakamura in [46]. Picture from [45]. **(b)** is the expected phase diagram based on the experimental results from [36], where "QCP" indicates the position of the supposed FM QCP. Picture from [36]. Nb atoms are substituted with Fe atoms on the Fe-rich side of the diagram ($y > 0$) and Fe atoms are substituted by Nb atoms on the Nb-rich side of the diagram ($y < 0$).

More recently, Brando et al. measured the magnetic properties in the slightly Fe-rich $Nb_{1-0.015}Fe_{2+0.015}$ polycrystal [1]. The Curie-Weiss behaviour of the inverse susceptibility and the positive intersects of the Arrott plots (upper inset) at 2K and at 20K, in Figure 3.3, indicate a FM state below 20K. The electrical resistivity measurement (lower inset in Figure 3.3) has a $T^{5/3}$ temperature-dependence, which suggest a break-down of the Fermi liquid behaviour.

Later measurements, by Friedemann et al., of $Nb_{1-y}Fe_{2+y}$ high quality single crystals also recorded a FM ground state in $Nb_{1-0.015}Fe_{2+0.015}$ and indications of a spin density wave (SDW) state at higher temperature [42]. The real part of the susceptibility, thermal expansion and resistivity measurements in Figure 3.4 show a Curie temperature of $T_C \approx 24K$ and a Néel temperature of $T_N \approx 32K$. The data also indicates strong thermal hysteresis at the possible SDW-FM phase transition, which is evidence of its 1st order nature..

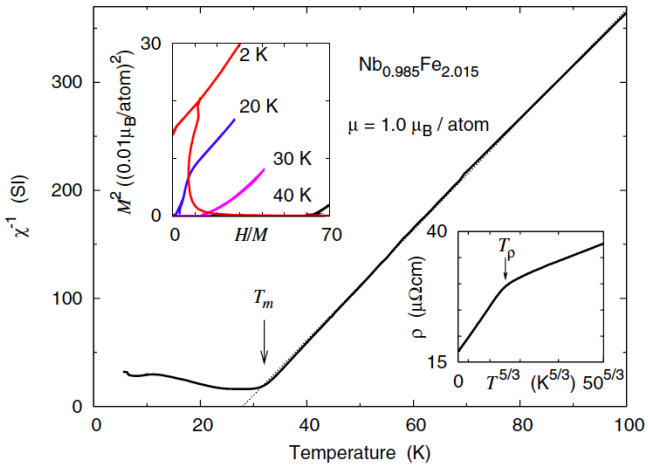

Figure 3.3: Magnetic properties of $Nb_{0.985}Fe_{2.015}$. The main figure represents the inverse susceptibility as a function of the temperature, the upper inset shows the Arrott plots measured at different temperatures and the lower inset contains a the resistivity measurement. Figure from [1]

The real part of the susceptibility of the stoichiometric sample and the slightly Nb-rich sample in Figure 3.4 have only one kink in their temperature dependence, which suggests that the ground state is a SDW. Additionally, a $T^{3/2}$ temperature-dependence of the resistivity (Figure 3.5a) and a $\log(T)$ temperature-dependence of the Sommerfeld coefficient $\gamma = C/T$ (Figure 3.5b) have been recorded in the slightly Nb-rich $Nb_{1.01}Fe_{1.99}$ [1]. This non-Fermi liquid (NFL) behaviour is the sign of a possible nearby quantum critical point (QCP) and experimental results are consistent with a two-order-parameter Landau theory [42]. The latter finding leads to a prediction of the precise location of the hidden FM QCP in the assumed SDW phase and of the first order nature of the FM-SDW phase transition [42]. Moreover, the $T^{3/2}$ temperature dependence of the resistivity is expected for 3D AFM fluctuations, whereas $T^{5/3}$ temperature dependence of the resistivity is expected for 3D FM fluctuations and thus, the resistivity might indicate the proximity to two types of magnetic order.

The two low temperature FM phases for $y \leq -0.02$ and for $y \geq 0.02$ are intrinsic to the $Nb_{1-y}Fe_{2+y}$ and are different in nature [36]. Based on magnetisation, resistivity, susceptibility and heat capacity measurements, Moroni et al. proposed the more complete version of the $Nb_{1-y}Fe_{2+y}$ phase diagram, given in Figure 3.2b. They also speculated that the AFM phase identified by Yamada and Sakata [45] is a helical or spiral SDW phase [36], which disappears at $y = -0.015$ and with a wave vector $\boldsymbol{Q}_{\mathbf{SDW}}$ connecting continuously to the FM ordering wave

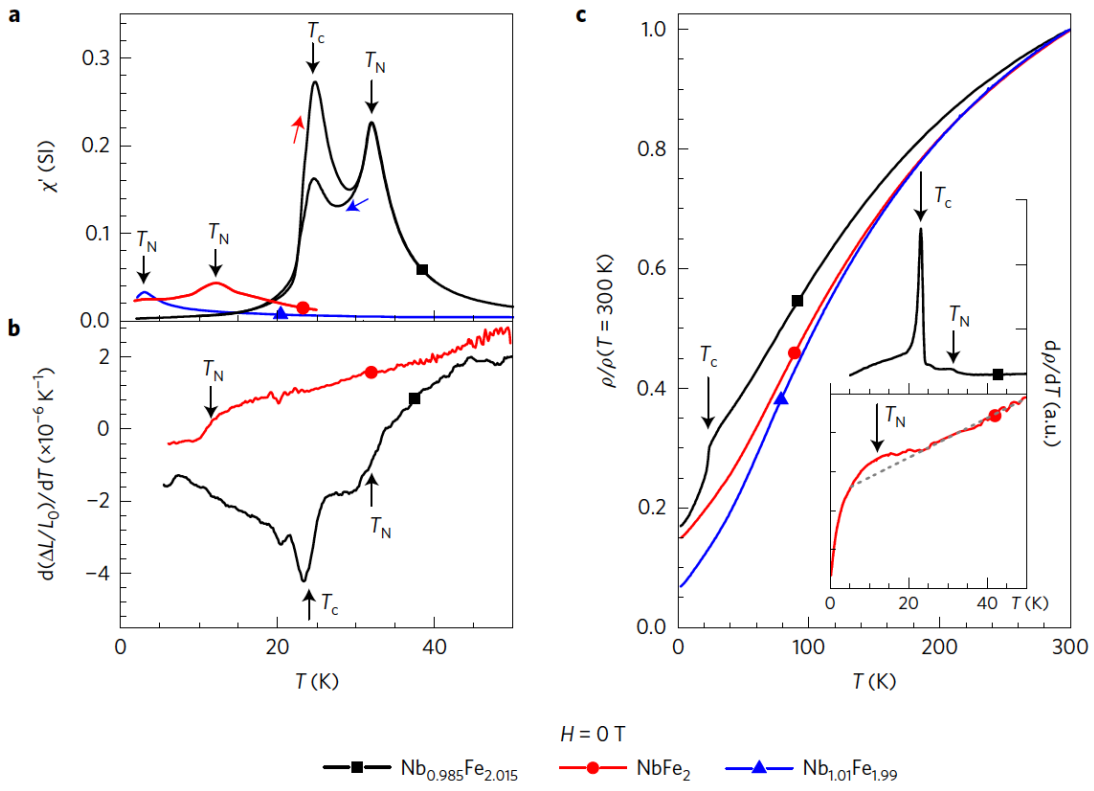

Figure 3.4: Temperature dependence of, the real part of the AC-susceptibility measured along the c axis **(a)**, the thermal expansion along the c axis **(b)** and the resistivity **(c)** in single crystals $Nb_{1.01}Fe_{1.99}$ (blue), $NbFe_2$ (red) and $Nb_{0.985}Fe_{2.015}$ (black). The inset in (c) gives the temperature-dependence of $\frac{d\rho}{dT}$. In (a), the red arrow is for warming and the blue arrow is for cooling. Results and figure from [42]

vector at the Lifshitz point (Figure 3.2b).

Thus $Nb_{1-y}Fe_{2+y}$ has a rich phase diagram, which four different magnetic phases (two FM phases, a possible SDW phase and a PM phase) across a small range of doping concentration. It is not clear however whether the ground state for $|y| \geq 0.02$ is ferromagnetic or ferrimagnetic. Subedi and Singh performed DFT calculations, within the local spin-density approximation and the general potential linearised augmented plane-wave method [47], to calculate the electronic structure of stoichiometric $NbFe_2$ and estimate the energy difference between the non-spin polarised case (Figure 3.6a) and several magnetic configurations. They found that the energetically most favourable ground state is the ferrimagnetic configuration given in Figure 3.6b with a moment of $1.18\mu_B$/Fe on the Fe($2a$) sites and an opposed moment of $-0.75\mu_B$/Fe on the Fe($6h$) sites [47]. The energy of this ferrimagnetic structure reduces the energy by 0.033eV

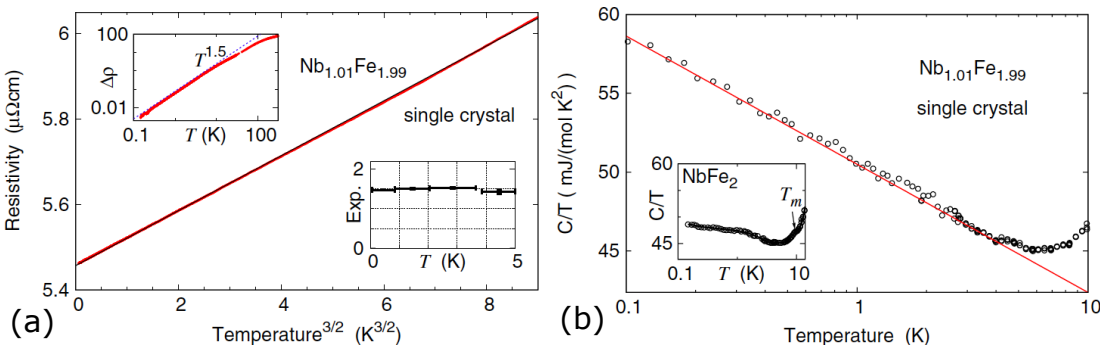

Figure 3.5: Resistivity measurements **(a)** and heat capacity measurements **(b)** in $Nb_{1.01}Fe_{1.99}$. Horizontal bars in the lower inset in (a) represent the temperature ranges and the vertical bars indicate the precision of the temperature-exponents. Figure from [1]

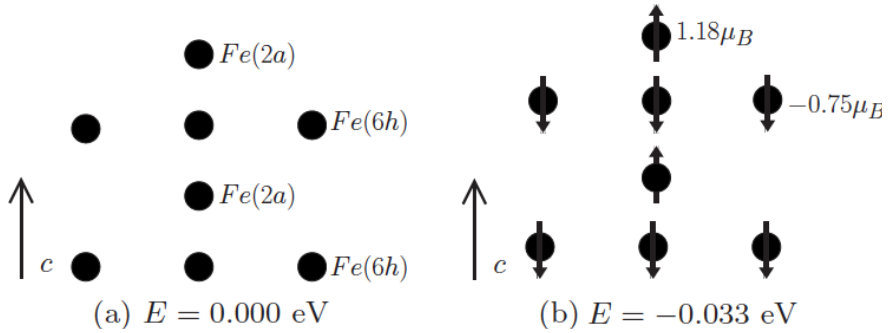

Figure 3.6: **(a)** shows the non-spin polarised structure of the $NbFe_2$ unit cell, which is used as reference energy for the other configurations of the magnetic structure calculated by Subedi and Singh [47]. **(b)** shows the spin configuration with the lowest calculated energy. Figure from [47]

compared to the non-spin polarised configuration. The authors also calculated a Nb-induced moment of $0.09\mu_B$/Nb in the same direction as the Fe($2a$)-induced moment for the ferrimagnetic configuration, which is thus significantly weaker than any Fe-induced moment.

The ferrimagnetic spin configuration was later supported by Compton scattering with a Fe($6h$)-induced moment of $0.4\mu_B$/Fe and a Fe($2a$)-induced moment of $-0.6\mu_B$/Fe [48]. However, muon spin relaxation and Mössbauer spectroscopy experiments point towards the FM ground state with a magnetic moment carried by the Fe atoms of about $0.15\mu_B$/Fe [2]. This contradicts the prior Compton scattering results and there is no definitive answer to how Fe-rich $Nb_{1-y}Fe_{2+y}$ orders magnetically in the ground state.

In conclusion, $Nb_{1-y}Fe_{2+y}$ presents a very good opportunity to study the scenario that pre-

dicts the emergence of a modulated magnetic ordered phase at the approach of a FM QCP. The second-order FM-PM phase transition extrapolates to 0K at zero pressure and zero field, which makes this compound very convenient to investigate. Many different experimental approaches were used to study $NbFe_2$, however, until today, neutron scattering measurements have always failed to detect experimental evidence representing the irrefutable confirmation of the presence of the SDW.

Chapter 4

Experimental

We investigate a possible ferromagnetic (FM) quantum critical point (QCP) hidden behind a spin density wave (SDW) phase in $NbFe_2$. To do that, we tune the $Nb_{1-y}Fe_{2+y}$ system across the temperature (T)-composition (y) phase diagram. The significant advantage with doping is that measurements are performed in an simpler experimental environment compared to other tuning parameters such as pressure of magnetic field. The inconvenience is that the ferromagnetic quantum critical point (FM QCP) is not approached continuously and that adding a new point across the phase diagram requires a new sample.

In this chapter we introduce the samples that are used to investigate magnetic order and excitations near the border of ferromagnetism in the $Nb_{1-y}Fe_{2+y}$ system and the instruments that we used for this purpose. The latter are all neutron based instruments that use the principle of neutron scattering. We will start with a presentation of the samples and their characteristics. Then we will have a look at the theory of neutron scattering, that includes unpolarised and polarised neutron scattering. Finally we will give an overview of the instruments, with some more emphasis on the polarised neutron instrument.

4.1 Samples

In the $Nb_{1-y}Fe_{2+y}$ system the 2nd order FM phase transition is tuned to low temperatures by doping, in particular the replacement of Fe by Nb. Doped samples do not show a significantly increased level of disorder as the relevant region of the phase diagram is within a 2% range in the Fe concentration. For this investigation, we have three high quality Fe-rich single crystals

of $NbFe_2$ at different concentrations (Figure 4.1): $y = 0.002$ (Sample A), $y = 0.14$ (Sample B) and $y = 0.019$ (Sample C). These samples were grown by William Duncan, Andreas Neubauer and Wolgang Münzer [49, 50] at the E21 institute of the Technical University of Munich.

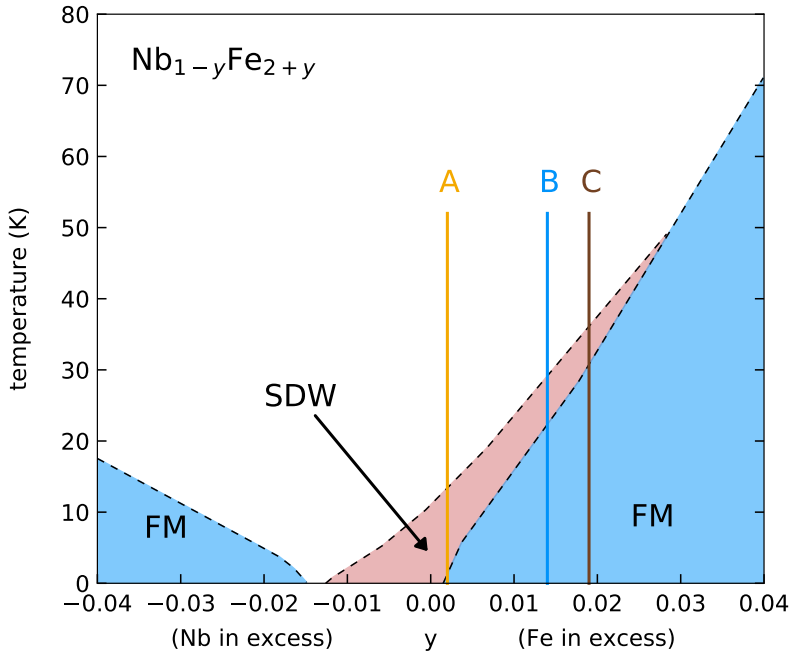

Figure 4.1: Temperature (T) - composition (y) phase diagram of $Nb_{1-y}Fe_{2+y}$. Nb atoms are substituted with Fe atoms on the Fe-rich side of the diagram (right) and Fe atoms are replaced by Nb atoms on the Nb-rich side of the diagram (left). The vertical plain lines labeled A, B and C indicate the Fe concentrations of Sample A ($y = +0.002$), Sample B ($y = +0.014$) and Sample C ($y = +0.019$).

Samples A,B and C were grown from polycrystalline feed and seed rods that were produced by William Duncan [51] with the RF furnace at Royal Holloway, University of London. The feed and seed rod for Sample A was synthesised from annealed 99.95% Niobium (Nb) and 99.99% vacuum re-melted Iron (Fe), whereas the rods for samples B and C were made of 99.99% Puratronic Nb powder and 99.995% Puratronic Fe powder. Before melted into rods, the raw powder compounds were degassed below a pressure of 8mbar. Then the Nb rods were annealed at 10^{-10}mbar at $\sim$ 2400K.

The polycrystals were then remelted into single crystals in an ultra high vacuum (UHV) optical floating zone (OFZ) furnace at the E21 institute. The atmosphere pressure in the growth chamber was maintained, during several days, below 10^{-6}mbar for Sample A and 10^{-9}mbar for

samples B and C and then flushed several time with purified 5N7 Argon. During the growth, a pressurised atmosphere of purified 5N7 Argon was maintained at 1.5bar. The growth speed was maintained between 5mm/h and 10mm/h.

The samples were characterised with neutron diffraction measurements and neutron depolarisation measurements.

4.1.1 Characterisation of Sample A

The designation for Sample A is OFZ12-x, where OFZ12 is the name of the growth, and its composition is the nearest to stoichiometric concentration: $Nb_{0.998}Fe_{2.002}$. Neutron diffraction measurements revealed a mosaicity $\sim 0.5°$ [49].

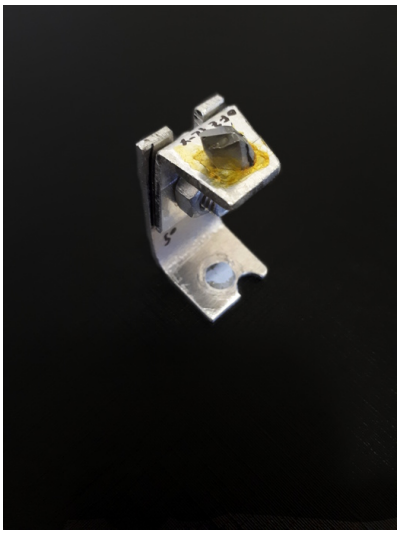

Figure 4.2: Sample A glued on its Aluminium holder with GE varnish for neutron measurements.

Additionally, magnetic susceptibility measurements suggest a SDW-paramagnetic (PM) transition temperature of $T_N = 13$K, but no FM-SDW transition (down to 2K, which is the lowest measured temperature with this sample) [3]. Sample A is significantly smaller than samples B and C.

4.1.2 Characterisation of Sample B

The designation for Sample B is OFZ27.3, where OFZ27 is the name of the growth and 3 is the section of the growth it has been cut out from. The composition of Sample B is $Nb_{0.986}Fe_{2.014}$ and its mosaicity of $\sim 1°$ is slightly bigger than in Sample A [49].

Figure 4.3: Sample B attached to its Aluminium holder with Aluminium wires for neutron measurements.

Magnetisation measurements performed on a fragment cut out of Sample B feature two anomalies suggesting phase transitions [3]. One anomaly is observed at $T_C = 24$K and it is expected to be the FM-SDW phase transition. Moreover, previous neutron depolarisation measurements indicate a depolarisation temperature between 24K and 26K [52]. The other anomaly is observed at $T_N = 30$K, which is expected to be the Néel temperature for the SDW-PM phase transition.

4.1.3 Characterisation of Sample C

The designation for Sample C is OFZ28.3.2.4, where OFZ28 is the name of the growth and 3.2.4 indicates the part of the growth this sample represents. The composition of Sample C is $Nb_{0.981}Fe_{2.019}$ and its mosaicity, between 0.3° and 0.4° [49], is the lowest of the three samples.

Depolarisation measurements indicate a depolarising temperature exceeding 30K [49]. AC-susceptibility measurements have also been done for this sample [48] and show two phase transition anomalies at $T_C = 33$K and at $T_N = 37$K. Diffraction measurements show an onset of the FM phase at 34.5K [3].

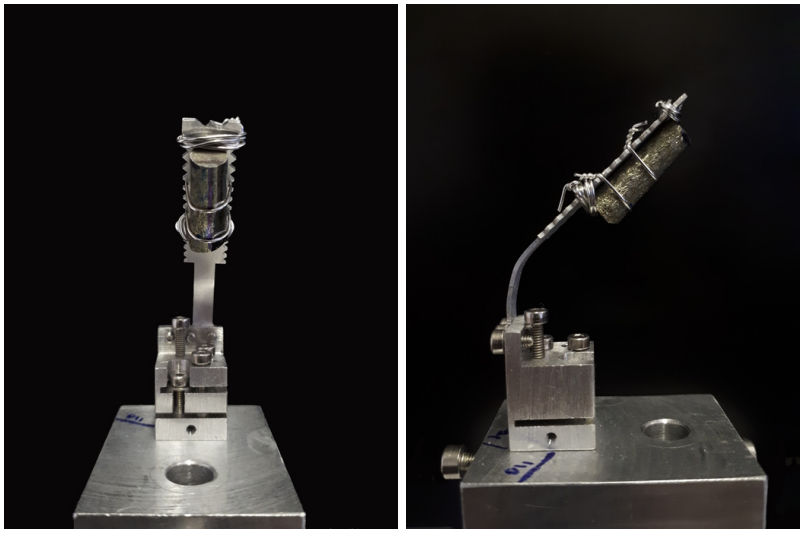

Figure 4.4: Sample C attached to its Aluminium holder with Aluminium wires for neutron measurements.

4.2 Neutron scattering theory

To go further in the investigation of the SDW phase and the magnetic excitations, we used different neutron measurement technics: polarised neutron diffraction and unpolarised elastic and inelastic neutron scattering. Neutron experiments rely on a common principle that consists in weakly perturbing a system and observe its response. The applied perturbation must be weak enough not to alter the intrinsic properties of the observed system and to remain in the linear regime. Neutron scattering is based on this principle, where our system is the sample and the weak perturbation is the incident neutron, which carries a magnetic moment: its spin.

The most common measurements are done with unpolarised neutron beams, in these experiments we make no use of the spin orientation. However, weak contributions to the overall neutron signal might be difficult to separate out with unpolarised neutron beam, but not with polarised neutron beams. First we will see the neutron scattering equations for unpolarised beams and then we will look at what these equations become when we consider the spin orientation of the neutrons.

4.2.1 Unpolarised neutron scattering

4.2.1.1 The scattering cross-section

The energy of a neutron E and its momentum $\hbar\boldsymbol{k}$ are linked by

$$E = \frac{\hbar^2 k^2}{2m}, \tag{4.2.1}$$

where m isj the neutron mass, $k = \frac{2\pi}{\lambda}$ is the amplitude of the neutron wave-vector and λ the neutron wavelength. When $E \approx \mathrm{k_B}T$ at room temperature, the wavelength of the neutron is $\lambda \approx 2\text{Å}$, which is of the order of the interatomic distance in condensed matter [53].

During a scattering event a neutron with initial (before the event) energy $E_i = \hbar^2 k_i^2/(2m)$ and momentum $\hbar\boldsymbol{k_i}$ will exchange energy and momentum with the system and end up with a final (after the event) energy $E_f = \hbar^2 k_f^2/(2m)$ and final momentum $\hbar\boldsymbol{k_f}$. If E_i and E_f denote the initial and final energies of the neutrons, the energy conservation law dictates [54]

$$\hbar\omega = E_i - E_f \tag{4.2.2}$$

$$\hbar\boldsymbol{\kappa} = \hbar\boldsymbol{k_i} - \hbar\boldsymbol{k_f}, \tag{4.2.3}$$

where $\hbar\omega$ is the energy gained by the sample and $\hbar\boldsymbol{\kappa}$ is the momentum gained by the sample.

We consider a beam of neutrons of flux $\phi(k_i)$ where all particles have a momentum $\boldsymbol{k_i}$. If σ denotes the scattering *cross-section*, then $\phi(k_i)\sigma$ is the scattering rate of neutrons by the system in all directions and with all final energies. In Figure 4.5, this would correspond to counting all the scattered neutrons crossing the sphere (only a fraction of which is depicted in the figure) surrounding the target. If instead of looking at all scattered neutrons, we only look at neutrons scattered in one direction delimited by the solid angle $d\Omega$, and thus crossing the infinitesimal surface dS in Figure 4.5, then the scattering rate is $\phi(k_i)(d\sigma/d\Omega)d\Omega$, where $d\sigma/d\Omega$ is the *differential cross-section*. Finally, if we only look at scattered neutrons in the restricted direction $d\Omega$ and with final energy $E_f \leq E \leq E_f + dE_f$, then the scattering rate is $\phi(k_i)d^2\sigma/(d\Omega d\omega)d\Omega dE_f$, where $d^2\sigma/(d\Omega dE_f)$ is the *partial differential cross-section*. The cross-section, the differential cross-section and the partial differential cross-section are related

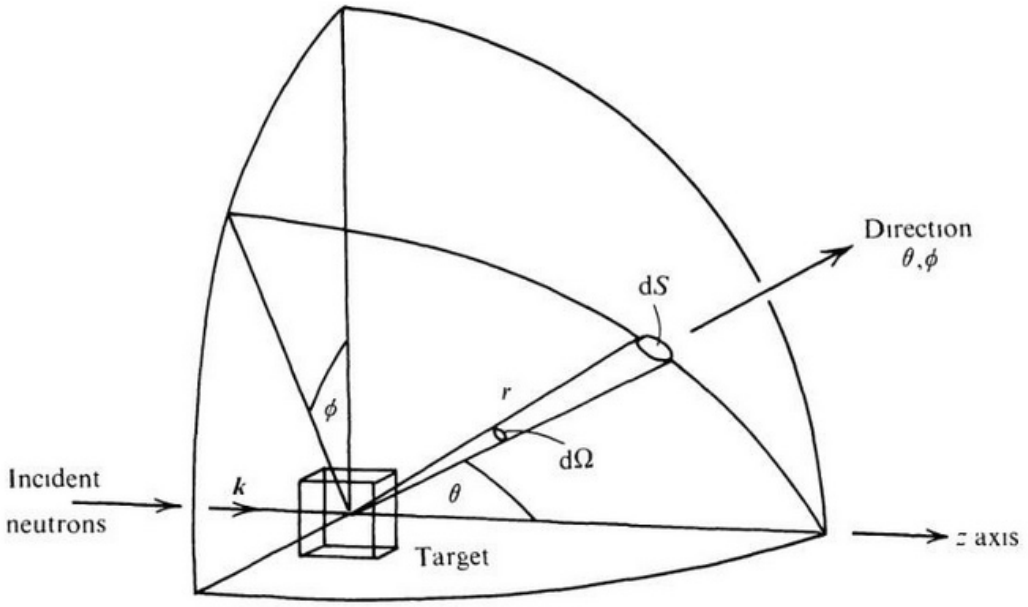

Figure 4.5: Illustration of scattering of a neutron beam from a target. Picture from [4].

with [4]

$$\sigma = \int_{\text{all directions}} \frac{\mathrm{d}\sigma}{\mathrm{d}\Omega}\mathrm{d}\Omega \tag{4.2.4}$$

$$\frac{\mathrm{d}\sigma}{\mathrm{d}\Omega} = \int_{\text{all energies}} \frac{\mathrm{d}^2\sigma}{\mathrm{d}\Omega \mathrm{d}E_f}\mathrm{d}E_f. \tag{4.2.5}$$

Incident neutrons can be represented by plane waves [4]. If the incident neutron beam propagates along $\boldsymbol{z}$, with the origin at the scattering centre, and ψ_i indicates the wave function of incident neutrons, then

$$\psi_i(z) = e^{ik_i z}. \tag{4.2.6}$$

Because of the spherical symmetry, the wave function of a neutron scattered by a single nucleus at distance r is [4]

$$\psi_f(r) = -\frac{b}{r}e^{ik_f r}, \tag{4.2.7}$$

where b is the *scattering length*, which depends on isotope and spin state of the nucleus [4].

If we now consider a targeted system composed of many scattering centres, the number of transitions per unit time and per solid angle $d\Omega$ from state λ_i to λ_f is the differential cross-

section for those states [4]

$$\left.\frac{d\sigma}{d\Omega_f}\right|_{\lambda_i\to\lambda_f} d\Omega = \frac{1}{\phi(k_i)} \sum_{\boldsymbol{k_f} \text{ in } d\Omega} W_{\boldsymbol{k_i},\lambda_i\to\boldsymbol{k_f},\lambda_f}, \tag{4.2.8}$$

where $W_{\boldsymbol{k_i},\lambda_i\to\boldsymbol{k_f},\lambda_f}$ is the number of transitions per unit time from state $\boldsymbol{k_i},\lambda_i$ to state $\boldsymbol{k_f},\lambda_f$. Fermi's golden rule gives

$$\sum_{\boldsymbol{k_f} \text{ in } d\Omega} W_{\boldsymbol{k_i},\lambda_i\to\boldsymbol{k_f},\lambda_f} = \frac{2\pi}{\hbar}\rho(\boldsymbol{k_f}) \left|\langle \boldsymbol{k_f}\lambda_f| V |\boldsymbol{k_i}\lambda_i\rangle\right|^2, \tag{4.2.9}$$

where $\rho(\boldsymbol{k_f})$ is the density of states at $\boldsymbol{k_f}$ and V is the potential though which the neutrons interact with the system and are scattered. With the *box normalisation* and a box volume Y we have [4]

$$\rho(\boldsymbol{k_f}) = \frac{Y}{(2\pi)^3} k_f \frac{m}{\hbar^2} d\Omega \tag{4.2.10}$$

$$\phi(k_i) = \frac{1}{Y}\frac{\hbar}{m}k_i \tag{4.2.11}$$

$$\psi(k_i) = \frac{1}{\sqrt{Y}} e^{i\boldsymbol{k_i}\cdot\boldsymbol{r}}, \tag{4.2.12}$$

and the partial differential cross-section becomes [4]

$$\left.\frac{\mathrm{d}^2\sigma}{\mathrm{d}\Omega \mathrm{d}E_f}\right|_{\lambda_i\to\lambda_f} = \frac{k_f}{k_i}\left(\frac{mY}{2\pi\hbar^2}\right)^2 \left|\langle \boldsymbol{k_f}\lambda_f| V |\boldsymbol{k_i}\lambda_i\rangle\right|^2 \delta(E_{\lambda_i} - E_{\lambda_f} + E_i - E_f). \tag{4.2.13}$$

If we now re-define $\psi(k_i) = e^{i\boldsymbol{k_i}\cdot\boldsymbol{r}}$ and $\langle \boldsymbol{k_f}\lambda_f| V |\boldsymbol{k_i}\lambda_i\rangle$ as $Y\langle \boldsymbol{k_f}\lambda_f| V |\boldsymbol{k_i}\lambda_i\rangle$, the previous equation becomes

$$\left.\frac{\mathrm{d}^2\sigma}{\mathrm{d}\Omega \mathrm{d}E_f}\right|_{\lambda_i\to\lambda_f} = \frac{k_f}{k_i}\left(\frac{m}{2\pi\hbar^2}\right)^2 \left|\langle \boldsymbol{k_f}\lambda_f| V |\boldsymbol{k_i}\lambda_i\rangle\right|^2 \delta(E_{\lambda_i} - E_{\lambda_f} + E_i - E_f). \tag{4.2.14}$$

If $V_l(\boldsymbol{r} - \boldsymbol{r_l})$ is the interaction potential between a neutron and the l^{th} nucleus at position $\boldsymbol{r_l}$ in the lattice, then the potential for the entire scattering system is [4]

$$V = \sum_l V_l(\boldsymbol{r} - \boldsymbol{r_l}). \tag{4.2.15}$$

Because neutrons are represented by plane waves in the Born approximation, the interaction

matrix can be written as

$$\langle \boldsymbol{k_f}\lambda_f | \, V \, | \boldsymbol{k_i}\lambda_i \rangle = \sum_l V_l(\boldsymbol{\kappa}) \, \langle \lambda_f | \, e^{i\boldsymbol{\kappa}\cdot\boldsymbol{r_l}} \, | \lambda_i \rangle \,, \tag{4.2.16}$$

with

$$V_l(\boldsymbol{\kappa}) = \int \mathrm{d}\boldsymbol{r} V(\boldsymbol{r}) e^{i\boldsymbol{\kappa}\cdot\boldsymbol{r}}, \tag{4.2.17}$$

and the scattering vector $\boldsymbol{\kappa} = \boldsymbol{k_i} - \boldsymbol{k_f}$.

Now, to consider all possible scattering processes, we average over the possible initial states λ_i and sum over the compatible final states λ_f. This gives

$$\frac{\mathrm{d}^2\sigma}{\mathrm{d}\Omega \mathrm{d}E_f} = \frac{k_f}{k_i}\left(\frac{m}{2\pi\hbar^2}\right)^2 \sum_{\lambda_i,\lambda_f} p_{\lambda_i} \left| \sum_l V_l(\boldsymbol{\kappa}) \, \langle \lambda_f | \, e^{i\boldsymbol{\kappa}\cdot\boldsymbol{r_l}} \, | \lambda_i \rangle \right|^2 \delta(E_{\lambda_i} - E_{\lambda_f} + E_i - E_f). \tag{4.2.18}$$

p_{λ_i} is the statistical weight for state $|\lambda_i\rangle$, which is given by the Boltzmann distribution:

$$p_{\lambda_i} = \frac{1}{Z} \exp\left(\frac{-E_{\lambda_i}}{k_B}\right), \tag{4.2.19}$$

where Z is the partition function:

$$Z = \sum_{\lambda_i} \exp\left(\frac{-E_{\lambda_i}}{k_B}\right). \tag{4.2.20}$$

Because the system is generally composed of many atoms, of different isotopes and with different spins, there is a random distribution of several different scattering lengths b. The partial differential cross-section can be written as a sum of two terms:

$$\frac{\mathrm{d}^2\sigma}{\mathrm{d}\omega \mathrm{d}\Omega} = \left.\frac{\mathrm{d}^2\sigma}{\mathrm{d}\omega \mathrm{d}\Omega}\right|_{\mathrm{coh}} + \left.\frac{\mathrm{d}^2\sigma}{\mathrm{d}\omega \mathrm{d}\Omega}\right|_{\mathrm{inc}}, \tag{4.2.21}$$

where $\mathrm{d}^2\sigma/(\mathrm{d}\omega\mathrm{d}\Omega)|_{\mathrm{coh}}$ contains the information about cooperative effects between the atoms (Bragg scattering, magnons, etc...) and $\mathrm{d}^2\sigma/(\mathrm{d}\omega\mathrm{d}\Omega)|_{\mathrm{inc}}$ contains the information about the dynamics in the system (e.g. motion or diffusion of individual scattering centre) [54].

The scattering length of an ion varies from one isotope to another or from spin state to another. If b_n denotes the scattering length of one particular isotope-spin state combination, and that this combination appears at frequency c_n within the system, then the average scattering

length $\overline{b}$ for this system is given by

$$\overline{b} = \sum_n c_n b_n, \tag{4.2.22}$$

which is the average of the scattering length of all isotope-spin state combinations present in the system and weighted by their frequency of apparition.

The average coherent cross-section is

$$\sigma_{\text{coh}} = 4\pi\overline{b}^2. \tag{4.2.23}$$

The total scattering cross-section is [54]

$$\begin{aligned} \sigma &= \sum_l c_l 4\pi b_l^2 \\ &= 4\pi\overline{b^2} \end{aligned} \tag{4.2.24}$$

The incoherent scattering cross-section is given by $\sigma_{\text{inc}} = \sigma - \sigma_{\text{coh}}$, and we have

$$\begin{aligned} \sigma_{\text{inc}} &= 4\pi(\overline{b^2} - \overline{b}^2) \\ &= 4\pi b_{\text{inc}}^2 \\ b_{\text{inc}} &= \sqrt{\overline{b^2} - \overline{b}^2}. \end{aligned} \tag{4.2.25}$$

4.2.1.2 Nuclear scattering

In the case of nuclear scattering, the potential can be modelled with a delta function [54]. The Fourier transform of the potential for the l^{th} nucleus with scattering length b_l then is

$$V_l(\boldsymbol{\kappa}) = \frac{2\pi\hbar^2}{m} b_l. \tag{4.2.26}$$

Equation 4.2.18 becomes

$$\frac{\mathrm{d}^2\sigma}{\mathrm{d}\Omega\mathrm{d}E_f} = \frac{k_f}{k_i} \sum_{\lambda_i,\lambda_f} p_{\lambda_i} \left| \sum_l b_l \left\langle \lambda_f \right| e^{i\boldsymbol{\kappa}\cdot\boldsymbol{r_l}} \left| \lambda_i \right\rangle \right|^2 \delta(E_{\lambda_i} - E_{\lambda_f} + E_i - E_f). \tag{4.2.27}$$

Using the fact that b_l is real, the integral expression of $\delta(E_{\lambda_i} - E_{\lambda_f} + E_i - E_f)$, the closure

relation for two operators and the Heisenberg representation (Equation A.1.1) gives [4]

$$\frac{\mathrm{d}^2\sigma}{\mathrm{d}\Omega \mathrm{d}E_f} = \frac{k_f}{k_i}\frac{1}{2\pi\hbar}\sum_{l,l'} b_l b_{l'} \int_{-\infty}^{\infty} \mathrm{d}t \langle e^{-i\boldsymbol{\kappa}\cdot\boldsymbol{r_{l'}}(0)} e^{i\boldsymbol{\kappa}\cdot\boldsymbol{r_l}(t)}\rangle e^{-i\omega t}, \tag{4.2.28}$$

where $\omega = (E_i - E_f)/\hbar$ and $\langle \dots \rangle$ is the thermal average (the average over all initial states).

4.2.1.2.1 Coherent and Incoherent nuclear scattering If we consider many different copies of a scattering system, all containing the same amount of nuclei with scattering length b_l, but each with a different distribution bs and every possible distribution is represented once. Then for scattering systems with a large numbers of nuclei, the measured cross-section is very close the the cross-section averaged over all copies [4], and

$$\frac{\mathrm{d}^2\sigma}{\mathrm{d}\Omega \mathrm{d}E_f} = \frac{k_f}{k_i}\frac{1}{2\pi\hbar}\sum_{l,l'} \overline{b_l b_{l'}} \int_{-\infty}^{\infty} \mathrm{d}t \langle l', l\rangle e^{-i\omega t}, \tag{4.2.29}$$

where $\langle l', l\rangle = \langle e^{-i\boldsymbol{\kappa}\cdot\boldsymbol{r_{l'}}(0)} e^{i\boldsymbol{\kappa}\cdot\boldsymbol{r_l}(t)}\rangle$.

With uncorrelated scattering lengths bs of the different nuclei

$$\overline{b_{l'} b_l} = (\bar{b})^2 \text{ for } l' \neq l, \tag{4.2.30}$$

$$\overline{b_{l'} b_l} = \overline{b^2} \text{ for } l' = l, \tag{4.2.31}$$

and from Equation 4.2.29, we obtain

$$\frac{\mathrm{d}^2\sigma}{\mathrm{d}\Omega \mathrm{d}E_f} = \underbrace{\frac{k_f}{k_i}\frac{1}{2\pi\hbar}(\bar{b})^2 \sum_{l,l'} \int_{-\infty}^{\infty} \mathrm{d}t \langle l', l\rangle e^{-i\omega t}}_{\text{coherent scattering cross-section}} + \underbrace{\frac{k_f}{k_i}\frac{1}{2\pi\hbar}\left[\overline{b^2} - (\bar{b})^2\right] \sum_{l} \int_{-\infty}^{\infty} \mathrm{d}t \langle l, l\rangle e^{-i\omega t}}_{\text{incoherent scattering cross-section}}. \tag{4.2.32}$$

Using Equation 4.2.23 gives the coherent nuclear scattering cross-section

$$\left.\frac{\mathrm{d}^2\sigma}{\mathrm{d}\Omega \mathrm{d}E_f}\right|_{\mathrm{coh}} = N\frac{\sigma_{\mathrm{coh}}}{4\pi}\frac{k_f}{k_i} S(\boldsymbol{\kappa}, \omega), \tag{4.2.33}$$

with

$$S(\boldsymbol{\kappa}, \omega) = \frac{1}{2\pi\hbar N}\sum_{l,l'} \int_{-\infty}^{\infty} \mathrm{d}t \langle e^{-i\boldsymbol{\kappa}\cdot\boldsymbol{r_{l'}}(0)} e^{i\boldsymbol{\kappa}\cdot\boldsymbol{r_l}(t)}\rangle e^{-i\omega t}, \tag{4.2.34}$$

known as the scattering function.

Equation 4.2.34 is often written as [4]

$$S(\boldsymbol{\kappa},\omega) = \frac{1}{2\pi\hbar}\int_{-\infty}^{\infty} \mathrm{d}t I\left(\boldsymbol{\kappa},t\right)\exp(-i\omega t), \tag{4.2.35}$$

where $I\left(\boldsymbol{\kappa},t\right)$ is the *intermediate function*; its expression is

$$I\left(\boldsymbol{\kappa},t\right) = \frac{1}{N}\sum_{l,l'}\langle\exp(-i\boldsymbol{\kappa}\cdot\boldsymbol{r_{l'}}(0))\exp(i\boldsymbol{\kappa}\cdot\boldsymbol{r_l}(t))\rangle, \tag{4.2.36}$$

and it verifies [4]

$$I\left(\boldsymbol{\kappa},t\right) = I\left(-\boldsymbol{\kappa},-t+i\frac{\hbar}{k_\mathrm{b}T}\right). \tag{4.2.37}$$

The incoherent part of the nuclear scattering cross-section is obtained from Equation 4.2.25:

$$\left.\frac{\mathrm{d}^2\sigma}{\mathrm{d}\Omega\mathrm{d}E_f}\right|_{\mathrm{inc}} = N\frac{\sigma_{\mathrm{inc}}}{4\pi}\frac{k_f}{k_i}S_i(\boldsymbol{\kappa},\omega), \tag{4.2.38}$$

with

$$S_i(\boldsymbol{\kappa},\omega) = \frac{1}{2\pi\hbar N}\sum_{l}\int_{-\infty}^{\infty}\mathrm{d}t\langle e^{-i\boldsymbol{\kappa}\cdot\boldsymbol{r_l}(0)}e^{i\boldsymbol{\kappa}\cdot\boldsymbol{r_l}(t)}\rangle e^{-i\omega t}, \tag{4.2.39}$$

known as the incoherent scattering function.

4.2.1.2.2 Principle of detailed balance From Equation 4.2.35, Equation 4.2.36 and the property of the intermediate function in Equation 4.2.37, we find that

$$S(\boldsymbol{\kappa},\omega) = \exp\left(\frac{\hbar\omega}{k_\mathrm{b}T}\right)S(-\boldsymbol{\kappa},-\omega). \tag{4.2.40}$$

Equation 4.2.40 is known as *the principle of detailed balance*, which expresses the equal probability for a neutron to gain or loose energy $\hbar\omega$ to the system; the difference between $S(\boldsymbol{\kappa},\omega)$ and $S(-\boldsymbol{\kappa},-\omega)$ is only due to a higher probability for the system to be in the lower energy state.

4.2.1.2.3 Nuclear scattering by a crystal We consider the case of nuclear scattering by a non-Bravais crystal, composed of N unit cells of volume v_0. The position of a the d^{th} scattering centre in the l^{th} unit cell is given by

$$\boldsymbol{r_{ld}} = \boldsymbol{l} + \boldsymbol{d} + \boldsymbol{u}\begin{pmatrix} l \\ d \end{pmatrix}, \tag{4.2.41}$$

where $\boldsymbol{l}+\boldsymbol{d}$ is the position at equilibrium of the scattering centre and $\boldsymbol{u}$ is displacement out of equilibrium. The coherent scattering cross-section in Equation 4.2.33 becomes

$$\left.\frac{\mathrm{d}^2\sigma}{\mathrm{d}\Omega\mathrm{d}E_f}\right|_{\mathrm{coh}} = \frac{k_f}{k_i}\frac{1}{2\pi\hbar}\sum_{l,d}\sum_{l',d'}\overline{b_d b_{d'}}e^{i\boldsymbol{\kappa}\cdot(\boldsymbol{l}+\boldsymbol{d}-\boldsymbol{l'}-\boldsymbol{d'})}\int_{-\infty}^{\infty}\mathrm{d}t\langle e^{-i\boldsymbol{\kappa}\cdot\boldsymbol{u}\binom{l'}{d'}(0)}e^{i\boldsymbol{\kappa}\cdot\boldsymbol{u}\binom{l}{d}(t)}\rangle e^{-i\omega t}. \tag{4.2.42}$$

The coherent nuclear scattering can be elastic[1], when no energy is transferred between the neutron and the system ($E_i = E_f$), or inelastic, when energy is transferred. The coherent differential cross-section for the elastic scattering is [4, 54]

$$\left.\frac{\mathrm{d}\sigma}{\mathrm{d}\Omega}\right|_{\mathrm{coh}}^{\mathrm{el}} = N\frac{(2\pi)^3}{v_0}\sum_{\boldsymbol{G}}\delta(\boldsymbol{\kappa}-\boldsymbol{G})\left|F_N(\boldsymbol{G})\right|^2, \tag{4.2.43}$$

with the nuclear unit cell structure factor

$$F_N(\boldsymbol{G}) = \sum_d \overline{b_d}e^{i\boldsymbol{G}\cdot\boldsymbol{d}}e^{-W_d}, \tag{4.2.44}$$

and

$$W_d = \frac{1}{2}\langle[\boldsymbol{\kappa}\cdot\boldsymbol{u}(0)]\rangle_t. \tag{4.2.45}$$

$\exp(-W_d)$ is known as the Debye-Waller factor that accounts for the fluctuations of the atoms around their position at equilibrium.

For incoherent nuclear scattering, the differential cross-section for the elastic scattering is [54]

$$\left.\frac{\mathrm{d}\sigma}{\mathrm{d}\Omega}\right|_{\mathrm{inc}}^{\mathrm{el}} = \frac{N}{4\pi}\sum_d \sigma_{\mathrm{inc},d}e^{-2W_d}. \tag{4.2.46}$$

4.2.1.3 Magnetic scattering

In a magnetic neutron scattering event, the dipole moment of the neutron $\boldsymbol{\mu_n}$ interacts with the magnetic field of the unpaired electrons, which for each electron is the combination of the dipole moment $\boldsymbol{\mu_e}$ and the orbital motion of the electron [4].

[1] called Bragg peaks.

4.2.1.3.1 The magnetic potential The dipole moment of the neutron ($\boldsymbol{\mu_n}$) and electron ($\boldsymbol{\mu_e}$) are

$$\boldsymbol{\mu_n} = -\gamma \mu_N \boldsymbol{\sigma} \tag{4.2.47}$$

$$\boldsymbol{\mu_e} = -2\mu_B \boldsymbol{s}, \tag{4.2.48}$$

where μ_N and μ_B are the nuclear and Bohr magneton, $\boldsymbol{\sigma}$ and $\boldsymbol{s}$ are the Pauli spin operator and spin angular momentum operators and $\gamma = 1.913$ is the gyromagnetic ratio. μ_N and μ_B are given by

$$\mu_N = \frac{e\hbar}{2m_p} \tag{4.2.49}$$

$$\mu_B = \frac{e\hbar}{2m_e}, \tag{4.2.50}$$

where e is the charge of the proton, m_p and m_e are the masses of a proton and electron respectively. If $\boldsymbol{p}$ is the momentum of an unpaired electron, then the magnetic field generated by the latter at $\boldsymbol{R}$ (unitary vector along $\boldsymbol{R}$ is $\hat{\boldsymbol{R}}$) is [4]

$$\begin{aligned} \boldsymbol{B} &= \boldsymbol{B_S} + \boldsymbol{B_L} \\ &= \frac{\mu_0}{4\pi} \left\{ \nabla \times \left(\frac{\boldsymbol{\mu_e} \times \hat{\boldsymbol{R}}}{R^2} \right) - \frac{2\mu_B}{\hbar} \frac{\boldsymbol{p} \times \hat{\boldsymbol{R}}}{R^2} \right\}, \end{aligned} \tag{4.2.51}$$

where $\boldsymbol{B_S}$ and $\boldsymbol{B_L}$ are the magnetic fields generated by the dipole moment and the orbital motion respectively and $\hat{}$ is used to represent unitary vectors: $\hat{\boldsymbol{r}} = \boldsymbol{r}/|\boldsymbol{r}|$. If we consider the j^{th} electron in the system, the potential $V_{m,j}$ of a neutron in the magnetic field, generated by this j^{th} electron, is then [4]

$$V_{m,j}(\boldsymbol{R}) = -\boldsymbol{\mu_n} \cdot \boldsymbol{B_j} = -\frac{\mu_0}{4\pi} \gamma \mu_N 2\mu_B \boldsymbol{\sigma_j} \cdot (\boldsymbol{W_{S,j}} + \boldsymbol{W_{L,j}}) \tag{4.2.52}$$

$$\boldsymbol{W_{S,j}} = \nabla \times \left(\frac{\boldsymbol{s_j} \times \hat{\boldsymbol{R}}}{R^2} \right) \tag{4.2.53}$$

$$\boldsymbol{W_{L,j}} = \frac{1}{\hbar} \frac{\boldsymbol{p_j} \times \hat{\boldsymbol{R}}}{R^2}. \tag{4.2.54}$$

The total interaction is then

$$V_m = \sum_j V_{m,j}. \tag{4.2.55}$$

4.2.1.3.2 The cross-section For magnetic neutron scattering, we must also take the spin state of the neutrons in consideration and therefore the partial differential cross-section must be adjusted. If $\boldsymbol{\sigma_i}$ and $\boldsymbol{\sigma_f}$ are the incident and scattered neutrons spin states, Equation 4.2.9 becomes

$$W_{\boldsymbol{k_i},\boldsymbol{\sigma_i},\lambda_i\to\boldsymbol{k_f},\boldsymbol{\sigma_f},\lambda_f} = \frac{2\pi}{\hbar}\left|\langle \boldsymbol{k_f}\boldsymbol{\sigma_f}\lambda_f|\, V_{\mathrm{m}}\,|\boldsymbol{k_i}\boldsymbol{\sigma_i}\lambda_i\rangle\right|^2 \delta(E_{\lambda_i}-E_{\lambda_f}+E_i-E_f), \tag{4.2.56}$$

and the partial differential cross-section in Equation 4.2.14 becomes [4]

$$\left.\frac{\mathrm{d}^2\sigma}{\mathrm{d}\Omega\mathrm{d}E_f}\right|_{\sigma_i\lambda_i\to\sigma_f\lambda_f} = \frac{k_f}{k_i}\left(\frac{m}{2\pi\hbar^2}\right)^2\left|\langle \boldsymbol{k_f}\boldsymbol{\sigma_f}\lambda_f|\, V_{\mathrm{m}}\,|\boldsymbol{k_i}\boldsymbol{\sigma_i}\lambda_i\rangle\right|^2 \delta(E_{\lambda_i}-E_{\lambda_f}+\hbar\omega). \tag{4.2.57}$$

Using equations 4.2.52, 4.2.53, 4.2.54 and 4.2.55 in Equation 4.2.57 yields [4]

$$\left.\frac{\mathrm{d}^2\sigma}{\mathrm{d}\Omega\mathrm{d}E_f}\right|_{\sigma_i\lambda_i\to\sigma_f\lambda_f} = (\gamma r_0)^2\frac{k_f}{k_i}\left|\langle \boldsymbol{\sigma_f}\lambda_f|\, \boldsymbol{\sigma}\cdot\boldsymbol{Q}_\perp\,|\boldsymbol{\sigma_i}\lambda_i\rangle\right|^2 \delta(E_{\lambda_i}-E_{\lambda_f}+\hbar\omega), \tag{4.2.58}$$

with [4]

$$r_0 = \frac{\mu_0}{4\pi}\frac{e^2}{m_{\mathrm{e}}} \quad \text{classical electron radius} \tag{4.2.59}$$

$$\begin{aligned}\boldsymbol{Q}_\perp &= \sum_j e^{i\boldsymbol{\kappa}\cdot\boldsymbol{r_j}}\left\{\hat{\boldsymbol{\kappa}}\times(\boldsymbol{s_j}\times\hat{\boldsymbol{\kappa}})+\frac{i}{\hbar\kappa}(\boldsymbol{p_j}\times\hat{\boldsymbol{\kappa}})\right\} \\ &= \hat{\boldsymbol{\kappa}}\times(\boldsymbol{Q}\times\hat{\boldsymbol{\kappa}})\end{aligned} \tag{4.2.60}$$

$$\boldsymbol{\kappa} = \boldsymbol{k_f}-\boldsymbol{k_i} \quad \text{(the scattering vector)} \quad . \tag{4.2.61}$$

$\boldsymbol{Q}$ is proportional to the spatial Fourier transform of the total magnetisation operator $\boldsymbol{M}(\boldsymbol{r})$ [4]

$$\boldsymbol{Q}(\boldsymbol{\kappa}) = -\frac{1}{2\mu_{\mathrm{B}}}\int \boldsymbol{M}(\boldsymbol{r})e^{i\boldsymbol{\kappa}\cdot\boldsymbol{r}}\mathrm{d}\boldsymbol{r} = -\frac{1}{2\mu_{\mathrm{B}}}\boldsymbol{M}(\boldsymbol{\kappa}), \tag{4.2.62}$$

which contains the spin and the orbital contributions to the magnetic scattering. This shows that the neutrons are scattered by the component of the magnetic field, generated by unpaired electrons, that is normal to the scattering vector $\hat{\boldsymbol{\kappa}}$.

If $\boldsymbol{Q}^\dagger$ designates the Hermitian conjugate of $\boldsymbol{Q}$, we have

$$\begin{gathered}\boldsymbol{Q}_\perp^\dagger\cdot\boldsymbol{Q}_\perp = \sum_{\alpha\beta}(\delta_{\alpha\beta}-\hat{\kappa_\alpha}\hat{\kappa_\beta})Q_\alpha^\dagger Q_\beta \\ \text{with } \alpha,\beta\in\{x,y,z\},\end{gathered} \tag{4.2.63}$$

with $\delta_{\alpha\beta}$ the Kronecker delta, and, for an unpolarised neutron beam, the partial differential cross-section summed over all final states σ_f, λ_f and averaged over the initial states σ_i, λ_i becomes [4]

$$\frac{\mathrm{d}^2\sigma}{\mathrm{d}\Omega \mathrm{d}E_f} = (\gamma r_0)^2 \frac{k_f}{k_i} \sum_{\alpha\beta} (\delta_{\alpha\beta} - \hat{\kappa_\alpha}\hat{\kappa_\beta}) \times \sum_{\lambda_i \lambda_f} p_{\lambda_i} \langle \lambda_i | Q_\alpha^\dagger | \lambda_f \rangle \langle \lambda_f | Q_\beta | \lambda_i \rangle \delta(E_{\lambda_i} - E_{\lambda_f} + \hbar\omega). \tag{4.2.64}$$

Considering that

$$\delta(E_{\lambda_i} - E_{\lambda_f} + \hbar\omega) = \frac{1}{2\pi\hbar} \int_{-\infty}^{\infty} e^{i \frac{E_{\lambda_f} - E_{\lambda_i}}{\hbar} t} e^{-i\omega t} \mathrm{d}t \tag{4.2.65}$$

and

$$e^{i\frac{H}{\hbar}t} |\lambda_i\rangle = e^{i\frac{E_{\lambda_i}}{\hbar}t} |\lambda_i\rangle , \tag{4.2.66}$$

then, from Equation 4.2.64, the expression of the partial differential cross-section with time-dependent operators becomes [4]

$$\frac{\mathrm{d}^2\sigma}{\mathrm{d}\Omega \mathrm{d}E_f} = \frac{(\gamma r_0)^2}{2\pi\hbar} \frac{k_f}{k_i} \sum_{\alpha\beta} (\delta_{\alpha\beta} - \hat{\kappa_\alpha}\hat{\kappa_\beta}) \int \langle Q_\alpha(-\boldsymbol{\kappa}, 0) Q_\beta(\boldsymbol{\kappa}, t) \rangle e^{-i\omega t} \mathrm{d}t. \tag{4.2.67}$$

$Q_\beta(\boldsymbol{\kappa}, t)$ is the time dependent operator $Q_\beta(\boldsymbol{\kappa})$ in the Heisenberg representation (see Section A.1.1):

$$Q_\beta(\boldsymbol{\kappa}, t) = e^{\frac{iHt}{\hbar}} Q_\beta(\boldsymbol{\kappa}) e^{-\frac{iHt}{\hbar}}. \tag{4.2.68}$$

The elastic differential cross-section for magnetic scattering is given by [4]

$$\left.\frac{\mathrm{d}\sigma}{\mathrm{d}\Omega}\right|_{el} = (\gamma r_0)^2 \sum_{\alpha\beta} (\delta_{\alpha\beta} - \hat{\kappa_\alpha}\hat{\kappa_\beta}) \langle Q_\alpha(-\boldsymbol{\kappa}) \rangle \langle Q_\beta(\boldsymbol{\kappa}) \rangle. \tag{4.2.69}$$

4.2.1.3.3 Spin scattering only We now assume the case where neutrons are only scattered by the spin of unpaired electrons in the system. We also consider the *Heitler-London* model, which supposes that the unpaired electrons are close to their equilibrium position. The quantum numbers S and L designate the combination of all unpaired electrons' individual spin s_i and individual orbital angular momentum l_i, respectively. We consider the quenched case of the resultant orbital angular momentum $L = 0$, which works often well for transition-metal based d-electron systems such as $NbFe_2$. For a non-Bravais crystal, if $\boldsymbol{R_{ld}}$ is the position of the d^{th} ion in the l^{th} unit cell and $\boldsymbol{r_v}$ is the position of the v^{th} electron with respect to the nucleus at

$\boldsymbol{R_{ld}}$ and with spin operator $\boldsymbol{s}_v$, then [4]

$$\boldsymbol{Q} = \boldsymbol{Q}_s = \sum_{ld} e^{i\boldsymbol{\kappa}\cdot\boldsymbol{R}_{ld}} \sum_{v} e^{i\boldsymbol{\kappa}\cdot\boldsymbol{r}_v} \boldsymbol{s}_v. \tag{4.2.70}$$

With time-dependent operators, the partial differential cross-section becomes [4]

$$\begin{aligned}\frac{\mathrm{d}^2\sigma}{\mathrm{d}\Omega \mathrm{d}E_f} = \frac{(\gamma r_0)^2}{2\pi\hbar}\frac{k_f}{k_i}\sum_{\alpha\beta}(\delta_{\alpha\beta} - \hat{\kappa_\alpha}\hat{\kappa_\beta}) \sum_{l'd'ld} \frac{1}{4} g_{d'} g_d F^*_{d'}(\boldsymbol{\kappa}) F_d(\boldsymbol{\kappa}) \\ \times \int_{-\infty}^{\infty} \langle e^{-i\boldsymbol{\kappa}\cdot\boldsymbol{R}_{l'd'}(0)} e^{-i\boldsymbol{\kappa}\cdot\boldsymbol{R}_{ld}(t)} \rangle \\ \times \langle S^\alpha_{l'd'}(0) S^\beta_{ld}(t)\rangle e^{-i\omega t}\mathrm{d}t,\end{aligned} \tag{4.2.71}$$

where $\boldsymbol{u}_l(t)$ is the distance of nucleus l from its position at equilibrium, g is the Landé splitting factor ($g = 2$) and S^β_l is the operator of the spin component along β at ion l. $F(\boldsymbol{\kappa})$ is the *magnetic form factor*

$$F_d(\boldsymbol{\kappa}) = \int \rho(\boldsymbol{r}) e^{i\boldsymbol{\kappa}\cdot\boldsymbol{r}} \mathrm{d}\boldsymbol{r}, \tag{4.2.72}$$

which is the Fourier transform of the density $\rho(\boldsymbol{r})$ of unpaired electrons on an atom.

4.2.1.3.4 Scattering cross-section and dissipation We will now see how the scattering cross-section relates to the dissipation in the system. The fluctuation-dissipation theorem (detailed in Appendix A.1) links the dissipation in the system –given by the imaginary part of the admittance (χ'')– to the fluctuations in the latter at thermodynamic equilibrium.

If we write

$$S^{\alpha\beta}(\boldsymbol{\kappa},\omega) = \frac{(2\mu_\mathrm{B})^2}{2\pi\hbar}\int \langle Q_\alpha(-\boldsymbol{\kappa},0) Q_\beta(\boldsymbol{\kappa},t)\rangle e^{-i\omega t}\mathrm{d}t, \tag{4.2.73}$$

then Equation 4.2.67 becomes

$$\frac{\mathrm{d}^2\sigma}{\mathrm{d}\Omega \mathrm{d}E_f} = \left(\frac{\gamma r_0}{2\mu_\mathrm{B}}\right)^2 \frac{k_f}{k_i}\sum_{\alpha\beta}(\delta_{\alpha\beta} - \hat{\kappa_\alpha}\hat{\kappa_\beta}) S^{\alpha\beta}(\boldsymbol{\kappa},\omega)\,. \tag{4.2.74}$$

$S^{\alpha\beta}(\boldsymbol{\kappa},\omega)$ can be separated between a static part, resulting from static magnetic moments in the system, and a fluctuating part, which describes the inelastic magnetic scattering [55]:

$$S^{\alpha\beta}(\boldsymbol{\kappa},\omega) = \underbrace{S^{\alpha\beta}_\mathrm{e}(\boldsymbol{\kappa})\,\delta(\hbar\omega)}_{\text{elastic (static)}} + \underbrace{S^{\alpha\beta}_\mathrm{i}(\boldsymbol{\kappa},\omega)}_{\text{inelastic (fluctuating)}}\,. \tag{4.2.75}$$

The elastic part is given by [55]

$$S_{\mathrm{e}}^{\alpha\beta}\left(\boldsymbol{\kappa}\right) = (2\mu_{\mathrm{B}})^2 \langle Q^{\alpha}\left(\boldsymbol{\kappa}\right)\rangle \langle Q^{\beta}\left(-\boldsymbol{\kappa}\right)\rangle, \tag{4.2.76}$$

which gives, after using Equation 4.2.76 in Equation 4.2.74 and integrating over all energies, the elastic differential cross-section for magnetic scattering already given in Equation 4.2.69.

The inelastic part $S_{\mathrm{i}}^{\alpha\beta}\left(\boldsymbol{\kappa},\omega\right)$, on the other hand, links the scattering intensity to the dissipation in the system and its expression is a function of the imaginary part of the dynamical magnetic susceptibility [55]:

$$S_{\mathrm{i}}^{\alpha\beta}\left(\boldsymbol{\kappa},\omega\right) = (\mathrm{n_b}(\hbar\omega)+1)\frac{\chi''_{\alpha\beta}\left(\boldsymbol{\kappa},\omega\right)}{\pi}. \tag{4.2.77}$$

$\mathrm{n_b}(\hbar\omega)$ is the Bose factor and its expression is

$$\mathrm{n_b}(\hbar\omega) = \frac{1}{\exp\left(\frac{\hbar\omega}{k_{\mathrm{B}}T}\right)-1}. \tag{4.2.78}$$

Finally, using $S_{\mathrm{e}}^{\alpha\beta}\left(\boldsymbol{\kappa}\right)$ from Equation 4.2.76 and $S_{\mathrm{i}}^{\alpha\beta}\left(\boldsymbol{\kappa},\omega\right)$ from Equation 4.2.77 into Equation 4.2.74 gives the partial differential cross-section for magnetic neutron scattering:

$$\frac{\mathrm{d}^2\sigma}{\mathrm{d}\Omega \mathrm{d}E_f} = \left(\frac{\gamma r_0}{2\mu_{\mathrm{B}}}\right)^2 \frac{k_f}{k_i} \sum_{\alpha\beta} (\delta_{\alpha\beta} - \hat{\kappa_\alpha}\hat{\kappa_\beta}) \left((2\mu_{\mathrm{B}})^2 \langle Q^{\alpha}\left(\boldsymbol{\kappa}\right)\rangle \langle Q^{\beta}\left(-\boldsymbol{\kappa}\right)\rangle \delta(\hbar\omega) + (\mathrm{n_b}(\hbar\omega)+1)\frac{\chi''_{\alpha\beta}\left(\boldsymbol{\kappa},\omega\right)}{\pi} \right). \tag{4.2.79}$$

4.2.2 Polarised neutrons scattering

So far we considered scattering events with momentum transfer between the neutron and the scattering system, but there are also scattering events that change the spin state of the neutrons. Measuring this change of the polarisation of the neutron beam provides valuable information about the system.

If we take the z axis as the polarisation axis, with u the *spin up* and v the *spin down* state of the neutrons, then

$$\sigma_z u = +1u \tag{4.2.80}$$

$$\sigma_z v = -1v, \tag{4.2.81}$$

where σ_z is the z component of the Pauli matrix. There are now four cross-sections, one for each incident-scattered neutron spin configuration, that are the *spin state* cross-sections. These four configurations are

with spin flip: $u \to v$ and $v \to u$

without spin flip: $u \to u$ and $v \to v$.

The cross-sections given before in the case of the unpolarised neutrons are the sum of these four processes.

4.2.2.1 Nuclear scattering

First we look at the cross-sections for the nuclear scattering case. We consider a sample composed of identical nuclei with spin I. Nucleus spin angular momentum is denoted by operator $\boldsymbol{I}$ and neutron spin angular momentum is denoted by $\frac{1}{2}\boldsymbol{\sigma}$, where $\boldsymbol{\sigma}$ is the Pauli spin operator. During a scattering event, a neutron and a nucleus form a system with spin t, which can have two values

$$t = I + \frac{1}{2} \quad \text{if neutron spin is parallel to the nuclear spin} \tag{4.2.82}$$

$$t = I - \frac{1}{2} \quad \text{if neutron spin is anti-parallel to the nuclear spin} \quad . \tag{4.2.83}$$

Each spin system has a different scattering length (b^+ if $t = I + \frac{1}{2}$ and b^- if $t = I - \frac{1}{2}$). We define $|+\rangle$ and $|-\rangle$ as the states corresponding to the spins $t = I + \frac{1}{2}$ and $t = I - \frac{1}{2}$, respectively. The corresponding operator is $\boldsymbol{t} = \boldsymbol{I} + \frac{1}{2}\boldsymbol{\sigma}$, and $|+\rangle$, $|-\rangle$ are eigenvectors of $\boldsymbol{t}^2$ [4]

$$\begin{aligned} \boldsymbol{t}^2 |+\rangle &= t(t+1) \quad \text{(here t=I+1/2)} \\ &= I^2 + 2I + \frac{3}{4} \end{aligned} \tag{4.2.84}$$

$$\begin{aligned} \boldsymbol{t}^2 |-\rangle &= t(t+1) \quad \text{(here t=I-1/2)} \\ &= I^2 - \frac{1}{4}. \end{aligned} \tag{4.2.85}$$

We define an operator $\hat{b}$ such that b^+ and b^- are eigenvalues for $|+\rangle$ and $|-\rangle$:

$$\hat{b} |+\rangle = b^+ |+\rangle \tag{4.2.86}$$

$$\hat{b} |-\rangle = b^- |-\rangle , \tag{4.2.87}$$

then

$$\begin{aligned}\hat{b} &= A + B\boldsymbol{\sigma}\cdot\boldsymbol{I} \\ A &= \frac{1}{2I+1}\left[(I+1)b^{+} + Ib^{-}\right] \\ B &= \frac{1}{2I+1}\left(b^{+} - b^{-}\right),\end{aligned} \tag{4.2.88}$$

and we obtain the matrix elements for the four spin state transitions [4]

$$\langle u|\,\hat{b}\,|u\rangle = A + BI_z \tag{4.2.89}$$

$$\langle v|\,\hat{b}\,|v\rangle = A - BI_z \tag{4.2.90}$$

$$\langle u|\,\hat{b}\,|v\rangle = B(I_x - iI_y) \tag{4.2.91}$$

$$\langle v|\,\hat{b}\,|u\rangle = B(I_x + iI_y). \tag{4.2.92}$$

If we use the Fermi pseudo-potential

$$V(\boldsymbol{r}) = \frac{2\pi\hbar}{m} b\delta(\boldsymbol{r}) \tag{4.2.93}$$

in Equation 4.2.14, the partial differential cross-section for transition from state $\sigma_i\lambda_i$ to $\sigma_f\lambda_f$ (with $\sigma_i, \sigma_f \in \{u, v\}$) becomes [4]

$$\left.\frac{\mathrm{d}^2\sigma}{\mathrm{d}\Omega\mathrm{d}\omega}\right|_{\sigma_i\lambda_i\to\sigma_f\lambda_f} = \frac{k_f}{k_i}\left|\sum_j \langle\sigma_f\lambda_f|\,\hat{b}_j e^{i\boldsymbol{\kappa}\cdot\boldsymbol{R}_j}\,|\sigma_i\lambda_i\rangle\right|^2 \delta(E_{\lambda_i} - E_{\lambda_f} + \hbar\omega). \tag{4.2.94}$$

The matrix element for the j^{th} nucleus is [4]

$$\langle\sigma_f\lambda_f|\,\hat{b}_j e^{i\boldsymbol{\kappa}\cdot\boldsymbol{R}_j}\,|\sigma_i\lambda_i\rangle = \langle\lambda_f|\,e^{i\boldsymbol{\kappa}\cdot\boldsymbol{R}_j}\,|\lambda_i\rangle\,\langle\sigma_f|\,\hat{b}_j\,|\sigma_i\rangle\,, \tag{4.2.95}$$

where $\langle\sigma_f|\,\hat{b}_j\,|\sigma_i\rangle$ are the matrix elements in equations 4.2.89.

4.2.2.1.1 Coherent nuclear scattering The coherent scattering is proportional to the average of the scattering length $\overline{b}$. We must average over the different isotopes composing the sample, but also over the nuclear spin states:

$$\overline{b} = \langle\langle b\rangle_{\text{spin}}\rangle_{\text{isotope}}. \tag{4.2.96}$$

Since I_z depends only on the spin states of the nuclei [4]

$$\langle I_x\rangle_{\text{spin}} = \langle I_y\rangle_{\text{spin}} = \langle I_z\rangle_{\text{spin}} = 0. \tag{4.2.97}$$

A and B in the expression of $\hat{b}$ (Equation 4.2.88) depend only on the isotope, and thus

$$\overline{b}_{u\to u} = \overline{\langle u|\,\hat{b}\,|u\rangle} = \langle A\rangle_{\text{isotope}} \tag{4.2.98}$$

$$\overline{b}_{v\to v} = \overline{\langle v|\,\hat{b}\,|v\rangle} = \langle A\rangle_{\text{isotope}} \tag{4.2.99}$$

$$\overline{b}_{u\to v} = \overline{\langle u|\,\hat{b}\,|v\rangle} = 0 \tag{4.2.100}$$

$$\overline{b}_{v\to u} = \overline{\langle v|\,\hat{b}\,|u\rangle} = 0. \tag{4.2.101}$$

This shows that coherent nuclear scattering happens with no spin flip only.

4.2.2.1.2 Incoherent Nuclear scattering We saw in Equation 4.2.25 that incoherent scattering is proportional to $\overline{b^2} - \overline{b}^2$. Thus, from equations 4.2.89

$$(\overline{b^2} - \overline{b}^2)_{u\to u} = \langle A^2\rangle_{\text{isotope}} - \langle A\rangle^2_{\text{isotope}} + \frac{1}{3}\langle B^2 I(I+1)\rangle_{\text{isotope}} \tag{4.2.102}$$

$$(\overline{b^2} - \overline{b}^2)_{v\to v} = \langle A^2\rangle_{\text{isotope}} - \langle A\rangle^2_{\text{isotope}} + \frac{1}{3}\langle B^2 I(I+1)\rangle_{\text{isotope}} \tag{4.2.103}$$

$$(\overline{b^2} - \overline{b}^2)_{u\to v} = \frac{2}{3}\langle B^2 I(I+1)\rangle_{\text{isotope}} \tag{4.2.104}$$

$$(\overline{b^2} - \overline{b}^2)_{v\to u} = \frac{2}{3}\langle B^2 I(I+1)\rangle_{\text{isotope}}. \tag{4.2.105}$$

4.2.2.2 Magnetic scattering

The magnetic scattering partial differential cross-section is given by Equation 4.2.58:

$$\begin{aligned}\left.\frac{\mathrm{d}^2\sigma}{\mathrm{d}\Omega\mathrm{d}\omega}\right|_{\sigma_i\lambda_i\to\sigma_f\lambda_f} &= \frac{k_f}{k_i}\left|\langle\boldsymbol{\sigma_f}\lambda_f|\,V_m(\boldsymbol{\kappa})\,|\boldsymbol{\sigma_i}\lambda_i\rangle\right|^2\delta(E_{\lambda_i}-E_{\lambda_f}+\hbar\omega)\\ &= \frac{k_f}{k_i}\left|\langle\boldsymbol{\sigma_f}\lambda_f|\,\gamma r_0\boldsymbol{\sigma}\cdot\boldsymbol{Q}_\perp(\boldsymbol{\kappa})\,|\boldsymbol{\sigma_i}\lambda_i\rangle\right|^2\delta(E_{\lambda_i}-E_{\lambda_f}+\hbar\omega)\\ &= \frac{k_f}{k_i}\left|\langle\boldsymbol{\sigma_f}\lambda_f|\,\boldsymbol{\sigma}\cdot\left(-\frac{\gamma r_0}{2\mu_{\text{B}}}\boldsymbol{M}_\perp(\boldsymbol{\kappa})\right)|\boldsymbol{\sigma_i}\lambda_i\rangle\right|^2\delta(E_{\lambda_i}-E_{\lambda_f}+\hbar\omega),\end{aligned} \tag{4.2.106}$$

where $\boldsymbol{M}_\perp(\boldsymbol{\kappa}) = \boldsymbol{M}(\boldsymbol{\kappa}) - (\boldsymbol{M}(\boldsymbol{\kappa})\cdot\hat{\boldsymbol{\kappa}})\hat{\boldsymbol{\kappa}}$ and $\boldsymbol{M}(\boldsymbol{\kappa}) = -2\mu_{\text{B}}\boldsymbol{Q}(\boldsymbol{\kappa})$ (Equation 4.2.62). We notice that $-\frac{\gamma r_0}{2\mu_{\text{B}}}\boldsymbol{\sigma}\cdot\boldsymbol{M}_\perp(\boldsymbol{\kappa})$ and $B\boldsymbol{\sigma}\cdot\boldsymbol{I}$ have similar form and replacing B with $-\frac{\gamma r_0}{2\mu_{\text{B}}}$ and all the components of $\boldsymbol{I}$ with the components of $\boldsymbol{M}_\perp$ and taking $A = 0$ gives the spin-states matrix

elements for the magnetic scattering [4]

$$\langle u|\, V_m(\boldsymbol{\kappa})\, |u\rangle = -\frac{\gamma r_0}{2\mu_\mathrm{B}}\left[M_{\perp z}(\boldsymbol{\kappa})\right] \tag{4.2.107}$$

$$\langle v|\, V_m(\boldsymbol{\kappa})\, |v\rangle = -\frac{\gamma r_0}{2\mu_\mathrm{B}}\left[-M_{\perp z}(\boldsymbol{\kappa})\right] \tag{4.2.108}$$

$$\langle u|\, V_m(\boldsymbol{\kappa})\, |v\rangle = -\frac{\gamma r_0}{2\mu_\mathrm{B}}\left[M_{\perp x}(\boldsymbol{\kappa}) - iM_{\perp y}(\boldsymbol{\kappa})\right] \tag{4.2.109}$$

$$\langle v|\, V_m(\boldsymbol{\kappa})\, |u\rangle = -\frac{\gamma r_0}{2\mu_\mathrm{B}}\left[M_{\perp x}(\boldsymbol{\kappa}) + iM_{\perp y}(\boldsymbol{\kappa})\right]. \tag{4.2.110}$$

We see from the equations 4.2.107 that the scattering without spin-flip is only sensitive to magnetisation components parallel to the polarisation and spin-flip scattering is only sensitive to magnetisation components normal to the polarisation.

4.2.2.3 Total scattering

Combining the nuclear and the magnetic scattering together gives the matrix elements [56]

$$|u\rangle \rightarrow |u\rangle = \langle A\rangle_\mathrm{isotope} - \frac{\gamma r_0}{2\mu_\mathrm{B}} M_{\perp z} + BI_z \tag{4.2.111}$$

$$|v\rangle \rightarrow |v\rangle = \langle A\rangle_\mathrm{isotope} + \frac{\gamma r_0}{2\mu_\mathrm{B}} M_{\perp z} - BI_z \tag{4.2.112}$$

$$|u\rangle \rightarrow |v\rangle = -\frac{\gamma r_0}{2\mu_\mathrm{B}}\left(M_{\perp x} - iM_{\perp y}\right) + B(I_x - iI_y) \tag{4.2.113}$$

$$|v\rangle \rightarrow |u\rangle = -\frac{\gamma r_0}{2\mu_\mathrm{B}}\left(M_{\perp x} + iM_{\perp y}\right) + B(I_x + iI_y), \tag{4.2.114}$$

for the coherent neutron scattering, and [56]

$$|u\rangle \rightarrow |u\rangle = \langle A\rangle_\mathrm{isotope} - \frac{\gamma r_0}{2\mu_\mathrm{B}} M_{\perp z} + b_{ii} + \frac{1}{3} b_{si} \tag{4.2.115}$$

$$|v\rangle \rightarrow |v\rangle = \langle A\rangle_\mathrm{isotope} + \frac{\gamma r_0}{2\mu_\mathrm{B}} M_{\perp z} + b_{ii} + \frac{1}{3} b_{si} \tag{4.2.116}$$

$$|u\rangle \rightarrow |v\rangle = -\frac{\gamma r_0}{2\mu_\mathrm{B}}\left(M_{\perp x} - iM_{\perp y}\right) + \frac{2}{3} b_{si} \tag{4.2.117}$$

$$|v\rangle \rightarrow |u\rangle = -\frac{\gamma r_0}{2\mu_\mathrm{B}}\left(M_{\perp x} + iM_{\perp y}\right) + \frac{2}{3} b_{si}, \tag{4.2.118}$$

for the incoherent neutron scattering, where $b_{ii} = \sqrt{\langle A^2\rangle_\mathrm{isotope} - \langle A\rangle^2_\mathrm{isotope}}$ and $b_{si} = \sqrt{B^2 I(I+1)}$.

4.3 Instrumentation

Neutrons are excellent probes to investigate magnetic and nuclear structures in condensed matter. There are two main types of neutron sources: continuous and pulsed sources. In a continuous or steady state source the neutron beam is produced with a nuclear reactor (LLB in Saclay, ILL in Grenoble (France) or FRM2 in Garching (Germany) for instance). A pulsed source consists in hitting a target (e.g. Tungsten) with a beam of accelerated particles (e.g. protons) during a very short time ($\approx 1\mu s$) and at a frequency between 10Hz and 50Hz. Pulses of neutrons are then *spalled* from the target by the incident particles. This source is therefore also called spallation source (e.g. ISIS in Didcot, UK). The neutrons are then thermalised in order to bring their energy spectra in an useful range for experiments. Typically thermal neutrons have an energy of 5-100meV [54]. For experiments that require low energy neutrons, the neutron source is moderated by a cryogenic moderator, which can be liquid H_2 or CH_4 at 20K [54]. Low energy neutrons with a typical energy of $0.1 \leq E \leq 10$meV are called *cold* neutrons [54]. When higher energy neutrons are needed ($E \geq 100$meV), the neutron source is moderated with graphite at 2400K like at ILL in Grenoble [54]. The neutron beams at different energies (cold, thermal and hot) are then directed toward the instruments to perform various types of measurements. We used a triple axis spectrometer (TAS) and a multi-choppers spectrometer (MCS) with unpolarised cold neutrons for all the elastic and inelastic neutron scattering measurements. We also did polarised neutrons diffraction measurements on POLI, which is a double axis diffractometer (DAD).

We can divide our measurements in two categories: measurements with unpolarised neutrons and measurements with polarised neutrons, which are presented in the following chapters. In the next section we will have an overview of the instruments that we used for the unpolarised neutrons measurements (4F2, Panda and LET). Then we will have a brief overview of POLI, the polarised neutrons instrument and we will finish with the theory of the polarisation with ^{3}He cells and the different cross-sections.

4.3.1 Unpolarised neutrons measurements

4.3.1.1 4F2 and Panda

4F2, operated by CEA-CNRS, at the Laboratoire Léon Brillouin (LLB) and Panda, operated by JCNS, at the Heinz Maier-Leibnitz Zentrum [57] are TAS instruments. TAS, represented in Figure 4.6, was invented by Bertram Brockhouse at the NRX nuclear experimental reactor

in Canada in 1956. The name *triple axis* comes from the fact that there are three (parallel) rotation axes perpendicular to the scattering plane: the first axis to select incoming neutron energy, the second axis to select the $\mathbf{q}$ position in the reciprocal lattice and the third axis to select the energy transfer between the neutrons and the sample. Collimators are used to remove from the beam the components that are not parallel to the beam axis. The beam shutter cuts the beam so that we can access the instrument. The adjustable slits act as a diaphragm. The monochromator sits on the first axis and its function is to deliver a monochromatic neutron beam to the sample. On 4F2 the monochromation is done with Bragg reflection on two monocrystals of pyrolytic graphite and k_i is chosen by adjusting the beam-monocrystals angle. The monitor, represented by a small empty rectangle located between the monochromator and the Be-filter in Figure 4.6, counts neutrons after the monochromator. The Beryllium-filter (Be-filter) cuts out the higher k_i harmonics that leak through the monochromator. The sample sits on the second axis. The analyser, which sits on the third axis, does the same work with the scattered beam k_f as the monochromator does with k_i. Finally the detector counts the number of neutrons scattered in its direction with the final energy selected by the analyser.

With a TAS we measure the probability that an incident neutron with initial momentum $\boldsymbol{k_i}$ and energy E_i scatters with the system into a final momentum $\boldsymbol{k_f}$ and energy E_f as seen previously. The conservation laws give the momentum and the energy exchange between the neutron and the sample:

$$\begin{cases} \hbar \boldsymbol{Q} & = \hbar(\boldsymbol{k_f} - \boldsymbol{k_i}) \\ \hbar\omega & = \frac{\hbar^2(k_f^2)}{2m_n} - \frac{\hbar^2(k_i^2)}{2m_n}, \end{cases} \tag{4.3.1}$$

where $\boldsymbol{Q}$ is the scattering vector. Figure 4.7 shows the connection between real space positioning of the TAS and reciprocal space scanning position. Selecting $\boldsymbol{k_i}$ and $\boldsymbol{k_f}$ (direction and amplitude) fixes $\boldsymbol{Q}$ the position observed in reciprocal space. In the reciprocal space, the right part of Figure 4.7, $\boldsymbol{Q}$ is defined as $\boldsymbol{Q} = \boldsymbol{k}_f - \boldsymbol{k}_i$, but there is an infinite number of ($\boldsymbol{k_i}$, $\boldsymbol{k_f}$) sets that give the same $\boldsymbol{Q}$. In inelastic neutron scattering measurements we perform energy scans at a constant $\boldsymbol{Q}$ position by changing the ($\boldsymbol{k_i}$, $\boldsymbol{k_f}$) set. Typically, either k_i or k_f is kept constant and its orientation and the other $\boldsymbol{k_f}$ or $\boldsymbol{k_i}$ (amplitude and orientation) is tuned to select the transferred energy ΔE and scattering vector $\boldsymbol{Q}$. At 4F2 and Panda, we maintain k_f constant and we tune $\boldsymbol{k_i}$. For the elastic measurements, on the other hand, we maintain k_i=k_f and only the relative orientation between the vectors changes, which allows to move $\boldsymbol{Q}$ in reciprocal space. A TAS works with three axis when doing inelastic measurements, but we freeze the

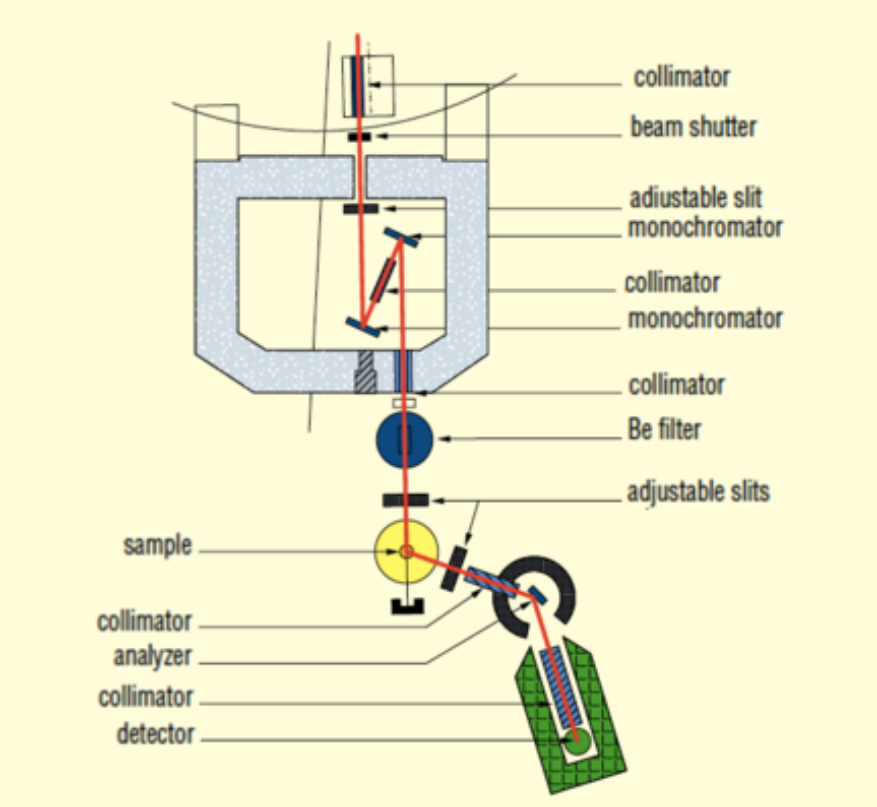

Figure 4.6: Representation of a TAS of the 4F2 experimental line at the LLB in Saclay [58].

analyser axis on zero transferred energy for the elastic measurements.

4.3.1.2 LET

LET is a multi-choppers spectrometer that uses the time of flight principle to measure the energy of a scattered neutron. It is operated by STFC at ISIS, is connected to the Tungsten target located in target station two (TS2). The pulse frequency of the synchrotron is $f_{sync} =$ 50Hz and one pulse in five reaches TS2. LET's work frequency is therefore $f_{LET} =$ 10Hz. Neutrons spalling from TS2 are moderated with solid methane and liquid hydrogen. After being moderated and while being guided toward the sample with super-mirrors, the neutrons go through several chopper discs to shape and clean the pulse and to select the incident energies (see Figure 4.8(a) [60]). Chopper 1 and 5 are both composed of two high speed counter-rotating discs that select the incident energy and the energy resolution. Chopper 2 is a slow rotating disc that prevents the overlapping of two consecutive 10Hz pulses, which happens when slow

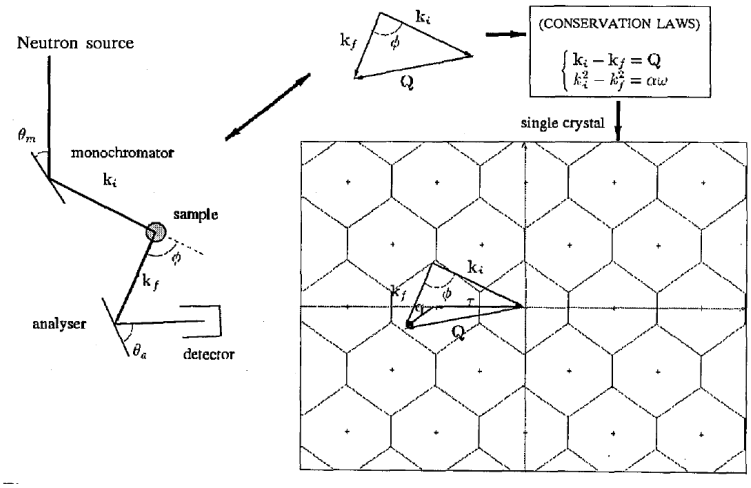

Figure 4.7: Real space and reciprocal space representation of a TAS in a specific position (picture from [59]). One position of the instrument in real space (left part), which sets $\boldsymbol{k_i}$ and $\boldsymbol{k_f}$, corresponds to a $\boldsymbol{Q}$ scattering vector in the reciprocal space (right part). The lattice invariance allows to define $\boldsymbol{q}$ in the first Brillouin zone such that $\boldsymbol{Q} = \boldsymbol{q} + \boldsymbol{\tau}$, where $\boldsymbol{\tau}$ is a reciprocal lattice vector.

neutrons from the previous pulse arrive at the same time as neutrons from the new pulse. LET is able to measure at more than one (usually three or four) incident energy within one single pulse. It is Chopper 3 that separates (in time) the measurements at different incident energies to prevent their overlapping in the time of flight. Figure 4.8(b) illustrates the role of the choppers in the case of three measured incident energies: $E_1 = 5$meV, $E_2 = 1.5$meV and $E_3 = 0.7$meV. Chopper 4 cuts out the tail of the signals with the different incident energies. The blue lines in the figure represent the trajectories of the neutrons through the multiple choppers. The split of the trajectories observed after the sample comes from the energy transfer between the latter and the neutrons: the slope increases(decreases) when neutrons gain (lose) energy before hitting the detectors.

The detector is composed of 384 vertical tubes positioned to form a half circle with the sample in its centre (red line in Figure 4.8(a)) and those form a detection array covering 180° in horizontal direction (from $-40°$ to 140°) and and 60° in vertical direction (from $-30°$ to 30°). Each tube, which is 4m long and 1 inch in diameter, is filled with ^{3}He at a pressure of 10atm and contains a thin Platinum wire on its axis. A neutron hitting a tube reacts with the ^{3}He:

$$ {}^3_2He + {}^1_0 n \rightarrow {}^3_1 T + {}^1_1 p, \tag{4.3.2} $$

where ${}^{3}_{2}He$ is an atom of helium 3, ${}^{1}_{0}n$ is a neutron, ${}^{3}_{1}T$ is a atom of tritium and ${}^{1}_{1}p$ is a proton. The proton hits the Pt-wire at the centre of the tube and generates a current. The vertical position of the neutron's hitting point is obtained by resistance calculation from the voltage amplitude measured at each end of the tube.

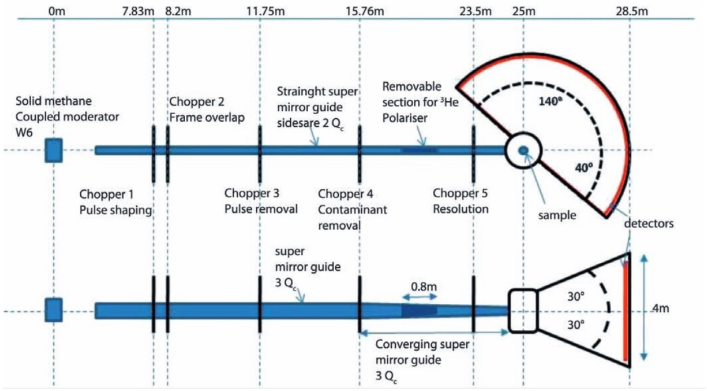

(a) global overview of the LET instrument

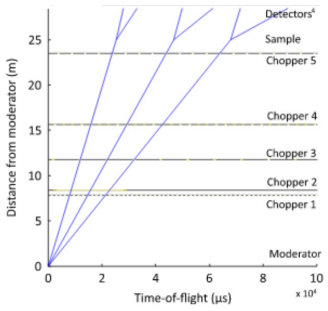

(b) effect of the choppers on the distance-time relation of the neutrons reaching the sample

Figure 4.8: Representation of LET spectrometer at ISIS (**a**) and the chopper system (**b**). (a) shows the 25 m primary flight path with the straight super-mirror guide, the five choppers installed on the beam path, the 110 m^3 vacuum tank where the sample is installed and the detector array. (b) illustrates how the chopper system produces three neutron beam with different incident energies. Figures from [60].

4.3.2 Polarised neutrons measurements

As explained already, neutrons are good probes to measure the magnetic structure and, because they do not carry any electrical charge, to measure the nuclear structure in a crystal. However it is often the case that the detected scattering intensity is a superposition of a nuclear intensity and a magnetic intensity. It would be nice if we could choose what part of the signal we want to look at and filter out all the *uninteresting* part. We saw previously that this is made possible with spin polarised neutrons. We measured with POLI instrument at Heinz Maier-Leibnitz Zentrum in Garching (Germany) and operated by RWTH Aachen University [61], which uses Helium 3 (^{3}He) cells to polarise the neutrons.

4.3.2.1 POLI instrument

POLI, a DAD, allows *spherical* polarisation analysis [2] and it uses hot neutrons, and thus covers a wider range of the reciprocal space. Like in the TAS, the monochromator sits on the first axis and the sample on the second axis (Figure 4.9). Apart from the absence of the third axis, the main differences between POLI and 4F2 or Panda are the polariser, the analyser and the nutators (7, 11 and 8 respectively in Figure 4.9). The polariser polarises the incoming neutron beam into one direction, the nutators orient the beam polarisation in space and the analyser removes depolarised neutrons from the scattered beam before it reaches the detector. Neutron beams can be polarised with ^{3}He cells, polarising mirrors or polarising crystals. POLI spectrometer uses ^{3}He cells, which principle is detailed in next paragraph.

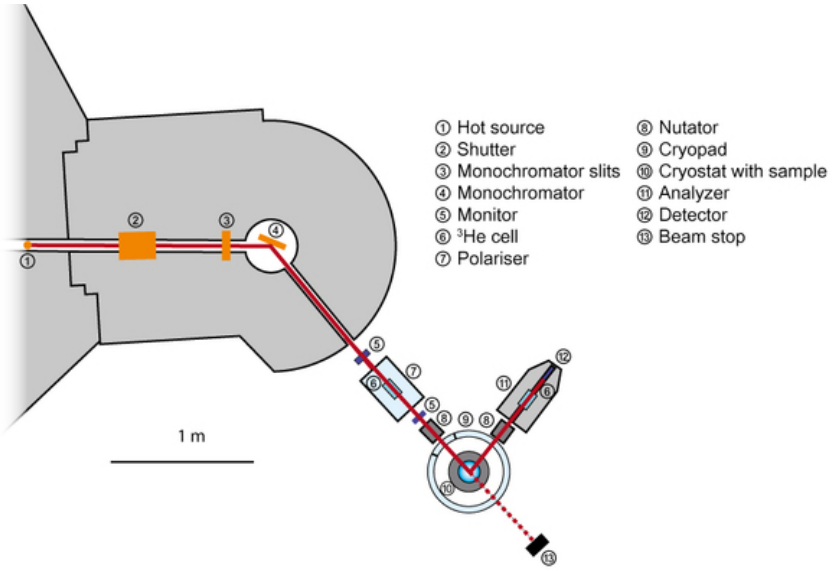

Figure 4.9: Overview of the different parts of the polarized neutrons instrument POLI at FRM2, Germany (figure from http://www.mlz-garching.de/poli)

4.3.2.2 Polarisation of the neutrons

4.3.2.2.1 Time dependent polarisation POLI uses identical ^{3}He cells to polarise the incident neutron beam and to analyse the scattered beam (see Figure 4.10b). The cells are placed in magneto-static cavities, where a very uniform and homogeneous magnetic field is generated. On the incident beam side the ^{3}He cell + magneto-static cavity are the polariser

[2] 3D polarisation of the neutrons (1D polarisation is called *longitudinal* polarisation analysis).

(right side in Figure 4.10a) and it is called the analyser (or Decpol) on the scattered beam side (left side in Figure 4.10a) [62]. ^{3}He has a very big absorption cross-section for neutrons with anti-parallel spin ($\sigma_{\uparrow\downarrow} \approx 6000$b), whereas this cross-section is very small when the ^{3}He and the neutron spins are parallel (($\sigma_{\uparrow\uparrow} \approx 5$b). Therefore by correctly orienting the spins of ^{3}He atoms in a cell, one can *filter out* neutrons with same spin orientation and polarise the beam (the term cell or filter will be used indifferently to designate a ^{3}He cell).

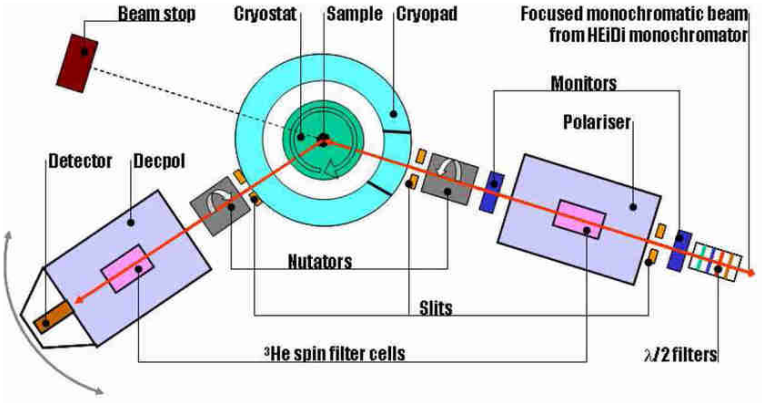

(a) Spherical neutron polymetry setup on POLI instrument

(b) ^{3}He cells used to polarise incident beam and analyse scattered beam

Figure 4.10: Incident neutron beam polarisation and scattered beam analysis system on POLI-HEIDI diffractometers. Figure from [62].

If $\sigma_\pm = \sigma_0 \pm \sigma_p$ are the spin dependent cross sections of the absorption processes in a ^{3}He cell, then the transmission is also spin dependent and writes [63, 64]

$$t^\pm = e^{-\tilde{N} d \sigma_0 (1 \mp P_{\mathrm{He}})}, \tag{4.3.3}$$

where $\tilde{N}$ is the atomic concentration of ^{3}He in the cell and d is the thickness of the latter. The total transmission for an unpolarised neutron beam is given by

$$T = \frac{t^+ - t^-}{2}, \tag{4.3.4}$$

and using Equation 4.3.3 and the absorption parameter of the cell, which is defined as $\mu = \tilde{N} d \sigma_0$, gives [63]

$$T(t) = e^{\mu} \cosh\left[\mu P_{\mathrm{He}}(t)\right]. \tag{4.3.5}$$

At POLI, instead of the absorption parameter μ, the opacity is used and is defined as [62, 65]

$$O(\lambda) = 0.0732 \times l \times \lambda \times p, \tag{4.3.6}$$

where 0.0732 is a dimensionless constant, l is the length of the cell (in cm), λ is the *de Broglie*-wavelength of the neutrons going through the cell (in Å) and p is the pressure of ^{3}He gas (in bar). The transmission coefficient for an unpolarised neutron beam is then [62, 65]

$$T(t) = T_0 e^{-O} \cosh\left[O P_{\mathrm{He}}(t)\right], \tag{4.3.7}$$

with

$$P_{\mathrm{He}}(t) = P_{\mathrm{He}}(0) e^{-\frac{t}{T_1}}. \tag{4.3.8}$$

T_0 in Equation 4.3.7 is the transmission of the empty filter. In Equation 4.3.8, $P_{\mathrm{He}}(0)$ is the initial polarisation of ^{3}He and T_1 is the relaxation time of the cell's polarisation ($\sim$ 120h).

Two monitors, that are located before (M1) and after (M2) the polariser (Number 5 in Figure 4.9), allow to continuously measure the transmission $T_p(t)$ of the polariser given by

$$T_p(t) = \frac{M_2(t)}{M_1(t)}, \tag{4.3.9}$$

where $M_1(t)$ and $M_2(t)$ are the counting rates of M1 and M2, respectively. Fitting the data with Equation 4.3.7 gives precise values of $P_{\mathrm{He}}(0)$ and T_1 for the polariser.

For the analyser we follow the same procedure, but this must be measured at a pure nuclear peak, such that no spin flip occurs in the sample, between the monitor and the analyser. Additionally, this is done without the polariser. Thus we can only measure before the polariser is inserted (when installing the new cells), and after it is removed at the end of the experiment

(when we change the cells). This gives only two data points, which we fit with Equation 4.3.7, and therefore the error on $P_{\mathrm{He}}(0)$ and T_1 are bigger for the analyser than for the polariser.

The asymmetry is what we measure during an experiment:

$$A = \frac{n^+ - n^-}{n^+ + n^-}, \tag{4.3.10}$$

where n^+ and n^- are the counting rates for polariser and analyser settings parallel or anti-parallel to each other. A can also be written as a function of the scattered beam polarisation P'_n and analyser efficiency A_n [62]

$$A = P'_n A_n, \tag{4.3.11}$$

with

$$A_n(t) = \tanh\left[OP_{\mathrm{He}}(t)\right], \tag{4.3.12}$$

where $P_{\mathrm{He}}(t)$ and O are the ^{3}He polarisation and the opacity, respectively, of the analyser cell. In the same way, the efficiency of the polariser is

$$P_n(t) = \tanh\left[OP_{\mathrm{He}}(t)\right], \tag{4.3.13}$$

where $P_{\mathrm{He}}(t)$ and O are now the ^{3}He polarisation and the opacity, respectively, of the polariser cell. With equations 4.3.10 and 4.3.11 the polarisation of the scattered beam becomes

$$P'_n(t_m) = \frac{n^+(t_1) - n^-(t_2)}{n^+(t_1) + n^-(t_2)} \frac{1}{A_n(t_m)}, \tag{4.3.14}$$

where t_1 is the time of measurement of n^+, t_2 is the time of measurement of n^- and $t_m = (t_1 + t_2)/2$.

4.3.2.2.2 Cell physical parameters To optimise the physical parameters of a filter (pressure of ^{3}He gas, dimensions,etc...), which allows for the most accurate determination of P', we use the quality factor. The aim is to maximise the square root of the latter [63]. To achieve that, we take ^{3}He polarisation constant and we consider the λ-dependence of the opacity in Equation 4.3.7. The quality factor Q is given by [63]:

$$Q(\lambda) = P_n(\lambda)^2 T_n(\lambda). \tag{4.3.15}$$

For a given ^{3}He polarisation P_{He} (usually 70% is a good value [62]), the optimal opacity is given by:

$$
\begin{aligned}
&\frac{\mathrm{d}\sqrt{Q}}{\mathrm{d}O} = 0 \\
\text{(i.e.)}\ &\frac{\mathrm{d}}{\mathrm{d}O}(P_n\sqrt{T_n}) = 0 \\
\text{(i.e.)}\ &\frac{\mathrm{d}}{\mathrm{d}O}(\sqrt{T_0 e^{-O}\tanh(OP_{\mathrm{He}})\sinh(OP_{\mathrm{He}})}) = 0 \\
\text{(i.e.)}\ &P_{\mathrm{He}}\tanh(OP_{\mathrm{He}})^2 + \tanh(OP_{\mathrm{He}}) - 2P_{\mathrm{He}} = 0
\end{aligned}
\qquad (4.3.16)
$$

.

Solving the 2$^{\mathrm{nd}}$ order equation in $\tanh(OP_{\mathrm{He}})$ (Equation 4.3.16) gives one physical solution for the optimal opacity as a function of P_{He}:

$$
O_{\mathrm{opt}} = \frac{0.0732}{P_{\mathrm{He}}}\,\mathrm{arctanh}\left(\sqrt{\frac{1}{4P_{\mathrm{He}}^2} + 2} - \frac{1}{2P_{\mathrm{He}}}\right), \qquad (4.3.17)
$$

which gives $O_{\mathrm{opt}} = 0.0732\lambda l p \approx 26\,\mathrm{barcm\,\AA}$ for a typical cell polarisation of $P_{\mathrm{He}} = 70\,\%$. On POLI l is fixed by the geometrical constraints of the instrument ($l = 13\,\mathrm{cm}$) and $p \approx 3\mathrm{bar}$. Figure 4.11 shows the λ-evolution of the quality factor of ^{3}He cells containing 2 bar and 3 bar of ^{3}He. We measured at $\lambda = 1.145\,\mathrm{\AA}$ and we see that $p = 3\mathrm{bar}$ is a good pressure to work with.

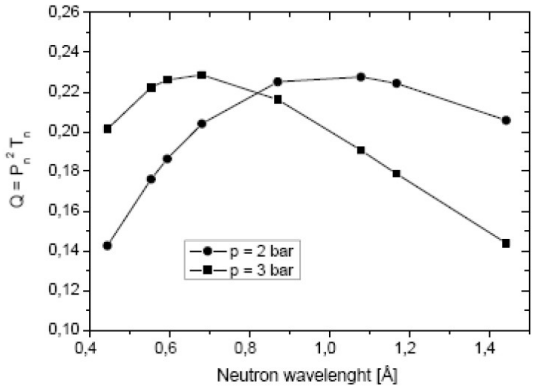

Figure 4.11: ^{3}He cell quality factor against neutron wavelength λ for $p_{\mathrm{He}} = 2\,\mathrm{bar}$ and $p_{\mathrm{He}} = 3\,\mathrm{bar}$ (figure from [62])

4.3.2.3 Measurements

4.3.2.3.1 Coordinates system The coordinate system of POLI instrument is as follow:

$$\begin{aligned} \boldsymbol{x} &= \frac{\boldsymbol{Q}}{Q} \\ \boldsymbol{y} &\perp \boldsymbol{x} \quad \text{and in the scattering plane} \\ \boldsymbol{z} &= \boldsymbol{x} \times \boldsymbol{y}. \end{aligned} \tag{4.3.18}$$

The incident neutron beam is polarised parallel to the polarisation of the filter in the polariser (right side in Figure 4.10a). This polariser can be rotated by 180° around the beam axis, which flips the incident polarisation from $\boldsymbol{z}$ to $-\boldsymbol{z}$. The beam polarisation is then spatially orientated by the nutator on the polariser side (right side in Figure 4.10a) by applying a magnetic field in a specific direction, which makes the neutron spin to precess. The same manipulations are done with the scattered beam (left side in Figure 4.10a). Like the polariser, the analyser can also be rotated by 180 °. Thus there are four possible configurations for the polariser and the analyser:

- **non spin flip:**
  - polariser and analyser parallel to $\boldsymbol{z}$
  - polariser and analyser parallel to $-\boldsymbol{z}$
- **spin flip:**
  - polariser parallel to $\boldsymbol{z}$ and analyser parallel to $-\boldsymbol{z}$
  - polariser parallel to $-\boldsymbol{z}$ and analyser parallel to $\boldsymbol{z}$

4.3.2.3.2 Spherical neutron polarimetry In Section 4.2.2 we saw the polarisation *spin state* cross-sections in the case of an uniaxial polarisation analysis. With the latter method, we cannot measure polarisation scattered in directions perpendicular to the initial polarisation orientation. Instead the scattered beam appears to be more depolarised, even if it is actually more polarised, but in different directions. The method that allows to measure the polarisation of the scattered beam in all directions is called spherical neutron polarimetry (SNP).

The total cross-section, that includes polarisations of all directions, was derived indepen-

dently by Blume [66] and Maleev [67]

$$\sigma = \begin{cases} NN^* & \text{nuclear} \\ +\boldsymbol{M}_\perp \cdot \boldsymbol{M}_\perp^* & \text{collinear magnetic} \\ -i\boldsymbol{P} \cdot (\boldsymbol{M}_\perp \times \boldsymbol{M}_\perp^*) & \text{chiral} \\ +2\boldsymbol{P} \cdot \mathrm{Re}\{\boldsymbol{M}_\perp N^*\} & \text{nuclear-magnetic interference,} \end{cases} \tag{4.3.19}$$

where $\boldsymbol{P}$ is the initial polarisation of the neutron beam. The authors also calculated the expression for the scattered polarisation

$$\boldsymbol{P}'\sigma = \begin{cases} \boldsymbol{P}NN^* & \text{nuclear} \\ -\boldsymbol{P}\,(\boldsymbol{M}_\perp \cdot \boldsymbol{M}_\perp^*) + 2\,\mathrm{Re}[\boldsymbol{M}_\perp\,(\boldsymbol{P} \cdot \boldsymbol{M}_\perp^*)] & \text{collinear magnetic} \\ +i\,(\boldsymbol{M}_\perp \times \boldsymbol{M}_\perp^*) & \text{chiral} \\ +2\,\mathrm{Re}\{\boldsymbol{M}_\perp N^*\} + 2\boldsymbol{P} \times \mathrm{Im}[\boldsymbol{M}_\perp N^*] & \text{nuclear-magnetic interference,} \end{cases} \tag{4.3.20}$$

where $\boldsymbol{P}'$ is the polarisation of the scattered neutron beam. In the $(\boldsymbol{x}, \boldsymbol{y}, \boldsymbol{z})$ basis defined previously, Equation 4.3.20 can also be written in a tensorial form as

$$\begin{pmatrix} P'_x \\ P'_y \\ P'_z \end{pmatrix} \sigma = \begin{pmatrix} N^2 - M^2 & -I_{nz} & I_{ny} \\ I_{nz} & N^2 - M^2 + R_{yy} & R_{yz} \\ -I_{ny} & R_{zy} & N^2 - M^2 + R_{zz} \end{pmatrix} \begin{pmatrix} P_x \\ P_y \\ P_z \end{pmatrix} + \begin{pmatrix} -I_{yz} \\ R_{ny} \\ R_{nz} \end{pmatrix}, \tag{4.3.21}$$

with

$$\begin{aligned} N^2 &= NN^* \\ M^2 &= \boldsymbol{M}_\perp \cdot \boldsymbol{M}_\perp^* \\ R_{ni} &= 2\,\mathrm{Re}[NM_{\perp i}^*] \\ I_{ni} &= 2\,\mathrm{Im}[NM_{\perp i}^*] \\ R_{ij} &= 2\,\mathrm{Re}[M_{\perp i}M_{\perp j}^*] \\ I_{ij} &= 2\,\mathrm{Im}[M_{\perp i}M_{\perp j}^*], \end{aligned}$$

and $P_x,\ P_y,\ P_z$ and $P'_x,\ P'_y,\ P'_z$ are the $\boldsymbol{x}$, $\boldsymbol{y}$ and $\boldsymbol{z}$ components of the incident and scattered polarisations respectively.

If we define the polarisation tensor $\mathbf{P}$ and the created polarisation vector $\boldsymbol{P''}$ as

$$\mathbf{P} = \begin{pmatrix} (N^2 - M^2)/\sigma_x & I_{nz}/\sigma_x & -I_{ny}/\sigma_x \\ -I_{nz}/\sigma_y & (N^2 - M^2 + R_{yy})/\sigma_y & R_{zy}/\sigma_y \\ I_{ny}/\sigma_z & R_{yz}/\sigma_z & (N^2 - M^2 + R_{zz})/\sigma_z \end{pmatrix} \tag{4.3.22}$$

$$\boldsymbol{P''} = \begin{pmatrix} -I_{yz}\sigma \\ R_{ny}/\sigma \\ R_{zy}/\sigma \end{pmatrix}, \tag{4.3.23}$$

with (from Equation 4.3.19)

$$\begin{aligned} \sigma_x &= N^2 + M^2 + P_x I_{yz} \\ \sigma_y &= N^2 + M^2 + P_y R_{ny} \\ \sigma_z &= N^2 + M^2 + P_z R_{nz}, \end{aligned}$$

the scattered polarisation in Equation 4.3.21 becomes

$$\boldsymbol{P'} = \mathbf{P}^{\mathrm{T}}\boldsymbol{P} + \boldsymbol{P''}, \tag{4.3.24}$$

or in terms of components, with $i, j \in \{x, y, z\}$

$$P'_i = \sum_j \mathrm{P}^{\mathrm{T}}_{ij} P_j + P''_i. \tag{4.3.25}$$

From Equation 4.3.24, for a pure magnetic state, we always have $|\boldsymbol{P'}| \geq |\boldsymbol{P}|$. This means that, with a sample with a single magnetic domain, the polarisation of the scattered beam is always higher or equal to the one of the incident beam. However in reality, samples can have multiple magnetic domains, which depolarise the neutron beam and thus $|\boldsymbol{P'}| < |\boldsymbol{P}|$.

A typical SNP experiment consists in measuring the polarisation matrix $\boldsymbol{\mathcal{P}}$, with elements

$$\mathcal{P}_{ij} = \frac{\sigma_{ij} - \sigma_{i\bar{j}}}{\sigma_{ij} + \sigma_{i\bar{j}}}. \tag{4.3.26}$$

σ_{ij}, with $i, j \in \{x, y, z\}$, is the spin-state cross-section (or theoretical intensity of the ij-channel) when the incident neutron beam is polarised along i and the scattered beam is polarised along j, $\bar{j}$ denotes the direction opposite to j. In practice, we polarise the incident beam along i (i is

$\boldsymbol{x}$, $\boldsymbol{y}$ or $\boldsymbol{z}$) and we measure the asymmetries when the scattered beam polarisation is along j (j is $\boldsymbol{x}$, $\boldsymbol{y}$ or $\boldsymbol{z}$). Repeating the procedure for all possible ij configurations gives the nine elements of the 3×3 polarisation matrix. With the tensorial expression of $\boldsymbol{P'}$, the polarisation elements of Equation 4.3.26 become

$$\mathcal{P}_{ij} = \langle \frac{P_i \mathrm{P}_{ij} + P''_j}{P_i} \rangle_{\mathrm{domains}}, \tag{4.3.27}$$

where $\langle ... \rangle_{\mathrm{domains}}$ denotes the average over the magnetic domains in the sample.

4.3.2.3.3 Scattering cross-sections In a SNP experiment, to observe a selected spin-state cross-section, we orient the incident polarisation along one direction and observe the scattered polarisation along the same or another direction. Since there are six possible orientations ($\boldsymbol{x}, \boldsymbol{y}, \boldsymbol{z}, -\boldsymbol{x}, -\boldsymbol{y}, -\boldsymbol{z}$), for either the polariser or the analyser, we can observe thirty-six spin-state cross-sections or channels and those are given by the I_{ij} in Table 4.1. In consequence, there are four possible polarisation matrices (two with spin-flip configurations and two with non-spin-flip configurations), but only two are linearly independent:

$$\mathcal{P}_{ij} = \frac{\sigma_{ij} - \sigma_{i\bar{j}}}{\sigma_{ij} + \sigma_{i\bar{j}}} \tag{4.3.28}$$

$$= -\frac{\sigma_{i\bar{j}} - \sigma_{ij}}{\sigma_{i\bar{j}} + \sigma_{ij}} \tag{4.3.29}$$

$$= -\frac{\sigma_{i\bar{j}} - \sigma_{i\bar{\bar{j}}}}{\sigma_{i\bar{j}} + \sigma_{ij}} \tag{4.3.30}$$

$$= -\mathcal{P}_{i\bar{j}}, \tag{4.3.31}$$

and the same with $\mathcal{P}_{\bar{i}j}$ and $\mathcal{P}_{\bar{i}\bar{j}}$.

When neutrons are scattered by the sample, their spin is either up or down, and therefore

$$\forall i, j \in \{x, y, z, -x, -y, -z\}, \sigma_i = \sigma_{ij} + \sigma_{i\bar{j}}, \tag{4.3.32}$$

where $\bar{j} = -j$. With Equation 4.3.32 we can rewrite Equation 4.3.20 as [65]

$$\boldsymbol{P'}\sigma_i = \begin{pmatrix} \sigma_{ix} - \sigma_{i\bar{x}} \\ \sigma_{iy} - \sigma_{i\bar{y}} \\ \sigma_{iz} - \sigma_{i\bar{z}} \end{pmatrix}. \tag{4.3.33}$$

If we consider the component along j of the matrix $\boldsymbol{P'}\sigma_i$ in Equation 4.3.33, then, with Equa-

Table 4.1 Intensities of the 36 possible channels measured with spherical polarised neutrons (from [65])

I_{ij}		nuclear		magnetic	chiral magnetic	nuc. magn. interference
xx	=	NN^*				
$x\bar{x}$	=			$\boldsymbol{M}_\perp \cdot \boldsymbol{M}_\perp^*$	$-\,\mathrm{i}(\boldsymbol{M}_\perp \times \boldsymbol{M}_\perp^*)_x$	
$\bar{x}x$	=			$\boldsymbol{M}_\perp \cdot \boldsymbol{M}_\perp^*$	$+\,\mathrm{i}(\boldsymbol{M}_\perp \times \boldsymbol{M}_\perp^*)_x$	
$\bar{x}\bar{x}$	=	NN^*				
yy	=	NN^*	+	$M_y M_y^*$		+ $2\Re(M_y^* N)$
$y\bar{y}$	=			$M_z M_z^*$		
$\bar{y}y$	=			$M_z M_z^*$		
$\bar{y}\bar{y}$	=	NN^*	+	$M_y M_y^*$		− $2\Re(M_y^* N)$
zz	=	NN^*	+	$M_z M_z^*$		+ $2\Re(M_z^* N)$
$z\bar{z}$	=			$M_y M_y^*$		
$\bar{z}z$	=			$M_y M_y^*$		
$\bar{z}\bar{z}$	=	NN^*	+	$M_z M_z^*$		− $2\Re(M_z^* N)$
$x\bar{y} = y\bar{x}$ =		$1/2(NN^*$	+	$\boldsymbol{M}_\perp \cdot \boldsymbol{M}_\perp^*$	$-\,\mathrm{i}(\boldsymbol{M}_\perp \times \boldsymbol{M}_\perp^*)_x$	$+2\Re(M_y^* N) + 2\Im(M_x^* N))$
$x\bar{y} = \bar{y}x$ =		$1/2(NN^*$	+	$\boldsymbol{M}_\perp \cdot \boldsymbol{M}_\perp^*$	$-\,\mathrm{i}(\boldsymbol{M}_\perp \times \boldsymbol{M}_\perp^*)_x$	$-2\Re(M_y^* N) - 2\Im(M_x^* N))$
$\bar{x}y = yx$ =		$1/2(NN^*$	+	$\boldsymbol{M}_\perp \cdot \boldsymbol{M}_\perp^*$	$+\,\mathrm{i}(\boldsymbol{M}_\perp \times \boldsymbol{M}_\perp^*)_x$	$+2\Re(M_y^* N) - 2\Im(M_x^* N))$
$\bar{x}y = \bar{y}x$ =		$1/2(NN^*$	+	$\boldsymbol{M}_\perp \cdot \boldsymbol{M}_\perp^*$	$+\,\mathrm{i}(\boldsymbol{M}_\perp \times \boldsymbol{M}_\perp^*)_x$	$-2\Re(M_y^* N) + 2\Im(M_x^* N))$
$xz = z\bar{x}$ =		$1/2(NN^*$	+	$\boldsymbol{M}_\perp \cdot \boldsymbol{M}_\perp^*$	$-\,\mathrm{i}(\boldsymbol{M}_\perp \times \boldsymbol{M}_\perp^*)_x$	$+2\Re(M_z^* N) - 2\Im(M_y^* N))$
$x\bar{z} = \bar{z}\bar{x}$ =		$1/2(NN^*$	+	$\boldsymbol{M}_\perp \cdot \boldsymbol{M}_\perp^*$	$-\,\mathrm{i}(\boldsymbol{M}_\perp \times \boldsymbol{M}_\perp^*)_x$	$-2\Re(M_z^* N) + 2\Im(M_y^* N))$
$\bar{x}z = zx$ =		$1/2(NN^*$	+	$\boldsymbol{M}_\perp \cdot \boldsymbol{M}_\perp^*$	$+\,\mathrm{i}(\boldsymbol{M}_\perp \times \boldsymbol{M}_\perp^*)_x$	$+2\Re(M_z^* N) + 2\Im(M_y^* N))$
$\bar{x}\bar{z} = \bar{z}x$ =		$1/2(NN^*$	+	$\boldsymbol{M}_\perp \cdot \boldsymbol{M}_\perp^*$	$+\,\mathrm{i}(\boldsymbol{M}_\perp \times \boldsymbol{M}_\perp^*)_x$	$-2\Re(M_z^* N) - 2\Im(M_y^* N))$
$yz = zy$ =		$1/2(NN^*$		$+\,\boldsymbol{M}_\perp \cdot \boldsymbol{M}_\perp^* + 2\Re(M_y M_z^*)$		$+2\Re(M_y^* N) + 2\Re(M_z^* N))$
$y\bar{z} = \bar{z}y$ =		$1/2(NN^*$		$+\,\boldsymbol{M}_\perp \cdot \boldsymbol{M}_\perp^* - 2\Re(M_y M_z^*)$		$+2\Re(M_y^* N) - 2\Re(M_z^* N))$
$\bar{y}z = z\bar{y}$ =		$1/2(NN^*$		$+\,\boldsymbol{M}_\perp \cdot \boldsymbol{M}_\perp^* - 2\Re(M_y M_z^*)$		$-2\Re(M_y^* N) + 2\Re(M_z^* N))$
$\bar{y}\bar{z} = \bar{z}\bar{y}$ =		$1/2(NN^*$		$+\,\boldsymbol{M}_\perp \cdot \boldsymbol{M}_\perp^* + 2\Re(M_y M_z^*)$		$-2\Re(M_y^* N) - 2\Re(M_z^* N))$

tion 4.3.32,

$$\begin{aligned}(\boldsymbol{P}'\sigma_i)_j &= \sigma_{ij} - \sigma_{i\bar{j}} \\ &= 2\sigma_{ij} - \sigma_i,\end{aligned} \tag{4.3.34}$$

and thus

$$\sigma_{ij} = \frac{1}{2}\left(\sigma_i + (\boldsymbol{P}'\sigma_i)_j\right) \tag{4.3.35}$$

$$\sigma_{i\bar{j}} = \frac{1}{2}\left(\sigma_i - (\boldsymbol{P}'\sigma_i)_j\right). \tag{4.3.36}$$

Equation 4.3.35 and Equation 4.3.36 are the cross-sections given in Table 4.1.By correctly combining the channels intensities, one can separate the magnetic scattering from the nuclear scattering.

Chapter 5

Polarised Neutron Diffraction Measurements

In chapter 3 we presented the phase diagram of $Nb_{1-y}Fe_{2+y}$ (Figure 4.1), which shows that the ground state on the iron-rich side is called a ferromagnetic (FM) state. There are indications suggesting that the ground state ordered moments are collinear and point along the c^* axis, but this has never been confirmed. With the hope to come up with a definitive answer to the question of the ordered moments' direction in the FM state and the presence or absence of any chirality in the magnetic structure, we measured all spin-state cross-sections allowed by spherical neutron polarimetry (SNP) diffraction at a magnetic Bragg position. We now present this work and the results.

5.1 Data acquisition

We measured the FM signal in sample C (properties are summarised in Table 5.1) with the polarised neutron double axis diffractometer (DAD) POLI presented in Section 4.3.2. The latter instrument uses Quartz cells containing polarised ^{3}He gas to perform SNP.

We measured all thirty-six polarisation channels allowed by SNP at two FM Bragg positions: $\boldsymbol{Q} = (1\ 0\ 2)$ r.l.u. and $\boldsymbol{Q} = (3\ 0\ 1)$ r.l.u.. These two positions have a high magnetic over nuclear intensity ratio and are close enough to the origin of the reciprocal space such that magnetic form factor is high. For each Bragg position we measured deep in the FM state, at 5 K, and in the paramagnetic (PM) state, at 40 K. The latter measurements, in addition to doing polarised

measurements, help to separate the magnetic signals from the nuclear background..

Table 5.1 Summary of the properties of Sample C.

doping concentration	$y = 0.019$
Curie temperature	$T_{\mathrm{C}} = 33\,\mathrm{K}$
Néel temperature	$T_{\mathrm{N}} = 37\,\mathrm{K}$
space group	$P6_3/mmc$
crystal structure	hexagonal
lattice parameters	$a = b = 4.84\,\text{Å}$, $c = 7.90\,\text{Å}$
	$\alpha = \beta = 90\,^\circ$, $\gamma = 120\,^\circ$

We use the same coordinates system as in Equation 4.3.18:

$$\begin{aligned} \boldsymbol{x} &= \frac{\boldsymbol{Q}}{Q} \\ \boldsymbol{y} &\perp \boldsymbol{x} \quad \text{and in the scattering plane} \\ \boldsymbol{z} &= \boldsymbol{x} \times \boldsymbol{y}. \end{aligned} \tag{5.1.1}$$

The sample is oriented with the b-axis along $\boldsymbol{z}$, and $a^* - c^*$ in the scattering plane. We reached the FM state at 5 K with zero field cooling. Each chanel was measured during fifteen minutes: 45 s at each background points (two background points, one on each side of the Bragg position) and 810 s at the Bragg positions. Adding two background points to the measurements allows us to use the software "FileScanner" developed by Henrik Thoma for the data analysis. This software corrects the measured intensities for the time-dependent efficiencies of the cells and gives the real intensities of the different physical quantities as well as the polarisation matrix as we will see in Section 5.2.

One pair of polarisation cells was used for each measured position. $\boldsymbol{Q} = (1\ 0\ 2)\,\text{r.l.u.}$ was measured with cell H03 (^{3}He pressure: 2.5 bar) for the polariser and H14 (^{3}He pressure: 2.5 bar) for the analyser. $\boldsymbol{Q} = (3\ 0\ 1)\,\text{r.l.u.}$ was measured with cell H13 (^{3}He pressure: 2.6 bar) for the polariser and HL4 (^{3}He pressure: 2.4 bar) for the analyser. Table 5.2 summarises all the cell characteristics as well as the transmission values at insertion into and removal from the instrument.

Table 5.2 Physical characteristics and transmissions of the ^{3}He cells used to measure the FM signal at $\boldsymbol{Q} = (1\ 0\ 2)$ r.l.u. and $\boldsymbol{Q} = (3\ 0\ 1)$ r.l.u. in sample C. "T_i" and "T_f" are the initial transmission at insertion and final transmission at removal respectively, "τ" is the time constant of the polarisation decay in the cell, and "λ" is the wavelength of the incident neutrons.

	$\boldsymbol{Q} = (1\ 0\ 2)$ r.l.u.		$\boldsymbol{Q} = (3\ 0\ 1)$ r.l.u.	
position	polariser	analyser	polariser	analyser
name	H03	H14	H13	HL4
length (cm)	13	13	13	16
$p_{^3\mathrm{He}}$ (bar)	2.5	2.5	2.6	2.4
τ (hours)	72.45	81.26	93.90	81.97
T_i (%)	27.14	30.50	27.90	27.84
T_f (%)	22.14	24.45	22.95	20.49
λ (Å)	0.714		0.714	

5.2 Data correction and analysis

Section 4.3.2.3 describes how different cross-sections are measured depending on the orientation of the polarisation cells (or channel) in the instrument, which are summarised in Table 4.1. However the latter table is true for perfectly polarised cells only and does not take into account the imperfect polarisation of the cells or the cell decay.

5.2.1 Correction for imperfect polarisation

The polarisation P of the neutron beam is not perfect ($P < 1$) and the analyser cell does not absorb all the neutrons with opposite polarity. If, for instance, the polariser is along $\boldsymbol{x}$, a small proportion of the beam is still polarised along $-\boldsymbol{x}$, due to the none-zero cell transmission for the neutrons with spin along $-\boldsymbol{x}$, and hits the sample. If the analyser is oriented along $-\boldsymbol{x}$, for instance, a small proportion of neutrons with polarisation along $\boldsymbol{x}$ go through the analyser cell and hits the detector. Figure 5.1 summarises the idea; it shows the neutron beam polarisation at the different stages of the neutron flow. This diagram, shows the real composition of the intensities measured during the experiments.

The total transmission $T(t)$ of a polarisation cell is (Equation 4.3.7):

$$T_n(t) = T_0 e^{-O} \cosh\left[OP_{\mathrm{He}}(t)\right], \tag{5.2.1}$$

but if we look at neutrons individually, the transmission is different if the spin is parallel or

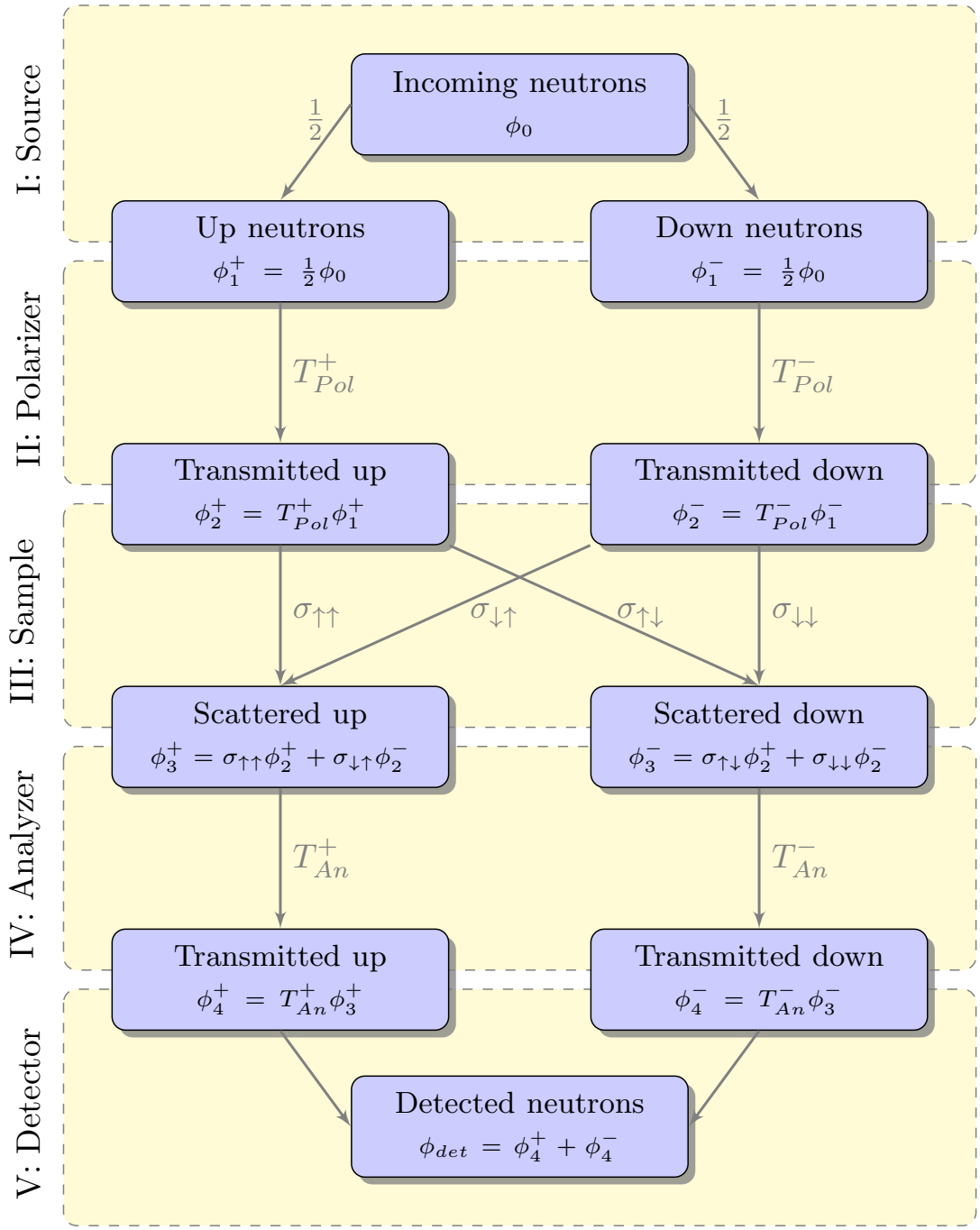

Figure 5.1: Neutron beam polarisation at the different stages of the beam flow (figure from [65])

anti-parallel to the cell's polarisation. The spin-dependent transmission is given by [65]

$$T^{+}(t) = T_0 e^{-O(1-P_{\mathrm{He}}(t))} \tag{5.2.2}$$

$$T^{-}(t) = T_0 e^{-O(1+P_{\mathrm{He}}(t))}, \tag{5.2.3}$$

where $O(\lambda) = 0.0732 \times l \times \lambda \times p$ is the opacity of the cell (Equation 4.3.6) and $P_{\mathrm{He}}(t) = P_{\mathrm{He}}(0)\exp(-t/T_1)$ is the time dependent polarisation of the ^{3}He gas contained in the cell (Equation 4.3.8). Using Equation 5.2.1 and the efficiency of the cell $P_n(t) = \tanh[OP_{\mathrm{He}}(t)]$ (Equation 4.3.13), we find that $T^{+}(t)$ and $T^{-}(t)$ are related to the total transmission of the cell and the produced polarisation of the beam with

$$T^{+}(t) = T(t)\left[1 + P(t)\right] \tag{5.2.4}$$

$$T^{-}(t) = T(t)\left[1 - P(t)\right]. \tag{5.2.5}$$

From the neutron flow diagram in Figure 5.1, we can see the spin composition of the detected neutron beam. We start with an unpolarised incident beam (I: Source in Figure 5.1), where the total flux is ϕ_0. The beam arrives at the polariser (II:Polariser in Figure 5.1) with half of the neutrons with spin parallel to the polariser polarisation (the + proportion) and the other half with spin anti-parallel to the cell polarisation (the − proportion)

$$\phi_1^{+} = \frac{1}{2}\phi_0 \tag{5.2.6}$$

$$\phi_1^{-} = \frac{1}{2}\phi_0. \tag{5.2.7}$$

The total polarisation is zero. The polarisation asymmetry is created by the different transmission values for ($'+'$) neutrons T_p^{+} and for ($'-'$) neutrons T_p^{-}. Since the polarisation of the polariser is not perfect, T_p^{-} is not zero and therefore the polarised beam is still composed of $'+'$ neutrons and $'-'$ neutrons.

$$\phi_2^{+}(t) = T_p^{+}(t)\phi_1^{+} \tag{5.2.8}$$

$$= \frac{1}{2}T_p^{+}(t)\phi_0 \tag{5.2.9}$$

$$\phi_2^{-}(t) = T_p^{-}(t)\phi_1^{-} \tag{5.2.10}$$

$$= \frac{1}{2}T_p^{-}(t)\phi_0. \tag{5.2.11}$$

The polarised beam is scattered by the sample (III:Sample in Figure 5.1) and the four scattering processes ($+ \to +, - \to -, + \to -, - \to +$) can potentially happen and therefore we consider the four spin-states cross-sections ($\sigma_{++}, \sigma_{--}, \sigma_{+-}, \sigma_{-+}$, where $+ \equiv \uparrow$ and $- \equiv \downarrow$ in Figure 5.1). After the sample, the scattered beam composition becomes

$$\phi_3^+(t) = \sigma_{++}\phi_2^+(t) + \sigma_{-+}\phi_2^-(t) \tag{5.2.12}$$

$$= \frac{1}{2}\phi_0 \left[\sigma_{++}T_p^+(t) + \sigma_{-+}T_p^-(t)\right] \tag{5.2.13}$$

$$\phi_3^-(t) = \sigma_{--}\phi_2^-(t) + \sigma_{+-}\phi_2^+(t) \tag{5.2.14}$$

$$= \frac{1}{2}\phi_0 \left[\sigma_{--}T_p^-(t) + \sigma_{+-}T_p^+(t)\right]. \tag{5.2.15}$$

After being scattered, the neutron beam goes through the analyser, which filters out the neutrons with opposite polarisation (IV:Analyser in Figure 5.1). However, the transmission of the opposite polarisation direction is not zero and therefore the detected beam is composed of $'+'$ and $'-'$ polarised neutrons

$$\phi_4^+(t) = T_a^+(t)\phi_3^+(t) \tag{5.2.16}$$

$$= \frac{1}{2}\phi_0 T_a^+(t) \left[\sigma_{++}T_p^+(t) + \sigma_{-+}T_p^-(t)\right] \tag{5.2.17}$$

$$\phi_4^-(t) = T_a^-(t)\phi_3^-(t) \tag{5.2.18}$$

$$= \frac{1}{2}\phi_0 T_a^-(t) \left[\sigma_{--}T_p^-(t) + \sigma_{+-}T_p^+(t)\right]. \tag{5.2.19}$$

Finally the scattered beam that hits the detector (V:Detector in Figure 5.1) is the combination of $\phi_4^+(t)$ and $\phi_4^-(t)$

$$\phi_{det}(t) = \phi_4^+(t) + \phi_4^-(t) \tag{5.2.20}$$

$$= \frac{1}{2}\phi_0 \left\{T_a^+(t) \left[\sigma_{++}T_p^+(t) + \sigma_{-+}T_p^-(t)\right] + T_a^-(t) \left[\sigma_{--}T_p^-(t) + \sigma_{+-}T_p^+(t)\right]\right\}. \tag{5.2.21}$$

We generalise Equation 5.2.20 to the three directions of space $i, j \in \{x, y, z, -x, -y, -z\}$, and the detected intensity becomes

$$I_{ij}(t) = \frac{1}{2}\phi_0 \left\{T_a^+(t) \left[\sigma_{ij}T_p^+(t) + \sigma_{\bar{i}j}T_p^-(t)\right] + T_a^-(t) \left[\sigma_{\bar{i}\bar{j}}T_p^-(t) + \sigma_{i\bar{j}}T_p^+(t)\right]\right\}, \tag{5.2.22}$$

where i is the direction of the polariser's polarisation, j is the direction of the analyser's po-

larisation and $\bar{i} = -i$ and $\bar{j} = -j$. The time dependence or the transmissions come from the polarisation decay of the ^{3}He in the polariser and analyser cells.

With Equations 5.2.4 and 5.2.5 for the polariser and the analyser, we rewrite Equation 5.2.22 as an expression of the total cell transmissions and polarisation efficiency, which are the known values

$$\begin{aligned} I_{ij}(t) = \frac{1}{2} T_p(t) T_a(t) \phi_0 \big\{ & \sigma_{ij} \left[1 + P_p(t)\right] \left[1 + P_a(t)\right] \\ & + \sigma_{i\bar{j}} \left[1 + P_p(t)\right] \left[1 - P_a(t)\right] \\ & + \sigma_{\bar{i}j} \left[1 - P_p(t)\right] \left[1 + P_a(t)\right] \\ & + \sigma_{\bar{i}\bar{j}} \left[1 - P_p(t)\right] \left[1 - P_a(t)\right] \big\}. \end{aligned} \tag{5.2.23}$$

Rearranging the cross-sections and the cell efficiencies in Equation 5.2.23, the intensity becomes

$$\begin{aligned} I_{ij}(t) = \frac{1}{2} T_p(t) T_a(t) \phi_0 \Big\{ & \left(\sigma_{ij} + \sigma_{i\bar{j}} + \sigma_{\bar{i}j} + \sigma_{\bar{i}\bar{j}}\right) \\ & + \left(\sigma_{ij} + \sigma_{i\bar{j}} - \sigma_{\bar{i}j} - \sigma_{\bar{i}\bar{j}}\right) P_p(t) \\ & + \left(\sigma_{ij} - \sigma_{i\bar{j}} + \sigma_{\bar{i}j} - \sigma_{\bar{i}\bar{j}}\right) P_a(t) \\ & + \left(\sigma_{ij} - \sigma_{i\bar{j}} - \sigma_{\bar{i}j} + \sigma_{\bar{i}\bar{j}}\right) P_p(t) P_a(t) \Big\}. \end{aligned} \tag{5.2.24}$$

5.2.2 Correction for cell decay

The intensities given by $I_{ij}(t)$ with $i, j \in \{x, y, z, -x, -y, -z\}$ are the real intensities measured during an experiment at POLI instrument. The time dependence comes from the polarisation decay of the ^{3}He gas contained in the polariser and analyser. This means that if we measure the same ij configuration at two different times, we will obtain different intensities (if $t_1 < t_2$ we will have $I_{ij}(t_1 > I_{ij}(t_2))$.

If we write $I_{i\bar{j}}(t)$, $I_{\bar{i}j}(t)$ and $I_{\bar{i}\bar{j}}(t)$ in the same way, we obtain a system of four equations and four variables $\sigma_{ij}, \sigma_{i\bar{j}}, \sigma_{\bar{i}j}, \sigma_{\bar{i}\bar{j}}$. Solving the system gives the theoretical spin-state cross-sections σ_{ij} as a function of the real measured intensities (we omit the (t) to make the equations more

readable)

$$\begin{aligned}\sigma_{ij} = \frac{1}{8T_pT_a\phi_0}\Bigg\{ & \frac{1}{P_p}\Big[(I_{ij}+I_{i\bar{j}})(1+P_p)-(I_{\bar{i}j}+I_{\bar{i}\bar{j}})(1-P_p)\Big] \\ & \frac{1}{P_pP_a}\Big[(I_{ij}-I_{i\bar{j}})(1+P_p)-(I_{\bar{i}j}-I_{\bar{i}\bar{j}})(1-P_p)\Big]\Bigg\} \\ = \frac{1}{8T_pT_a\phi_0}\frac{1}{P_pP_a}\Big[& I_{ij}(1+P_p)(1+P_a)-I_{i\bar{j}}(1+P_p)(1-P_a) \\ & -I_{\bar{i}j}(1-P_p)(1+P_a)+I_{\bar{i}\bar{j}}(1-P_p)(1-P_a)\Big],\end{aligned} \tag{5.2.25}$$

where the second equality is just a re-arrangement of the first equality.

Finally, using Equation 5.2.25 in the equation of the elements of the polarisation matrix:

$$\mathcal{P}_{ij} = \frac{\sigma_{ij}-\sigma_{i\bar{j}}}{\sigma_{ij}+\sigma_{i\bar{j}}} \tag{5.2.26}$$

gives the polarisation matrix elements (the (t) are omitted to make the equations more readable)

$$P_{ij} = \frac{1}{P_a}\frac{(I_{ij}-I_{i\bar{j}})(1+P_p)-(I_{\bar{i}j}-I_{\bar{i}\bar{j}})(1-P_p)}{(I_{ij}+I_{i\bar{j}})(1+P_p)-(I_{\bar{i}j}+I_{\bar{i}\bar{j}})(1-P_p)}. \tag{5.2.27}$$

5.2.3 Correcting and analysing the data

The correction for the imperfect polarisation and for the cell decay is done with "FileScanner", a software developed by H. Thoma. The software also computes the real cross-sections with correcting for the time-dependent polarisation of the cells and provides the physical quantities and the polarisation matrices.

5.3 Results

This section presents the results of the polarisation measurements at $\boldsymbol{Q} = (1\ 0\ 2)$ r.l.u. and at $\boldsymbol{Q} = (3\ 0\ 1)$ r.l.u..

5.3.1 Q = (1 0 2) r.l.u.

Table 5.3 gives the polarisation matrices at $\boldsymbol{Q} = (1\ 0\ 2)$ r.l.u., measured in the FM state at 5 K and in the PM state at 40 K. The off-diagonal terms are zero for both temperatures, which

suggests no rotation of the polarisation[1]. Only P_{xx} and P_{zz} are significantly different between 5 K and 40 K.

Table 5.3 Polarisation matrices of the Bragg position $\boldsymbol{Q} = (1\ 0\ 2)$ r.l.u. measured at 5 K (FM state) and 40 K (FM state). x, y, z are the polarisation axes of the polariser (left) and analyser (top).

5 K		analyser		
		x	y	z
polariser	x	0.8246 ±0.0237	−0.0234 ±0.0019	0.0028 ±0.0022
	y	0.0159 ±0.0025	0.9424 ±0.0120	−0.0110 ±0.0027
	z	−0.0053 ±0.0025	−0.0063 ±0.0026	0.8890 ±0.0101

40 K		analyser		
		x	y	z
polariser	x	0.9107 ±0.0300	−0.0152 ±0.0021	0.0108 ±0.0024
	y	0.0124 ±0.0025	0.9535 ±0.0145	−0.0116 ±0.0027
	z	−0.0097 ±0.0026	−0.0076 ±0.0026	0.9555 ±0.0142

Using the PM polarisation matrix as reference and considering the errors, we see that the depolarisation caused by the FM state when the initial polarisation is along $\boldsymbol{x}$ ($\Delta P_{xx} \approx 0.09$) is not significantly different than when the initial polarisation is along $\boldsymbol{z}$ ($\Delta P_{zz} \approx 0.07$) and that they are both very low. The polarisation along $\boldsymbol{y}$ remains constant between 40 K and 5 K.

Table 5.4 gives the intensities of the different physical quantities composing the scattered beam at 5 K and at 40 K. The reason for negative values of some scattering factors in the latter table (magnetic, chiral magnetic and nuclear-magnetic interference) is because they are not measured directly. In Table 4.1, we see that there is no channel that gives directly $2\,\mathrm{Re}[M_y M_z^*]$, $i(M_\perp \times M_\perp^*)_x$ or $2\,\mathrm{Re}[N M_y^*]$, and we obtain those with linear combinations of the intensities measured through different channels. If the intensity of the calculated scattering factor is of the order of the uncertainties of the intensities of the other contributions, it is possible that the former becomes negative. For instance, the intensity for $2\,\mathrm{Re}[N M_y^*]$ is given by

$$2\,\mathrm{Re}[N M_y^*] = \frac{I_{yy} - I_{\overline{yy}}}{2}, \tag{5.3.1}$$

where I_{yy} and $I_{\overline{yy}}$ are the theoretical channels' intensities given in Table 4.1. The other contributions to these intensities are NN^* (nuclear) and $M_y M_y^*$ (magnetic). We see in Table 5.4 that the uncertainties of NN^* and $M_y M_y^*$ are of the order or bigger than the calculated $2\,\mathrm{Re}[N M_y^*]$, which explains its negative value. We consider negative values as zero.

The non-zero magnetic components and the imaginary nuclear-magnetic interference terms

[1] if the incident beam is polarised along $\boldsymbol{i}$ ($i \in \boldsymbol{x}, \boldsymbol{y}, \boldsymbol{z}$), the scattered beam may be depolarised along $\boldsymbol{i}$, but the polarisation along $\boldsymbol{j}$ ($\boldsymbol{j} \neq \boldsymbol{i}$) remains zero

Table 5.4 Intensities of the scattering factors at the Bragg position $\boldsymbol{Q} = (1\ 0\ 2)$ r.l.u. measured in the FM state at 5 K and in the PM state at 40 K.

scattering factors at (1 0 2) r.l.u.		5 K	40 K
nuclear	NN^*	3016.4 ± 85.1	3127.0 ± 103.5
magnetic	$M_y M_y^*$	183.0 ± 21.2	73.0 ± 25.0
	$M_z M_z^*$	94.5 ± 22.0	75.9 ± 25.5
	$2\,\mathrm{Re}[M_y M_z^*]$	-24.7 ± 4.7	-26.0 ± 5.9
chiral magnetic	$i(M_\perp \times M_\perp^*)_x$	-12.5 ± 4.6	2.7 ± 3.9
nuclear-magnetic interference	$2\,\mathrm{Re}[NM_y^*]$	-11.5 ± 6.3	-11.9 ± 5.4
	$2\,\mathrm{Re}[NM_z^*]$	4.1 ± 6.0	1.3 ± 5.2
	$2\,\mathrm{Im}[NM_y^*]$	21.7 ± 4.6	32.9 ± 5.8
	$2\,\mathrm{Im}[NM_z^*]$	64.1 ± 4.9	52.4 ± 6.0

at 40 K suggest that we are not in the paramagnetic state at this temperature. However, at 40 K we are very close to the Curie temperature of sample C, and the two measured temperatures are sufficiently far apart to discriminate any signal that does not emerge in the FM phase. We observe a significant increase of the intensity scattered by $M_{\perp y}$ between 40 K and 5 K. The increase of $M_{\perp z}$ between the latter temperatures is 0 within the error.

5.3.2 Q = (3 0 1) r.l.u.

The polarisation matrices for $\boldsymbol{Q} = (3\ 0\ 1)$ r.l.u., measured in the FM state at 5 K and in the PM state at 40 K are given in Table 5.5. Like for $\boldsymbol{Q} = (1\ 0\ 2)$ r.l.u., the off-diagonal terms of the polarisation matrices at both temperatures are zero. This suggests that there is no rotation of the polarisation. Only P_{xx} and P_{zz} change significantly.

Table 5.5 Polarisation matrices of the Bragg position $\boldsymbol{Q} = (3\ 0\ 1)$ r.l.u. measured at 5 K (FM state) and 40 K (FM state). x, y, z are the polarisation axes of the polariser (left) and analyser (top).

5 K		analyser		
		x	y	z
polariser	x	0.6414 ±0.0155	−0.0035 ±0.0019	0.0133 ±0.0019
	y	−0.0012 ±0.0024	0.9559 ±0.0100	−0.0127 ±0.0024
	z	−0.0175 ±0.0023	−0.0123 ±0.0023	0.6799 ±0.0040

40 K		analyser		
		x	y	z
polariser	x	0.9026 ±0.0225	−0.0025 ±0.0017	0.0123 ±0.0019
	y	−0.0070 ±0.0022	0.9535 ±0.0108	−0.0175 ±0.0024
	z	−0.0196 ±0.0023	−0.0155 ±0.0023	0.9501 ±0.0106

Again, the depolarisation occurs when the incident polarisation is either along $\boldsymbol{x}$ or $\boldsymbol{z}$, with similar values of the depolarisation caused by the FM state for both directions ($\Delta P_{xx} \approx 0.26$ and $\Delta P_{zz} \approx 0.27$). However at $\boldsymbol{Q} = (3\ 0\ 1)$ r.l.u. the scattered beam is much more depolarised than at $\boldsymbol{Q} = (1\ 0\ 2)$ r.l.u..

Table 5.6 gives the intensities of the different physical quantities composing the scattered beam at 5 K and at 40 K. Here again, negative values have no physical meaning and are considered as zero.

Table 5.6 Intensities of the scattering factors at the Bragg position $\boldsymbol{Q} = (3\ 0\ 1)$ r.l.u. measured in the FM state at 5 K and in the PM state at 40 K.

scattering factors at (3 0 1) r.l.u.		5 K	40 K
nuclear	NN^*	4302.3 ± 139.6	3796.2 ± 104.7
magnetic	$M_y M_y^*$	737.2 ± 30.7	111.9 ± 26.5
	$M_z M_z^*$	101.4 ± 25.4	104.3 ± 26.8
	$2\,\mathrm{Re}[M_y M_z^*]$	-27.3 ± 5.0	-39.7 ± 6.0
chiral magnetic	$i(M_\perp \times M_\perp^*)_x$	9.3 ± 6.1	-4 ± 4.7
nuclear-magnetic interference	$2\,\mathrm{Re}[N M_y^*]$	-31.0 ± 8.6	-38.9 ± 6.8
	$2\,\mathrm{Re}[N M_z^*]$	-29.1 ± 7.8	-29.5 ± 6.4
	$2\,\mathrm{Im}[N M_y^*]$	51.9 ± 4.9	59.3 ± 6.0
	$2\,\mathrm{Im}[N M_z^*]$	25.3 ± 4.9	7.3 ± 5.7

The non-zero magnetic components and the imaginary nuclear-magnetic interference terms at 40 K seem to indicate that we are not in the paramagnetic state at this temperature. However, there is the possibility that an imperfect correction of finite cell polarisation leads to a systematic error, which emphasises the importance of the 40 K measurements as background to the 5 K signal. We observe a significant increase of the intensity scattered by the $M_{\perp y}$ between 40 K and 5 K, which is much more intense than at $\boldsymbol{Q} = (1\ 0\ 2)$ r.l.u., whereas no increase of $M_{\perp z}$ has been measured. We also record a slight increase of $\mathrm{Im}[N M_z^*]$, but no significant change of $\mathrm{Im}[N M_y^*]$, while the real part of the nuclear-magnetic interference is zero at both temperatures. The nuclear term is slightly more intense than at $\boldsymbol{Q} = (1\ 0\ 2)$ r.l.u..

5.4 Discussion

The polarised measurements have been done with zero field cooling and therefore we expect magnetic domains to have formed in the FM state. The polarisation matrices can help to

identify whether there are such domains in the sample and, if present, what type of domains. The polarisation matrix, as well as the intensities of the magnetic scattering factors, give the orientation of the moment in the FM phase.

Four different types of magnetic domains may form in the ordered phase, depending on the lost symmetry between the high symmetry phase (here the PM phase) and the lower symmetry phase (here the FM phase) [68]:

- **configuration domains:** they form when the translation symmetry is lost, and these domains do not depolarise the scattered beam. Instead new scattering signals appear at different $\boldsymbol{Q}$-positions.

- **180° domains:** they form when the time reversal symmetry is lost and the direction of $\boldsymbol{M}_\perp$ is inverted. If the nuclear and magnetic structures are centrosymmetric, due to nuclear-magnetic interference, the total cross-section is polarisation dependent [68] and the polarisation is rotated in directions that depend on the sign of $\mathrm{Re}[\boldsymbol{M}_{\perp y}N^*]$ and $\mathrm{Re}[\boldsymbol{M}_{\perp z}N^*]$ (if $\neq 0$). If the centrosymmetry applies only to the nuclear structure and the moments of two centrosymmetric atoms are anti-parallel, then the total cross-section is not polarisation dependent and the scattered polarisation rotates in a direction perpendicular to $\boldsymbol{P}$ and $\boldsymbol{M}_\perp$ [68]. The orientation of $\boldsymbol{M}_\perp$ depends on the domain, and thus a multi-domain sample will depolarise a neutron beam initially polarised along $\boldsymbol{x}$.

- **orientation domains:** they appear when loosing the rotation symmetry. In a multi-domain sample, the beam depolarises and the depolarisation is maximum for incident polarisation directions perpendicular to the axes of the lost symmetry [68].

- **chirality domains:** these domains form when loosing the centrosymmetry. $\boldsymbol{M}_\perp$ in two different chiral domains are complex conjugates of each other. If the latter are non-zero, they are not parallel and additional polarisation appears along $\boldsymbol{x}$ [68]. Additionally, the incident polarisation along $\boldsymbol{y}$ or $\boldsymbol{z}$ are rotated along $\boldsymbol{x}$ and the off-diagonal terms $\mathcal{P}_{yx}$ and $\mathcal{P}_{zx}$ are non-zero. In a sample featuring the two chiral domains, the chiral terms in the polarisation matrix are averaged over the two domains with a weight proportional to the population of each domain. Because of the opposite signs of the terms in each domain, scattered beam will depolarise if the incident polarisation is along $\boldsymbol{y}$ or $\boldsymbol{z}$.

At both positions $\boldsymbol{Q} = (1\ 0\ 2)$ r.l.u. and $\boldsymbol{Q} = (3\ 0\ 1)$ r.l.u., only the diagonal terms are non vanishing, which indicates the presence of two opposed 180°-domains in the sample with equal

population. This also explains the depolarisation of the beam when initially polarised along $\boldsymbol{x}$. The depolarisation along $\boldsymbol{y}$, given by $\mathcal{P}_{yy}$ is not significant considering the error. This suggests that the $\boldsymbol{M}_{\perp}$ is parallel to $\boldsymbol{y}$ and with no component along $\boldsymbol{z}(=\boldsymbol{b})$, which would otherwise depolarise the beam along $\boldsymbol{y}$. Since $\boldsymbol{b}$ and $\boldsymbol{a}$ axes are equivalent, there is, *a fortiori*, no moment along $\boldsymbol{a}$ either and thus we conclude that the moment points along $\boldsymbol{c}$. We arrive at the same conclusion with the scattering factors' intensities: $\Delta M_{\perp z} M^*_{\perp z} = 0$ and $\Delta M_{\perp y} M^*_{\perp y} > 0$ when decreasing the temperature from 40 K to 5 K (Table 5.4 and Table 5.6). At $\boldsymbol{Q} = (1\ 0\ 2)$ r.l.u. the $\boldsymbol{y}$ axis makes an angle $\theta_{102} \approx 50.92°$ with the $\boldsymbol{c}$ axis and at $\boldsymbol{Q} = (3\ 0\ 1)$ r.l.u. this angle is much smaller with $\theta_{301} \approx 11.60°$. With the previous conclusion about the magnetic moment pointing along $\boldsymbol{c}$, the y-component of the moment is bigger at $\boldsymbol{Q} = (3\ 0\ 1)$ r.l.u. than at $\boldsymbol{Q} = (1\ 0\ 2)$ r.l.u. and this explains why $\Delta M_{\perp y} M^*_{\perp y}$ is much bigger at the former position (Table 5.6) than at the latter (Table 5.4).

The absence of depolarisation along $\boldsymbol{y}$ excludes the presence of different equally populated chiral domains. On the other hand, if only one chiral domain were present, we would observe off-diagonal terms. Thus we can exclude chirality from the magnetic structure.

Chapter 6

Unpolarised Elastic Neutron Scattering Measurements

Preliminary non-neutron-based observations recorded bulk modulated magnetic order in $NbFe_2$ [36, 49], which suggests the presence of a spin density wave (SDW) phase. However, there was no definitive proof of the latter until it has been directly measured with unpolarised elastic neutrons scattering technics. We then performed additional measurements with unpolarised elastic neutrons to confirm and complete the already existing dataset and we discovered a strong temperature hysteresis of the spin density wave ordering wave vector ($\boldsymbol{Q}_{\mathbf{SDW}}$). In this chapter we see the evolution of the SDW characteristics as we approach the ferromagnetic (FM) quantum critical point (QCP) with measurements of the three samples presented in Chapter 4. We studied the temperature-dependence of $\boldsymbol{Q}_{\mathbf{SDW}}$ and the intensity of the SDW phase in all three samples with neutron diffraction techniques ([3]).

6.1 Data acquisition

We performed elastic neutron scattering ($k_{\mathrm{f}} = k_{\mathrm{i}}$) in the a^* - c^* plane of samples A, B and C, with two triple axis spectrometers (TASs), 4F2 and Panda. The settings are summarised in Table 6.1.

The higher order neutrons were filtered out with Be-filters at both instruments. We kept the monochromator and the analyser with no horizontal focus in order to increase the q-resolution.

We measured the temperature-dependence of the SDW intensity and $\boldsymbol{Q}_{\mathbf{SDW}}$ with increasing

Table 6.1 Settings of the two TAS used for the neutron diffraction experiments.

	4F2	**Panda**
scattering plane	a^* - c^*	a^* - c^*
monochromator horizontal	flat	flat
monochromator vertical	focused	focused
analyser horizontal	flat	flat
analyser vertical	focused	focused
$\boldsymbol{k}_\mathbf{f}(=\boldsymbol{k}_\mathbf{i})$	1.30Å^{-1}	1.57Å^{-1}
collimation	no	no
higher order filter	Beryllium	Beryllium

and decreasing temperatures. The latter was initially set such that the measurements start outside the hysteresis region described below. This is important because, as we will see later, $NbFe_2$ shows temperature-hysteresis behaviour. The temperature-dependence of the elastic neutron scattering are determined with 1K temperature-steps. At each temperature step, we first performed a q-scan along l and centred on $h = 1$ r.l.u., followed by a q-scan along h and centred on the l value of maximum measured intensity. The latter gives l_{SDW}, the l-component of $\boldsymbol{Q}_{\mathbf{SDW}}$. The steps increments in the l- and h-directions are $(\Delta\text{Q}_\text{l}, \Delta\text{Q}_\text{h}) = (0.004, 0.0025)$ r.l.u. in sample A, $(\Delta\text{Q}_\text{l}, \Delta\text{Q}_\text{h}) = (0.0025, 0.0075)$ r.l.u. in Sample B and $(\Delta\text{Q}_\text{l}, \Delta\text{Q}_\text{h}) = (0.003, 0.0025)$ r.l.u. in Sample C.

6.2 Data analysis

6.2.1 Correction and Normalisation

6.2.1.1 Correction

The monitor, which measures the incoming neutron flux (see Section 4.3.1.1), is also sensitive to higher order incident neutrons. We remove the latter from the measured monitor counts by applying the k_i-dependent correction factors[1] given in Figure 6.1. Since the energy transfer is $\Delta E = 0$meV by maintaining k_i=k_f, the correction merely consists in applying a constant factor to all the data measured with a same instrument. Therefore it does not affect the relative intensities of the SDW peaks.

[1] the monitor corrections are obtained experimentally [69] and are specific to each monitor.

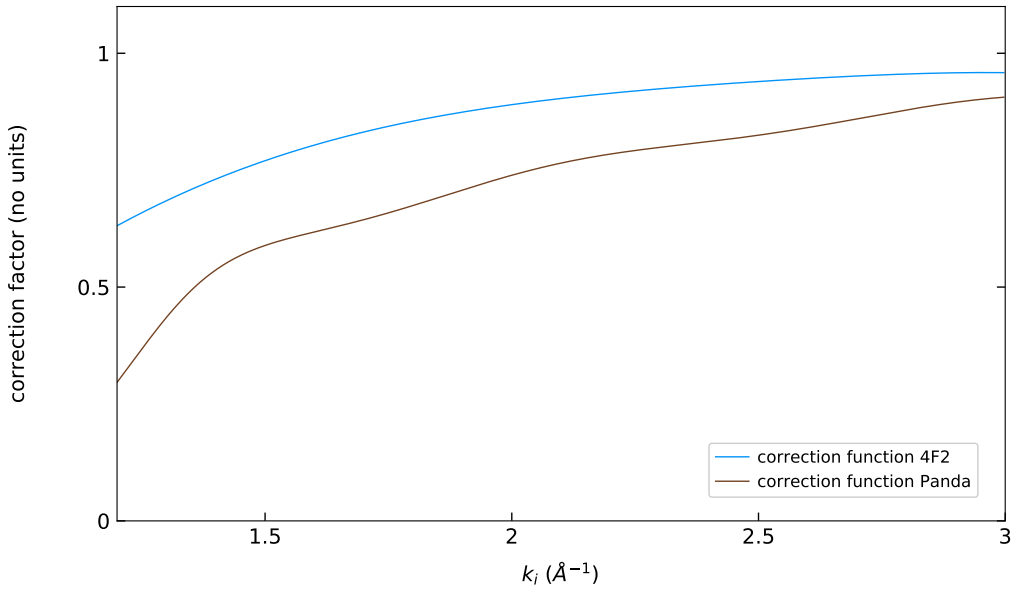

Figure 6.1: Monitor correction functions for 4F2 (blue) and Panda (brown).

6.2.1.2 Normalisation

In order to safe time but obtain reasonable statistics at all measurement positions, we have adjusted the counting time to the signal strength; we counted longer where the signal is weaker. In order to have comparable data, we have normalised those to a unique monitor count, which we take as the corrected monitor counts that corresponds to approximately 5 minutes of measuring time. For 4F2 the appropriate value is $N_{\text{norm}}^{\text{4F2}} = 2500\,\text{counts/5min}$ and for Panda it is $N_{\text{norm}}^{\text{Panda,A}} = 157000\,\text{counts/5min}$ with sample A and $N_{\text{norm}}^{\text{Panda,C}} = 239000\,\text{counts/5min}$ with Sample C. There are two different normalisation values for Panda because we measured during two separate beamtimes.

6.2.2 Fitting the data

Due to the resolution of the instruments and the horizontal distribution of the signal, the detected signal is composed of several Gaussians. Thus nuclear and SDW signals in the h and the l directions are fitted with either one, two or three Gaussian(s). The equation of a Gaussian is given by:

$$g(x) = A \exp\left(-\frac{(x-b)^2}{2\sigma^2}\right), \tag{6.2.1}$$

where A is the amplitude of the Gaussian, b its centre, σ is the standard deviation, such that the full-width half-maximum (FWHM) is FWHM $= 2\sigma\sqrt{2\ln 2}$. From the h- and l-scans of the (1 0 1) r.l.u. nuclear peak we deduce the shape of the nuclear signal in sample A, B and C (Figure 6.2). The nuclear signal at $\boldsymbol{Q} = (1\ 0\ 1)$ r.l.u. is composed of two non-aligned Gaussians in samples A and C (the centres are given by the two black crosses in Figure 6.2a and Figure 6.2c), whereas the signal in Sample B is composed of three Gaussians aligned along the h axis (the centres are given by the three black crosses in Figure 6.2b).

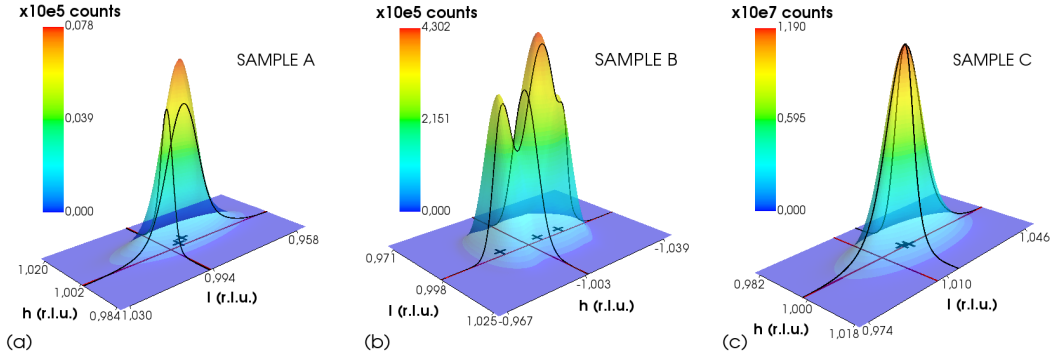

Figure 6.2: Fitting of the nuclear signal at $\boldsymbol{Q} = (1\ 0\ 1)$ r.l.u. in samples A **(a)**, B **(b)** and C **(c)**. The nuclear signal is composed of two Gaussians in sample A and Sample C, and three Gaussians in Sample B. The red lines are the axes corresponding to $h = 1$ and $l = 1$ and the black curves represent the h- and l-scans done with 4F2 (Sample B) and Panda (samples A and C). The nuclear signals have been deduced from the h- and l-scans and the centres of the Gaussians composing the signal are depicted by the black crosses.

We expect a similar shape for the SDW signal and the nuclear signal within a sample, and that only the overall amplitude and the width of the peaks are changing. Thus, for the analysis, we consider that the SDW signal is composed of two Gaussians along h and l in sample A and C, and three Gaussians along h and one Gaussian along l in Sample B. Only one Gaussian is fitted with three free parameters (amplitude A_0, centre b_0 and standard deviation σ_0). The remaining parameters (one or two amplitude(s), one or two centre(s) and one or two standard deviations) are deduced from the fitted parameters and the nuclear shape:

$$A_i = A_0 \times \frac{A_{\mathrm{n},i}}{A_{\mathrm{n},0}} \tag{6.2.2}$$

$$b_i = b_0 + b_{\mathrm{n},i} - b_{\mathrm{n},0} \tag{6.2.3}$$

$$\sigma_i = \sigma_0 + \sigma_{\mathrm{n},i} - \sigma_{\mathrm{n},0}, \tag{6.2.4}$$

where $A_{n,0}$, $b_{n,0}$, $\sigma_{n,0}$ are the parameters of the strongest nuclear Gaussian and $A_{n,i}$, $b_{n,i}$, $\sigma_{n,i}$ are the parameters of the other Gaussians contributing to the nuclear signal.

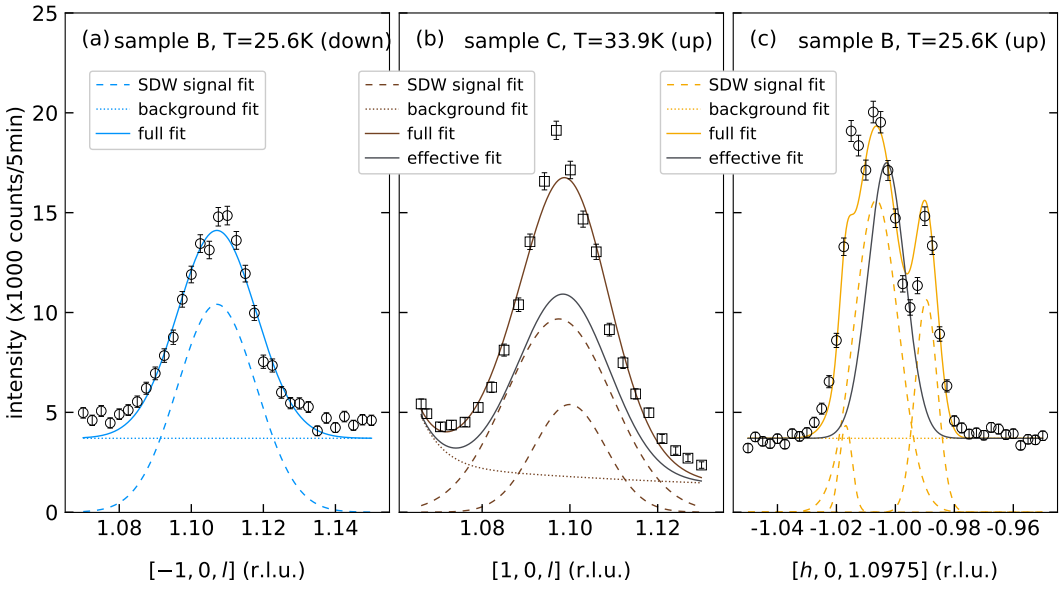

Figure 6.3: This figure shows data sets fitted with one Gaussian **(a)**, two Gaussians **(b)**, and three Gaussians **(c)**. The *up* and *down* between the brackets indicate whether the measurements are with increasing temperatures (up) or decreasing temperatures (down). The small dashes line is the background, the large dashes line is the SDW signal fitted with either one (a), two (b) or three (c) Gaussians, and the plain line is the fully fitted signal (SDW and background). The gray line in (b) and (c) is the effective Gaussian, calculated with the parameters of the fitted Gaussians (Equations 6.2.5). The background in (a) and (c) is constant over $\boldsymbol{Q}$, whereas in (b) it also contains the tail of the $\boldsymbol{Q} = (1\ 0\ 1)$ r.l.u. nuclear signal. Square markers correspond to data measured with Panda and circle markers are the data measured with 4F2.

If more than one Gaussian composes the SDW signal, then we estimate an effective Gaussian which parameters are the average of the parameters of each Gaussian composing the signal, weighted with their intensities:

$$A_{\text{eff}} = \frac{\sum_{i=1}^{n} A_i I_i}{\sum_{i=1}^{n} I_i} \tag{6.2.5}$$

$$b_{\text{eff}} = \frac{\sum_{i=1}^{n} b_i I_i}{\sum_{i=1}^{n} I_i} \tag{6.2.6}$$

$$\sigma_{\text{eff}} = \frac{\sum_{i=1}^{n} \sigma_i I_i}{\sum_{i=1}^{n} I_i}, \tag{6.2.7}$$

where n is the amount of Gaussians composing the SDW signal, A_i is the amplitude, b_i the

centre and σ_i the standard deviation of the i^{th} Gaussian. I_i is the i^{th} Gaussian's intensity, which we estimate as:

$$\begin{aligned} I &= A \times \text{FWHM}_h \times \text{FWHM}_l \\ &= A \times \sigma_h \times \sigma_l \times (2\sqrt{2\ln 2})^2, \end{aligned} \tag{6.2.8}$$

where A is the amplitude of the Gaussian, FWHM_h its FWHM along h and FWHM_l its FWHM along l. If the signal is composed by one Gaussian, the effective parameters are the parameters of the Gaussian. Figure 6.3b and Figure 6.3c show the effective Gaussian calculated for Sample C along l and Sample B along h.

Outside of the SDW state, in the FM and paramagnetic (PM) states, we measured non-zero intensities which suggests significant background signal. We remove those temperature-independent backgrounds from the SDW measurements along h and l. When the SDW signal is close to a Bragg position, the background includes the tail of a Gaussian function as illustrated with an example in Figure 6.3b. This is observed in the results of samples B and C during the increasing temperature measurements. For the other measurements, the background is a simple constant as shown in Figure 6.3a.

6.3 Results

In this section we report the observation of SDW order in the three $NbFe_2$ samples A, B, C covering a wide portion of the iron-rich side of the composition-temperature phase diagram.

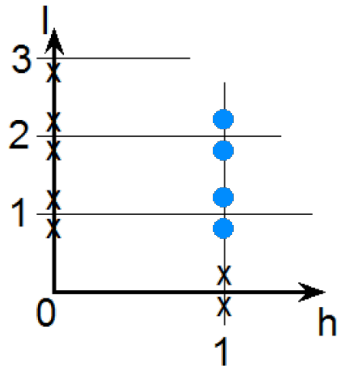

Figure 6.4: The blue dots indicate the reciprocal lattice positions around which the SDW signal has been measured and the crosses represent those positions where no signal was found. Figure from [3].

Previous to this PhD project preliminary incomplete data sets had been collected (Figure 3a and empty markers in Figure 3b and Figure 3c in [3]), which indicated the existence of a SDW order at $\boldsymbol{Q}_{\mathbf{SDW}} = (1\ 0\ 1)$ r.l.u.. Other lattice positions were measured and Figure 6.4 shows where SDW order has been detected and where it has not. A particular unusual feature was the temperature dependence of l_{SDW}. In order to confirm the results and test the reproducibility of the temperature dependence, we have done comprehensive measurements of the SDW characteristic around the reciprocal lattice position $\boldsymbol{Q} = (1\ 0\ 1)$ r.l.u. in all three samples as described previously. In particular the temperature dependence turns out to be hysteretic emphasising the first order nature of the SDW-FM phase transition.

6.3.1 Sample A: $\mathbf{Nb_{0.998}Fe_{2.002}}$ (y=0.002)

We measured Sample A with Panda from T_{base}= 5.2K to T_{N_A}= 13.4K and Table 6.2 gives all the measured temperatures. All the data is fitted with two Gaussians, in accordance with the shape of the nuclear signal represented in Figure 6.2a.

Table 6.2 Measured temperatures in Sample A. *T up* stands for a measurement sequence with increasing temperatures and *T down* for decreasing temperatures. All data have been measured at Panda, FRM2.

Panda	**SAMPLE A - measured temperatures**
T up	5.2K, 6.2K, 7.2K, 8.2K, 9.3K, 10.3K, 11.4K, 12.4K, 13.4K, 14.5K
T down	5.2K, 6.2K, 7.2K, 8.3K, 9.3K, 10.4K, 11.4K, 12.4K, 13.4K

Figure 6.5 shows the temperature dependence of the SDW signal in Sample A. The h-scans in Figure 6.5b and Figure 6.5d are slightly off centred, and because of the high quality of the samples, even a slight mis-alignment results in a significant intensity loss. Since we scanned along l with $h = 1$ r.l.u., the l-scans are not at optimal positions and the maxima in Figure 6.5a and Figure 6.5c are not the SDW signal's maxima. The h-scans, however, are centred on the maximum intensities measured along l, thus the maxima in Figure 6.5b and Figure 6.5d are the SDW signal's maxima[2].

The l-scans contains more data points than the h-scans and thus the fits along l are, in general, more precise.

For measurements with increasing temperatures (Figure 6.5a, Figure 6.5b) or with decreas-

[2]the datapoint at $h = 1$ in Figure 6.5b or in Figure 6.5d corresponds to the maximum in Figure 6.5a or in Figure 6.5c respectively.

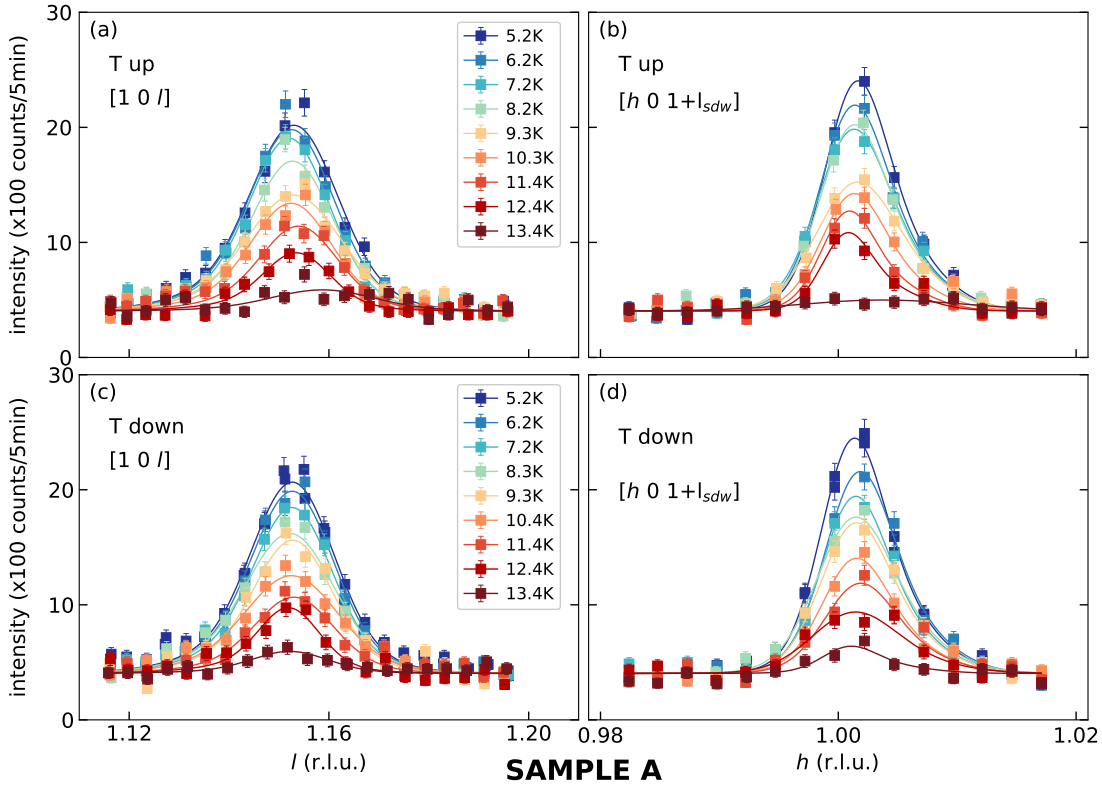

Figure 6.5: Temperature-dependence of the SDW signal in Sample A from $T_{base} = 5.2$K to $T_{N_A} \approx 13$K along h and l. **(a)** and **(b)** represent the data measured with increasing temperatures. **(c)** and **(d)** represent the data measured with decreasing temperatures. One additional temperature has been measured at $T = 14.5$K with increasing temperature steps, but no SDW intensity was detected and therefore not represented in (a) and (b). h and l at $T = 5.2$K in (c) and (d) were measured twice, which gives the doubled points.

ing temperatures (Figure 6.5c, Figure 6.5d) the SDW signal increases continuously when the temperature decreases from $T_{N_A} = 13.4$K to $T_{base} = 5.2$K. There is no sign of a downturn of the intensity, which we would expect near the temperature of the strongest SDW signal. This suggests that the Curie temperature is significantly lower than 5.2K. This is consistent with [49], who did not measure any FM ordered phase down to 2K. For increasing temperatures, the SDW signal is completely gone at 13.4K, whereas some intensity is still present with decreasing temperatures scans.

The position of the signal remains relatively constant along h and l, with $h \approx 1.00$ r.l.u. and $1.150 \leq l \leq 1.160$ r.l.u. for increasing and decreasing temperatures. Comparing Figure 6.5a with Figure 6.5b and Figure 6.5c with Figure 6.5d also shows that the SDW signal's width

remains constant with temperature changes and that the width along l as it about twice the width along h ($\sigma_l \approx 2\sigma_h$).

6.3.2 Sample B: $Nb_{0.986}Fe_{2.014}$ (y=0.014)

We measured Sample B with 4F2 from T = 17.9K ($<T_{C_B}$) to T = 33.8K with decreasing temperatures, and up to T = 34.9K ($>T_{N_B}$) with increasing temperatures. The measured temperatures are given in Table 6.3. Figure 6.6 shows selected h- and l-scans with increasing and decreasing temperatures. For the same reason as for Sample A, the maxima are given by the h-scans, which are centred on the maximum intensities measured along l. All the h-scans are fitted with three Gaussians and the l-scans with one Gaussian.

Table 6.3 Measured temperatures in Sample B. *T up* stands for a measurement sequence with increasing temperatures and *T down* for decreasing temperatures. All data have been measured at 4F2, LLB.

4F2	**SAMPLE B - measured temperatures**
T up	17.9K, 18.7K, 19.4K, 20.2K, 20.9K, 21.7K, 22.5K, 23.4K, 24.4K, 25.6K, 27.0K, 28.4K, 30.0K, 31.4K, 32.7K, 33.8K, 34.9K
T down	17.9K, 19.0K, 20.2K, 20.9K, 21.6K, 22.4K, 23.3K, 24.4K, 25.6K, 27.0K, 28.4K, 30.0K, 31.4K, 32.7K, 33.8K

The h-scans (Figure 6.6c-d and Figure 6.6g-h) clearly show the three peaks shape of the nuclear signal along h.

Along h, the position (h_{SDW}) and the width of the SDW signal are relatively constant with increasing and decreasing temperatures, and the amplitude is maximum at T = 24.4K for increasing and decreasing temperatures.

Along l, the width of the SDW signal is relatively constant over the temperatures and the maximum amplitude is also measured at T = 24.4K (Figure 6.6.a-b for increasing temperatures and Figure 6.6.e-f for decreasing temperatures). The position of the SDW signal (l_{SDW}) shifts toward higher values with increasing temperatures, with a stronger shift occurring between 24.4K and 27K.

Because the signal along h is composed of three Gaussians, it looks like that signal's width is the same along h and along l. However after computing the effective width along h with Equation 6.2.5, we find that the signal's width along l is twice the effective width along h, with is consistent with our observations in Sample A.

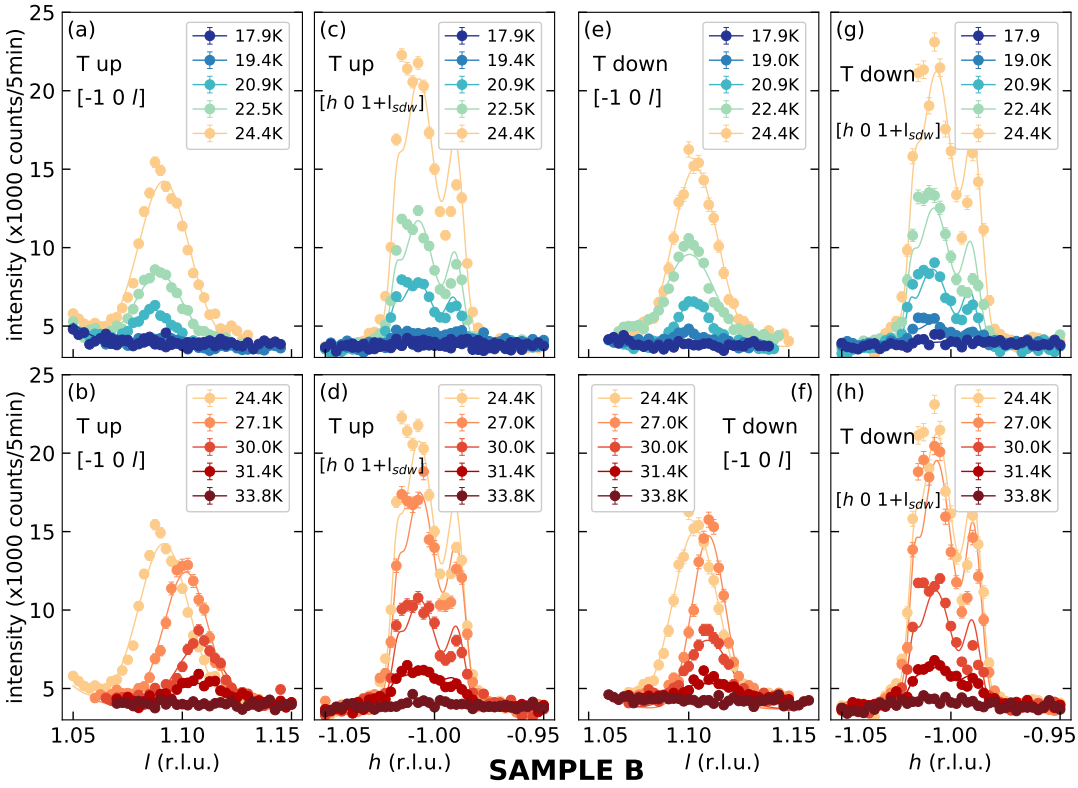

Figure 6.6: Temperature-dependence of the SDW signal in Sample B from 17.9K to 33.8K. To make the figure more readable, only a selection of temperatures is represented (all the measured temperatures are listed in Table 6.3). **(a)** and **(b)** represent the l-scans and **(c)** and **(d)** represent the h-scans with increasing temperatures (T *up*). **(e)** and **(f)** represent the l-scans and **(g)** and **(h)** represent the h-scans with decreasing temperatures (T *down*). The l-scans are centred on $h = -1$ r.l.u. and the h-scans are centred at the l-position of maximum intensity measured with the l-scans, which gives l_{SDW}.

6.3.3 Sample C: $Nb_{0.981}Fe_{2.019}$ (y=0.019)

We measured Sample C with Panda from T = 27.8K ($<T_{C_C}$) to T = 40.1K ($>T_{N_C}$) with increasing temperatures, and from T = 40.1K to T = 34.9K with decreasing temperatures (temperatures below 34.9K were measured by [70] before). All the measured temperatures are given in Table 6.4.

Figure 6.7 shows selected h- and l-scans with increasing temperatures and all the h- and l-scans with decreasing temperatures. As shown by the plain black lines in Figure 6.2c, the h- and l-scans where made at optimal position and across the maximum intensity. Thus the h- and l-scans have comparable amplitudes. All the data is fitted with two Gaussians along h and

Table 6.4 Measured temperatures in Sample C. *T up* stands for a measurement sequence with increasing temperatures and *T down* for decreasing temperatures. All data have been measured at Panda, FRM2.

Panda	**SAMPLE C - measured temperatures**
T up	27.8K, 28.8K, 29.8K, 30.8K, 31.9K, 32.9K, 33.9K, 35.0K, 36.0K, 37.0K, 38.0K, 39.1K, 40.1K
T down	34.9K, 36.0K, 37.0K, 38.0K, 39.1K, 40.1K

l, accordingly to the shape of the nuclear signal represented in Figure 6.2.

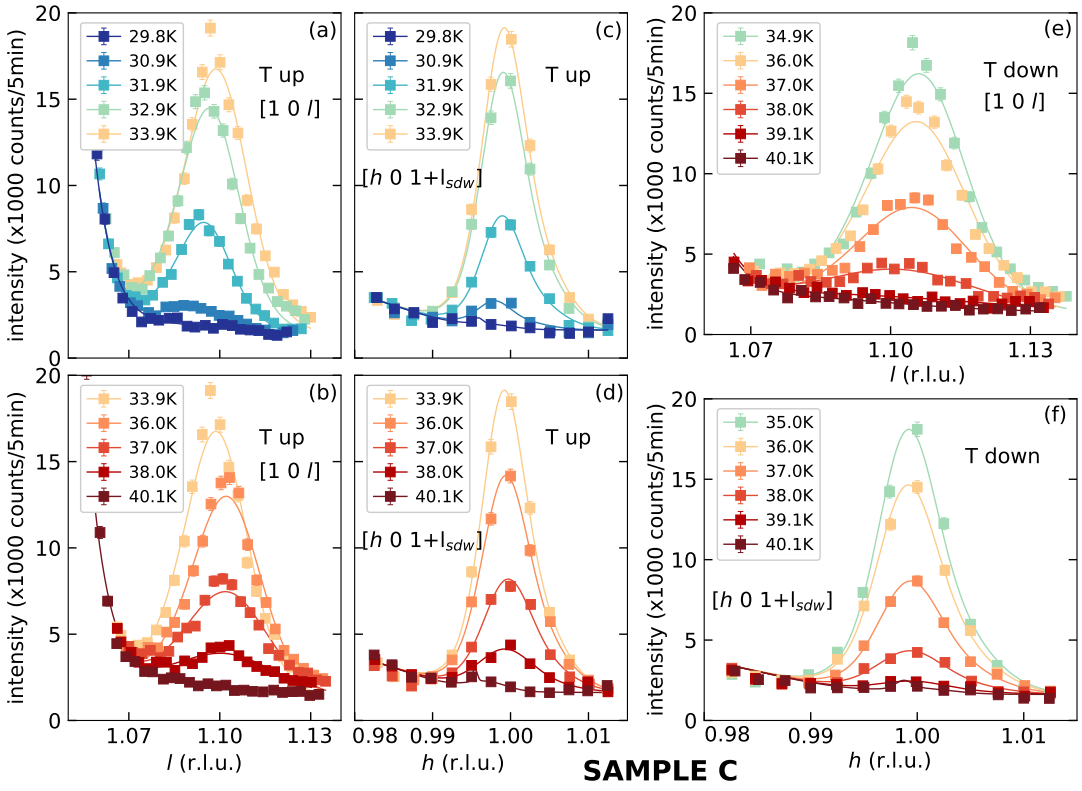

Figure 6.7: Temperature-dependence of the SDW signal in Sample C from 27.8K to 40.1K with increasing temperatures and from 40.1K to 34.9K with decreasing temperatures. **(a)** and **(b)** represent the l-scans and **(c)** and **(d)** represent the h-scans with increasing temperatures (T *up*). **(e)** represents the l-scans and **(f)** represents the h-scans with decreasing temperatures (T *down*). To make the figure more readable, only a selection of increasing temperatures measurements is represented in (a), (b), (c) and (d) (all the measured temperatures are listed in Table 6.4). The l-scans are centred on $h = 1$ r.l.u. and the h-scans are centred at the l-position of maximum intensity measured with the l-scans, which gives l_{SDW}.

Along h, the position (h_{SDW}) and the width of the SDW signal are relatively constant with increasing and decreasing temperatures ($h \approx -1$ and $x_{\mathrm{FWHM},h} \approx 0.015$r.l.u). The amplitude is maximum at $T = 33.9$K (Figure 6.6c and Figure 6.6d).

Along l, the width of the SDW signal is relatively constant over the temperatures with $x_{\mathrm{FWHM},l} \approx 0.03$ r.l.u., which is approximately twice the width of the signal along h, and the maximum amplitude is also measured at $T = 33.9$K (Figure 6.6a). l_{SDW} shifts continuously towards higher values with increasing temperatures.

6.4 Discussion

Figure 6.8 combines the results of measurements done prior to this PhD project and our latest results described in the previous section. The temperature evolution of the FM intensity at the nuclear position $\boldsymbol{Q} = (1\ 0\ 2)$ r.l.u. is given in Figure 6.8a, Figure 6.8b shows the temperature evolution of the SDW intensity and Figure 6.8c shows that the temperature evolution of l_{SDW}. h_{SDW} is temperature independent. The empty markers correspond to the data measured before this PhD project and we will refer to those as the *previous data*. The data that we measured are consistent with the previous data. This shows a good reproducibility, considering that the results were measured during different periods and at different instruments.

From the onset of the FM signal shown in Figure 6.8a, we record Curie temperatures in samples B and C, with $\mathrm{T_{C_B}} \approx 24.4$K and $\mathrm{T_{C_C}} \approx 33.9$K. In Sample A, however, no FM signal has been detected.

We observe a temperature hysteresis in the temperature evolution of l_{SDW} in Sample B and Sample C when entering the SDW state from the FM state, which suggests that the FM-SDW transition is first order. This is consistent with the AC-susceptibility measurements from [42] and presented in Figure 3.4. In Sample A, l_{SDW} shows no significant temperature dependence, whereas in samples B and C (Figure 6.8.b), the decrease of l_{SDW} with decreasing temperature (i.e. when approaching the FM phase) indicates that the Q-dependent susceptibility in the SDW phase χ_{q} is modified near the FM phase [3]. Also the average l_{SDW} in Sample A being higher than in Sample B, itself higher than in Sample C, indicates an increasing ordering wave vector as we approach the FM QCP.

Below 13.4K in Sample A, below 32.6K in Sample B and below 38K in Sample C (vertical dashed lines on the high temperature side in Figure 6.8b), the SDW intensity grows continuously with decreasing temperatures until its maximum at $\mathrm{T_{C_B}}$ (24.4K) in Sample B and $\mathrm{T_{C_C}}$ (33.9K)

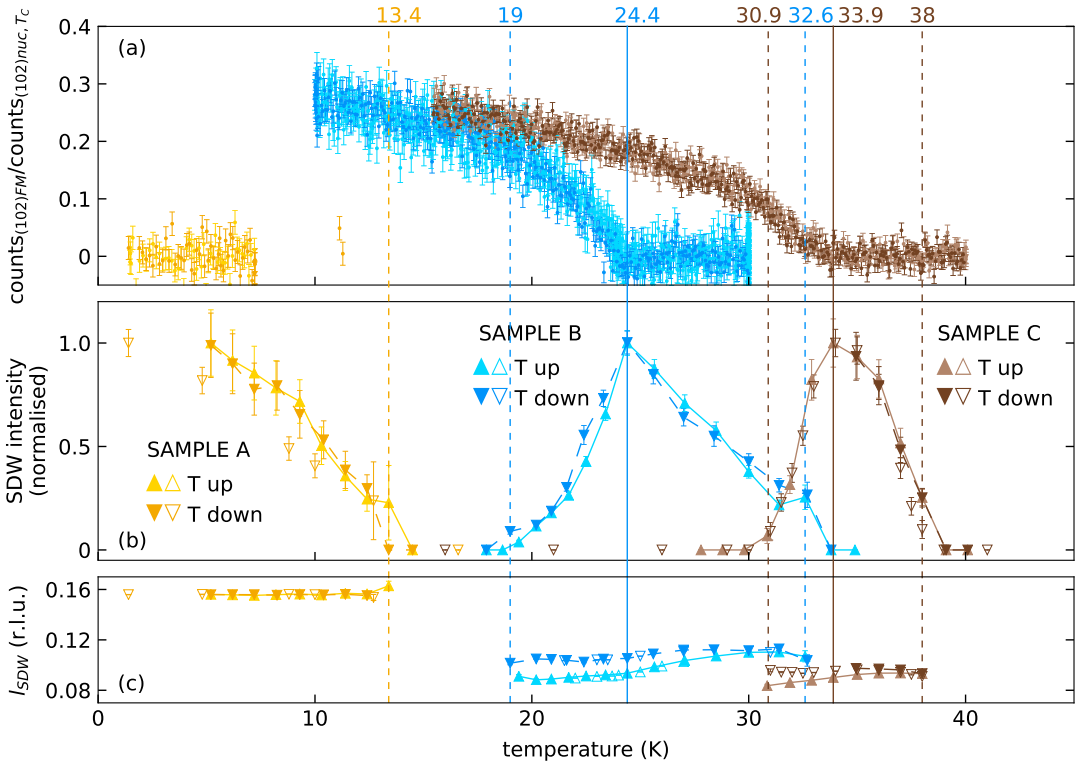

Figure 6.8: Temperature evolution of the FM signal and the SDW characteristics. **(a)** shows the temperature evolution of the FM signal measured at $\boldsymbol{Q} = (1\ 0\ 2)$ r.l.u. and normalised by the nuclear intensity measured at T_C. **(b)** shows the temperature evolution of the normalised SDW signal intensity in Sample A (yellow), Sample B (blue) and Sample C (brown). The intensities are normalised with the highest value measured with increasing temperatures (T up). **(c)** shows the temperature evolution of l_{SDW} (the l-component of $\boldsymbol{Q}_{\mathbf{SDW}}$) in the three samples. The dashed lines indicate the onset temperatures of the SDW signal and the plain lines are the temperatures of maximum SDW intensity, which also corresponds to the onset of the FM signal at T_C. Full markers are the data measured in the framework of this PhD project and the empty markers represent the previous data [3].

in Sample C (vertical plain lines in Figure 6.8b). This suggests that the PM-SDW phase transition is second order and that $T_{N_A} = 13.4$K, $T_{N_B} = 32.6$K and $T_{N_C} = 38$K. Below T_{C_B} in Sample B and T_{C_C} in Sample C, the SDW intensity decreases when the temperature decreases, until the signal disappears completely at 19K in Sample B and 30.9K in Sample C (vertical dashed lines on the low temperature side in Figure 6.8.a). This suggests that the FM state and the SDW state coexist over a temperature range of 5.4K in Sample B and 3K in Sample C, although the SDW-FM phase transition is first order. We explain this coexistence by a

distribution of the SDW-FM transition temperature through the samples due to a gradient in the Fe concentration. If we refer to the phase diagram of $Nb_{1-y}Fe_{2+y}$ (Figure 4.1 in Section 4.1), we see that a variation in T_{C_B} of $\pm$2.7K and in T_{C_C} of $\pm$1.5K originates from a variation in y of $\pm$0.00148 in Sample B and y of $\pm$0.00078 in Sample C. This variation in y incurs a variation in T_{N_B} of $\pm$2.1K and in T_{N_C} of $\pm$1.1K. Thus the bulk SDW-FM transition temperature (the bulk Curie temperature) is $T_{C_{B,bulk}}$= 21.7K in Sample B and $T_{C_{C,bulk}}$= 32.4K in Sample C, and the bulk PM-SDW transition temperature (the bulk Néel temperature) is $T_{N_{B,bulk}}$= 30.5K in Sample B and $T_{N_{C,bulk}}$= 36.9K in Sample C. This is in good agreement with the transition temperatures measured with AC-susceptibility and magnetisation measurements, which give T_{C_B}= 24K [3] and T_{C_C}= 33K [48] for the SDW-FM transition temperatures and T_{N_A}= 13K, T_{N_B}= 30K [3] and T_{N_C}= 37K [48] for the PM-SDW transition temperatures.

Chapter 7

Unpolarised Inelastic Neutron Scattering Measurements

Previously we looked at the characteristics of the spin density wave (SDW), which emerges when approaching the ferromagnetic quantum critical point (FM QCP). The question arises how magnetic excitations evolve in the vicinity of the masked FM QCP. Like previously in chapter 6, we approach the FM QCP by using our three samples (A, B and C) and we observe the evolution of the magnetic excitation spectrum around the FM QCP with inelastic neutron scattering experiments.

7.1 Introduction

We measured the magnetic excitations in Sample A, Sample B and Sample C with two triple axis spectrometers (TASs) –4F2 and Panda– and also, in Sample C only, with a multi-choppers spectrometer (MCS) –LET. The latter instrument allows simultaneous measurements using neutrons with different E_is. Neutrons with higher incident energy (E_i) are used to observe higher excitation energies and cover a wider q-range in the reciprocal space, but this comes with the cost of lower resolution. Therefore measuring with lower E_i is necessary to resolve very low energy excitations. Figure 7.1 shows the resolution for various E_is. For our experiments we used: $E_i = 9.5\,\text{meV}$, $E_i = 4.35\,\text{meV}$, $E_i = 2.48\,\text{meV}$ and $E_i = 1.6\,\text{meV}$. We chose $E_i = 9.5\,\text{meV}$ and $E_i = 4.35\,\text{meV}$ to cover the whole spectrum of the magnetic excitations that we intended to measure, which we estimated from the TASs results that are presented below. $E_i = 2.48\,\text{meV}$

and $E_{\mathrm{i}} = 1.6\,\mathrm{meV}$, on the other hand, were chosen to increase the energy resolution to resolve the softer excitations rather than to the cover a wide energy range.

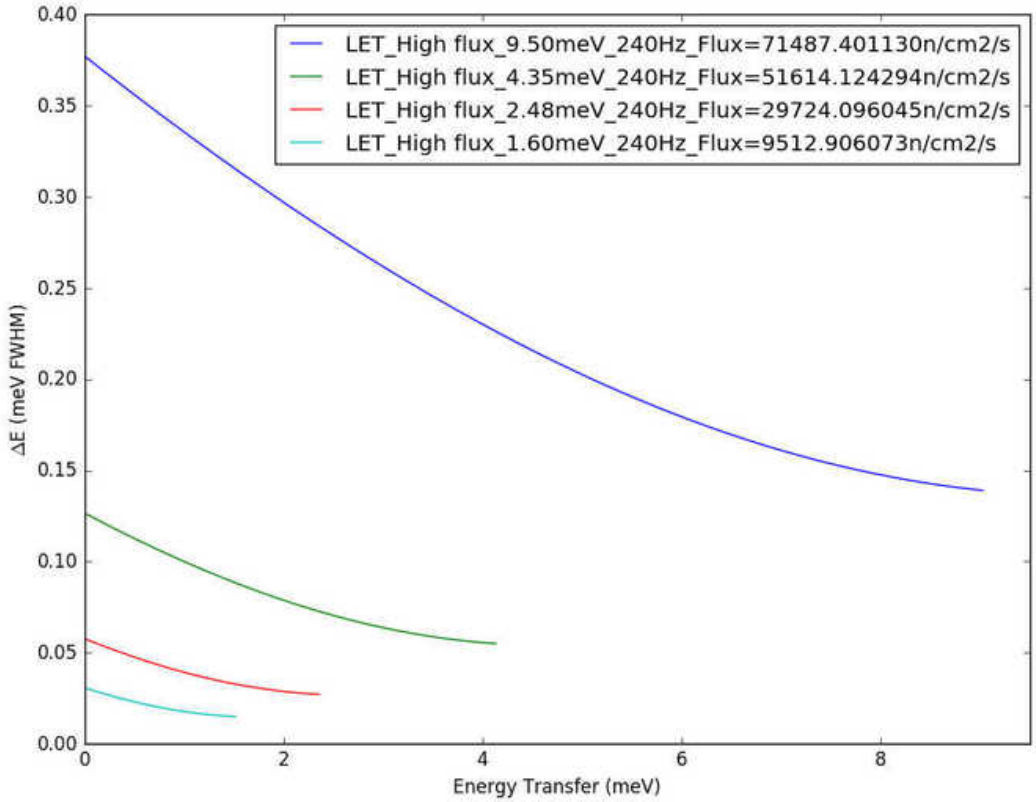

Figure 7.1: Resolution and flux at LET for the energies of the incident neutrons selected during the experiments. Those values were provided by the instrument software.

The instrument's software –Horace– automatically corrects and normalises the data after acquisition and therefore no manual corrections are required before analysis.

Now we discuss the settings of the two TASs instruments: 4F2 and Panda. Measurements on 4F2 and Panda were made with vertically and horizontally focused monochromator and analyser. k_{f} was kept constant and we tuned k_{i}: $k_{\mathrm{f}} = 1.30\text{Å}^{-1}$ for measurements in Sample B and Sample C with 4F2 and Sample B with Panda, and $k_{\mathrm{f}} = 1.57\text{Å}^{-1}$ for measurements in Sample A with Panda[1].

Before the physical analysis, correction and background substraction of the raw data col-

[1] $k_{\mathrm{f}} = 1.30\text{Å}^{-1}$ corresponds to a final neutron energy of 3.50 meV and $k_{\mathrm{f}} = 1.57\text{Å}^{-1}$ corresponds to a final neutron energy of 5.11 meV.

lected with 4F2 and Panda is necessary. These procedures are explained in the following sections. The resolution of each TAS instrument is given in Figure 7.2.

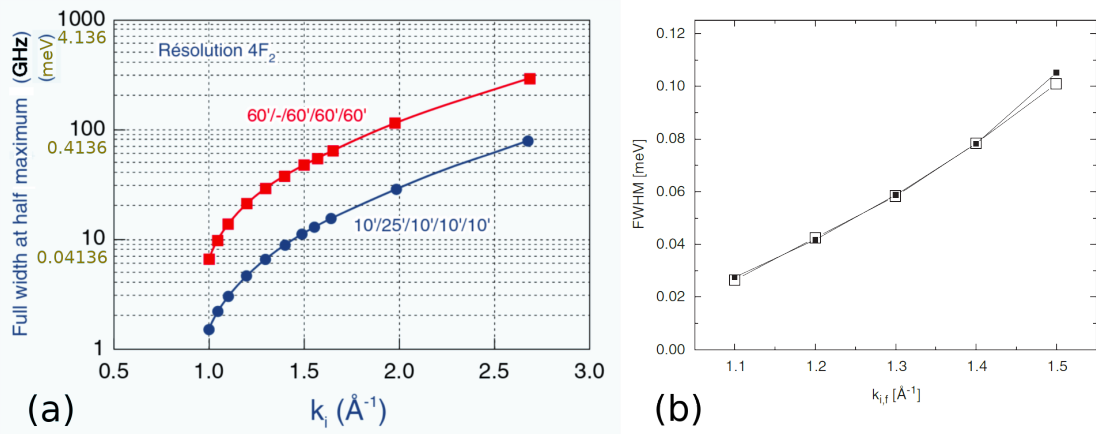

Figure 7.2: k_i-dependent resolution of 4F2 **(a)** and Panda **(b)**. Collimations in (a) correspond to in-pile/M1-M2/M2-sample/sample-analyser/analyser-counter and in (b) only the monochromator-sample collimation was 60' and none elsewhere. In (b), small solid squares correspond to an analyser scan and large empty squares correspond to a monochromator scan. Figures from [71] (a) and [72] (b).

7.2 Data correction and analysis

In this section we present the corrections and/or the background subtraction to perform on the raw data before the physical analysis. We start with time of flight spectrometer (TOF) data, followed by the TASs data . Finally we present the fit functions used to analyse the data.

7.2.1 LET

With LET large ranges of reciprocal space are scanned at once, which gives a four-dimensional picture of the scattered intensities in reciprocal space (the three reciprocal space directions and the energy). From this whole data set, we make 1D cuts along the energy dimension at given position $\boldsymbol{Q}$ and at a given temperature T. This gives data sets, which are similar to those obtained with a TAS. We collected data at four different E_is: 9.5 meV, 4.35 meV, 2.48 meV and 1.6 meV. The energy resolution of the instrument decreases as E_i increases (Figure 7.1). Thus the higher the resolution, the smaller the energy window to look at the magnetic excitations. The energy resolution of the 9.5 meV data is significantly lower than for the three other E_is

and results in poor fits. For that reason, we excluded the 9.5 meV data from the analysis. At base temperature (4 K), the energy ranges covered by the neutrons with 1.6 meV and 1.6 meV E_is are smaller or of the order of the magnetic excitations; therefore we considered only the 4.35 meV data. Near Curie and Néel temperatures, we analysed the data with all three E_is (1.6 meV, 2.48 meV and 4.35 meV).

The necessary corrections of the signal have been supplied by the instrument software; however these corrections exclude the subtraction of the background signal, which we do manually.

7.2.1.1 Background subtraction

Knowing the background during an experiment is important, because it tells us what is relevant in the detected signal. It mainly depends on the instrument and its environment, including the temperature of the sample environment. Therefore, we measured the background at 4 K, 32 K, 38 K and 211 K. For E_is of 9.5 meV and 4.35 meV we chose the $\boldsymbol{Q}_\mathbf{b} = (\pm 0.23\ 0\ 2.68)$ r.l.u. position (+ for 4 K and 211 K, − for 32 K and 38 K) and for E_is of 2.48 meV and 1.6 meV we chose the $\boldsymbol{Q}_\mathbf{b} = (\pm 0.23\ 0\ 1.32)$ r.l.u. position[2] (+ for 4 K and 211 K, − for 32 K and 38 K), far away from the location of any low energy excitations. We measured at $h = -0.23$ r.l.u. at 32 K and 38 K because $h = +0.23$ r.l.u. might not properly represent the background due to the proximity of the scanned limit. The background positions are shown by the yellow markers in Figure 7.11.

Figure 7.3, shows the fits of the background signals measured with E_i 1.6 meV. The figures for E_is 2.48 meV, 4.35 meV and 9.5 meV are given in Appendix A.2.1.1, Appendix A.2.1.2 and Appendix A.2.1.3, respectively.

We fitted the background signals with a Gaussian function for the elastic line and a constant for the tail of the signal:

$$\text{fit function} \quad f : x \mapsto a \exp\left(-\frac{(x-b)^2}{2\sigma^2}\right) + \text{cst}, \tag{7.2.1}$$

where cst is the constant function, a is the amplitude of the Gaussian, b its centre and σ is the standard deviation. The half-width half-maximum (HWHM) is proportional to σ:

$$x_{\text{HWHM}} = \sigma\sqrt{2\log(2)} \quad (= \frac{x_{\text{FWHM}}}{2}). \tag{7.2.2}$$

[2] $\boldsymbol{Q}_\mathbf{b} = (0.23\ 0\ 2.68)$ r.l.u. is out of reach or only a small energy range is covered for E_is of 2.48 meV and 1.6 meV.

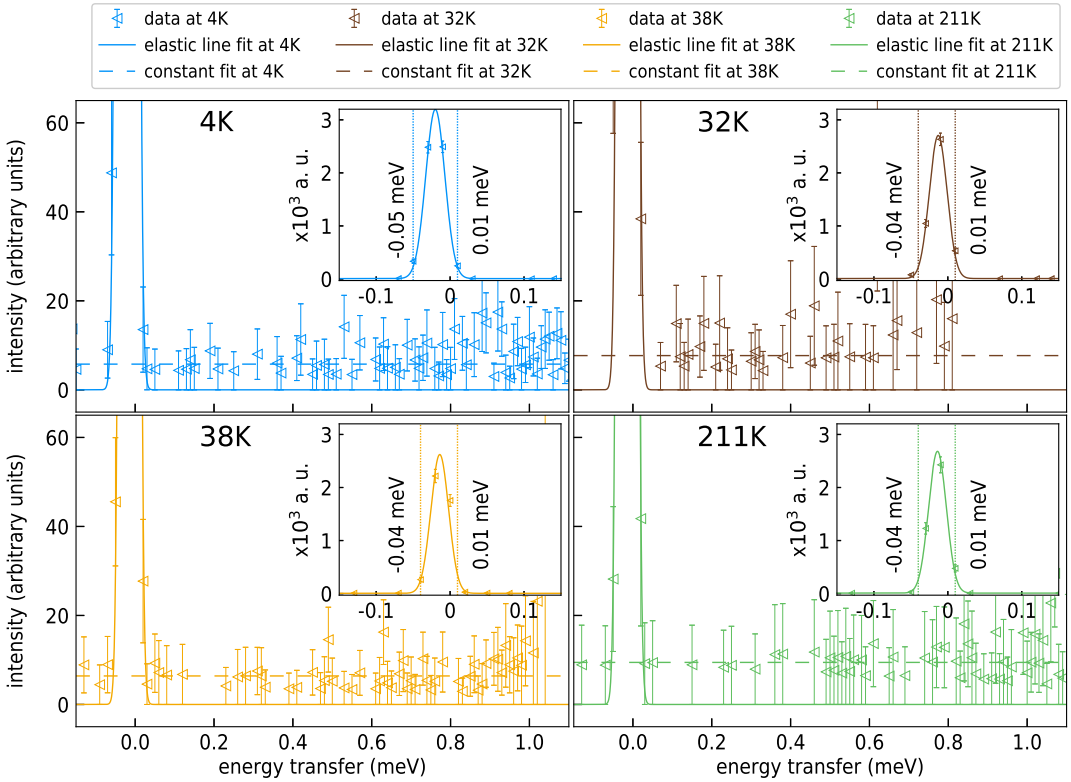

Figure 7.3: Background measured at $\boldsymbol{Q}_\mathbf{b} = (0.23\ 0\ 1.32)$ (r.l.u.) for LET with Sample C and E_i of 1.6 meV. The solid lines represent Gaussian fits. The insets show the elastic lines and the limits where the Gaussian fits exceed 10 % of their maximum amplitudes (marked by vertical dotted lines). The parameters of the background fits are given in Table 7.1.

All the fit parameters of the backgrounds are given in Table 7.1.

7.2.2 4F2 and Panda

Several corrections and normalisation of the raw data measured with TASs are necessary to identify the magnetic excitations. This is not done automatically with 4F2 or Panda, and therefore we implement those manually.

7.2.2.1 Monitor correction

As previously mentioned in Subsection 6.2.1.1, the monitor is also sensitive to higher order incident neutrons, which we remove from the readings by applying the correction factors given in Figure 6.1. Our energy scans are made by sweeping k_i and therefore the correction factors

Table 7.1 Fit parameters of the different backgrounds measured in Sample C with LET. The first column gives the E_i of the neutrons, the second column gives the temperatures of the measurements and the last column gives the fit parameters. a is the amplitude of the Gaussian, b its centre, σ its standard deviation and cst is the constant fit. The values in brackets are the errors of the fit parameters.

1.6 meV	4 K	$a = 3172(159),\ b = -0.0205(6),\ \sigma = 0.0134(4), \text{cst} = 5.77(40)$
	32 K	$a = 2695(114),\ b = -0.0130(4),\ \sigma = 0.0124(3), \text{cst} = 7.69(73)$
	38 K	$a = 2609(153),\ b = -0.0135(6),\ \sigma = 0.0125(4), \text{cst} = 6.41(38)$
	211 K	$a = 2662(149),\ b = -0.0137(6),\ \sigma = 0.0126(4), \text{cst} = 9.45(63)$
2.48 meV	4 K	$a = 3532(159),\ b = -0.0312(9),\ \sigma = 0.0247(7), \text{cst} = 7.08(46)$
	32 K	$a = 3254(119),\ b = -0.0170(7),\ \sigma = 0.0226(5), \text{cst} = 8.87(57)$
	38 K	$a = 3375(116),\ b = -0.0174(7),\ \sigma = 0.0228(5), \text{cst} = 7.52(44)$
	211 K	$a = 2935(137),\ b = -0.0192(9),\ \sigma = 0.0233(6), \text{cst} = 14.32(97)$
4.35 meV	4 K	$a = 2941(80),\ b = -0.0533(13),\ \sigma = 0.0578(9), \text{cst} = 9.96(71)$
	32 K	$a = 2584(86),\ b = -0.0214(14),\ \sigma = 0.0522(9), \text{cst} = 10.19(75)$
	38 K	$a = 2568(80),\ b = -0.0204(13),\ \sigma = 0.0526(8), \text{cst} = 8.57(38)$
	211 K	$a = 2169(97),\ b = -0.0197(19),\ \sigma = 0.0536(13), \text{cst} = 18.94(96)$
9.5 meV	4 K	$a = 1508(63),\ b = -0.1365(79),\ \sigma = 0.1728(60), \text{cst} = 2.47(15) \times 10^1$
	32 K	$a = 1462(80),\ b = -0.0439(76),\ \sigma = 0.1562(54), \text{cst} = 2.80(13) \times 10^1$
	38 K	$a = 1480(67),\ b = -0.0373(66),\ \sigma = 0.1668(51), \text{cst} = 2.51(13) \times 10^1$
	211 K	$a = 1291(92),\ b = -0.0434(103),\ \sigma = 0.1659(83), \text{cst} = 5.72(39) \times 10^1$

are energy-dependent.

7.2.2.2 Attenuator correction

For the measurements at ferromagnetic (FM) position $\boldsymbol{Q}_{\mathbf{FM}}$= (0 0 2) (r.l.u.) with Sample B on Panda, the scattered signal was too intense for the detector[3] and we attenuated the incoming signal. Attenuators consist of plates of Schott glass inserted between the monitor and the sample. The attenuation factor ($F_{\text{att}}(d, k_i)$) depends on the thickness of theses plates and on k_i:

$$F_{\text{att}}(d, k_i) = \exp\left(\frac{2\pi d(m - 0.1107)}{k_i}\right), \tag{7.2.3}$$

where d is the total thickness of the attenuation plates and m is a fit constant. To correct the signal we multiply the detected signal with this factor $F_{\text{att}}(d, k_i)$.

However the factor given by Equation 7.2.3 does not account for neutrons that are reflected back through the monitor by the attenuation plates and which are counted twice.

Figure 7.4 shows count rates measured with (blue) and without (brown) attenuation. Although the monitor is placed before the attenuation plates, a straight line fit over the attenuated

[3] attenuation is necessary on Panda when the detection rate of scattered neutrons exceeds 100000 s^{-1}

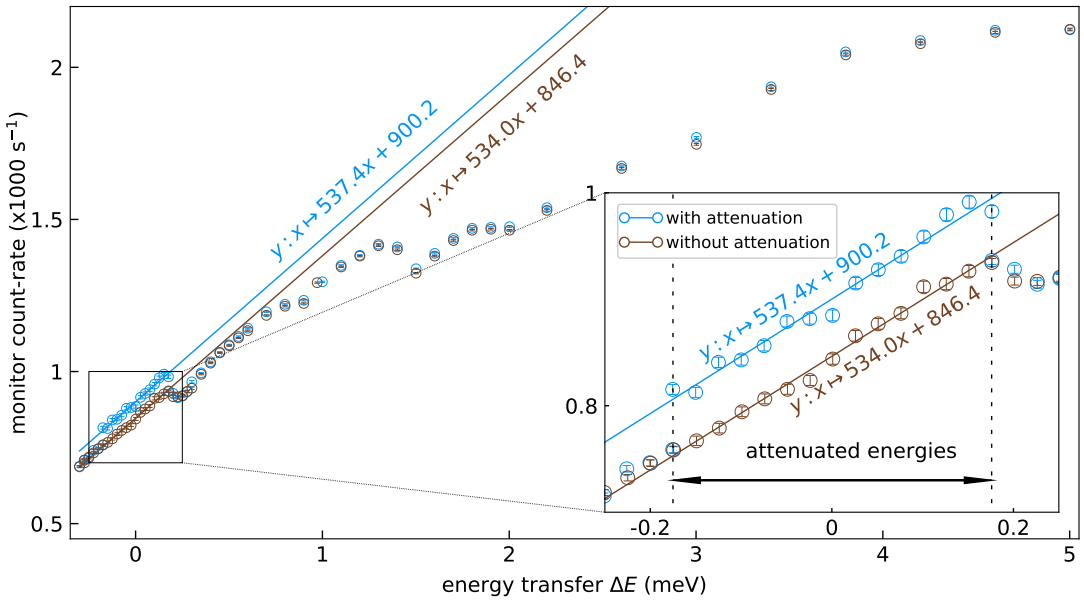

Figure 7.4: k_i-dependent count rate of Panda monitor with (blue) and without (brown) attenuation. The attenuator is only activated near the elastic line ($|\Delta E| \lessapprox 0.175\,\mathrm{meV}$). The insert, which is a zoom-in around the elastic line, shows an increase of the count rate when attenuation is active. The plain blue line is a linear fit of the count rates over energies with active attenuation and the plain brown line is a linear fit over the same energies but without attenuation.

energies ($-0.175\,\mathrm{meV} \leq \Delta E \leq 0.176\,\mathrm{meV}$) shows a sudden increase in the monitor count rates when attenuation is active. Therefore the detected signal in an under-estimation of the detected intensity because of the over-estimated monitor count rate. Since the count rate is independent of the measured position and temperature, we compensate for this reflection effect by re-evaluating the monitor counts with the count rates of a non-attenuated scan done at the SDW position and at the same temperature (brown data points in Figure 7.4). Using the non-attenuated count rates and the counting durations, we compute the real monitor counts, which are used to normalise the data.

7.2.2.3 Data normalisation

During a scan, different measuring times were set, depending on the intensity of the detected signal: longer counting times were set at energies where the signal was weaker. We then normalise the data to a unique monitor count value N_norm corresponding to approximately 5min of counting time. For our experiments the following normalisation values have been

chosen:

$$\begin{aligned} N_{\text{norm}}^{\text{4F2}} &= 3775 \text{ counts} \\ N_{\text{norm}}^{\text{Panda}} &= 429967 \text{ counts} \end{aligned} \tag{7.2.4}$$

7.2.2.4 Energy shift

Typical magnetic excitations observed in this study have resonance energies of the order of 0.5 meV with an error of the order of $\delta E_{\text{e}} \approx 5\%$. The energy shift observed by the shift of the elastic line from the nominal energy position at 0 meV is of the order of 0.02 meV , i.e. of the same order of magnitude as the error of the observed excitation energies. ΔE values have therefore been corrected to compensate for the shift.

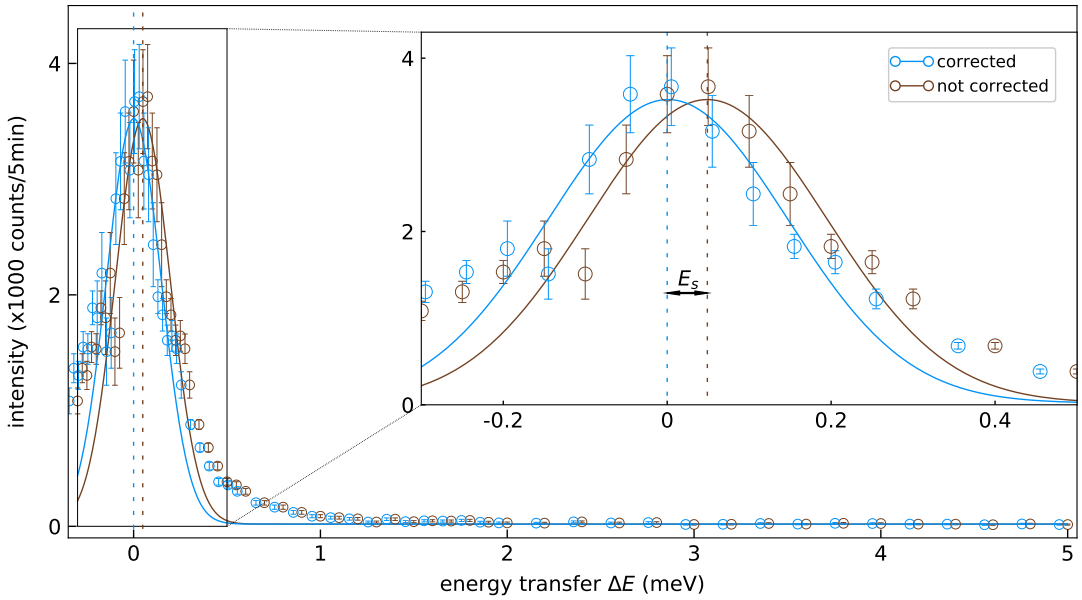

Figure 7.5: Energy scan with (blue) and without (brown) correction for energy shift. The insert is a zoom-in of the elastic line and the solid lines are Gaussian fits. The Gaussian fit of the corrected data is centred on 0 meV –blue dashed line– and the Gaussian fit of the raw data is centred on E_{s} –brown dashed line–, which is also the energy shift.

Figure 7.5 illustrates the energy shift correction [4], which consists of fitting the non-corrected data (brown points in Figure 7.5) with a three parameters Gaussian function (brown line in

[4] Figure 7.5 shows the energy scan of Sample C at reciprocal position $\boldsymbol{Q}$= (0 0 2.1) r.l.u. and temperature $T = 31.8$ K measured with 4F2.

Figure 7.5):

$$\text{Gaussian function} \quad f : x \mapsto a \exp\left(-\frac{(x-b)^2}{2\sigma^2}\right), \tag{7.2.5}$$

where a is the amplitude, b is the centre and σ is the standard deviation. The centre of the Gaussian b gives the energy shift ($E_s = +0.049\,\text{meV}$ in our example). We correct the data by adding an offset of $-E_s$ to the energy transfer values ΔE.

7.2.2.5 Background substraction

Figure 7.6 shows the background of 4F2 and Panda at several temperatures, that we measured during the different experiments and with all three samples. We chose the $\boldsymbol{Q}_\mathbf{b} = (0.85\ 0\ 1.4)\,\text{r.l.u.}$ position, far away from the location of any low-energy excitations.

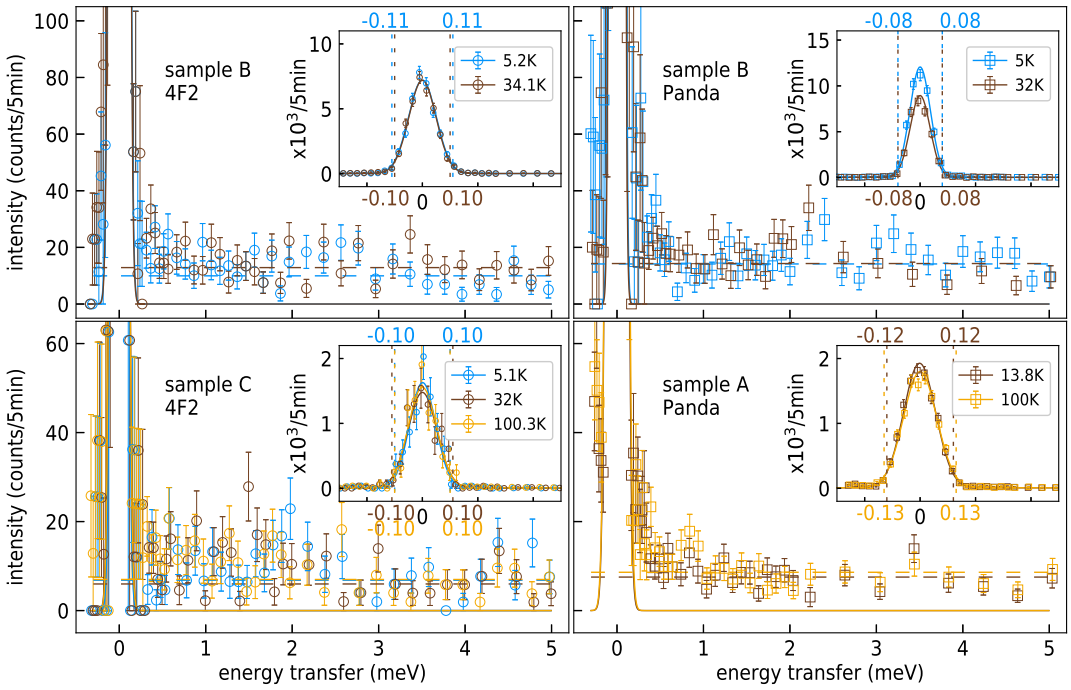

Figure 7.6: Background measured at $\boldsymbol{Q}_\mathbf{b} = (0.85\ 0\ 1.4)\,\text{(r.l.u.)}$ for Panda and 4F2 with Sample A, Sample B and Sample C. The solid lines represent Gaussian fits of the elastic line and the dashed lines are the constant background fits. The insets show the elastic lines and the limits where the Gaussian fits exceed 10 % of their maximum amplitudes (marked by vertical dotted lines). The parameters of the background fits are given in Table 7.2.

We fitted the background signals with the same function as the one used for LET, which is given in Equation 7.2.1 (Gaussian + constant). The fit parameters, which are given in Table 7.2, indicate that the constant is temperature independent.

Table 7.2 Fit parameters of the background measured during the experiments on TASs instruments. **I** are the instruments, **S** are the samples and **T** are the temperatures of the measurements. a is the amplitude of the Gaussian, b its centre, σ its standard deviation and cst is the constant fit.

I	**S**	**T**	**fit parameters**
4F2	B	5.2 K	$a = 7208(308),\ b = 0.0001(17),\ \sigma = 0.0495(12),\ \text{cst} = 9.95(90)$
		34.1 K	$a = 7182(290),\ b = -0.0001(16),\ \sigma = 0.0486(11),\ \text{cst} = 12.86(96)$
	C	5.1 K	$a = 1623(216),\ b = 0.0009(52),\ \sigma = 0.0469(38),\ \text{cst} = 6.82(75)$
		32 K	$a = 1473(201),\ b = 0.0001(59),\ \sigma = 0.0518(41),\ \text{cst} = 5.98(73)$
		100.3 K	$a = 1549(192),\ b = 0.0000(51),\ \sigma = 0.0507(37),\ \text{cst} = 6.99(71)$
Panda	A	13.8 K	$a = 1920(82),\ b = -0.0018(20),\ \sigma = 0.0576(13),\ \text{cst} = 7.53(71)$
		100 K	$a = 1791(78),\ b = 0.0001(21),\ \sigma = 0.0596(14),\ \text{cst} = 8.61(76)$
	B	5 K	$a = 12065(502),\ b = 0.0002(13),\ \sigma = 0.0369(9),\ \text{cst} = 1.42(11) \times 10^1$
		32 K	$a = 8942(420),\ b = -0.0005(14),\ \sigma = 0.0358(10),\ \text{cst} = 1.43(12) \times 10^1$

7.2.3 Data fitting

7.2.3.1 Fitted energies

Whenever possible, we fit the whole signal, including the elastic line; however that is not possible for intensities of the latter too high compared to the intensities of the excitations because of the high error on the fitted parameters of the excitations. This happens when the measured position is near the (0 0 2) r.l.u. Bragg peak (i.e. positions (0 0 2) r.l.u. and (0 0 2.05) r.l.u. or equivalent). In these situations we cut out part of the elastic line and fit its tail only. The cut out region corresponds to the energy range where the Gaussian fit of the background exceeds 10 % of its maximum amplitude (marked by vertical dashed lines in the insets of Figure 7.3, Figure 7.6, Appendix A.2.1.1, Appendix A.2.1.2 and Appendix A.2.1.3). Excluding part of the elastic line gives two energy intervals over which the data is simultaneously fitted.

7.2.3.2 Fit functions

After removing the background from the detected signal, we fit the magnetic excitations with an over-damped harmonic oscillator (ODHO) function for temperatures above T_C, as suggested

by the spin fluctuation theory (see Section 2.3):

$$\text{over-damped: } \mathrm{f_{odho}}(E) = \frac{E\chi_0\Gamma}{E^2+\Gamma^2}, \tag{7.2.6}$$

where E is the neutron energy loss to the sample (in meV), Γ is the line width (in meV) and χ_0 is the resonance amplitude or static susceptibility (in counts). T

In the FM regime, the ODHO does not fit the data well and we use the three parameters damped harmonic oscillator (DHO) function instead:

$$\mathrm{f_{dho}}(E) = \frac{E\chi_0 D E_0^2}{(E^2-E_0^2)^2+E^2D^2}, \tag{7.2.7}$$

where E_0 is the resonance energy (in meV) and D is the damping factor (in meV).

In the over-damped regime ($D >> E_0$), the ODHO function does not fit the data when the signal is within the resolution of the instrument. We then used an alternative fit function derived from Equation 7.2.7 and Equation 7.2.6, depending on the value of D. The validity of the fit is checked *a posteriori* by comparing the fitted parameter D with the fitted energy range.

If $D \approx E$, taking the limit of Equation 7.2.7 gives

$$\text{soft over-damped: } \mathrm{f_{sodho}}(E) = \frac{AD^2}{E(E^2+D^2)}. \tag{7.2.8}$$

We refer to this function as soft over-damped harmonic oscillator (SODHO). This case was encountered at 25 K for position $\boldsymbol{Q_{FM}}$= (0 0 2) r.l.u. in Sample B and at 32.1 K for position $\boldsymbol{Q_{FM}}$= (0 0 2) r.l.u. in Sample C.

7.2.3.3 Detailed Balance

As we saw in Section 4.2.1.2.2, the imbalance due to the principle of detailed balance must be considered. This is done by multiplying the previous fit functions with the Bose factor[5]:

$$\mathrm{db}(E,T) = \frac{\exp\left(\frac{E}{k_\mathrm{B}T}\right)}{\left|\exp\left(\frac{E}{k_\mathrm{B}T}\right)-1\right|}, \tag{7.2.9}$$

[5]the absolute value in Equation 7.2.9 is to account for the energy gain side.

where E is the neutron energy loss to the sample, k_B is the Boltzmann constant, T the temperature in Kelvin.

7.2.3.4 Fitting examples

Figure 7.7 shows two examples of data fits for Sample B measured with Panda. The magnetic excitation in Figure 7.7a is fitted with the DHO function and the magnetic excitation in Figure 7.7b is fitted with the ODHO function.

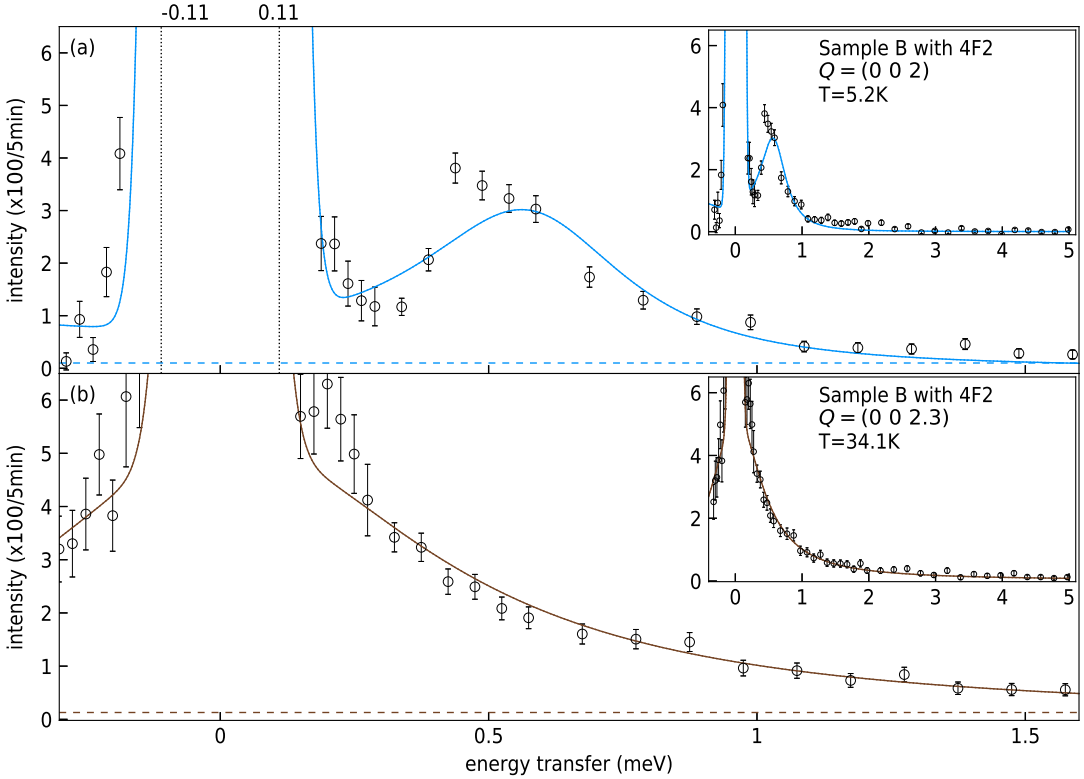

Figure 7.7: Magnetic excitation fitted with a harmonic oscillator in **(a)** the *damped* regime and **(b)** the *over-damped* regime. The dashed curves represent the background. The continuous lines indicate the fitted data. The black dotted vertical lines delimit the cut out energy interval excluded from the fit range. The full range of scanned energies are shown in the insets (same units as the main axes).

In the damped regime the magnetic excitation is separated from the elastic line and forms a distinct peak (Figure 7.7a). In the over-damped regime, on the other hand, the signature of the excitation is much closer to the elastic line and the resonance energy is of the order of the

instrument's resolution; one only sees a broadening of the elastic line (Figure 7.7b).

When the scanned position is in the vicinity of the Bragg position $\boldsymbol{Q}_{\mathbf{FM}}$= (0 0 2) r.l.u., the instrument's resolution ellipsoid hits the latter and the detected signal features an additional peak. An example is represented in Figure 7.8.

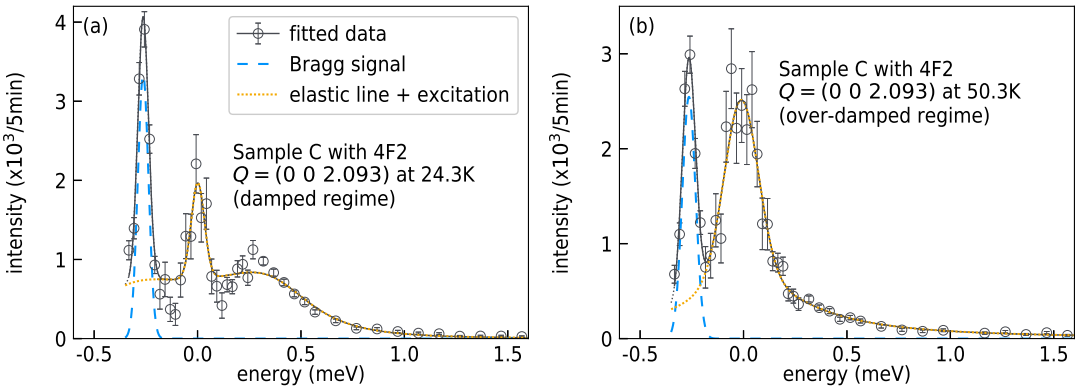

Figure 7.8: Signal featuring an additional peak measured with 4F2 in Sample C. **(a)** shows a magnetic excitation in the damped regime and **(b)** in the over-damped regime. This additional peak is observed when the scanned position is within close range of $\boldsymbol{Q}_{\mathbf{FM}}$, which crosses the instrument's resolution ellipsoid during the energy scan. The blue dashed lines are the fits of the additional peaks coming from the nuclear signal and the yellow dashed lines are the fits of the elastic line and the excitation together, with a DHO function in (a) and an ODHO function in (b). The grey lines are the fits of the overall signals.

When such a peak is observed, we add a Gaussian function to the fit function, which becomes:

$$\mathrm{f}_{\mathrm{fit}}(E) = \mathrm{f}_{\mathrm{odho/dho}}(E)\mathrm{db}(E,T) + a_e \exp\left(-\frac{(E-b_e)^2}{2\sigma_e^2}\right) + a_b \exp\left(-\frac{(E-b_b)^2}{2\sigma_b^2}\right), \qquad (7.2.10)$$

where a_e, b_e and σ_e are the parameters of the elastic line Gaussian, and a_b, b_b and σ_b are the parameters of the additional peak Gaussian. The additional signal is not centred on $E = 0\,\mathrm{meV}$ because the resolution ellipsoid usually hits the Bragg position when the instrument is measuring at none-zero energies. When the additional peak is on the edge of one of the fit intervals, the fit may fail. If this occurs, we exclude the interval containing the peak and use the fit function without the additional Gaussian on the other interval.

7.3 Results

Our investigation of the magnetic excitations near the masked FM QCP is divided in two parts. First we look at the temperature dependence of the FM and SDW magnetic excitations as we approach the FM QCP. Then we observe the dispersion along l and h deep in the FM state, at the FM-SDW transition, and at the SDW-paramagnetic (PM) transition as we approach the FM QCP.

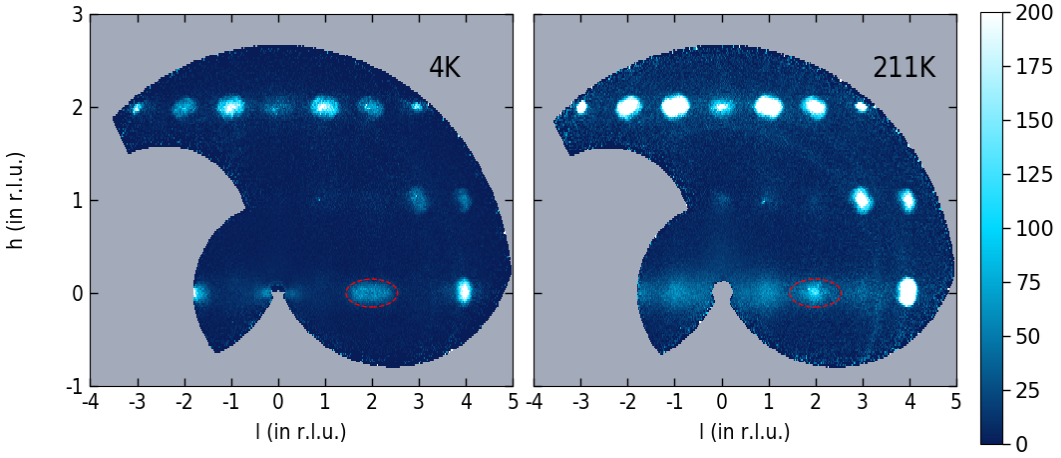

Figure 7.9: 2D cuts of LET data of Sample C in the h-l plane. The colour scale, which represents the intensity of scattered neutrons, is saturated at 200(a.u.) in order to make the magnon signals visible. The E_i of the neutrons is 9.5 meV, the h and l resolutions are 0.02 r.l.u., the third direction (η) normal to h and l is integrated over $[-0.1, 0.1]$ r.l.u. and the energy is integrated over $[0.5, 5]$ meV (cutting out most of the elastic line). The red dashed ellipse shows the position of magnons near $\boldsymbol{Q}_{\mathbf{FM}}$= (0 0 2) r.l.u..

Figure 7.9 shows two large range reciprocal space scans at T_{base}= 4 K and at high temperature T_{max} = 211 K measured in Sample C with LET. To see the weak magnon signals, the color scale on the right side is saturated at 200 (a.u.). By comparing Figure 7.9a with Figure 7.9b, we can distinguish phonons from magnons; the latter are weakened at high temperatures whereas phonons increase in intensity. In particular we see that the strongest observed magnons are at $\boldsymbol{Q}_{\mathbf{FM}}$= (0 0 2) (r.l.u.) (red dashed ellipses in Figure 7.9), which weaken and broaden at T_{max} = 211 K where a weak phonon becomes visible (Figure 7.9b).

Figure 7.10 gives the l-dispersion of the magnetic excitation centred on $\boldsymbol{Q}_{\mathbf{FM}}$= (0 0 2) (r.l.u.) at 4 K, 32 K, 38 and 211 K, measured in Sample C with LET. The latter results were obtained with 2D cuts along the (0 0 l) axis and the energy. At 4 K sample C lies deep in the FM state

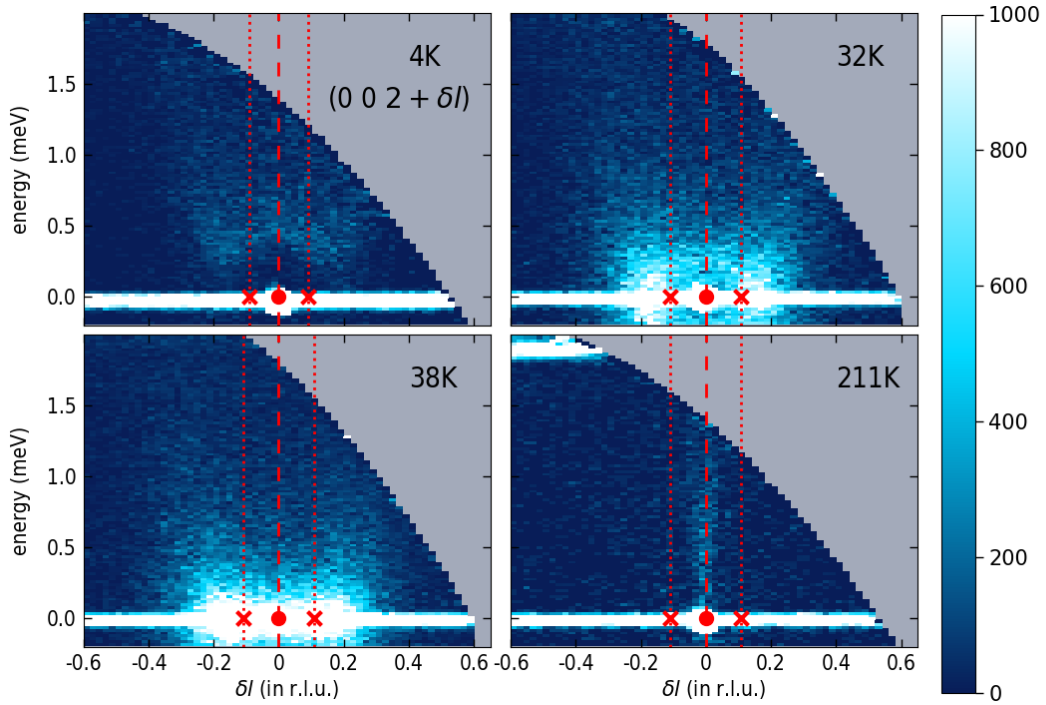

Figure 7.10: 2D cuts along the l direction and the energy showing the l dependence of the magnetic excitation energies near $\boldsymbol{Q}_{\mathbf{FM}}$= (0 0 2) (r.l.u.) at T_{base}= 4 K, near $\mathrm{T_{C_C}}$ at T = 32 K, near $\mathrm{T_{N_C}}$ at T = 38 K and at T_{max} = 211 K. $\boldsymbol{Q}_{\mathbf{FM}}$= (0 0 2) r.l.u. is given by the red dot and $\boldsymbol{Q}_{\mathbf{SDW}}$= (0 0 2.09) r.l.u. at 4 K, and $\boldsymbol{Q}_{\mathbf{SDW}}$= (0 0 2.109) r.l.u. at the other temperatures, is given by the red cross. The $\mathrm{E_i}$ of the neutrons is 2.48 meV, the l resolution is 0.02 r.l.u., h and η directions are integrated over $[-0.2, 0.2]$ r.l.u. and the energy resolution is 0.01 meV. The colour scale, which represents the intensity of scattered neutrons, is saturated at 1000(a.u.) in order to make the magnetic excitations visible. At T_{max}, the magnon dispersion disappears completely and a weak phonon becomes visible.

and we expect the excitation at $\boldsymbol{Q}_{\mathbf{FM}}$= (0 0 2) r.l.u. (red dot on the 0 meV axis in Figure 7.10) to have the lowest energy. However Figure 7.10 shows that the minimum energy is obtained for magnetic excitations near $\boldsymbol{Q}_{\mathbf{SDW}}$ (red crosses on the 0 meV axis in Figure 7.10) instead. We also see a that the energy gap observed in the FM state reduces as the temperature increases and disappears in the instrument resolution around $\boldsymbol{Q}_{\mathbf{SDW}}$ near $\mathrm{T_C}$. It is only near $\mathrm{T_N}$ that the gap seems to close at $\boldsymbol{Q}_{\mathbf{FM}}$. At 211 K the magnetic excitations have disappeared.

To characterise the l dependence of magnetic excitations measured with LET in Sample C, we make 1D cuts in the energy direction at different positions and temperatures, which are represented with red dots in Figure 7.9. The integration widths are δh = 0.04 r.l.u., $\delta\eta$ = 0.3 r.l.u., δl = 0.08 r.l.u. and δe = 0.04 meV.

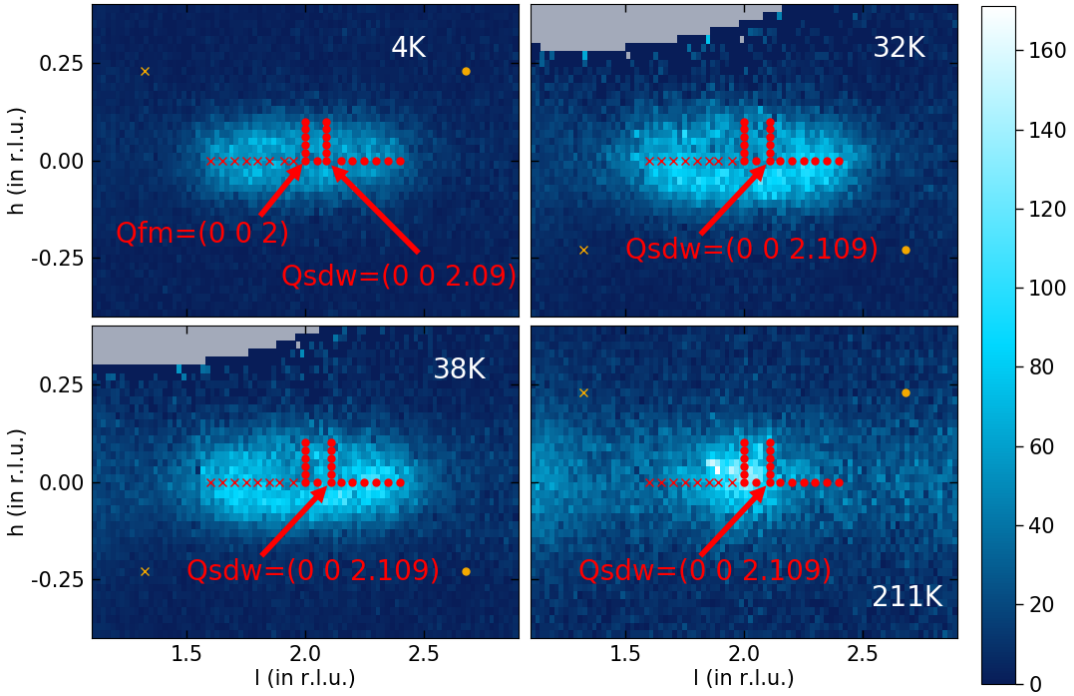

Figure 7.11: Positions that we analysed in Sample C from the data measured with LET at $T_{\text{base}}= 4K$, near $\text{T}_{\text{C}_\text{C}}$ at $T = 32\,\text{K}$, near $\text{T}_{\text{N}_\text{C}}$ at $T = 38\,\text{K}$ and at $T_{\text{max}} = 211\,\text{K}$. The E_i, in the figure, is $E_\text{i} = 9.5\,\text{meV}$, the h and l resolutions are 0.02 r.l.u., the third direction (η) normal to h and l is integrated over $[-0.1, 0.1]$ r.l.u. and the energy is integrated over $[0.5, 5]$ meV (cutting out most of the elastic line). The colour scale represents the intensity of scattered neutrons. The red dots are the different measured positions with E_i of 4.35 meV and the red crosses are the different measured positions with E_i of 2.48 meV and 1.6 meV. The yellow dot and cross give the positions of the measured background signals with E_is of 4.35 meV and 2.48 meV or 1.6 meV respectively.

Appendix A.2.2.1, Appendix A.2.2.2, Appendix A.2.2.3 and Appendix A.2.2.4 list all the positions and temperatures that we measured in Sample A, Sample B and Sample C, respectively, as well as the functions used to fit the excitation and the instruments used for the measurements.

Additional data, which was previously measured with Sample C at 4F2 by [70] and given in Table 7.3, has been included in the present study. However, the energy scans in the latter do not cover the elastic line and therefore correction for the energy shift cannot be implemented. To compensate for the unknown energy shift, we enhance the error of all the resonance energies

Table 7.3 Additional data of the temperature dependence of the excitations at $\boldsymbol{Q}_{\mathbf{FM}}$ measured with Sample C. *dho* or *sodho* near the *hkl*-positions indicates whether the data is fitted with a DHO or a SODHO function. This data was measured by J. Poulten at 4F2 [70].

SAMPLE C			
7.7 K	(0 0 2): dho	34.9 K	(0 0 2): dho
8.5 K	(0 0 2): dho	37.8 K	(0 0 2): odho
18.8 K	(0 0 2): dho	50.4 K	(0 0 2): odho
24.5 K	(0 0 2): dho	93.8 K	(0 0 2): odho
29.3 K	(0 0 2): dho	194.3 K	(0 0 2): odho
32.1 K	(0 0 2): sodho		

E_0 fitted within this data set with a systematic error equal to

$$\begin{aligned} \delta E_0 &= \overline{\delta E_{0,i}} + 3\sigma\left(\delta E_{0,i}\right) \\ &= 0.0258\,\text{meV}, \end{aligned} \tag{7.3.1}$$

where $\overline{\delta E_{0,i}}$ is the mean value and $\sigma\left(\delta E_{0,i}\right)$ the standard deviation of all energy shift corrections applied to measurements performed with 4F2 instrument. The error propagates to the E_0 dependent parameters Γ and A as:

$$\delta\Gamma = \Gamma\sqrt{2}\frac{\delta E_0}{E_0} \tag{7.3.2}$$

$$\delta A = A\frac{\delta\Gamma}{\Gamma}. \tag{7.3.3}$$

7.3.1 Temperature dependence of the magnetic excitations

First we look at the temperature dependence of the excitations at $\boldsymbol{Q}_{\mathbf{SDW}}$ and its evolution as we approach the FM QCP. Then we do the same with the excitations at $\boldsymbol{Q}_{\mathbf{FM}}$.

7.3.1.1 Temperature dependence of the excitations at $\boldsymbol{Q}_{\mathbf{SDW}}$

Figure 7.12 shows the temperature evolution of the magnetic excitations at $\boldsymbol{Q}_{\mathbf{SDW}}$= (0 0 2 + l_{SDW}) r.l.u. measured with Sample A, Sample B and Sample C. The figure also shows the fits of the magnetic excitations (solid lines) with either a DHO or an ODHO function.

In the FM state in Sample B and Sample C, the magnetic excitation has a distinct peak outside the elastic line and can be described with a resonance energy parameter. The latter gets softer as the temperature increases. At T_C and above, in the SDW and PM states, the

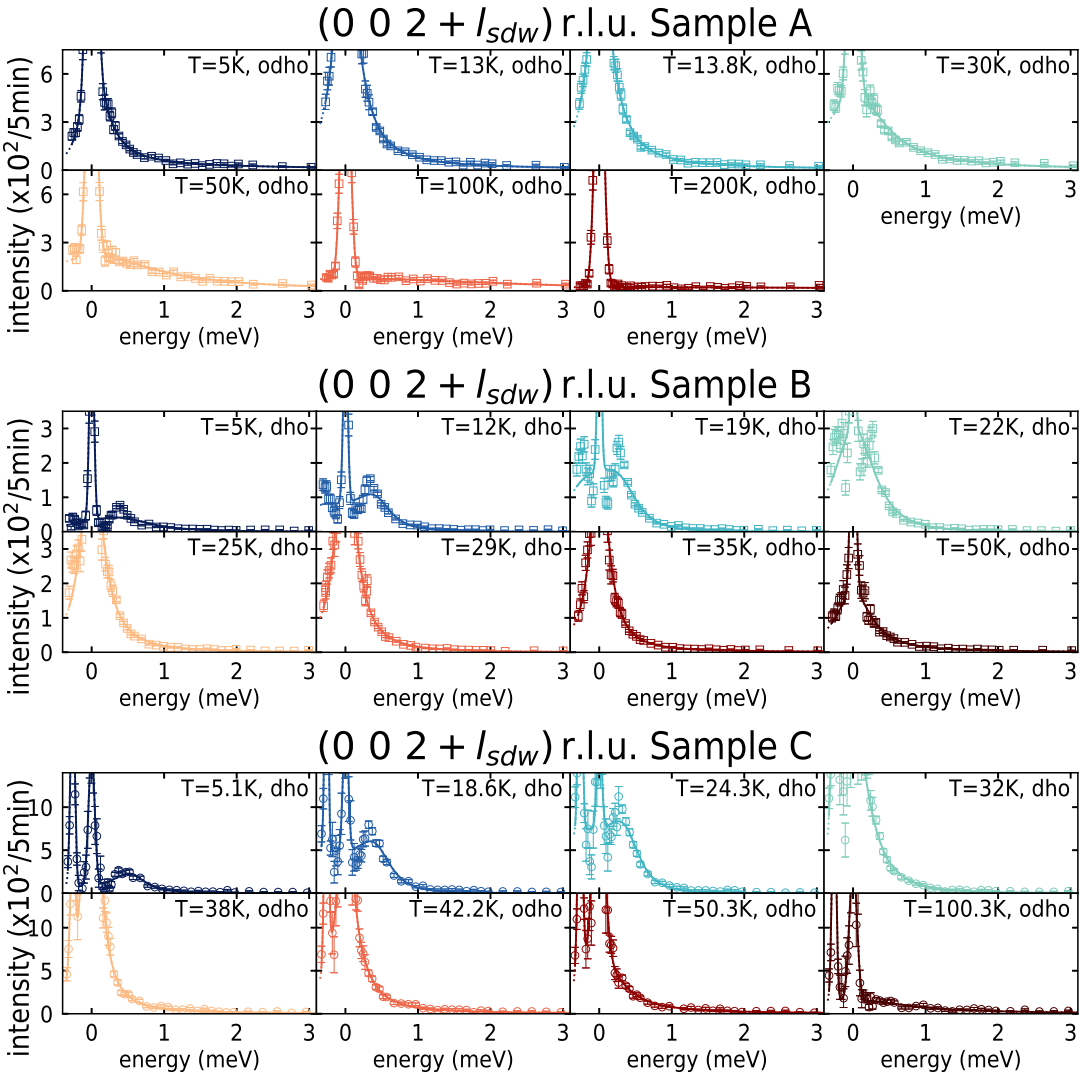

Figure 7.12: Temperature dependence of the excitations measured at $\boldsymbol{Q}_{\mathbf{SDW}}$= (0 0 2 + l_{SDW}) r.l.u. and fitted with the DHO or ODHO model (solid lines). Squares represent data measured with Panda and circles represent data measured with 4F2. Only a selection of scans is represented.

signal becomes quasi elastic in all three samples.

The fitted parameters describing the temperature dependence of the magnetic excitations measured at $\boldsymbol{Q}_{\mathbf{SDW}}$ in Sample A, Sample B and Sample C are shown in Figure 7.13. To simplify comparisons between the samples, the temperatures have an offset of T_{N} ($\mathrm{T_{N_A}}$= 13.4 K, $\mathrm{T_{N_B}}$= 30.5 K and $\mathrm{T_{N_C}}$= 36.9 K, as seen in Section 6.4). Figure 7.13a shows the temperature

dependence of the line width Γ and the resonance amplitude χ_0 of the excitations at $\boldsymbol{Q_{SDW}}$ in all three samples down to base temperature $T_{base} \approx 5\,\mathrm{K}$. χ_0 is normalised with the values at $\Delta T \approx 15\,\mathrm{K}$, which is the highest ΔT at which measurements have been performed in all three samples.

In the FM state, with increasing temperatures, the resonance amplitude increases slowly in Sample B and Sample C, whereas the line with and the resonance energy decrease. In Sample B, the maximum resonance amplitude $\chi_0 \approx 4$ is measured between 22 K and 29 K, the minimum line width $\Gamma \approx 0.1\,\mathrm{meV}$ is measured near $\mathrm{T_{N_B}}$ between 25 K and 35 K and the minimum resonance energy $E_0 \approx 0.5\,\mathrm{meV}$ is measured near $\mathrm{T_{C_B}}$ at 22.4 K. In Sample C, the maximum resonance amplitude $\chi_0 \approx 3$ is measured at 32 K, the minimum line width $\Gamma \approx 0.1\,\mathrm{meV}$ is measured between 32 K and 38 K, and the minimum resonance energy $E_0 \approx 0.5\,\mathrm{meV}$ is measured between 24.3 K and 32 K. The damping factor of the excitation at $\boldsymbol{Q_{SDW}}$ is fairly constant at $D \approx 1\,\mathrm{meV}$ and begins to increase steeply at $\mathrm{T_C}$. In Sample A, which shows no FM state in the measured temperature range, the maximum resonance amplitude $\chi_0 = 3.43$ is measured at 5 K and the minimum line width $\Gamma = 0.18\,\mathrm{meV}$ is measured at 5 K. Because of the absence of FM state, neither the resonance energy nor the damping factor have been fitted. The minimum line width measured in all three samples is within the resolution of the measuring instruments.

In the PM state, with increasing temperatures, the resonance amplitude decreases and the line width increases in all three samples. The decrease of the resonance amplitude is relatively slow, which is surprising as we would expect it to diverge at the second order SDW-PM phase transition. The big error bars for the line width at high temperatures are due to the weakness of the fitted signal.

7.3.1.2 Temperature dependence of the excitations at Q_{FM}

Figure 7.14 shows the temperature evolution of the FM signal measured at $\boldsymbol{Q_{SDW}} = (0\ 0\ 2)$ r.l.u. (only a selection among all the measured temperatures is represented). We fitted the FM magnetic excitations with either a DHO or an ODHO function (solid lines in the figure).

In the FM state in Sample B and Sample C, the magnetic excitation has a distinct peak outside the elastic line and can, again, be described with a resonance energy parameter. The latter gets softer and broadens as the temperature increases. At $\mathrm{T_C}$ and above, in the SDW and PM states, the signal becomes quasi elastic in all three samples.

At 8.5 K, 18.8 K, 24.5 K, 29.3 K, 32.1 K and 34.9 K, the additional data presented in Table 7.3 has not been measured over the elastic line and thus the tail of the latter cannot be fitted. At

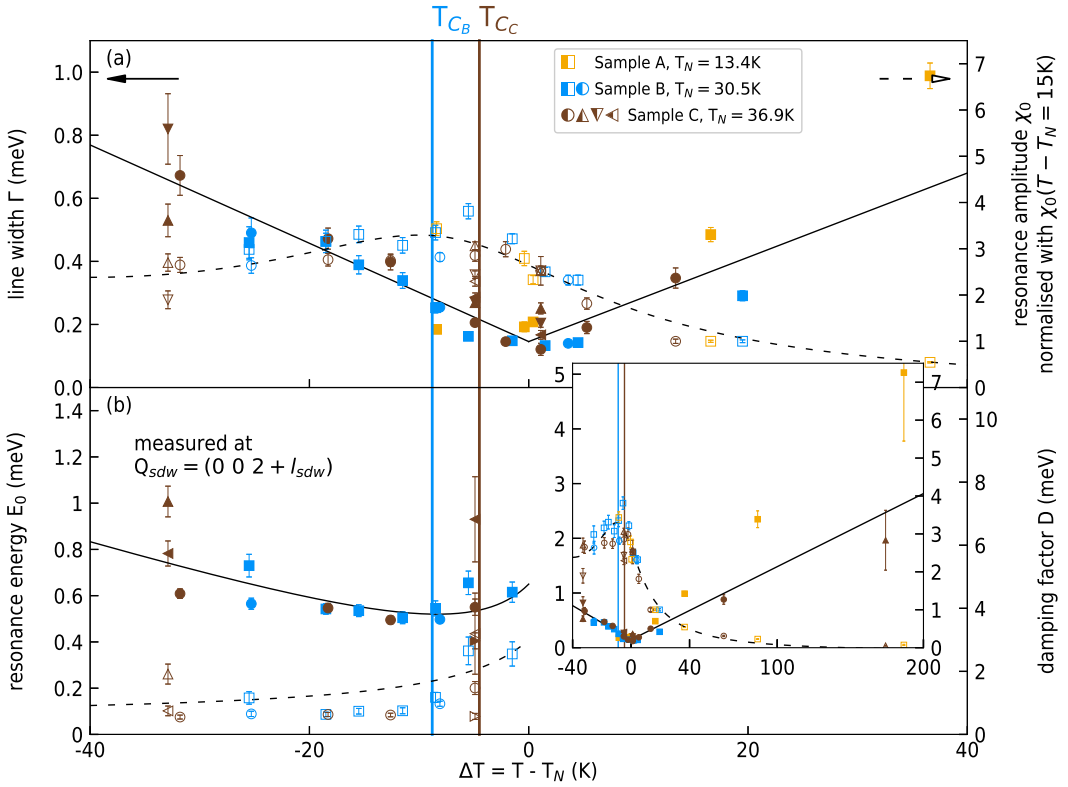

Figure 7.13: Temperature dependence of the parameters of the excitation at $\boldsymbol{Q_{SDW}}$= (0 0 2 + l_{SDW}) in Sample A (yellow), Sample B (blue) and Sample C (brown). To simplify comparison between samples, the data is plotted against $\Delta T = T - T_N$ (Néel temperatures are given in the legend). **(a)** shows the temperature dependence of the line width (full markers and solid lines) and the resonance amplitude (normalised with the value at $\Delta T \approx 15$ K) (empty markers and dashed lines). **(b)** shows the temperature dependence of the resonance energy (full markers and solid lines) and the damping factor (empty markers and dashed lines). Solid and dashed lines are guide to the eye. Squares represent data measured with Panda, circles represent data measured with 4F2 and triangles represent data measured with LET (up, down and left triangles for data measured with E_i of 4.35 meV, 2.48 meV and 1.6 meV respectively). The vertical solid lines labelled T_{C_B} and T_{C_C} indicate the Curie temperatures of Sample B (T_{C_B}= 21.7 K) and C (T_{C_C}= 32.4 K) respectively. The inset shows the line width and the resonance amplitude (a) of all measured temperatures. The large error-bar for Γ at ΔT = 186.2 K is because of the very weak signal intensity.

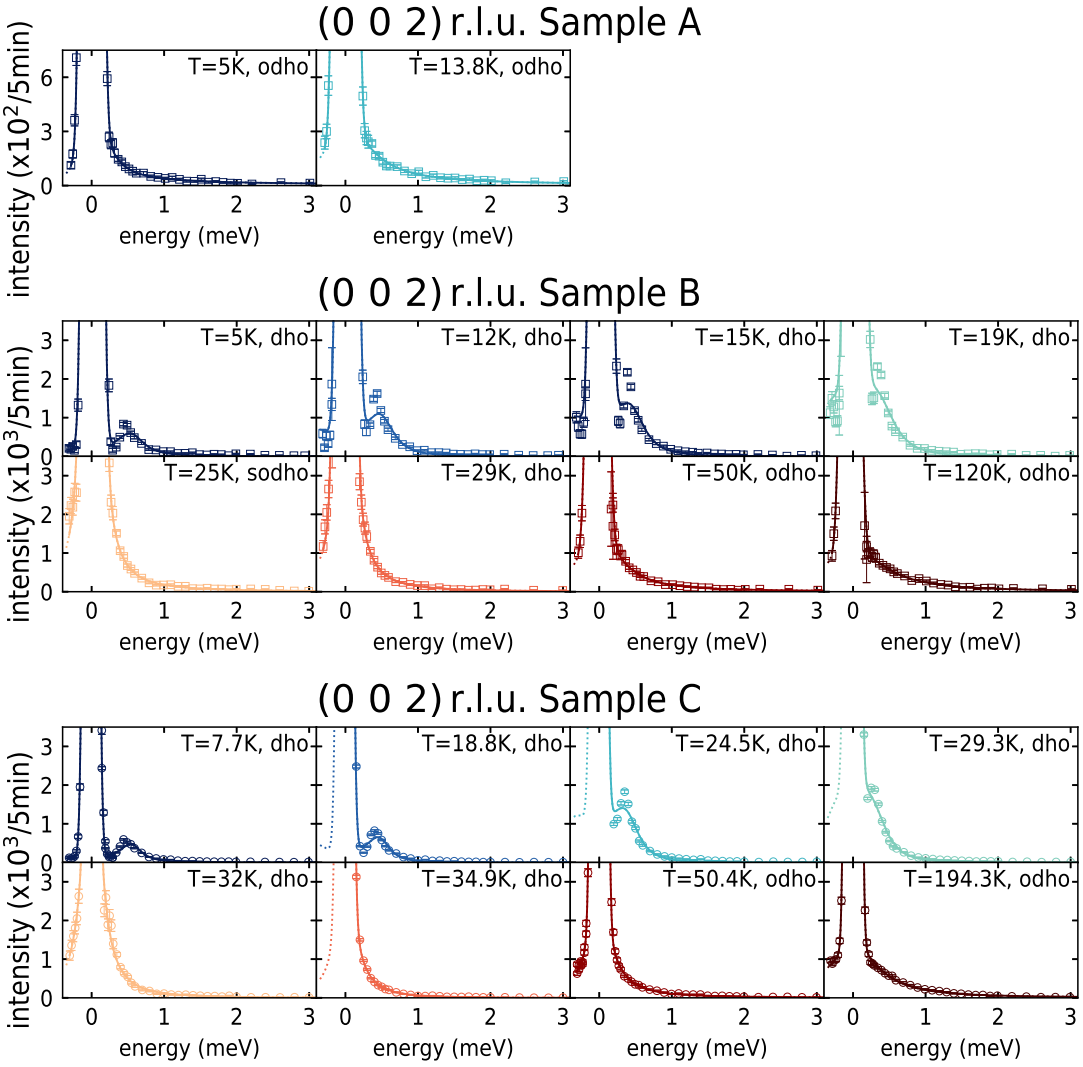

Figure 7.14: temperature dependence of the excitations measured at $\boldsymbol{Q}_{\mathbf{FM}}$= (0 0 2) r.l.u. and fitted with the DHO, ODHO or SODHO model (solid lines). The dotted line is the prolongation of the fitting curve over non-fitted energies. Squares represent data measured with Panda and circles represent data measured with 4F2. Only a selection of scans is represented. Apart from 32.0 K, all the data related to Sample C has been measured by J. Poulten and P. Niklowitz (see Table 7.3).

the other temperatures listed in Table 7.3, the energy scans include the elastic line. For those latter points the data is fitted on $[-0.12\,\text{meV}; 0.12\,\text{meV}]$. We use the Gaussian tail that fitted the elastic line of the 7.7 K data as a constant background in the fit function to fit the data

without the elastic line. To assess the validity of these fits, we also used this same *constant Gaussian background* fit function to fit the data measured at 37.8 K, 50.4 K, 93.8 K and 194.3 K, which include the elastic line, and we compare compare those results with the fits made with the *normal* function that includes a free Gaussian for the tail of elastic line.

Table 7.4 Fit parameters of the additional data given in Table 7.3. D, χ_0, E_0, Γ and A are the fit parameters of the different DHO functions used to fit the excitations. The *free* column indicates if the Gaussian in the fit function was free (meaning that the *normal* fit function was used to fit the data) or not (meaning that the *constant Gaussian background* function was used to fit the data).

T	$\boldsymbol{D}$	$\boldsymbol{\chi_0}$	$\boldsymbol{E_0}$	$\boldsymbol{\Gamma}$	$\boldsymbol{A}$	**free**
7.7 K	0.59(2)	166(9)	0.37(4)	0.93(7)	154(14)	yes
8.5 K	0.64(6)	200(18)	0.54(10)	0.75(15)	150(31)	no
18.8 K	0.52(4)	118(7)	0.39(5)	0.69(11)	82(13)	no
24.5 K	0.44(4)	221(12)	0.50(6)	0.44(7)	97(15)	no
29.3 K	0.42(4)	219(9)	0.61(6)	0.29(5)	64(9)	no
32.1 K	x	x	2.1(8)	x	32(2)	no
34.9 K	0.49(5)	159(7)	1.8(2)	0.14(2)	22(2)	no
37.8 K	x	437(239)	x	0.05(3)	22(1)	yes
	x	170(10)	x	0.16(2)	27(2)	no
50.4 K	x	110(4)	x	0.20(1)	22(1)	yes
	x	103(4)	x	0.23(2)	24(2)	no
93.8 K	x	53(1)	x	0.37(2)	20(1)	yes
	x	54(2)	x	0.35(2)	19(2)	no
194.3 K	x	33(1)	x	0.41(1)	14(1)	yes
	x	33(1)	x	0.42(3)	14(1)	no

Appendix A.2.3 shows the fits of the additional data, where the dotted curves indicate the non fitted energies. One sees the absence of elastic line on the negative energies at 8.5 K, 18.8 K, 24.5 K, 29.3 K, 32.1 K and 34.9 K, whereas it is present and fitted at the other temperatures. The black dashed line at 37.8 K, 50.4 K, 93.8 K and 194.3 K represents the fit made with the *constant Gaussian background* fit function, using the tail of the elastic line fitted at 7.7 K. The solid coloured lines, at these same temperatures, represent the fits made with the *normal* fit function, using a free Gaussian for the tail of the elastic line. Table 7.4 gives the fit parameters for the additional data. At 50.4 K and above, one sees that the parameters fitted with the two different functions agree within the errors. At 37.8 K, however, the fit parameters are very different, but the errors of the parameters fitted with the *normal* function are also very high. This is due to the proximity to the second order SDW-PM phase transition at this temperature. We also notice that the fitting errors are much smaller with the *constant Gaussian background*

fit function.

The fitted parameters describing the temperature dependence of the magnetic excitations measured at $\boldsymbol{Q}_{\mathbf{FM}}$ in Sample A, Sample B and Sample C are shown in Figure 7.15. The temperatures are shifted by T_C for Sample B and Sample C. For Sample A, we shift the data by $-2\,K$ such that the line widths overlap with the line widths measured in Sample B and Sample C. We refer to that temperature as $T_{C_A} = -2\,K$. In Figure 7.15a, the resonance amplitudes χ_0 measured in Sample B and in Sample C are normalised with the values measured at the highest temperature (120 K in Sample B and 211 K in Sample C). At these temperatures, χ_0 is almost constant, which justifies the normalisation.

In the FM state, with increasing temperatures, the resonance amplitude and the damping factor remain fairly constant in Sample B and Sample C until it diverges around T_C. The line with and the resonance energy both decrease, the former quickly and the latter slowly. In Sample B, the maximum resonance amplitude $\chi_0 \approx 9$ is measured in the SDW state at 25 K, the minimum line width $\Gamma \approx 0.1\,meV$ is measured between 25 K and 29 K, also in the SDW state, and the minimum resonance energy $E_0 \approx 0.5\,meV$ is measured near T_{C_B} at between 19 K and 25 K. In Sample C, the maximum resonance amplitude $\chi_0 \approx 13$ is measured near T_{C_C} at 32 K, the minimum line width $\Gamma = 0.12\,meV$ is measured near the SDW state at 32 K, and the minimum resonance energy $E_0 \approx 0.4\,meV$ is measured at the same temperature. The damping factor of the excitation at $\boldsymbol{Q}_{\mathbf{FM}}$ is fairly constant at $D \approx 1\,meV$ and diverges in the SDW state. In Sample A, the maximum resonance amplitude $\chi_0 = 7.1$ and the minimum line width $\Gamma = 0.15\,meV$ are measured at 5 K, the lowest measured temperature. Again, the minimum line width measured in all three samples is within the resolution of the measuring instruments.

In the PM state, with increasing temperatures, the resonance amplitude decreases and the line width increases in all three samples. Although the error bars are significant, one sees an enhancement of the resonance energy near the FM-SDW phase transition in Sample B and in Sample C.

7.3.2 l dependence of the magnetic excitations

We measured the l dependence and h dependence of the magnetic excitations at base, Curie and Néel temperatures. These results are presented in the following sections.

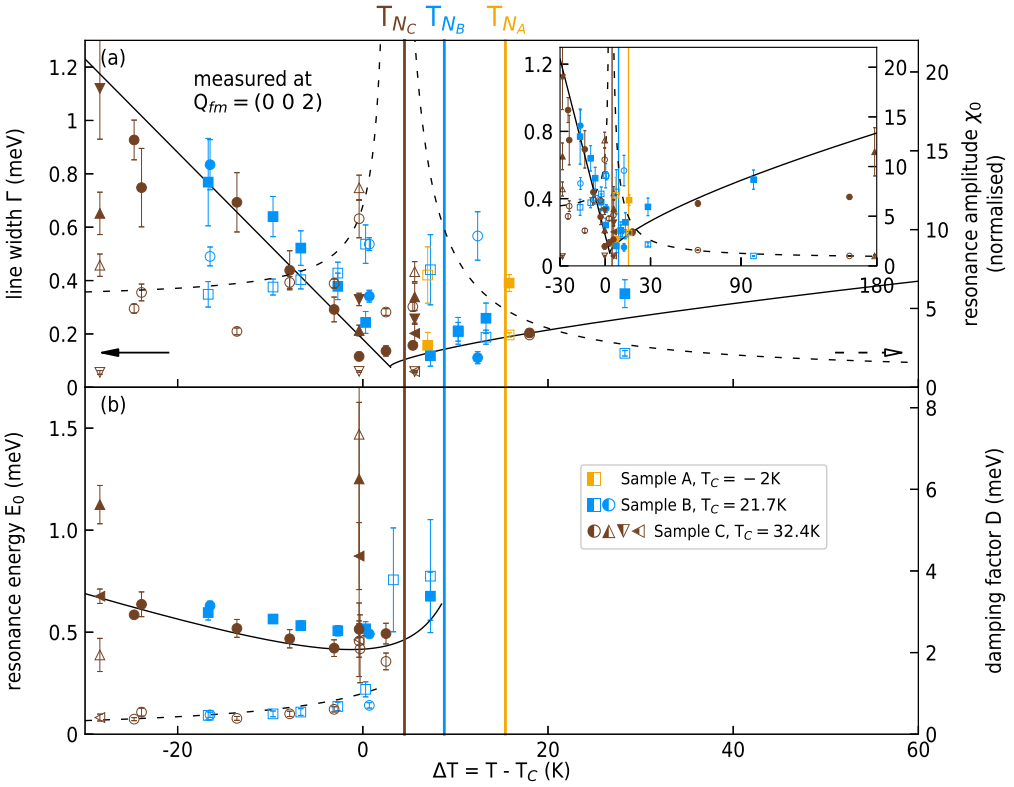

Figure 7.15: Temperature dependence of the parameters of the excitations at $\boldsymbol{Q}_{\mathbf{FM}}$= (0 0 2) r.l.u. in samples A (yellow), B (blue) and C (brown). To simplify comparison between samples, the data is plotted against $\Delta T = T - \mathrm{T_C}$ (Curie temperatures are given in the legend). Data points represented with brown circles, except at $\Delta T = -0.2\,\mathrm{K}$, correspond the additional data measured by J. Poulten [70] and given in Table 7.3. **(a)** shows the temperature dependence of the line width (full markers and solid lines) and the normalised resonance amplitude (empty markers and dashed lines). For samples B and C, the latter is normalised with the value at the highest measured temperature. For Sample A the normalisation factor is such that χ_0 at 13.8 K (the highest measured temperature with Sample A) equals χ_0 in Sample C at 50.4 K (the closest data point). **(b)** shows the temperature dependence of the resonance energy (full markers and solid lines) and the damping factor (empty markers and dashed lines). Solid and dashed lines are guide to the eye. Squares represent data measured with Panda, circles represent data measured with 4F2 and triangles represent data measured with LET (up, down and left triangles for data measured with $\mathrm{E_i}$ of 4.35 meV, 2.48 meV and 1.6 meV respectively). The vertical solid lines labeled $\mathrm{T_{N_A}}$, $\mathrm{T_{N_B}}$ and $\mathrm{T_{N_C}}$ indicate the Néel temperatures of Sample A ($\mathrm{T_{N_A}}$= 13.4 K), B ($\mathrm{T_{N_A}}$= 30.5 K) and C ($\mathrm{T_{N_C}}$= 36.9 K) respectively. The inset shows Γ and χ_0 over the whole measured temperature range.

7.3.2.1 l dependence in the FM state

The purpose of these measurements is to look at the low energy magnetic excitations deep in the FM state. These excitations have been measured in Sample B at 5.2 K and in Sample C

at 4 K. Sample A, however, was still in the SDW state at the lowest measured temperature of 5 K and results will be presented in a later section. Figure 7.16 shows the signal measured in Sample B and in Sample C.

δl is defined as $\delta l = Q_l - 2$ r.l.u., where Q_l is the amplitude along l of a reciprocal lattice vector. In both samples, the signal forms a distinct peak, which is shifted to lower energies as δl increases until $\delta l = 0.2$ r.l.u.. The intensity of the signal decreases and its width increases. As $|\delta l|$ increases further, the signal broadens and shifts to higher energies, while its intensity decreases, in both samples.

Figure 7.17 shows the l dependence of the parameters of the DHO or ODHO models obtained by fitting the magnetic excitations in Sample B and Sample C at base temperature (Figure 7.16). The resonance amplitude is normalised to the value measured at $\boldsymbol{Q}_{\mathbf{FM}}$= (0 0 2) r.l.u. for both samples.

As δl increases until $\delta l = 0.2$ r.l.u. in Sample B and until $\delta l = 0.15$ r.l.u. in Sample C, the resonance amplitudes increase until maximum values of $\chi_0 \approx 1.6$ in Sample B and $\chi_0 \approx 1.3$ in Sample C. The line widths decrease continuously until minimum values of $\Gamma \approx 0.3$ meV in Sample B and $\Gamma \approx 0.5$ meV in Sample C. In a similar fashion, the resonance energies decrease slowly towards a minimum of $E_0 \approx 0.5$ meV in Sample B and $E_0 \approx 0.9$ meV in Sample C measured at $\delta l = 0.15$ r.l.u.. The damping factor increases slowly from a minimum value of $D = 0.48$ meV in Sample B, whereas it remains fairly constant at $D \approx 2$ meV in Sample C. When δl increases further, the resonance amplitudes decrease, and the line widths increase, rapidly in both samples. The resonance energies increase in both samples, as well as the damping factor in Sample B, whereas the damping factor in Sample C remains constant.

7.3.2.2 l dependence near Curie temperature

Here we look at the magnetic excitations near the FM-SDW transition. Figure 7.18 shows the signals measured in Sample B at 22.4 K and in Sample C at 32 K. $|\delta l|$, which is the absolute value of δl, is convenient to use for comparing the data, since LET data with E_is of 1.6 meV and 2.48 meV was measured at $Q \leq 2$ r.l.u., whereas $Q \geq 2$ r.l.u. for all other data.

As $|\delta l|$ increases, the signal moves to lower energies in Sample B, with the peak of the signal disappears in the quasi-elastic scattering at $|\delta l| = 0.15$ r.l.u., and the intensity of the signal increases. In Sample C, the peak of the signal remains at the same position until $|\delta l| = 0.15$ r.l.u., and the intensity of the signal increases. When $|\delta l|$ increases further, the signal moves to higher energies and broadens in both samples.

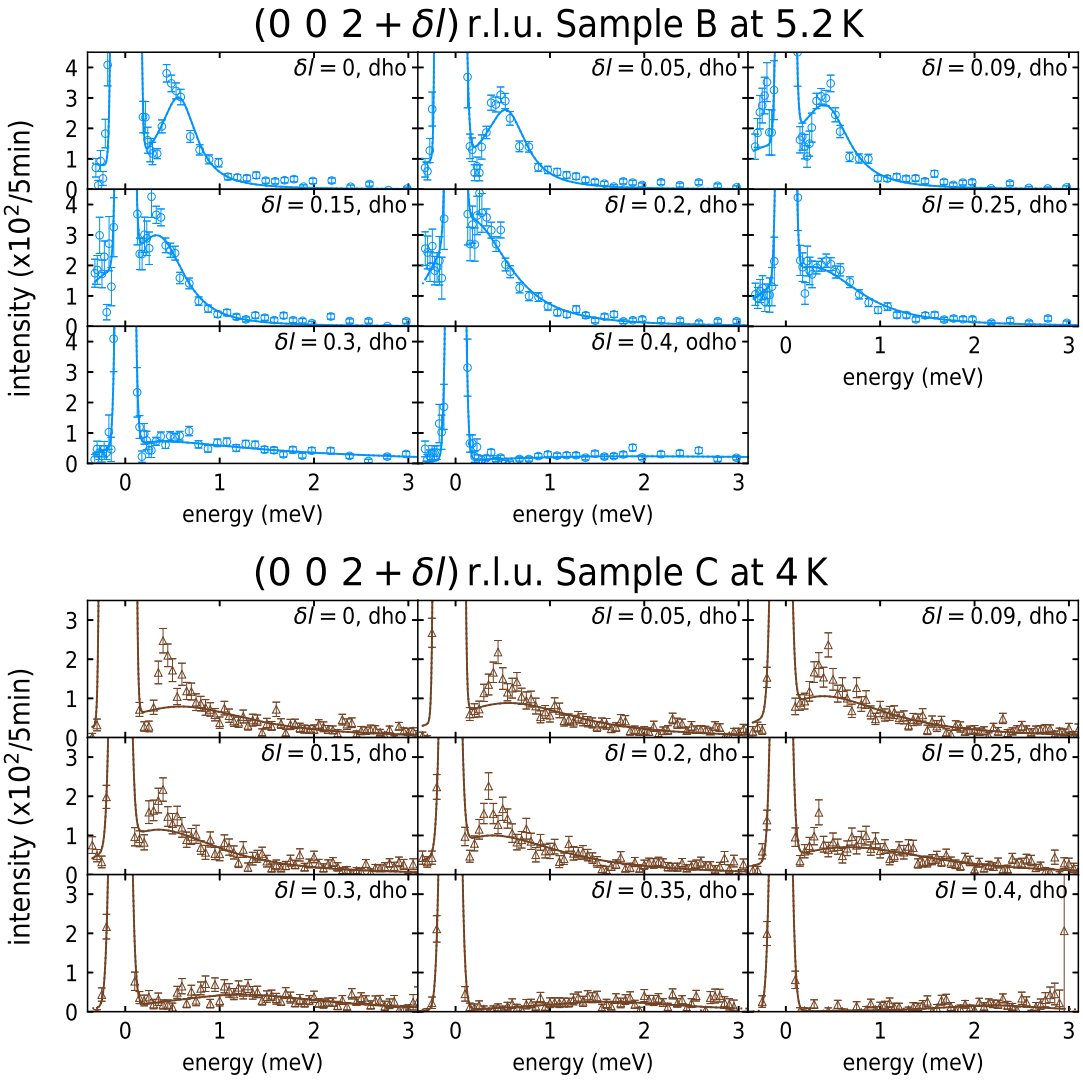

Figure 7.16: l dependence of the excitations measured deep in the FM state in Sample B and Sample C, and fitted with the DHO or ODHO model (solid lines). Circles represent data measured with 4F2 and triangles represent data measured with LET.

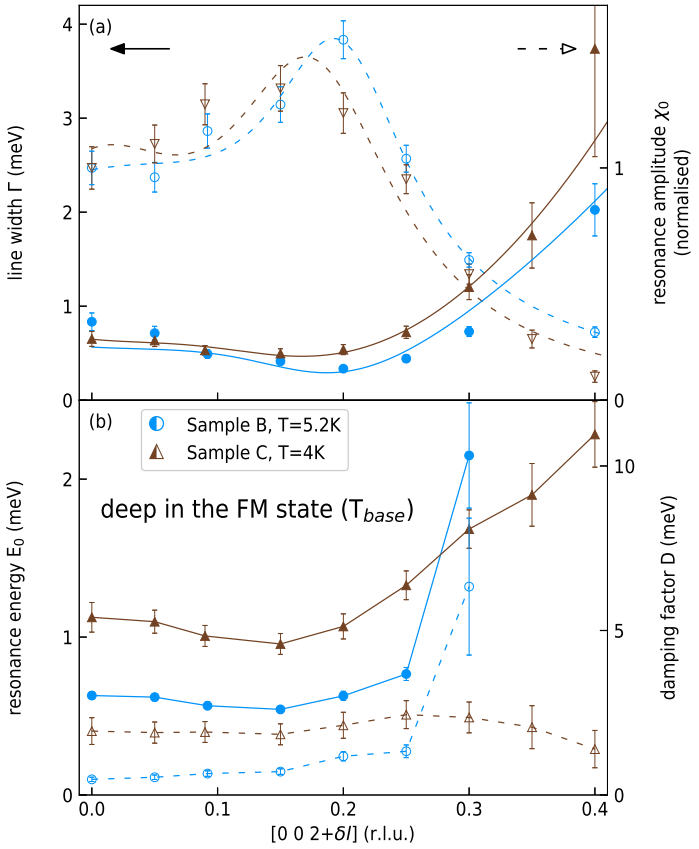

Figure 7.17: Parameters of the DHO model used to fit the l dependence of the magnetic excitations at base temperature in samples B (blue) and C (brown). **(a)** shows the line width (full markers and solid lines) and the resonance amplitude (empty markers and dashed lines). **(b)** shows the resonance energy (full markers and solid lines) and the damping factor (empty markers and dashed lines). The resonance amplitude is normalised to its value measured at $l = 2$ r.l.u.. Solid and dashed lines are guides to the eye. Circles represent data measured with 4F2 and triangles represent data measured with LET.

Figure 7.19 shows the l dependence of the parameters of the DHO or ODHO models obtained by fitting the magnetic excitations in Sample B and Sample C near the Curie temperature (Figure 7.18). The resonance amplitude is normalised to the value measured at $\boldsymbol{Q}_{\mathbf{FM}} = (0\ 0\ 2)$ r.l.u. for both samples.

As $|\delta l|$ increase until $|\delta l| = 0.15$ r.l.u., the resonance amplitudes increase until their maxima: in Sample B, the maximum is $\chi_0 \approx 1.5$ and in Sample C $\chi_0 \approx 1.6$. The line width decreases continuously in Sample B from $\Gamma = 0.34$ meV (above the resolution of the instrument) to a minimum value of $\Gamma = 0.17$ meV (below the resolution of the instrument). In Sample C, the

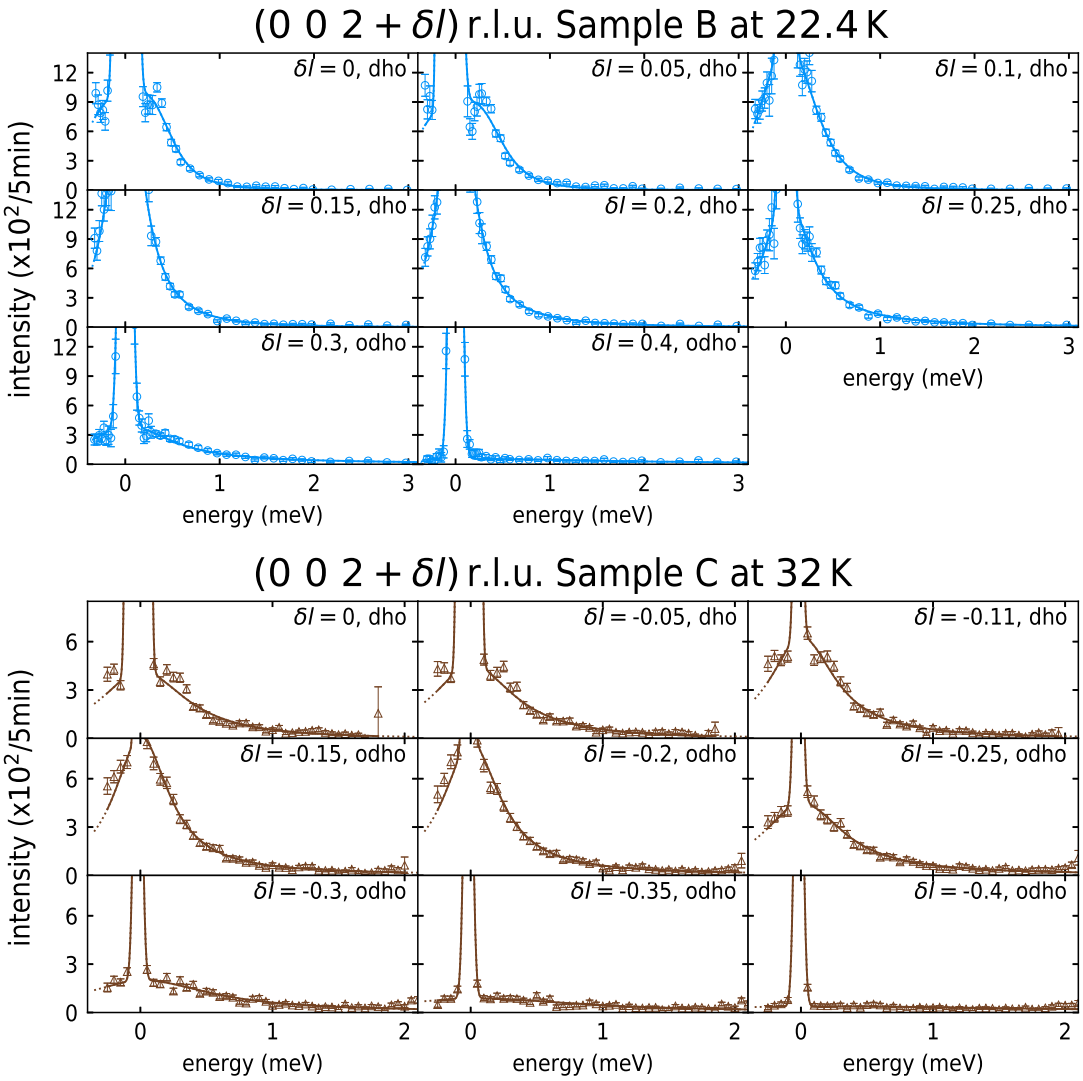

Figure 7.18: l dependence of the excitations measured near the Curie temperature and fitted with the DHO or ODHO model (solid lines). The dotted lines are extensions of the fits over non-fitted energies. Circles represent data measured with 4F2 and triangles represent data measured with LET.

LET data shows that the line width remains fairly constant at $\Gamma \approx 0.3\,\text{meV}$, with, however, a weak minimum of $\Gamma = 0.24\,\text{meV}$ at $\delta l = -0.15\,\text{r.l.u.}$ for $E_\text{i} = 1.6\,\text{meV}$ or $E_\text{i} = 2.48\,\text{meV}$, whereas the data measured with 4F2 gives a constant line width of $\Gamma \approx 0.13\,\text{meV}$, within the resolution of the instrument. The jump at $\delta l = 0.05\,\text{r.l.u.}$ in the line width values measured in Sample C with 4F2 remains within the resolution of the instrument and is therefore considered irrelevant.

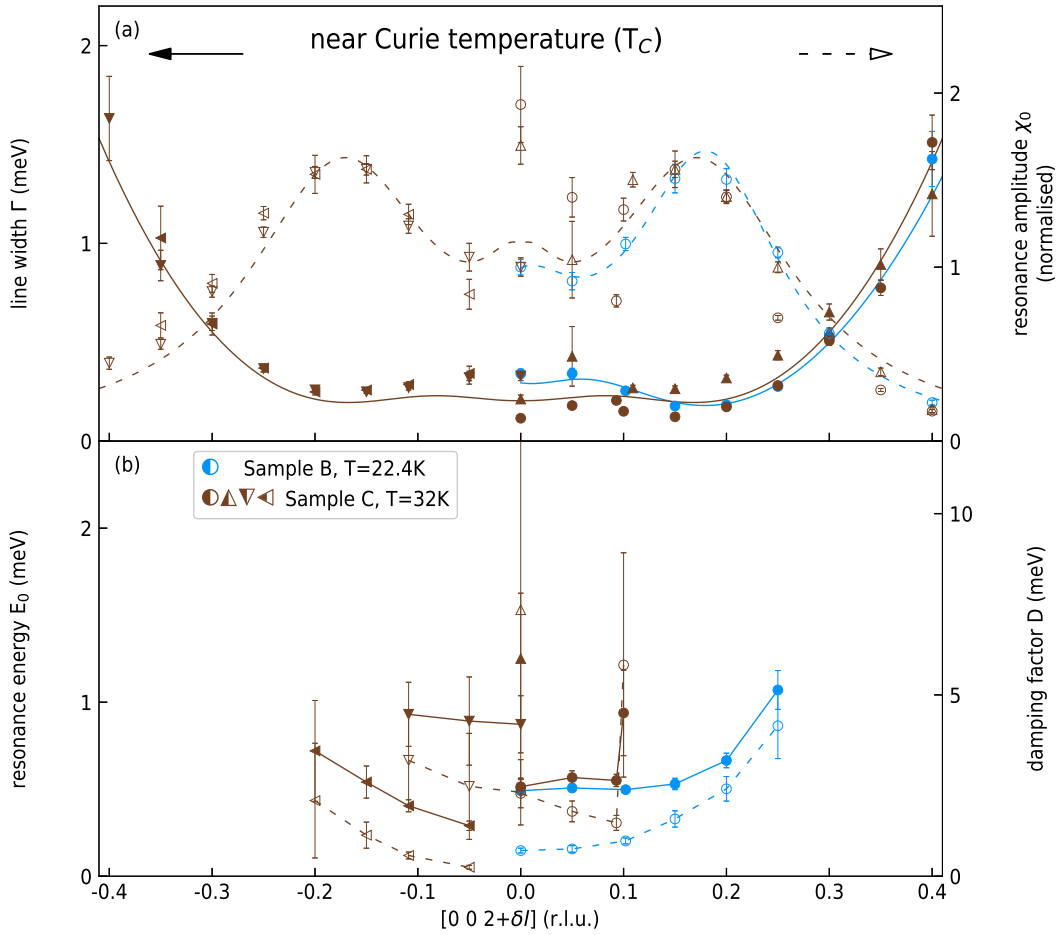

Figure 7.19: Parameters of the DHO model used to fit the l dependence of the magnetic excitations near the Curie temperature in samples B (blue) and C (brown). **(a)** shows the of the line width (full markers and solid lines) and the resonance amplitude (empty markers and dashed lines). **(b)** shows the resonance energy (full markers and solid lines) and the damping factor (empty markers and dashed lines). For Sample B the resonance amplitude is normalised to the value measured at $l = 2$ r.l.u.. For Sample C, we first multiplied the resonance amplitude of the data measured on 4F2 and on LET with E_is of 4.35 meV and 1.6 meV by $\chi_{4F2}(l = 2.15)/\chi_{LET,2.48}(l = 1.85)$, $\chi_{LET,4.35}(l = 2.15)/\chi_{LET,2.48}(l = 1.85)$ and $\chi_{LET,1.6}(l = 1.85)/\chi_{LET,2.48}(l = 1.85)$ respectively, and then we normalised the data to $\chi_{LET,2.48}(l = 2)$. Solid and dashed lines are guides to the eye. Circles represent data measured with 4F2 and triangles represent data measured with LET (up, down and left triangles for data measured with E_is of 4.35 meV, 2.48 meV and 1.6 meV respectively).

The resonance energy remains fairly constant at $E_0 \approx 0.5\,\text{meV}$ in Sample B and in Sample C measured with 4F2. LET data with E_i of 2.48 meV also suggests a rather constant resonance energy of $E_0 \approx 1.0\,\text{meV}$, but with significant error bars, whereas data measured with E_i of 1.6 meV indicates an increase of the resonance energy from a minimum $E_0 \approx 0.28\,\text{meV}$ measured at $\delta l = -0.05\,\text{r.l.u.}$ (the fit at $\delta l = 0.0\,\text{r.l.u.}$ was unsuccessful, because the magnetic excitation was outside of the scanned energy range), which is above the resolution of the instrument. The damping factor increases with $|\delta l|$. In Sample B the minimum $D = 0.71\,\text{meV}$ was measured at $|\delta l| = 0.0\,\text{r.l.u.}$ and in Sample C the minimum $D = 0.24\,\text{meV}$ was measured at $\delta l = -0.05\,\text{r.l.u.}$ with E_i of 1.6 meV. When $|\delta l| > 0.15\,\text{r.l.u.}$ and increasing, the resonance amplitudes decrease quickly and the line widths increase rapidly in both samples. The resonance energies and the damping factors follow a similar rapid increase.

7.3.2.3 l dependence in the SDW state

This section presents the results of the low energy magnetic excitations observed in the SDW state. Only Sample A has been measured in this state at 5 K and Figure 7.20 shows the scans.

The signal is included in the quasi-elastic scattering and its intensity and width increase as $|\delta l|$ increases until $|\delta l| = 0.2\,\text{r.l.u.}$. When $|\delta l|$ increases further, the signal broadens and shifts to higher energies, while its intensity decreases.

Figure 7.21 shows the l dependence of the parameters of the ODHO model obtained by fitting the signals presented in Figure 7.20. The resonance amplitude is normalised to the value measure at $\boldsymbol{Q}_{\mathbf{FM}} = (0\ 0\ 2)\,\text{r.l.u.}$.

As $|\delta l|$ increase until $|\delta l| = 0.2\,\text{r.l.u.}$, the resonance amplitude first decreases to a local minimum of $\chi_0 \approx 0.9$ at $|\delta l| = 0.1\,\text{r.l.u.}$ before increasing to its maximum value $\chi_0 \approx 1.7$ at $|\delta l| = 0.2\,\text{r.l.u.}$. The line width is relatively constant and minimum with $\Gamma \approx 0.17\,\text{meV}$, which is within the resolution of the instrument.

7.3.2.4 l dependence near the Néel temperature

Now we look at the magnetic excitations near the SDW-PM transition. Figure 7.22 shows the signals measured in Sample A at 13.8 K, in Sample B at 34.1 K[6] and in Sample C at 38 K.

In all three samples, the excitations at $\delta l = 0\,\text{r.l.u.}$ are within the energy resolution of the instrument and lead to quasi-elastic scattering. As δl increases, the intensities of the signals

[6]The temperature at which we measured Sample B is slightly higher than the bulk Néel temperature $T_{N_B} = 30.5\,\text{K}$. The reason is that the inelastic experiment was prior to the elastic scattering measurements and we only had an estimate of the real bulk Néel temperature in Sample B.

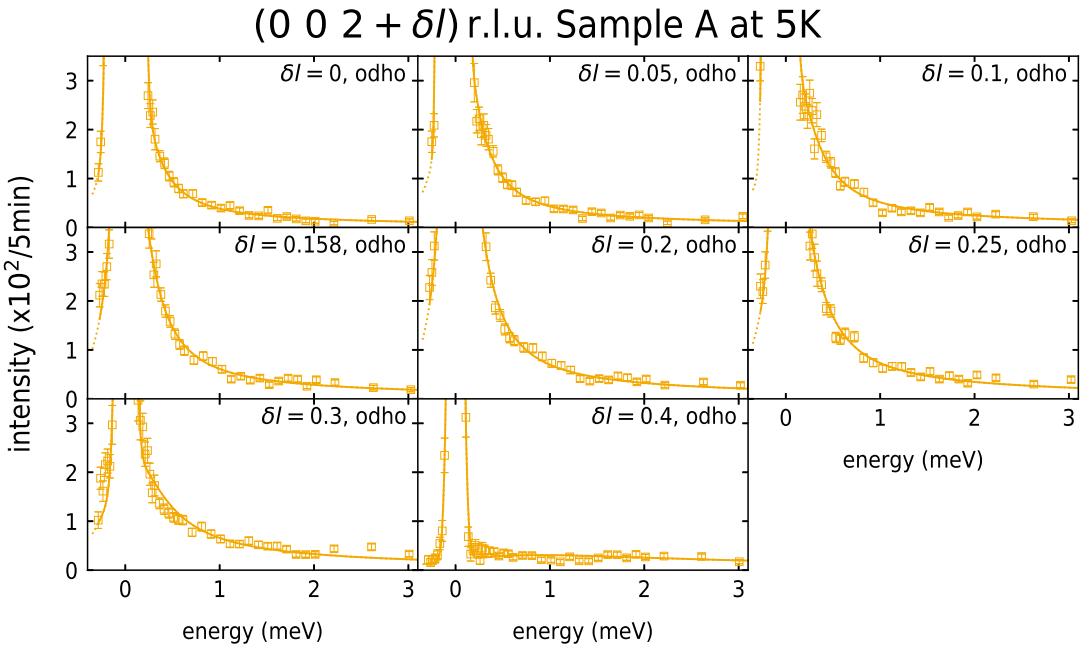

Figure 7.20: l dependence of the excitations measured in the SDW state in Sample A, and fitted with the ODHO model (solid lines). All the data has been measured with Panda.

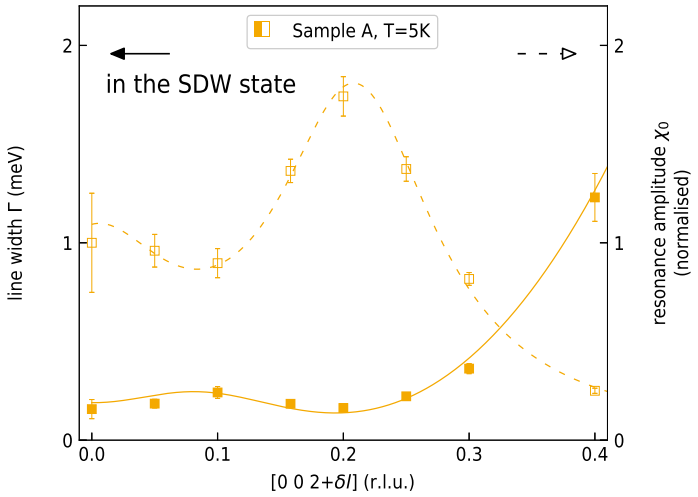

Figure 7.21: Parameters of the ODHO model used to fit the l dependence of the magnetic excitations the SDW state in Sample A. The line width on the left (full markers and solid lines) and the resonance amplitude on the right (empty markers and dashed lines). The resonance amplitude is normalised to its value measured at $l = 2$ r.l.u.. Solid and dashed lines are guides to the eye. All the data was measured with Panda.

increase in all samples until $\delta l = 0.2$ r.l.u., and then the signals loose their intensities, broaden and move to higher energies.

Figure 7.23 shows the l dependence of the parameters of the ODHO models obtained by fitting the magnetic excitations in Sample A, Sample B and Sample C near the Neél temperature (Figure 7.22). The resonance amplitude is normalised to the value measured at $\boldsymbol{Q}_{\mathbf{FM}}$= (0 0 2) r.l.u. for the three samples.

As $|\delta l|$ increase until $|\delta l| = 0.15$ r.l.u., the resonance amplitudes increase until maximum values of $\chi_0 \approx 1.9$ in Sample A and $\chi_0 \approx 1.3$ in Sample C. In Sample B, the resonance amplitude remains constant at $\chi_0 \approx 1$ with a dip to $\chi_0 \approx 0.7$ around $\delta l = 0.05$ r.l.u.. The line widths is minimum at $\delta l = 0.151$ r.l.u. in Sample A with $\Gamma \approx 0.2$ meV, whereas it remains fairly constant at $\Gamma \approx 0.2$ meV in Sample C with E_i of 1.6 meV and 2.48 meV, and at $\chi_0 \approx 0.3$ in Sample C with E_i of 4.35 meV. In Sample B, the line remains within the resolution of the instrument (0.22 meV) for $\delta l \leq 0.15$ r.l.u.. When $|\delta l| > 0.15$ r.l.u. and increasing, the resonance amplitudes decrease quickly and the line widths increase rapidly in all three samples.

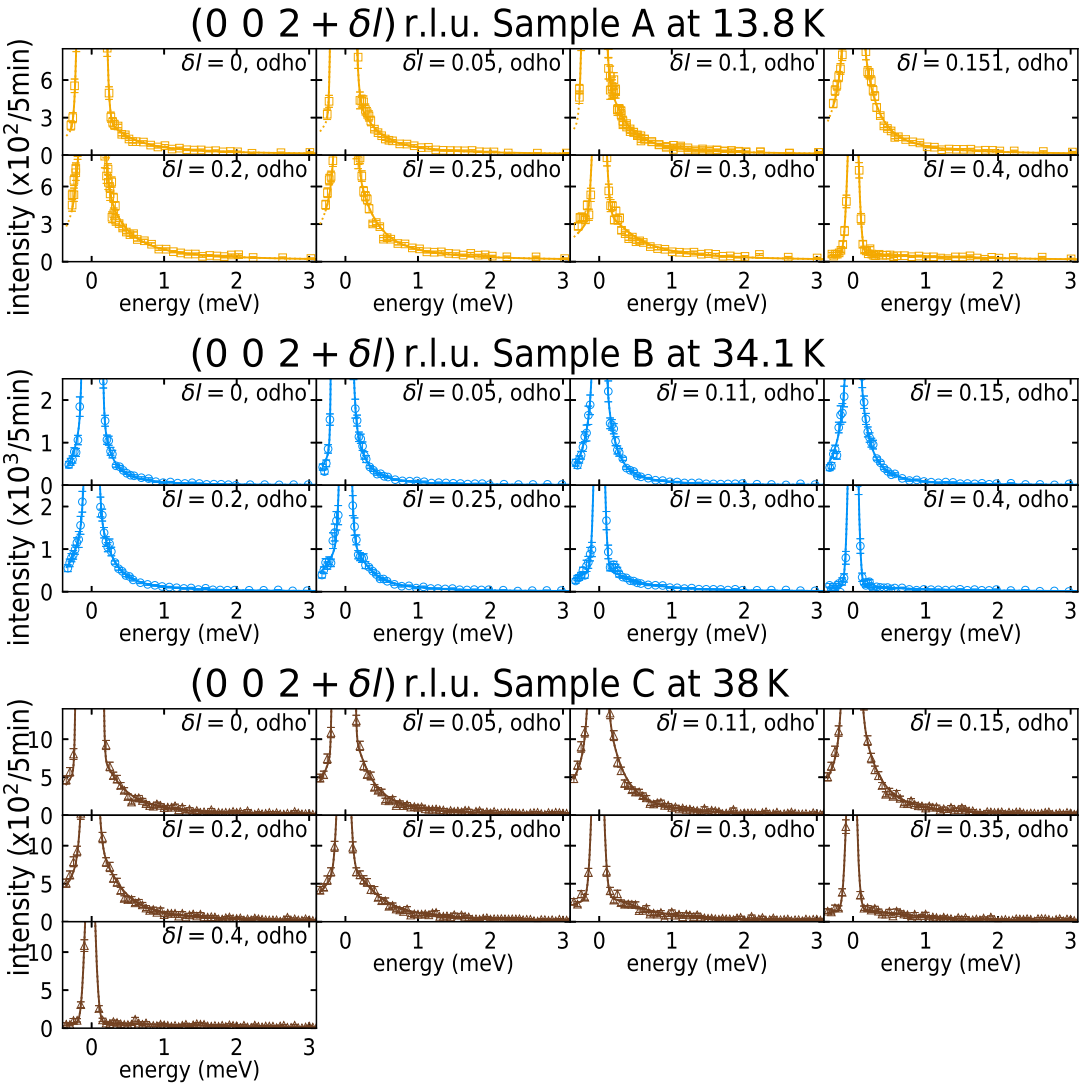

Figure 7.22: l dependence of the excitations measured near the Néel temperature and fitted with the DHO or ODHO model (solid lines). Squares represent data measured with Panda, circles represent data measured with 4F2 and triangles represent data measured with LET.

7.3.3 h dependence of the magnetic excitations

We also measured the h dispersion of the magnetic excitations at $l = 2$ r.l.u. in samples B and C and at $l = 2 + l_{\mathrm{SDW}}$ r.l.u. in samples A, B and C. These measurements show all very similar results and therefore only the h dispersion at $l = 2 + l_{\mathrm{SDW}}$ r.l.u. in Sample C at base, Curie and Néel temperatures shown in Figure 7.24 will be presented. The other fit parameters are

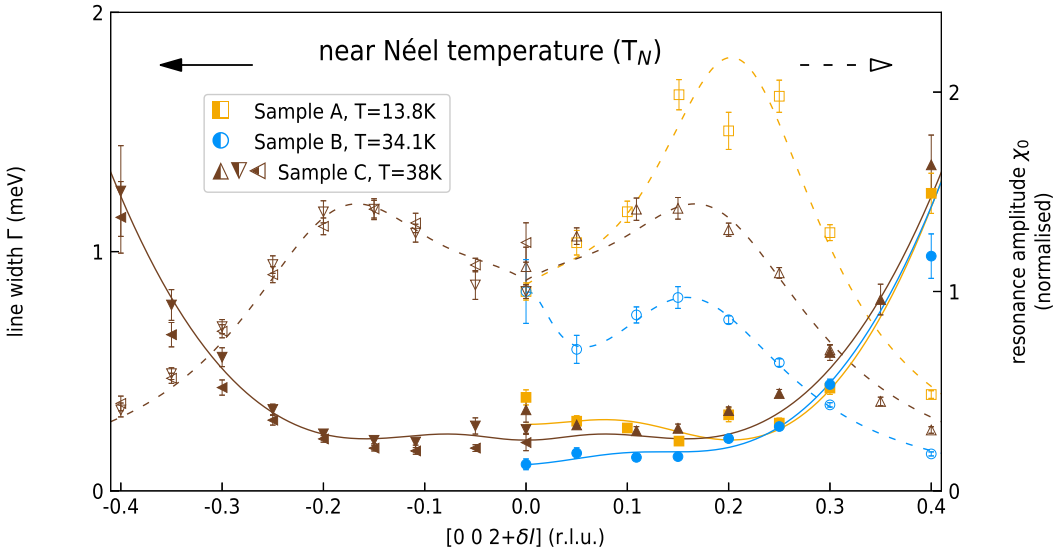

Figure 7.23: Parameters of the ODHO model used to fit the l dependence of the magnetic excitations near the Néel temperature in samples A (yellow), B (blue) and C (brown). **(a)** shows the of the line width (full markers and solid lines) and the resonance amplitude (empty markers and dashed lines). For samples A and B the resonance amplitude is normalised to their value measured at $l = 2$ r.l.u. ($\chi_A(l = 2)$ and $\chi_B(l = 2)$). For Sample C, we first multiplied the resonance amplitude of LET data measured with E_is of 4.35 meV and at 1.6 meV by $\chi_{LET,4.35}(l = 2.15)/\chi_{LET,2.48}(l = 1.85)$ and $\chi_{LET,1.6}(1.85)/\chi_{LET,2.48}(l = 1.85)$ respectively, and then we normalised the data to $\chi_{LET,2.48}(l = 2)$. Solid and dashed lines are guides to the eye. Squares represent data measured with Panda, circles represent data measured with 4F2 and triangles represent data measured with LET (up, down and left triangles for data measured with E_is of 4.35 meV, 2.48 meV and 1.6 meV respectively).

given in appendix A.2.4. δh is defined as $\delta h = Q_h - 0$ r.l.u. $(= Q_h)$, where Q_h is the amplitude along h of a reciprocal lattice vector.

Only the data measured at 4 K shows peaks in the signals within the fitted range and thus separated from the elastic line. At 32 K and 38 K the peaks of the signals are within the resolution of the instrument. At all the measured temperatures, the signal decreases in intensity, broadens and moves to higher energies as δh increases.

Figure 7.25 shows the h dependence of the parameters of the DHO or ODHO models obtained by fitting the magnetic excitations in Sample C at base temperature, near Curie and Neél temperatures (Figure 7.24) and one point has also been measured at 211 K. The resonance amplitude is normalised to the value measured at $\boldsymbol{Q_{FM}} = (0\ 0\ 2 + l_{SDW})$ r.l.u..

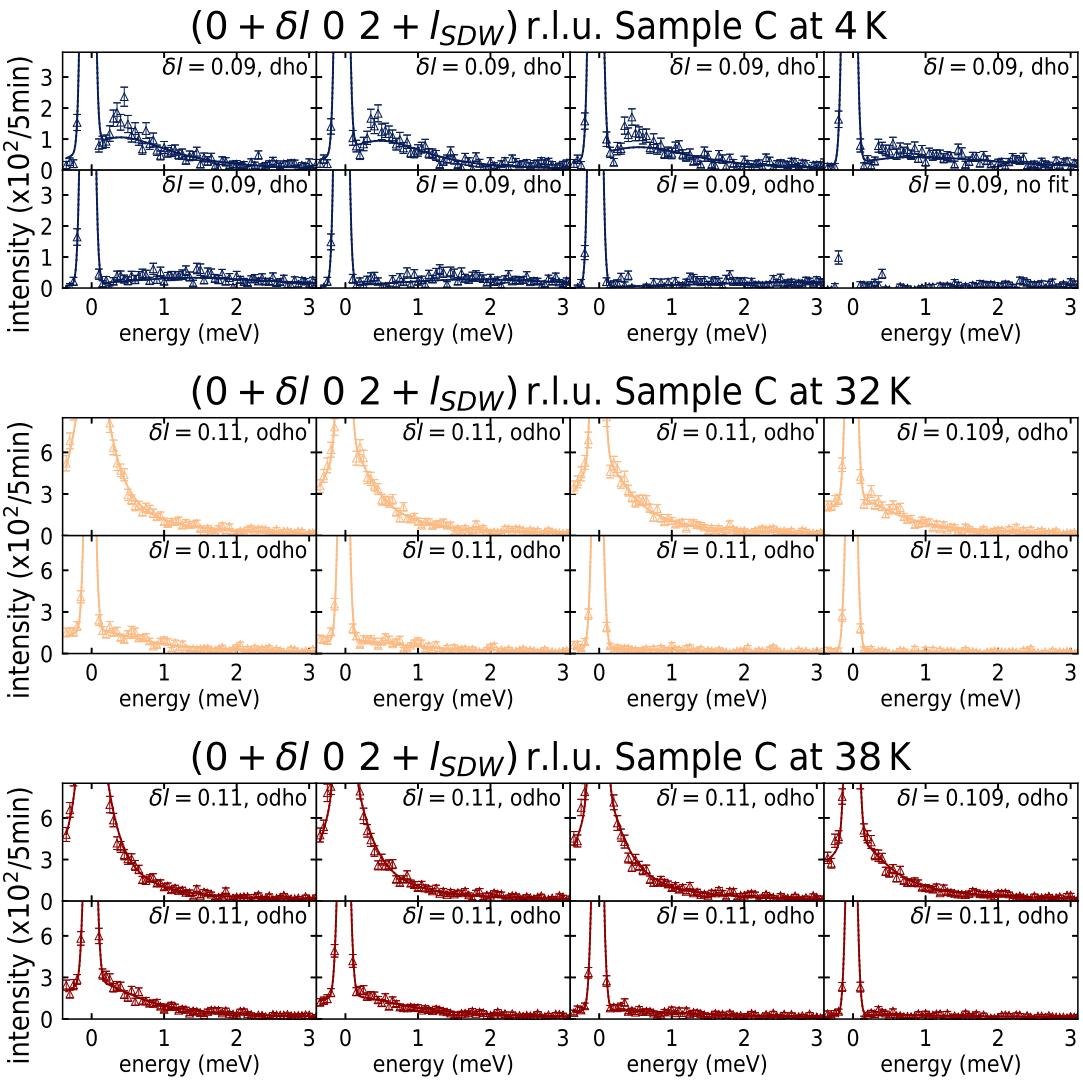

Figure 7.24: h dependence of the excitations measured at $l = 2 + l$sdw in Sample C with E_i of 4.35 meV and fitted with the DHO or ODHO model (solid lines). All the data has been measured with LET.

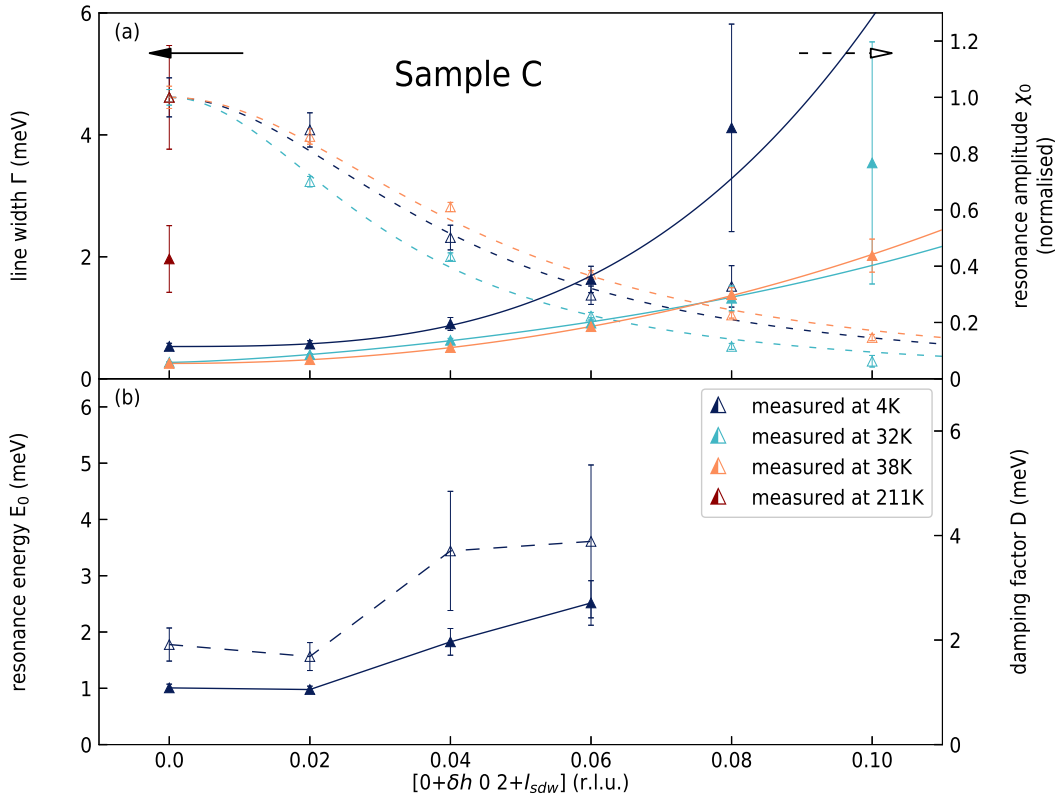

Figure 7.25: h- and T-dependence of the DHO model's parameters used to fit the magnetic excitations. **(a)** shows the of the line width on the left (full markers and solid lines) and the resonance amplitude on the right (empty markers and dashed lines). Solid and dashed lines are guides to the eye. **(b)** shows the resonance energy on the left (full markers and solid lines) and the damping factor on the right (empty markers and dashed lines). All the data has been measured with LET.

When δh increases, the resonance amplitudes decrease rapidly and monotonously in comparison to the l dependences at the same temperatures. The line widths increase from minimum values of $\Gamma = 0.53\,\text{meV}$ at 4 K, $\Gamma = 0.21\,\text{meV}$ at 32 K and $\Gamma = 0.34\,\text{meV}$ at 38 K, above the resolution of the instrument. The increase in the FM state is steeper than near Curie and Néel temperatures. The big error bars at $\delta h = 0.08\,\text{r.l.u.}$ at 4 K and at $\delta h = 0.1\,\text{r.l.u.}$ at 32 K come from the weakness of the signal. The same explains the big error bars of the parameters measured at 211 K. The resonance energy measured at 4 K increases slightly from a minimum $E_0 = 1.0\,\text{meV}$ and so does the damping factor from a minimum $D = 1.9\,\text{meV}$, but, due to the significant error bars, the intensity of the increase is hard to assess.

7.4 Discussion

The damping regime boundaries of the magnetic excitations measured at $\boldsymbol{Q}_{\mathbf{FM}}$= (0 0 2) r.l.u. and at $\boldsymbol{Q}_{\mathbf{SDW}}$= (0 0 l_{SDW}) r.l.u. seem to correspond to the phase boundaries. Magnetic excitations are well fitted with the DHO model in the under-damped or critical regime up to T_C. Above the latter, the damping factor D increases and the magnetic excitations are well fitted with the ODHO model in the over-damped regime at T_N and above. In the FM state, the l-dependent resonance energy E_0 is gapped with a minimum around $\delta l \approx 0.15\,\text{r.l.u.}$. The gap reduces as temperature increases and although Figure 7.10 suggests a first closure of the gap near T_C around $\delta l \approx 0.15\,\text{r.l.u.}$ and a closure at $\boldsymbol{Q}_{\mathbf{FM}}$= (0 0 2) r.l.u. near T_N, this is less obvious from the fit parameters due to their significant error bars. In the FM state, at $\delta l \approx 0.2\,\text{r.l.u.}$, the line width Γ approaches the resolutions of the instruments and the resonance amplitude χ_0 is maximum. At T_C, Γ is within the energy resolution of the TASs for $\delta l \in [0.1, 0.2]\,\text{r.l.u.}$, and this range extends to $\delta l \in [0, 0.2]\,\text{r.l.u.}$ around T_N in Sample B. The maximum resonance amplitude stays at $\delta l \in [0.1, 0.2]\,\text{r.l.u.}$, but it decreases in intensity in comparison to the other positions at T_C and T_N.

7.4.1 Damping factor and relaxation time of the excitations

The resonance energy E_0 and the damping factor D are not fitted in the over-damped regime. Therefore, only the line width Γ and the resonance amplitude χ_0 are available at almost[7] all scanned positions to compare the magnetic excitations throughout the different regimes. In the

[7] Γ and χ_0 are not available at position (0 0 2) r.l.u. at 29.3 K and 32.1 K, at positon (0 0 2.1) r.l.u. at 32 K and at all positions where fits where unsuccessful

over-damped regime, $1/\Gamma$ is proportional to the relaxation time of the excitations. However, this is not the case in under-damped regime, where the line width has no evident physical meaning. To allow comparison between the different damping regimes, we compute the relaxation time τ of the magnetic excitations. The equation used to compute τ depends on the damping regime, which is identified with the value of the damping ratio ζ.

7.4.1.1 Temperature dependence

In Section 2.2.3.2 we saw that $D = 2\zeta E_0$, which gives

$$\zeta = \frac{D}{2E_0}.$$

Since ζ is given by D and E_0, it can only be calculated in the under-damped regime. Equation 2.2.22 and $D = 2\zeta E_0$ give the relaxation time of the excitations in the under-damped regime:

$$\tau_{\mathrm{u}} = \frac{\hbar}{\zeta E_0}. \tag{7.4.1}$$

In the strongly over-damped regime, we use Equation 2.2.24 to calculate the relaxation time of the excitations:

$$\tau_{\mathrm{so}} = \frac{\hbar}{\Gamma}. \tag{7.4.2}$$

In the slightly over-damped regime ($1 < \zeta \leq 3$) we use the approximation of τ_0 in Equation 2.2.8, τ_{a2} given in Figure 2.4b:

$$\begin{aligned} \tau_{\mathrm{o}} &= \frac{T_0}{\zeta + \sqrt{2}\sqrt{\zeta - 1}\left[1 + \frac{\zeta - 1}{4} - \frac{(\zeta-1)^2}{32}\right]} \\ &= \frac{\hbar}{E_0\left[\zeta + \sqrt{2}\sqrt{\zeta - 1}\left[1 + \frac{\zeta - 1}{4} - \frac{(\zeta-1)^2}{32}\right]\right]}. \end{aligned} \tag{7.4.3}$$

Figure 7.26 shows the damping ratio ζ and relaxation time of the excitations at $\boldsymbol{Q}_{\mathbf{SDW}}$ calculated from the fit parameters presented above.

In the FM state, the excitations at $\boldsymbol{Q}_{\mathbf{SDW}}$ are under-damped in samples B and C with a damping ratio $\zeta < 1$. The relaxation time is constant with $\tau \approx 2 \times 10^{-12}\,\mathrm{s}$. At $\mathrm{T_C}$ and above, $\zeta > 1$ and the excitations are over-damped. The relaxation time increases until a maximum $\tau_{\mathrm{A}} = 3.6 \times 10^{-12}\,\mathrm{s}$ in Sample A at 5 K, $\tau_{\mathrm{B}} = 4.9 \times 10^{-12}\,\mathrm{s}$ in Sample B at 32 K and $\tau_{\mathrm{C}} = 5.43 \times 10^{-12}\,\mathrm{s}$ in Sample C at 38 K. Above $\mathrm{T_N}$, in the PM state, the relaxation time of

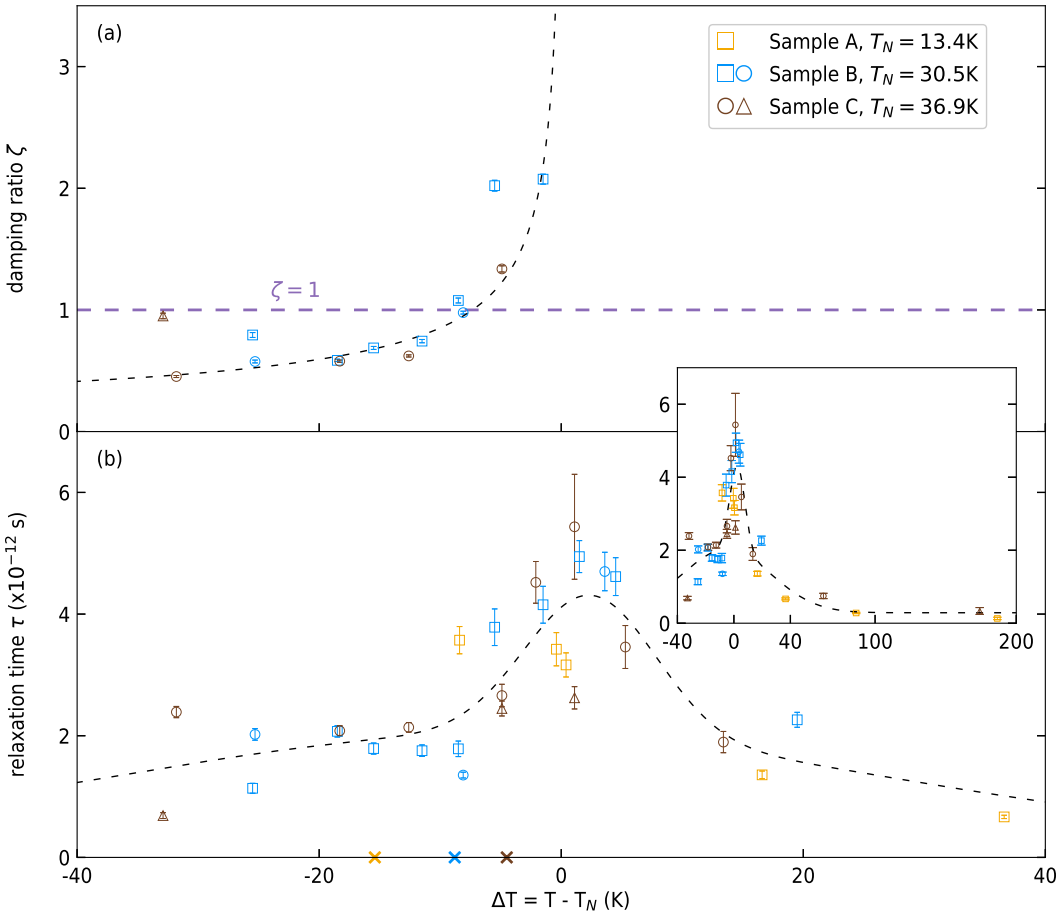

Figure 7.26: Temperature dependence of the damping ratio ζ **(a)** and relaxation time τ **(b)** of the excitations at $\boldsymbol{Q}_{\mathbf{SDW}}$ in samples A, B and C. Data measured with Panda, 4F2 and LET are represented with squares, circles and triangles respectively. The horizontal violet dashed line in (a) shows the transition limit between the damped and the over-damped regime, the dashed curves in (a) and (b) are guides to the eye and the crosses on the horizontal axis place the Curie temperature for each sample. The inset shows the whole measured temperature range for τ.

the excitations decreases slowly.

Figure 7.27a shows that the excitations at $\boldsymbol{Q}_{\mathbf{FM}}$ are under-damped in the FM state and the relaxation time at $\boldsymbol{Q}_{\mathbf{FM}}$ is close to $\tau_{\mathrm{B}} \approx 3 \times 10^{-12}$ s. In the SDW state, the damping ratio increases suddenly and the regime becomes over-damped. The relaxation time increases to a maximum value $\tau_{\mathrm{B}} \approx 5.9 \times 10^{-12}$ s at 34.1 K in Sample B and $\tau_{\mathrm{C}} \approx 5.4 \times 10^{-12}$ s at 32 K in Sample C. In the PM state, the damping ratios decrease slowly and consequently the relaxation

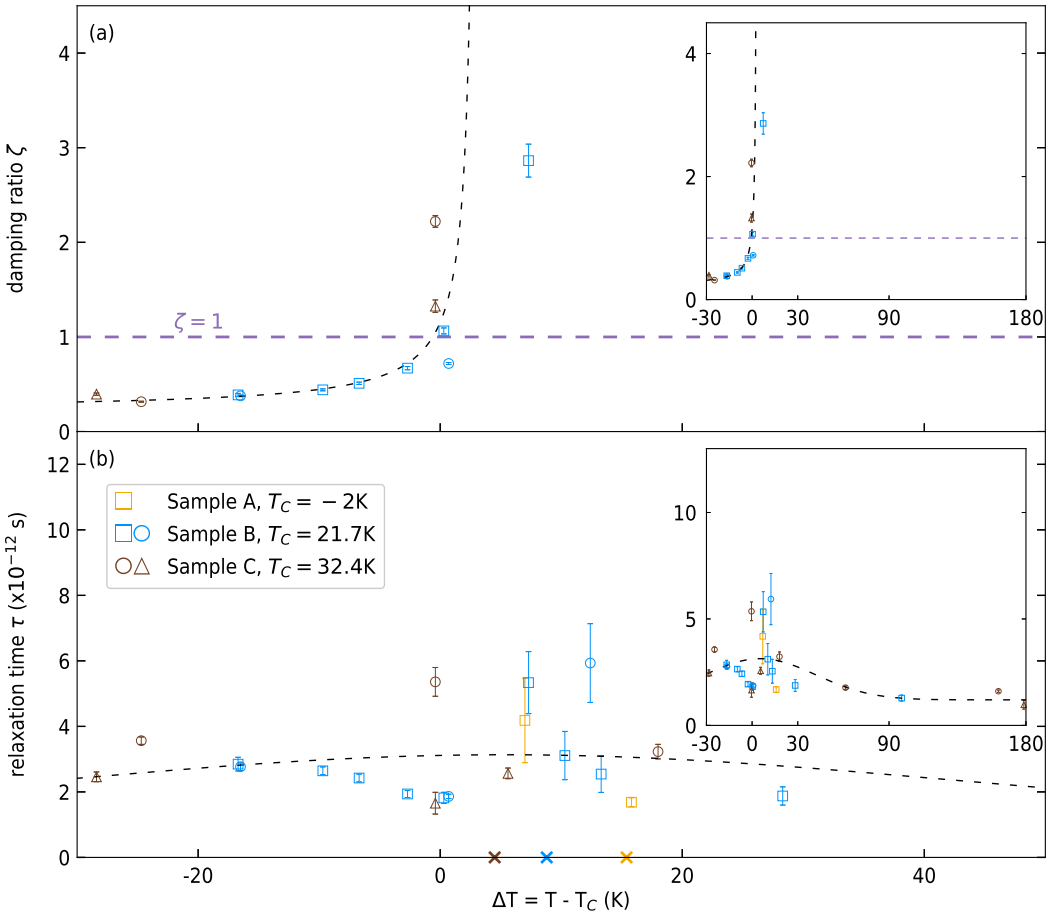

Figure 7.27: Temperature dependence of the damping ratio ζ **(a)** and relaxation time τ **(b)** of the excitations at $\boldsymbol{Q}_{\mathbf{FM}}$ in samples A, B and C. Data measured with Panda, 4F2 and LET are represented with squares, circles and triangles respectively. The brown circles with $\Delta T \in [-24.3\text{K}, -23.5\text{K}, -13.2\text{K}, -7.5\text{K}, -2.7\text{K}, 0.1\text{K}, 2.9\text{K}, 5.8\text{K}, 18.4\text{K}, 61.8\text{K}, 162.3\text{K}]$ represent the additional data measured by J. Poulten [70] and given in Table 7.3. The horizontal violet dashed line in (a) shows the transition limit between the damped and the over-damped regime. The dashed curves in (a) and (b) are guides to the eye and the crosses on the horizontal axis place the Néel temperature for each sample. The insets in (a) and (b) show the whole measured temperature range for ζ and τ respectively.

time of the excitations at $\boldsymbol{Q}_{\mathbf{FM}}$ reduces as the temperature gets higher.

7.4.1.2 l dependence

Figure 7.28a shows the l dependence of the damping ratio ζ and the relaxation time τ of the magnetic excitations deep in the FM state. Until $\delta l = 0.2$ r.l.u., the excitations are under-damped in Sample B and critical in Sample C. For $\delta l \geq 0.2$ r.l.u., excitations in Sample B become over-damped, whereas the damping ratio decreases in Sample C. In Sample B, the relaxation time of the magnetic excitations is maximum at $l = 2$ r.l.u. and drops by almost an order of magnitude when l increases to $l = 2.4$ r.l.u., whereas it remains constant in Sample C (Figure 7.28b).

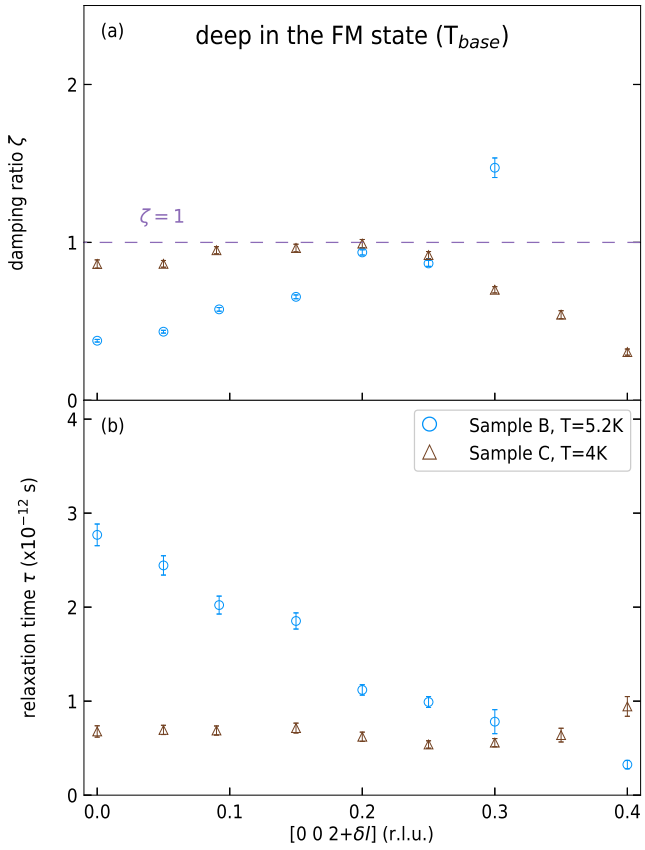

Figure 7.28: l dependence of the damping ratio ζ **(a)** and the relaxation time τ **(b)** of the magnetic excitations deep in the FM state in samples B (blue) and C (brown). ζ and τ are calculated with the equations detailed in Section 7.3.1.1. Circles represent data measured with 4F2 and triangles represent LET data measured with E_i of 4.35 meV.

Figure 7.29 shows the l-dependence of ζ and τ near the FM-SDW phase transition. Only

Sample B at $\boldsymbol{Q}_{\mathbf{FM}}$= (0 0 2) r.l.u. is under-damped. As δl increases, ζ increases rapidly in Sample B and Sample C. The relaxation time is maximum around $|\delta l| = 0.15$ r.l.u., with $\tau \approx 3.2{\times}10^{-12}$ s in Sample B, $\tau \approx 5.4 \times 10^{-12}$ s in Sample C measured with 4F2 and $\tau \approx 2.6 \times 10^{-12}$ s in Sample C measured with LET. As $|\delta l|$ increases further to 0.4 r.l.u., τ decreases towards 0.

Figure 7.30 shows the l-dependence of τ in the SDW phase in Sample A. The excitations are in the over-damped regime and only the relaxation time could be computed. τ has two maxima, one at $l = 2$ r.l.u. with $\tau = 4.2 \times 10^{-12}$ s and another at $l = 2.2$ r.l.u. with $\tau = 4.0 \times 10^{-12}$ s. τ then drops to almost zero when l increases to $l = 2.4$ r.l.u.

Figure 7.31 shows the relaxation time near the SDW-PM phase transition in Sample A, Sample B and Sample C. The excitations are in the over-damped regime and only the relaxation time could be computed. In Sample B and Sample C τ seems constant within the error bars until $l = 2 + l_{\mathrm{SDW}}$ r.l.u., whereas it increases to a maximum near l_{SDW} in Sample A. For $|\delta l| \geq l_{\mathrm{SDW}}$, the relaxation time decreases linearly towards 0.

7.4.1.3 h dependence

Figure 7.32 shows the h dependence of the damping ratio ζ and the relaxation time τ of the magnetic excitations in Sample C at $\mathrm{T_{base}}$, near $\mathrm{T_C}$, near $\mathrm{T_N}$ and at high temperature. The DHO function was used for $\delta h \in [0, 0.02, 0.04, 0.06]$ at $\mathrm{T_{base}}$. All other data points were fitted with the ODHO function.

The damping ratios in Figure 7.32a remain relatively constant with $\zeta \approx 1$, indicating that the excitations are in the critical regime. At each temperature the relaxation time of the magnetic excitations follows a similar trend, with a shift to higher values as the temperature increases. The longest living excitations are at $h = 0$ r.l.u. and as we move to higher h the relaxation time decreases until almost zero at $h = 0.1$ r.l.u. (Figure 7.32b).

7.4.2 Models from the spin fluctuation theory

We saw, in Section 2.3, that the inverse static susceptibility χ_q^{-1} has a quadratic q-dependence, and that the line width Γ_q has a cubic q-dependence[8]

$$\chi_q^{-1} = a + c(q-2)^2 \tag{7.4.4}$$

$$\Gamma_q = \gamma(q-2)\chi_q^{-1}, \tag{7.4.5}$$

[8]here q is replaced by $(q-2)$, because we measured around $\boldsymbol{Q}_{\mathbf{FM}}$= (0 0 2) r.l.u..

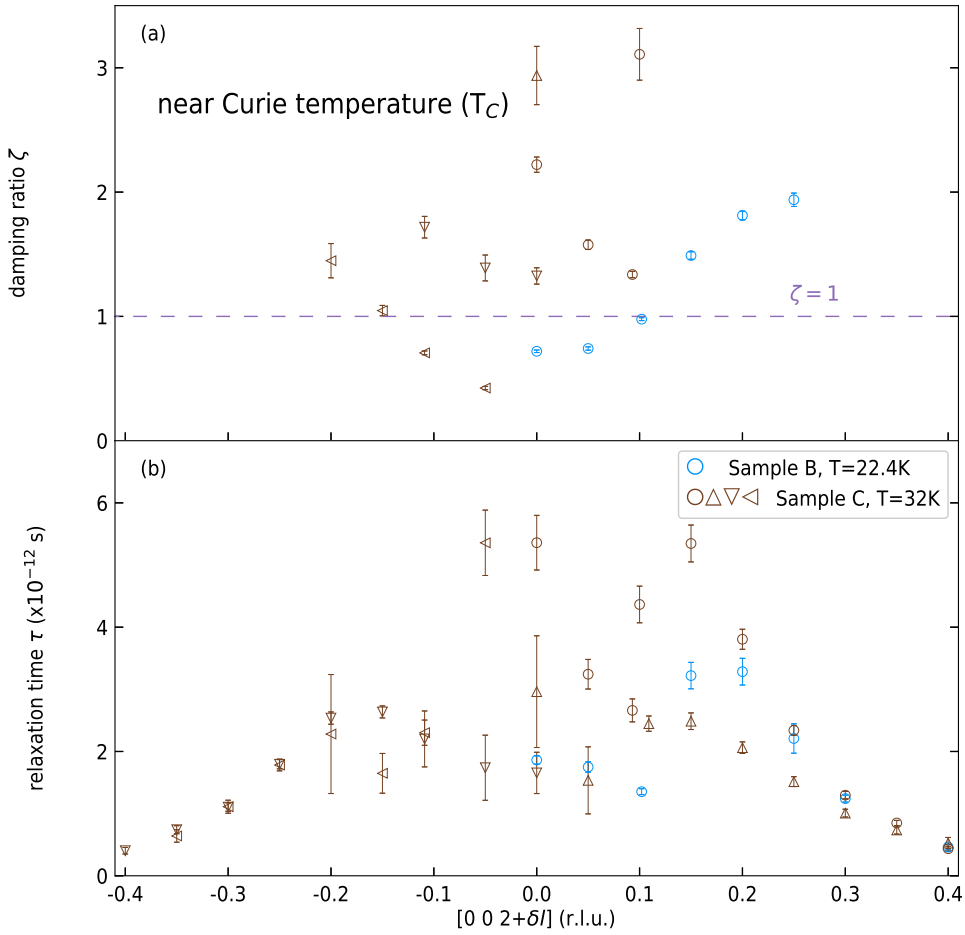

Figure 7.29: l dependence of the damping ratio ζ **(a)** and the relaxation time τ **(b)** of the magnetic excitations near the Curie temperature in samples B (blue) and C (brown). Circles represent data measured with 4F2 and triangles represent data measured with LET (up, down and left triangles for data measured with E_is of 4.35 meV, 2.48 meV and 1.6 meV respectively).

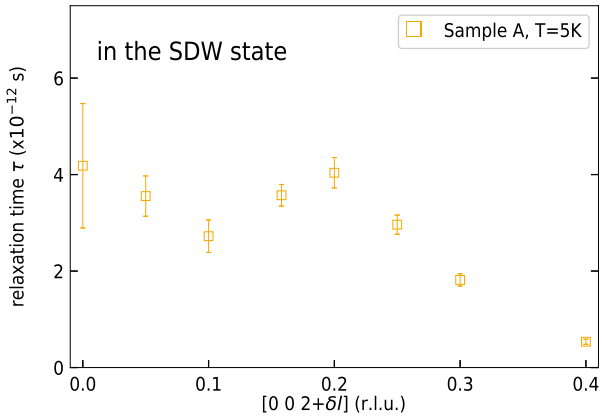

Figure 7.30: l dependence of the relaxation time τ of the magnetic excitations in the SDW state in Sample A. τ are calculated with the equations detailed in Section 7.4.1.1. All the data was measured with Panda.

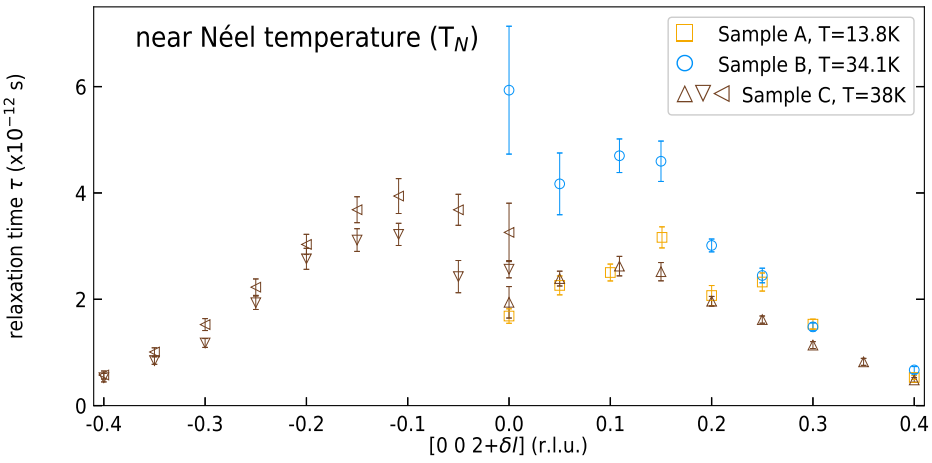

Figure 7.31: l dependence of the relaxation time τ of the magnetic excitations near the Néel temperature in samples A (yellow), B (blue) and C (brown). Squares represent data measured with Panda, circles represent data measured with 4F2 and triangles represent data measured with LET (up, down and left triangles for data measured with E$_i$s of 4.35 meV, 2.48 meV and 1.6 meV respectively).

where a, c and γ are experimental parameters.

From these models we would expect the static susceptibility to be maximum and the line width to be minimum at $q = 0$ r.l.u.. However, we saw in Figure 7.17, Figure 7.19, Figure 7.21 and Figure 7.23, that the susceptibility is maximum, and the line width minimum, near l_{SDW}.

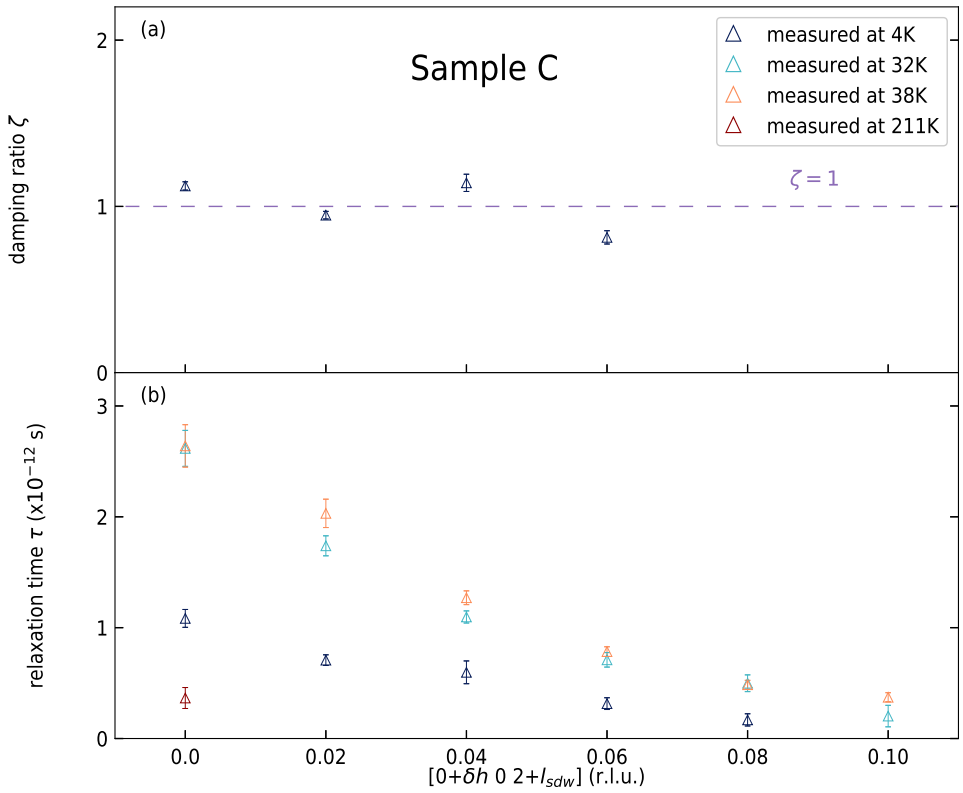

Figure 7.32: h- and T-dependence of the damping ratio ζ **(a)** and the relaxation time τ **(b)** of the magnetic excitations at base temperature (dark blue), near Curie temperature (light blue) and near Néel temperature (orange) in Sample C. The horizontal dotted line indicates the under-damped/over-damped transition of the regime. All the data has been measured with LET.

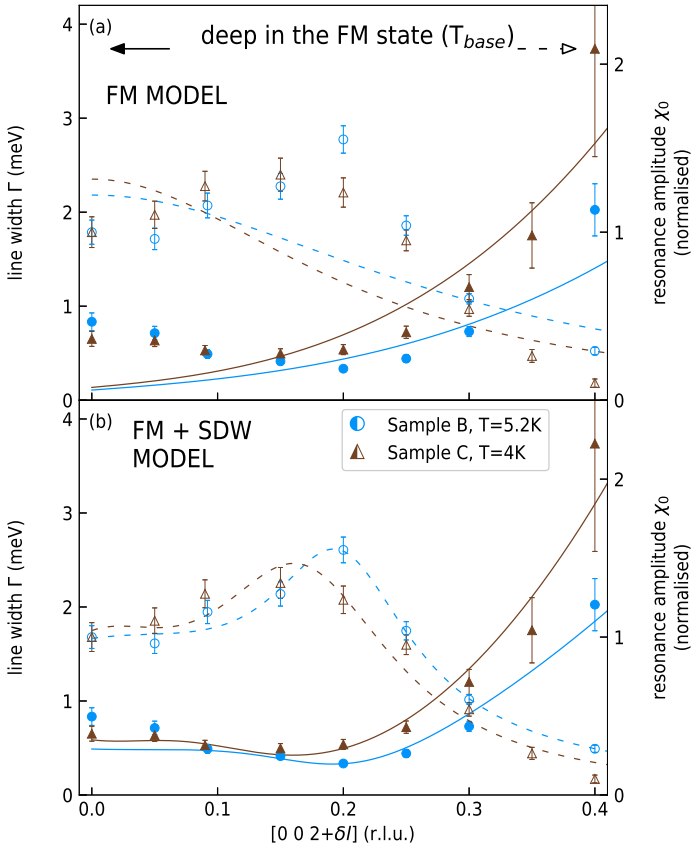

Figure 7.33: Fit of the magnetic excitations measured along l, deep in the FM state, in samples B and C with the FM model **(a)** and the FM+SDW model **(b)**. The full markers represent the line width and the empty markers represent the resonance amplitude. For Sample B the resonance amplitude is normalised to its value measured at $l = 2$ r.l.u.. For Sample C, we first multiplied the resonance amplitude of the data measured with LET at 4.35 meV by $\chi_{\mathrm{LET},4.35}(2.15)/\chi_{\mathrm{LET},2.48}(1.85)$, and then we normalised the data to $\chi_{\mathrm{LET},2.48}(2)$. Circles represent data measured with 4F2 and triangles represent data measured with LET (up and down triangles for data measured with E_i of 4.35 meV, and 2.48 meV respectively).

Figure 7.33a, Figure 7.34a, Figure 7.35a and Figure 7.36a show the q-dependence in the l direction of the static susceptibility and the line width that are fitted with the FM model of the spin fluctuation theory. The latter model only considers the excitations at $\boldsymbol{Q}_{\mathbf{FM}}$.

If we also include the excitation at $\boldsymbol{Q}_{\mathbf{SDW}}$ in the model, the static susceptibility, which is

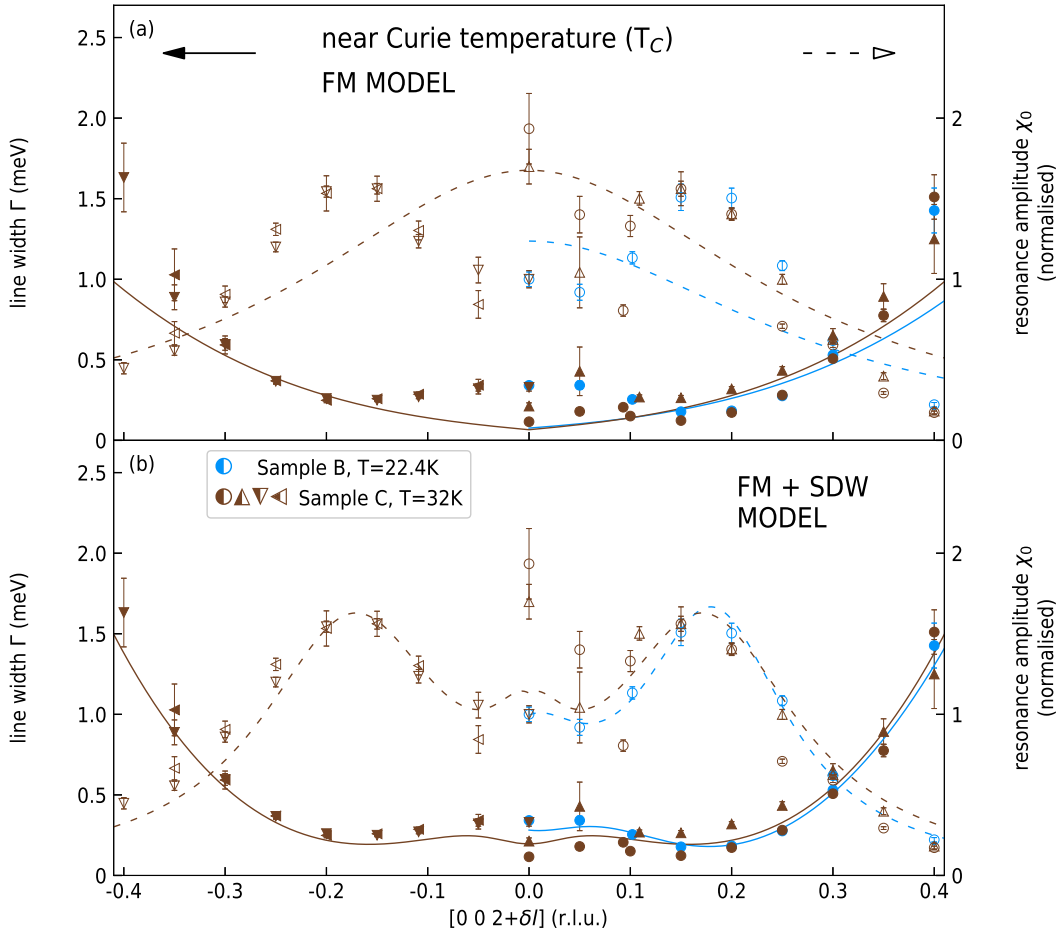

Figure 7.34: Fit of the magnetic excitations measured along l near the Curie temperature in samples B and C with the FM model **(a)** and the FM+SDW model **(b)**. The full markers represent the line width and the empty markers represent the resonance amplitude. For Sample B the resonance amplitude is normalised to the value measured at $l = 2$ r.l.u.. For Sample C, we first multiplied the resonance amplitude of the data measured with 4F2 and with LET at 4.35 meV and 1.6 meV by $\chi_{4F2}(2.15)/\chi_{LET,2.48}(1.85)$, $\chi_{LET,4.35}(2.15)/\chi_{LET,2.48}(1.85)$ and $\chi_{LET,1.6}(1.85)/\chi_{LET,2.48}(1.85)$ respectively, and then we normalised the data to $\chi_{LET,2.48}(2)$. Circles represent data measured with 4F2 and triangles represent data measured with LET (up, down and left triangles for data measured with E_i of 4.35 meV, 2.48 meV and 1.6 meV respectively).

the sum of the FM and the SDW susceptibilities, is given by

$$\chi_q = \chi_{q\mathrm{FM}} + \chi_{q\mathrm{SDW}} \tag{7.4.6}$$

$$= \frac{1}{a_{\mathrm{FM}} + c_{\mathrm{FM}}(q-2)^2} + \frac{1}{a_{\mathrm{SDW}} + c_{\mathrm{SDW}}(q-2-l_{\mathrm{SDW}})^2}. \tag{7.4.7}$$

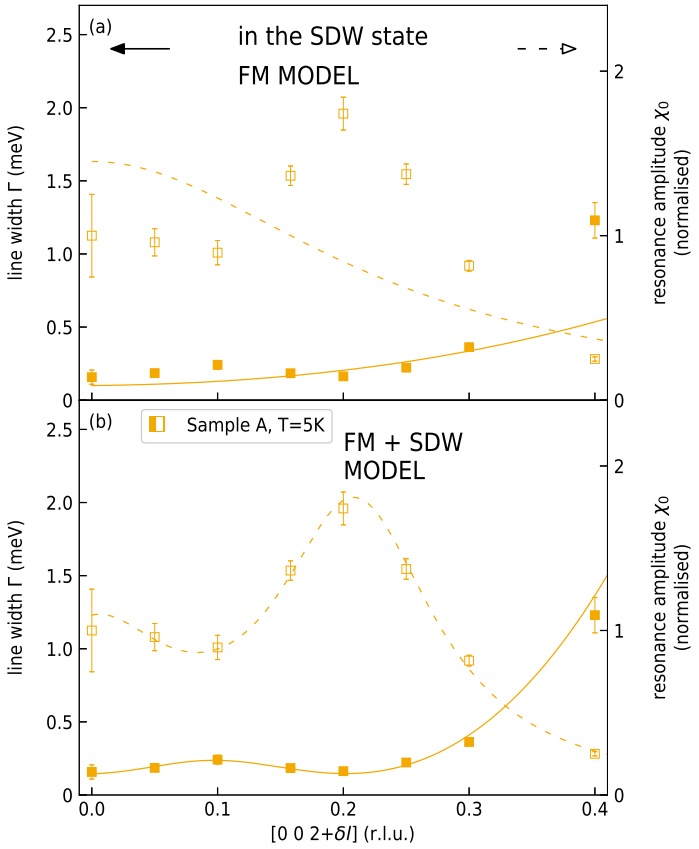

Figure 7.35: Fit of the magnetic excitations measured along l in the SDW state in Sample A with the FM model **(a)** and the FM+SDW model **(b)**. The full markers represent the line width and the empty markers represent the resonance amplitude. The resonance amplitude is normalised to the value measured at $l = 2$ r.l.u.. All the data was measured with Panda.

The line width in Equation 7.4.5 then becomes

$$\Gamma_q = \gamma(q-2+q_c)\frac{\left[a_{\mathrm{FM}} + c_{\mathrm{FM}}(q-2)^2\right]\left[a_{\mathrm{SDW}} + c_{\mathrm{SDW}}(q-2-l_{\mathrm{SDW}})^2\right]}{a_{\mathrm{FM}} + a_{\mathrm{SDW}} + c_{\mathrm{FM}}(q-2)^2 + c_{\mathrm{SDW}}(q-2-l_{\mathrm{SDW}})^2}, \tag{7.4.8}$$

were q_c is a cut-off frequency that we add to accounts for the finite relaxation time of the excitations.

Figure 7.33b, Figure 7.34b, Figure 7.35b and Figure 7.36b show how the FM model of the spin fluctuation theory is modified when considering the excitation at $\boldsymbol{Q_{\mathrm{SDW}}}$. One sees that the FM+SDW model fits much better the data than the FM model.

Figure 7.37 shows all the parameters of the FM+SDW model that have been fitted in the

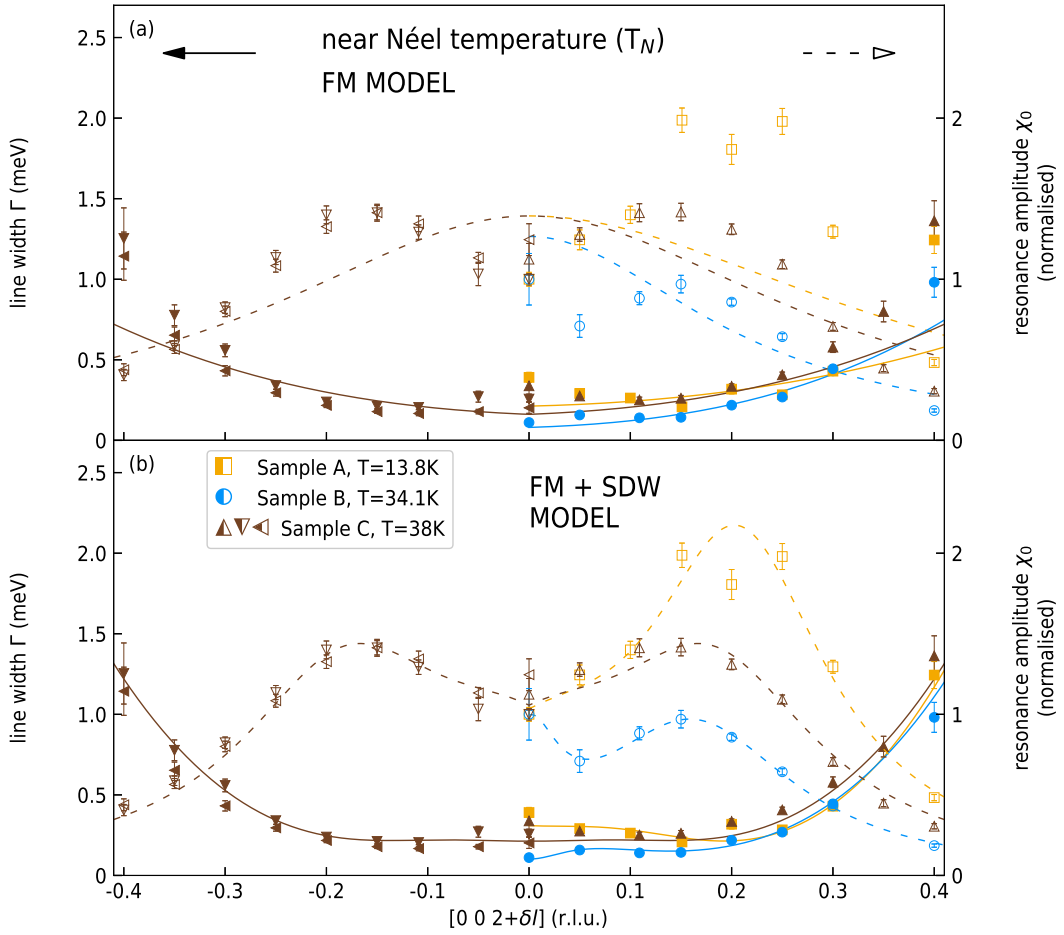

Figure 7.36: Fit of the magnetic excitations measured along l near the Néel temperature in samples A,B and C with the FM model **(a)** and the FM+SDW model **(b)**. The full markers represent the line width and the empty markers represent the resonance amplitude. For samples A and B the resonance amplitude is normalised to their value measured at $l = 2$ r.l.u. ($\chi_A(2)$ and $\chi_B(2)$). For Sample C, we first multiplied the resonance amplitude of the data measured with LET at 4.35 meV and 1.6 meV by $\chi_{LET,4.35}(2.15)/\chi_{LET,2.48}(1.85)$ and $\chi_{LET,1.6}(1.85)/\chi_{LET,2.48}(1.85)$ respectively, and then we normalised the data to $\chi_{LET,2.48}(2)$. Squares represent data measured with Panda, circles represent data measured with 4F2 and triangles represent data measured with LET (up and down triangles for data measured with E_i of 4.35 meV, and 2.48 meV respectively).

different temperature regimes. The intensity of both the FM static susceptibility $\chi_{0,FM}$ and the SDW static susceptibility $\chi_{0,SDW}$ decrease systematically as the Fe concentration y increases, with $\chi_{0,FM}$ near T_N at $y = 0.002$ as the only exception. There is no clear temperature

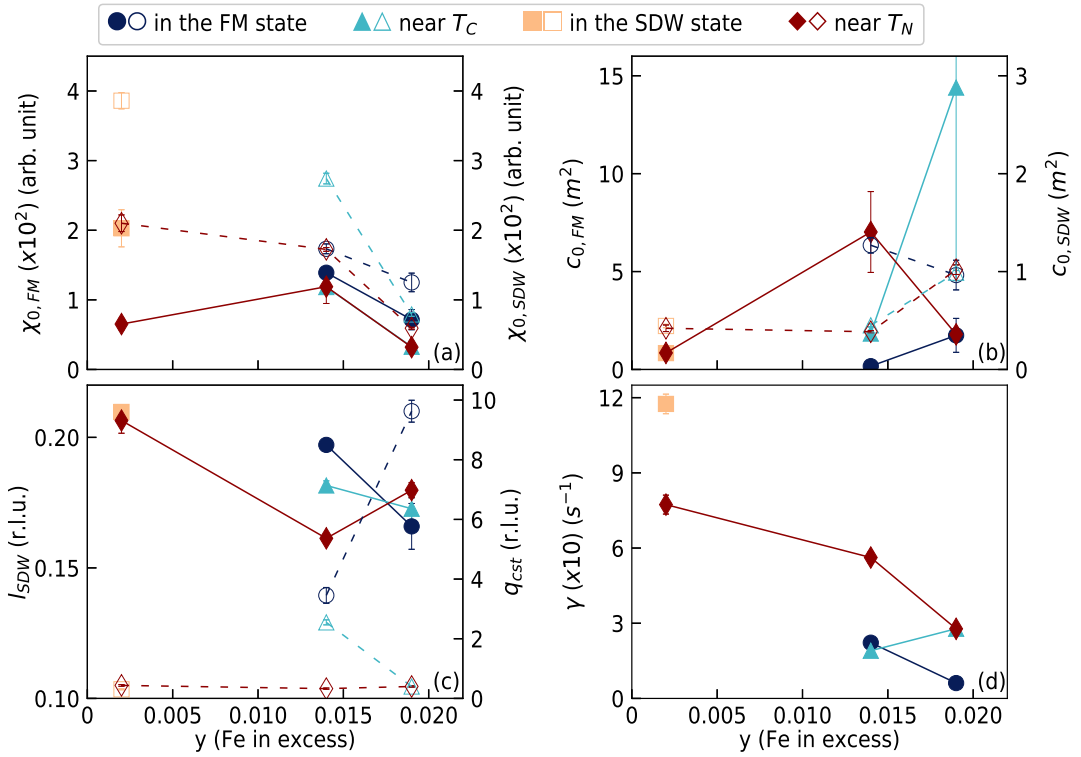

Figure 7.37: Composition dependence of the different parameters of the FM+SDW model of the spin fluctuation theory fitted in the FM state (dark blue circles), near T_C (light blue triangles), in the SDW state (orange squares) and near T_N (red diamonds). $\chi_{0,\mathrm{FM}}$ (left axis in a) is the Q-dependent FM susceptibility and $\chi_{0,\mathrm{SDW}}$ (right axis in a) is the Q-dependent SDW susceptibility. $c_{0,\mathrm{FM}}$ (left axis in b) is the stiffness of the magnetic excitation at $\boldsymbol{Q}_{\mathbf{FM}}$ and $c_{0,\mathrm{SDW}}$ (right axis in b) is the stiffness of the magnetic excitation at $\boldsymbol{Q}_{\mathbf{SDW}}$. l_{SDW} (left axis in c)is the l component of the SDW wave vector $\boldsymbol{Q}_{\mathbf{SDW}}$ and q_{cst} (right axis in c) is the constant cut-off frequency added in Equation 7.4.8. γ (left axis in d) is the relaxation function. Solid markers correspond to the parameters given on the left axis and empty markers correspond to the parameters of the right axis.

dependence of $\chi_{0,FM}$ and $\chi_{0,SDW}$.

The stiffness of the excitations at $\boldsymbol{Q}_{\mathbf{FM}}$ $c_{0,FM}$ is significantly higher than at $\boldsymbol{Q}_{\mathbf{SDW}}$, and again, there is no clear temperature dependence for these parameters.

The fitted SDW wave vectors $\boldsymbol{Q}_{\mathbf{SDW}}$ indicate higher values than the wave vectors suggested by the elastic neutron scattering results presented in Section 6, which gave 0.091 r.l.u.$\leq l_{\mathrm{SDW}} \leq$ 0.158 r.l.u., whereas the values shown in Figure 7.37c (left axis) suggest 0.16 r.l.u.$\leq l_{\mathrm{SDW}} \leq$ 0.22 r.l.u.. A possible reason could be that l_{SDW} measured with elastic neutron scattering experiments are underestimated because of the system's proximity to the FM state. Figure 7.38 shows

a calculated l_{av} (solid markers), which is the average of l_{FM} and the fitted l_{SDW}, weighted with the fitted intensities of the static susceptibilities $\chi_{0,FM}$ and $\chi_{0,SDW}$, respectively. The empty markers correspond to the values of l_{SDW} measured with elastic neutron scattering $l_{\mathrm{SDW,el}}$ and presented in Section 6. We see that l_{av} is fairly consistent with the measured values of $l_{\mathrm{SDW,el}}$, which could indicate that the actual l_{SDW} values correspond more to the values fitted by the FM+SDW model and that those are of the order of 0.2 r.l.u. rather than 0.1 r.l.u. as suggested by the elastic neutron scattering data.

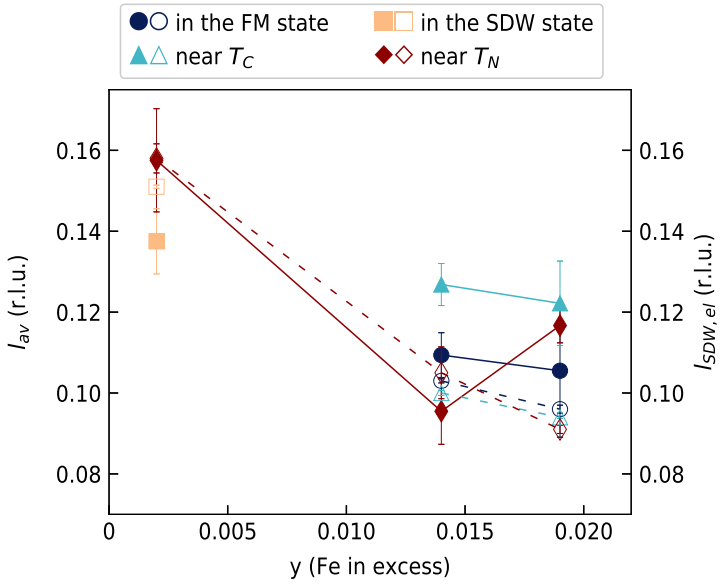

Figure 7.38: Solid markers correspond to the left axis and show the average l_{av} of l_{FM} and l_{SDW} weighted with the fitted intensities of the static susceptibilities $\chi_{0,FM}$ and $\chi_{0,SDW}$ shown in Figure 7.37a. Empty markers corresponding to the right axis, represent the l components of the SDW wave vectors $\boldsymbol{Q}_{\mathbf{SDW}}$ measured with elastic neutron scattering experiments and presented in Section 6.

The cut-off constant q_c added to the model to account for the finite relaxation time of the excitations decreases in the higher temperature phases. The parameter shows a strong composition dependence in the FM state with higher values at higher concentrations of Fe. This y-dependence seems to be gone near $\mathrm{T_N}$.

Finally, the relaxation function γ shows a strong composition dependence with a strong enhancement at lower y. Γ should go to 0 and $1/\Gamma$ should diverge in the quantum critical region. However, γ could be linked to the Fermi velocity (i.e. it expresses how fast the electrons and their spins move to cancel any excitations) and therefore, since the doping range is small and

big changes in the bare electronic structure are not expected, we expect this latter parameter to be fairly constant, which is not what we observe.

Chapter 8

Summary and Outlook

The characteristic behaviour observed in $Nb_{1-y}Fe_{2+y}$ as the second order ferromagnetic (FM)-paramagnetic (PM) phase transition is suppressed towards 0 K, make of this compound a promising candidate to study the theoretically predicted scenario of a spin density wave (SDW) masking a ferromagnetic quantum critical point (FM QCP). In this thesis we used different neutron scattering techniques on $NbFe_2$ to investigate the nature of the order and excitations near the border of ferromagnetism. To approach the latter we used three high quality single crystal with different compositions. We moved across the temperature T-composition y phase diagram of $Nb_{1-y}Fe_{2+y}$ by using Sample A with $y = 0.002$, Sample B with $y = 0.014$ and Sample C with $y = 0.019$. The positions of the samples in the phase diagram are shown in Figure 8.1.

We used spherically polarised neutron diffraction to establish the nature of the FM phase at two FM Bragg peaks: (1 0 2) r.l.u. and (3 0 1) r.l.u.. The goal was to address the pending question of the direction of the magnetic moment in the ordered phase. At both positions, only polarisation-matrix elements P_{xx} and P_{zz} showed a small increase between the FM state, measured at 5 K, and the PM state, measured at 40 K; all off-diagonal terms are zero. Further considerations of the elements of the polarisation matrix, indicated the presence of two opposed and equally populated 180°-domains, and excluded the present of chiral domains. Additionally, the intensities of the physical quantities showed an increase for $M_{\perp y}$, but not for $M_{\perp z}$, and considering the hexagonal structure of the crystal, we could conclude that the moment points along $\boldsymbol{c}$ in the FM state.

Interesting measurements for the future would be the FM and the SDW structure refine-

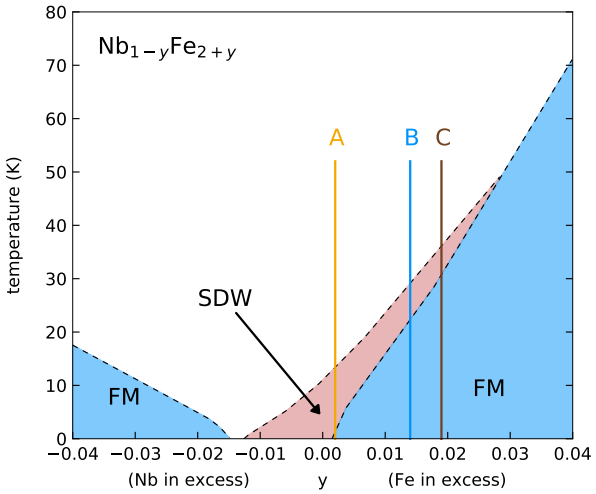

Figure 8.1: T-y phase diagram of $Nb_{1-y}Fe_{2+y}$. Nb atoms are substituted with Fe atoms on the Fe-rich side of the diagram (right) and Fe atoms are replaced by Nb atoms on the Nb-rich side of the diagram (left). The vertical plain lines labeled A, B and C indicate the Fe concentrations of Sample A ($y = +0.002$), Sample B ($y = +0.014$) and Sample C ($y = +0.019$).

ments, by measuring polarisation matrices at more Bragg positions and by measuring the full polarisation matrix at the SDW position, respectively. It would be useful to apply a small magnetic field along the easy axis $\boldsymbol{c}^*$ during cooling to suppress the magnetic domains, this could give non-zero off-diagonal terms in the polarisation matrix, which are not be observed with zero-field cooling. We could also suggest to measure again the positions where no SDW signal has been detected (e.g. (1 0 0), (1 0 1), (1 0 2) and (1 0 3)) with polarised neutrons in order to confirm the absence of SDW signals.

We used unpolarised elastic neutron scattering to measure the temperature T and composition y dependence of the intensity and the wave vector of the SDW signal. The synthesis of the results is contained in Figure 8.2. From these results we estimated bulk Curie temperatures of T_{C_B}= 21.7 K for Sample B, T_{C_C}= 32.4 K for Sample C and bulk Neél temperatures of T_{N_A}= 13 K for Sample A, T_{N_B}= 30.5 K for Sample B and T_{N_C}= 36.9 K for Sample C. No ferromagnetism was measure in Sample A down to 2 K. The temperature hysteresis of l_{SDW} observed in Sample B and Sample C in Figure 8.2c, confirmed the first order nature of the FM-SDW phase transition. The change of l_{SDW} with temperature in Sample B and Sample C indicated that the Q-dependent susceptibility in the SDW state changes when approaching the FM state. We also observed that l_{SDW} is the highest in Sample A and the lowest in Sample

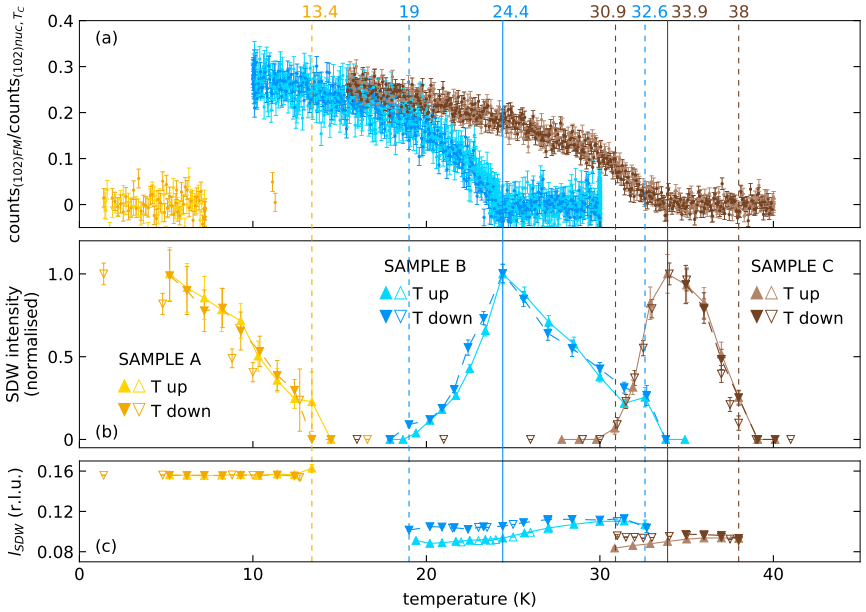

Figure 8.2: Temperature evolution of the FM signal and the SDW characteristics. **(a)** shows the temperature evolution of the FM signal measured at $\boldsymbol{Q} = (1\ 0\ 2)$ r.l.u. and normalised by the nuclear intensity measured at T_C. **(b)** shows the temperature evolution of the normalised SDW signal intensity in Sample A (yellow), Sample B (blue) and Sample C (brown). The intensities are normalised with the highest value measured with increasing temperatures (T up). **(c)** shows the temperature evolution of l_{SDW} (the l-component of $\boldsymbol{Q_{SDW}}$) in the three samples. The dashed lines indicate the onset temperatures of the SDW signal and the plain lines are the temperatures of maximum SDW intensity, which also corresponds to the onset of the FM signal at T_C. Solid markers are the data measured in the framework of this PhD project and the empty markers represent the previous data [3].

C; l_{SDW} increases as we approach the FM QCP. The continuous growth of SDW intensity indicated a second order PM-SDW phase transition. We also observed a coexistence of the FM and the SDW states, which we explained by a possible composition gradient in the samples.

Finally, we used unpolarised inelastic neutron scattering to measure the T, y and $\boldsymbol{Q}$ dependence of the low energy magnetic excitations in the different sections of the $T-y$ phase diagram of $NbFe_2$, and we tested our results with the spin fluctuation theory. From the over-damped harmonic oscillator model derived in the latter theory and applied near the SDW-PM phase transition, we extrapolated the damped harmonic oscillator model for the FM state and near the FM-SDW phase transition. Then, to compare the different regimes, we derived two physical parameters from the fitted parameters: the damping ratio ζ, which provides information of the damping regime of the magnetic excitations and the relaxation time τ, which is the lifetime

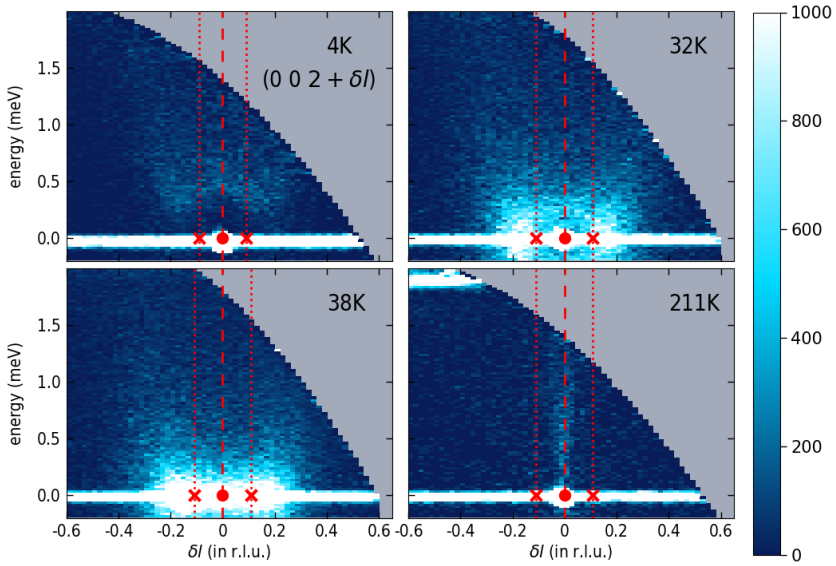

Figure 8.3: 2D cuts along the l direction and the energy showing the l dependence of the magnetic excitation energies near $\boldsymbol{Q}_{\mathbf{FM}}$= (0 0 2) (r.l.u.) at T_{base}= 4 K, near $\mathrm{T_{C_C}}$ at $T = 32$ K, near $\mathrm{T_{N_C}}$ at $T = 38$ K and at $T_{\text{max}} = 211$ K. $\boldsymbol{Q}_{\mathbf{FM}}$= (0 0 2) r.l.u. is given by the red dot and $\boldsymbol{Q}_{\mathbf{SDW}}$= (0 0 2.09) r.l.u. at 4 K, and $\boldsymbol{Q}_{\mathbf{SDW}}$= (0 0 2.109) r.l.u. at the other temperatures, is given by the red cross. The $\mathrm{E_i}$ of the neutrons is 2.48 meV, the l resolution is 0.02 r.l.u., h and η directions are integrated over $[-0.2, 0.2]$ r.l.u. and the energy resolution is 0.01 meV. The colour scale, which represents the intensity of scattered neutrons, is saturated at 1000(a.u.) in order to make the magnetic excitations visible. At T_{max}, the magnon dispersion disappears completely and a weak phonon becomes visible.

of the magnetic excitations. A general observation that we made is that unusual excitations spectra were observed along l only; spectra observed along h were as expected with a minimum at $h = 0$ r.l.u. and a decreasing static susceptibility χ_0 with increasing h. We first looked at the temperature dependence of the magnetic excitations at l_{SDW} and l_{FM}. The damping regime correspond to the phase boundaries, with under-damped or critical damping regimes in the FM state and over-damped in the SDW and PM states. The lifetime of the magnetic excitations at l_{SDW} and at l_{FM} are enhanced around $\mathrm{T_N}$ and $\mathrm{T_C}$, respectively. We then looked at the l-dependence of the magnetic excitations in the different phases and at their transitions. In the FM state in Sample B and Sample C, we observed an energy gap with minimums closer to l_{SDW} than to l_{FM}= 0 r.l.u. where we would have expected the minimum for the spectrum of the excitations in the FM state. An illustration of this energy gap is shown for Sample C in Figure 8.3 at 4 K. The calculated τ showed an enhancement of the lifetime of the excitations around l_{SDW}. Near the FM-SDW phase transition, we observed a closure of the gap around l_{SDW} as shown for Sample C in Figure 8.3 at 32 K. Longest lifetimes were still observed around l_{SDW}. Near the SDW-PM phase transition the energy gap seemed to have closed at l_{FM} as shown for Sample C in Figure 8.3 at 38 K. In the SDW state and near the SDW-PM phase transition, lifetimes of excitation at l_{FM} and at l_{SDW} were similar. The last step was the comparison of the results with two models derived from the spin fluctuation theory: the FM model and the FM+SDW model. In the FM model we considered magnetic excitations only at l_{FM}, whereas in the FM+SDW model we considered coexisting magnetic excitations at l_{FM} and l_{SDW}. We fitted the l-dependent linewidths Γ and static susceptibilities χ_0, that were obtained from fitting the neutron data, and we arrived at the conclusion that the FM+SDW describes much better our results. Spin-fluctuation spectrum reflects the proximity to two types of magnetic order. The intensities of FM and SDW excitations are similar, which points to a common origin. The findings are a testing ground for theories of masked FM QCPs, like quantum order by disorder [32].

Particular challenge for any theories will be to explain unusual observations like the minimum of the gap in the FM state away from $\boldsymbol{Q}_{\mathbf{FM}}$ and the closure of the gap at $\boldsymbol{Q}_{\mathbf{FM}}$ near $\mathrm{T_N}$ and not $\mathrm{T_C}$. It is also not expected to find a whole range in reciprocal space with closed gap. A path for the near future would be to perform spin echo measurement for high energy resolution, which would more information about the observed energy gap and its closure. Another interesting direction would be in field measurements. By applying a field $\boldsymbol{H} \parallel \boldsymbol{a}$ allows to reach an unmasked FM QCP and by applying a field $\boldsymbol{H} \parallel \boldsymbol{c}$ (along the easy axis) one can hit

the tricritical line at finite temperature. Finally, in a more further future, one could consider growing a new sample in order to search for the predicted quantum tricritical point (QTCP).

Bibliography

[1] M Brando, WJ Duncan, D Moroni-Klementowicz, C Albrecht, D Grüner, Rafik Ballou, and FM Grosche. Logarithmic fermi-liquid breakdown in NbFe2. *Physical review letters*, 101(2):026401, 2008.

[2] D Rauch, M Kraken, FJ Litterst, S Süllow, H Luetkens, M Brando, T Förster, J Sichelschmidt, A Neubauer, C Pfleiderer, et al. Spectroscopic study of metallic magnetism in single-crystalline $Nb_{1-y}Fe_{2+y}$. *Physical Review B*, 91(17):174404, 2015.

[3] P. G. Niklowitz, M. Hirschberger, M. Lucas, P. Cermak, A. Schneidewind, E. Faulhaber, J.-M. Mignot, W. J. Duncan, A. Neubauer, C. Pfleiderer, and F. M. Grosche. Ultrasmall moment incommensurate spin density wave order masking a ferromagnetic quantum critical point in $NbFe_2$. *Phys. Rev. Lett.*, 123:247203, Dec 2019.

[4] G. L Squires. *Introduction to the theory of thermal neutron scattering*. Cambridge University Press, Cambridge, 1978.

[5] Shivaji Lal Sondhi, SM Girvin, JP Carini, and D Shahar. Continuous quantum phase transitions. *Reviews of modern physics*, 69(1):315, 1997.

[6] JAS Kelso, John P Scholz, and Gregor Schöner. Nonequilibrium phase transitions in coordinated biological motion: critical fluctuations. *Physics Letters A*, 118(6):279–284, 1986.

[7] Mark M Millonas. Swarms, phase transitions, and collective intelligence. *arXiv preprint adap-org/9306002*, 1993.

[8] FM Grosche, IR Walker, SR Julian, ND Mathur, DM Freye, MJ Steiner, and GG Lonzarich. Superconductivity on the threshold of magnetism in $CePd_2Si_2$ and $CeIn_3$. *Journal of Physics: Condensed Matter*, 13(12):2845, 2001.

[9] Shuai Jiang, Hui Xing, Guofang Xuan, Cao Wang, Zhi Ren, Chunmu Feng, Jianhui Dai, Zhu'an Xu, and Guanghan Cao. Superconductivity up to 30 k in the vicinity of the quantum critical point in $BaFe_2(As_{1-x}P_x)_2$. *Journal of Physics: Condensed Matter*, 21(38):382203, 2009.

[10] O Trovarelli, C Geibel, S Mederle, C Langhammer, FM Grosche, P Gegenwart, M Lang, G Sparn, and F Steglich. $YbRh_2Si_2$: Pronounced non-Fermi-liquid effects above a low-lying magnetic phase transition. *Physical Review Letters*, 85(3):626, 2000.

[11] P Gegenwart, J Custers, C Geibel, K Neumaier, T Tayama, K Tenya, O Trovarelli, and F Steglich. Magnetic-field induced quantum critical point in $YbRh_2Si_2$. *Physical Review Letters*, 89(5):056402, 2002.

[12] Michael Nicklas, Manuel Brando, Georg Knebel, Franz Mayr, Wilfried Trinkl, and Alois Loidl. Non-fermi-liquid behavior at a ferromagnetic quantum critical point in Ni_xPd_{1-x}. *Physical review letters*, 82(21):4268, 1999.

[13] H v Löhneysen, T Pietrus, G Portisch, HG Schlager, A Schröder, M Sieck, and T Trappmann. Non-fermi-liquid behavior in a heavy-fermion alloy at a magnetic instability. *Physical Review Letters*, 72(20):3262, 1994.

[14] Manuel Brando, D Belitz, FM Grosche, and TR Kirkpatrick. Metallic quantum ferromagnets. *Reviews of Modern Physics*, 88(2):025006, 2016.

[15] Ch Pfleiderer, GJ McMullan, SR Julian, and GG Lonzarich. Magnetic quantum phase transition in MnSi under hydrostatic pressure. *Physical Review B*, 55(13):8330, 1997.

[16] RS Perry, K Kitagawa, SA Grigera, RA Borzi, AP Mackenzie, K Ishida, and Y Maeno. Multiple first-order metamagnetic transitions and quantum oscillations in ultrapure $Sr_3Ru_2O_7$. *Physical review letters*, 92(16):166602, 2004.

[17] M Uhlarz, C Pfleiderer, and SM Hayden. Quantum phase transitions in the itinerant ferromagnet $ZrZn_2$. *Physical review letters*, 93(25):256404, 2004.

[18] V Taufour, Dai Aoki, G Knebel, and Jacques Flouquet. Tricritical point and wing structure in the itinerant ferromagnet UGe_2. *Physical review letters*, 105(21):217201, 2010.

[19] Dietrich Belitz, Theodore R Kirkpatrick, and Thomas Vojta. First order transitions and multicritical points in weak itinerant ferromagnets. *Physical review letters*, 82(23):4707, 1999.

[20] D Belitz, TR Kirkpatrick, and Thomas Vojta. How generic scale invariance influences quantum and classical phase transitions. *Reviews of modern physics*, 77(2):579, 2005.

[21] SS Saxena, P Agarwal, K Ahilan, FM Grosche, RKW Haselwimmer, MJ Steiner, E Pugh, IR Walker, SR Julian, P Monthoux, et al. Superconductivity on the border of itinerant-electron ferromagnetism in UGe_2. *Nature*, 406(6796):587–592, 2000.

[22] NT Huy, A Gasparini, DE De Nijs, Y Huang, JCP Klaasse, T Gortenmulder, Anne de Visser, A Hamann, T Görlach, and H v Löhneysen. Superconductivity on the border of weak itinerant ferromagnetism in UCoGe. *Physical Review Letters*, 99(6):067006, 2007.

[23] Adam P Pikul. The influence of magnetic sublattice dilution on magnetic order in $CeNiGe_3$ and $UNiSi_2$. *Journal of Physics: Condensed Matter*, 24(27):276003, 2012.

[24] Sara Ubaid-Kassis, Thomas Vojta, and Almut Schroeder. Quantum griffiths phase in the weak itinerant ferromagnetic alloy $Ni_{1-x}V_x$. *Physical review letters*, 104(6):066402, 2010.

[25] John A Hertz. Quantum critical phenomena. *Physical Review B*, 14(3):1165, 1976.

[26] Toru Moriya. *Spin fluctuations in itinerant electron magnetism*. Springer-Verlag, 1985.

[27] AJ Millis. Effect of a nonzero temperature on quantum critical points in itinerant fermion systems. *Physical Review B*, 48(10):7183, 1993.

[28] Andrey V Chubukov, Catherine Pépin, and Jerome Rech. Instability of the quantum-critical point of itinerant ferromagnets. *Physical review letters*, 92(14):147003, 2004.

[29] Thomas Vojta, D Belitz, TR Kirkpatrick, and R Narayanan. Quantum critical behavior of itinerant ferromagnets. *arXiv preprint cond-mat/9907404*, 1999.

[30] Philipp Gegenwart, Qimiao Si, and Frank Steglich. Quantum criticality in heavy fermion metals. *Nature Physics*, 4(186-197), 2008.

[31] Dietrich Belitz, Theodore R Kirkpatrick, and Thomas Vojta. Nonanalytic behavior of the spin susceptibility in clean fermi systems. *Physical Review B*, 55(15):9452, 1997.

[32] Una Karahasanovic, Frank Krüger, and Andrew G Green. Quantum order-by-disorder driven phase reconstruction in the vicinity of ferromagnetic quantum critical points. *Physical Review B*, 85(16):165111, 2012.

[33] C Lester, Silvia Ramos, RS Perry, TP Croft, RI Bewley, T Guidi, P Manuel, DD Khalyavin, EM Forgan, and SM Hayden. Field-tunable spin-density-wave phases in $Sr_3Ru_2O_7$. *Nature materials*, 14(4):373–378, 2015.

[34] Gino Abdul-Jabbar, Dmitry A Sokolov, Christopher D O'neill, Christopher Stock, Didier Wermeille, Franz Demmel, Frank Krüger, Andrew G Green, Florence Lévy-Bertrand, Béatrice Grenier, et al. Modulated magnetism in PrPtAl. *Nature Physics*, 11(4):321–327, 2015.

[35] R Khasanov, A Amato, P Bonfà, Z Guguchia, H Luetkens, E Morenzoni, R De Renzi, and ND Zhigadlo. High-pressure magnetic state of mnp probed by means of muon-spin rotation. *Physical Review B*, 93(18):180509, 2016.

[36] D Moroni-Klementowicz, M Brando, C Albrecht, WJ Duncan, FM Grosche, D Grüner, and G Kreiner. Magnetism in $Nb_{1-y}Fe_{2+y}$: Composition and magnetic field dependence. *Physical Review B*, 79(22):224410, 2009.

[37] Michèle Héritier. Transition de phase - généralités, 2007. Lecture notes - Chapter two.

[38] LD Landau. Ld landau, phys. z. sowjetunion 11, 26 (1937). *Phys. Z. Sowjetunion*, 11:26, 1937.

[39] Paul M Chaikin and Tom C Lubensky. *Principles of condensed matter physics*, volume 1. Cambridge university press Cambridge, 2000.

[40] S. Blundell. *Magnetism in Condensed Matter*. Oxford Master Series in Condensed Matter Physics. OUP Oxford, 2001.

[41] GG Lonzarich and Michael Springford. *Electron: a centenary volume*, chapter 6, pages 109–147. Cambridge University Press, 1997.

[42] Sven Friedemann, Will J Duncan, Max Hirschberger, Thomas W Bauer, Robert Küchler, Andreas Neubauer, Manuel Brando, Christian Pfleiderer, and F Malte Grosche. Quantum tricritical points in $NbFe_2$. *Nature Physics*, 14(1):62, 2017. DOI:10.1038/NPHYS4242.

[43] DA Tompsett, RJ Needs, FM Grosche, and GG Lonzarich. Doping-driven magnetic instabilities and quantum criticality of $NbFe_2$. *Physical Review B*, 82(15):155137, 2010.

[44] Yoshihiro Yamada, Yoshio Kitaoka, Kunisuke Asayama, and Akihiko Sakata. Nmr study of coexistence of ferro-and antiferromagnetism in the itinerant electron system $(Zr_{1-x}Nb_x)Fe_2$. i. *Journal of the Physical Society of Japan*, 53(9):3198–3209, 1984.

[45] Yoshihiro Yamada and Akihiko Sakata. Weak antiferromagnetism in $NbFe_2$. *Journal of the Physical Society of Japan*, 57(1):46–49, 1988.

[46] Masayuki Shiga and Yoji Nakamura. Magnetic properties of stoichiometric and off-stoichiometric $NbFe_2$. *Journal of the Physical Society of Japan*, 56(11):4040–4046, 1987.

[47] Alaska Subedi and David J Singh. Band structure and itinerant magnetism in quantum critical $NbFe_2$. *Physical Review B*, 81(2):024422, 2010.

[48] TD Haynes, I Maskery, MW Butchers, JA Duffy, JW Taylor, SR Giblin, C Utfeld, J Laverock, SB Dugdale, Y Sakurai, et al. Ferrimagnetism in Fe-rich $NbFe_2$. *Physical Review B*, 85(11):115137, 2012.

[49] William Duncan. *Quantum phase transitions in NbFe2 and BaFe2As2.* PhD thesis, Royal Holloway, University of London, 2010.

[50] A Neubauer, J Bœuf, A Bauer, B Russ, H v Löhneysen, and C Pfleiderer. Ultra-high vacuum compatible image furnace. *Review of Scientific Instruments*, 82(1):013902, 2011.

[51] WJ Duncan, OP Welzel, C Harrison, XF Wang, XH Chen, FM Grosche, and PG Niklowitz. High pressure study of $BaFe_2As_2$ - the role of hydrostaticity and uniaxial stress. *Journal of Physics: Condensed Matter*, 22(5):052201, 2010.

[52] A. Neubauer. *Ph.D. thesis.* PhD thesis, Technische Universität München, 2011.

[53] Noëlle Pottier. Physique statistique hors d'équilibre: équation de Boltzmann, réponse linéaire. DEA., 2006. <cel-00092930>.

[54] Gen Shirane, Stephen M Shapiro, and John M Tranquada. *Neutron scattering with a triple-axis spectrometer: basic techniques.* Cambridge University Press, 2002.

[55] I.A. Zaliznyak and S.H. Lee. *Magnetic Neutron Scattering*, chapter 1, pages 1–88. Brookhaven National Laboratory (US), Brookhaven National Laboratory (US), 7 2004.

[56] RM Moon, T Riste, and WC Koehler. Polarization analysis of thermal-neutron scattering. *Physical Review*, 181(2):920, 1969.

[57] Heinz Maier-Leibnitz Zentrum, Astrid Schneidewind, and Petr Čermák. Panda: Cold three axes spectrometer. *Journal of large-scale research facilities*, 1, 2015.

[58] Laboratoire Léon Brillouin - CEA / CNRS. *Experimental facilities*, 2003 edition edition, 2003.

[59] B Hennion. Structural and magnetic dynamical properties of solids. experimental approach with inelastic neutron scattering. *Acta Physica Polonica-Series A General Physics*, 96(5):629–640, 1999.

[60] RI Bewley, JW Taylor, and SM Bennington. Let, a cold neutron multi-disk chopper spectrometer at ISIS. *Nuclear Instruments and Methods in Physics Research Section A: Accelerators, Spectrometers, Detectors and Associated Equipment*, 637(1):128–134, 2011.

[61] Heinz Maier-Leibnitz Zentrum, Vladimir Hutanu, and Hao Deng. Poli: Polarised hot neutron diffractometer. *Journal of large-scale research facilities*, 1, 2015.

[62] Vladimir Hutanu, M Meven, S Masalovich, Gernot Heger, and Georg Roth. ^{3}He spin filters for spherical neutron polarimetry at the hot neutrons single crystal diffractometer POLI-HEiDi. In *Journal of Physics: Conference Series*, volume 294. IOP Publishing, 2011.

[63] F Tasset and E Ressouche. Optimum transmission for a ^{3}He neutron polarizer. *Nuclear Instruments and Methods in Physics Research Section A: Accelerators, Spectrometers, Detectors and Associated Equipment*, 359(3):537–541, 1995.

[64] L Passell and RI Schermer. Measurement of the spin dependence of the ^{3}He (n, p) t reaction and of the nuclear susceptibility of adsorbed ^{3}He. *Physical Review*, 150(1):146, 1966.

[65] H Thoma and V Hutanu. Polarization corrections for spherical neutron polarimetry with ^{3}He spin filter cells, 2017. in preparation.

[66] M Blume. Polarization effects in the magnetic elastic scattering of slow neutrons. *Physical Review*, 130(5):1670, 1963.

[67] SV Maleev, VG Bar'yakhtar, and RA Suris. The scattering of slow neutrons by complex magnetic structures. *Soviet Phys.-Solid State (English Transl.)*, 4, 1963.

[68] PJ Brown and Tapan Chatterji. *Neutron scattering from magnetic materials*, chapter 5, pages 215–244. Elsevier, 2005.

[69] P. Link and A. Schneidewind. *Monitor correction for higher order neutrons.* Jülich Forschungszentrum, June 2007.

[70] James Nicholas Poulten. *Composition-tuned magnetic order and excitations in $Nb_{1-x}Fe_{2+x}$ and pressure-induced changes in structural and optical properties of Cu_2OSeO_3*. PhD thesis, Royal Holloway, University of London, 2018.

[71] 4F2: Cold Neutron Three Axis Spectrometer. `http://www-drecam.cea.fr/llb/spectros/pdf/4f2-llb.pdf`, 2003. Accessed: 2019-08-14.

[72] Astrid Schneidewind, P Link, D Etzdorf, R Schedler, M Rotter, and M Loewenhaupt. PANDA-first results from the cold three-axes spectrometer at FRM-II. *Physica B: Condensed Matter*, 385:1089–1091, 2006.

[73] Ryogo Kubo. Statistical-mechanical theory of irreversible processes. i. general theory and simple applications to magnetic and conduction problems. *Journal of the Physical Society of Japan*, 12(6):570–586, 1957.

[74] Ryogo Kubo. The fluctuation-dissipation theorem. *Reports on progress in physics*, 29(1):255, 1966.

[75] Harry Nyquist. Thermal agitation of electric charge in conductors. *Physical review*, 32(1):110, 1928.

[76] Lars Onsager. Reciprocal relations in irreversible processes. i. *Physical review*, 37(4):405, 1931.

[77] Lars Onsager. Reciprocal relations in irreversible processes. ii. *Physical review*, 38(12):2265, 1931.

Appendix A

APPENDIX

A.1 Fluctuation-dissipation theorem

The common way to measure a system is by observing its response to a weak perturbation field. Three different information can be extracted from this: the response function (ϕ), the relaxation function (Φ) and the admittance (χ).

The response function gives the temporal evolution of the system.

The relaxation function is the evolution of the system towards equilibrium after turning off the perturbation field.

The admittance is the behaviour of the system when the perturbation is harmonic.

We will see that these quantities are linked together by the different correlation functions [73].

A.1.1 Heisenberg representation

In quantum mechanics any observable physical quantity has an associated *hermitian operator*. Let A be such an operator. In the Heisenberg representation the time-dependence of A is given by [53]:

$$A(t) = e^{\frac{iH_0t}{\hbar}} A e^{\frac{-iH_0t}{\hbar}}, \tag{A.1.1}$$

where H_0 is the time-independent Hamiltonian of the system at thermodynamical equilibrium. The time-evolution of $A(t)$ is given by the Heisenberg equation [53]:

$$i\hbar\frac{\mathrm{d}A(t)}{\mathrm{d}t} = [A(t), H_0], \tag{A.1.2}$$

where the square brackets represent the commutator.

A.1.2 Density matrix

We consider $|\psi_i\rangle$, a wave function describing a microscopic state of a quantum system. $|\psi_i\rangle$ is a linear combination of the eigenvectors of the system:

$$|\psi_i\rangle = \sum_n c_{ni} |\phi_n\rangle . \tag{A.1.3}$$

If A is a quantum operator associated to an observable, the average value of A is given by

$$\begin{aligned} \langle A\rangle &= \sum_i p_i \langle\psi_i| A |\psi_i\rangle \\ &= \sum_i p_i \sum_{m,n} \langle\phi_m| A |\phi_n\rangle c^*_{mi} c_{ni}, \end{aligned} \tag{A.1.4}$$

where p_i is the probability of observing the microscopic state i. The density matrix is defined as

$$\rho = \sum_i |\psi_i\rangle p_i \langle\psi i| , \tag{A.1.5}$$

and the average value of A becomes

$$\langle A\rangle = \mathrm{Tr}\,(\rho A) , \tag{A.1.6}$$

Where Tr is the trace. The element at the m^{th} row, n^{th} column in ρ is :

$$\begin{aligned} \rho_{mn} &= \langle\phi_m| \rho |\phi_n\rangle \\ &= \sum_i p_i c_{mi} c^*_{ni}. \end{aligned} \tag{A.1.7}$$

Using the Schrödinger equation for ψ_k

$$i\hbar\frac{\mathrm{d}\,|\psi_k\rangle}{\mathrm{d}t} = H |\psi_k\rangle , \tag{A.1.8}$$

where H is the Hamiltonian of the system, and the definition of the ρ in Equation A.1.5 gives the equation of evolution of the density operator is given by the Liouville-von Neumann equation

$$\begin{aligned} \frac{\partial \rho}{\partial t} &= -\frac{i}{\hbar}\left[H, \rho\right] \\ &= -i\mathscr{L}\rho, \end{aligned} \tag{A.1.9}$$

where the square brackets represent the commutator and $\mathscr{L}$ is the quantum Liouville operator defined as

$$\mathscr{L}\rho = \frac{1}{\hbar}\left[H, \rho\right]. \tag{A.1.10}$$

A.1.3 Response function

We consider a system, initially at thermodynamical equilibrium and Hamiltonian H_0. At $t = -\infty$ we turn on a weak perturbation field a and A is the operator conjugated to the perturbation (e.g.: if a is a magnetic field, then A would be the magnetisation). The response function ϕ_{BA} gives the change observed on the physical quantity B when the system is perturbed by the field a.

A.1.3.1 First order correction of the density matrix

The Hamiltonian of the system at equilibrium is H_0 and the density matrix is ρ_0. When the weak perturbation $a(t)$ with Hamiltonian $H_1(t) = -a(t)A(t)$ is turned on, at first order the Hamiltonian and the density matrix of the perturbed system become [74, 53]

$$\begin{aligned} H(t) &= H_0 + H_1(t) \\ \rho(t) &= \rho_0 + \delta\rho(t), \end{aligned} \tag{A.1.11}$$

where $\delta\rho(t)$ is the first order correction to the perturbation field a.

Using the Equation A.1.9, in first order approximation, the correction of the density matrix is [74]

$$\delta\rho(t) = \frac{1}{i\hbar}\int_{-\infty}^{t} e^{-i\mathscr{L}_0(t-t')}\left[-i\mathscr{L}_1(t')\rho_0\right]\mathrm{d}t', \tag{A.1.12}$$

where $\mathscr{L}_0$ and $\mathscr{L}_1$ are the quantum Liouville operators, introduced in Equation A.1.10, for H_0, Hamiltonian of the system at equilibrium and H_1, the Hamiltonian of the perturbation. Using $H_1(t) = -a(t)A(t)$ and the time evolution of an operator in the Heisenberg representation

(Equation A.1.1) [53]

$$\begin{aligned} \delta\rho(t) &= \frac{1}{i\hbar}\int_{-\infty}^{t} a(t')\left[\rho_0, A^{\mathrm{H}}(t'-t)\right]\mathrm{d}t' \\ \text{with} \quad A^{\mathrm{H}}(t) &= e^{\frac{iH_0t}{\hbar}}A(0)e^{\frac{-iH_0t}{\hbar}}. \end{aligned} \tag{A.1.13}$$

A.1.3.2 Response function ϕ

In the Schrödinger representation, the time dependence of an observable B perturbed by $a(t)$ is carried by the density operator ρ [53]:

$$\begin{aligned} \langle B(t)\rangle_a &= \mathrm{Tr}\left(\rho(t)B\right) \\ &= \mathrm{Tr}\left(\rho_0 B\right) + \mathrm{Tr}\left(\delta\rho(t)B\right). \end{aligned} \tag{A.1.14}$$

$\mathrm{Tr}\left(\rho_0 B\right)$ is the average value of B of the unperturbed system at thermodynamical equilibrium, which is null if B is centred. The change of the physical quantity B due to the perturbation $a(t)$ is

$$\begin{aligned} \delta\langle B(t)\rangle_a &= \mathrm{Tr}\left(\rho(t)B\right) - \mathrm{Tr}\left(\rho_0 B\right) \\ &= \mathrm{Tr}\left(\delta\rho(t)B\right). \end{aligned} \tag{A.1.15}$$

Replacing $\delta\rho(t)$ in Equation A.1.15 by the expression derived in Equation A.1.13 yields:

$$\begin{aligned} \delta\langle B(t)\rangle_a &= \frac{1}{i\hbar}\int_{-\infty}^{t} a(t')\mathrm{Tr}\left(\left[\rho_0, A^{\mathrm{H}}(t'-t)\right]B(0)\right)\mathrm{d}t' \\ &= \frac{1}{i\hbar}\int_{-\infty}^{t} a(t')\mathrm{Tr}\left(A^{\mathrm{H}}(t'-t), \left[B(0)\right]\rho_0\right)\mathrm{d}t' \\ &\text{(we used} \quad \mathrm{Tr}(ABC) = \mathrm{Tr}(CAB) = \mathrm{Tr}(BCA)) \\ &= \frac{1}{i\hbar}\int_{-\infty}^{t} a(t')\langle\left[A(0), B^{\mathrm{H}}(t-t')\right]\rangle\mathrm{d}t' \\ &\text{(we used the invariance by time shift at equilibrium)} \quad . \end{aligned} \tag{A.1.16}$$

$B^{\mathrm{H}}(t-t')$ is the time dependence of B in the Heisenberg representation (Equation A.1.1), which only depends on the Hamiltonian of the system at equilibrium H_0. We will refer to $B^{\mathrm{H}}(t)$ as $B(t)$. Equations A.1.16 show that the time evolution of $\delta\langle B(t)\rangle_a$ only depends on properties of

the non-perturbed system. The response function is defined as [74]

$$\begin{aligned}\phi_{BA}(t) &= \frac{1}{i\hbar}\mathrm{Tr}\left(\rho_0\left[A(0), B(t)\right]\right) \\ &= \frac{1}{i\hbar}\langle[A(0), B(t)]\rangle,\end{aligned} \tag{A.1.17}$$

and it is called the *Kubo* response function. $\delta\langle B(t)\rangle_a$ becomes

$$\delta\langle B(t)\rangle_a = \int_{-\infty}^{t} a(t')\phi_{BA}(t-t')\mathrm{d}t'. \tag{A.1.18}$$

If we use the spectral function, which is defined as [53]

$$\xi_{BA}(t) = -\frac{1}{2\hbar}\langle[A(0), B(t)]\rangle, \tag{A.1.19}$$

then the Kubo response function becomes

$$\phi_{BA}(t) = 2i\xi_{BA}(t). \tag{A.1.20}$$

A.1.4 Relaxation Φ

For a system in which a perturbation is switched on at $t = -\infty$, the relaxation of a physical quantity B is its evolution back to equilibrium *after* that the perturbation is turned off. For instance, if a magnetic field (the perturbation) is applied to a paramagnetic system, when we turn off the field the magnetisation relaxes back to zero, its equilibrium state. It the perturbation $a(t)$ is applied to the system at $t = -\infty$, and A its conjugated physical quantity, the relaxation of $\delta\langle B(t)\rangle_a$ after the perturbation is switched off (at $t = 0$) is [73]

$$\delta\langle B(t)\rangle_a = \int_{-\infty}^{0} a(t')\phi_{BA}(t-t')\mathrm{d}t'. \tag{A.1.21}$$

If we consider the example of a constant perturbation ($a(t) = a_0, \forall t \leq 0$), then, by posing $\tau = t - t'$, we have

$$\delta\langle B(t)\rangle_a = a_0\int_{t}^{\infty}\phi_{BA}(\tau)\mathrm{d}\tau \quad \text{for} \quad t > 0 \tag{A.1.22}$$

and the relaxation function is given by [73]

$$\Phi_{BA}(t) = \lim_{\epsilon\to 0^+}\int_{t}^{\infty}\phi_{BA}(\tau)e^{-\epsilon\tau}\mathrm{d}\tau. \tag{A.1.23}$$

A.1.5 Admittance χ

When the perturbation $a(t)$ is harmonic, it can be written as $a(t) = \mathrm{Re}[a(\omega)]$, where $a(\omega) = a_0 e^{i\omega t}$. Using this harmonic perturbation in Equation A.1.16 yields

$$\begin{aligned}\delta\langle B(t)\rangle_a &= \int_{-\infty}^{t} \mathrm{Re}\left[a_0 e^{i\omega t'}\right] \phi_{BA}(t-t')\mathrm{d}t' \\ &= \mathrm{Re}\left[a_0 e^{i\omega t} \int_0^{\infty} \phi_{BA}(\tau) e^{-i\omega\tau}\mathrm{d}\tau\right].\end{aligned} \tag{A.1.24}$$

The *admittance* is defined as (theorem 1 in [73])

$$\begin{aligned}\chi_{BA}(\omega) &= \lim_{\epsilon\to 0^+} \int_0^{\infty} \phi_{BA}(t) e^{-i\omega t} e^{-\epsilon t}\mathrm{d}t \\ &= \int_0^{\infty} \phi_{BA}(t) e^{-i\omega t}\mathrm{d}t \\ &= 2i\int_0^{\infty} \xi_{BA}(t) e^{-i\omega t}\mathrm{d}t.\end{aligned} \tag{A.1.25}$$

Thus we can write Equation A.1.24

$$\delta\langle B(t)\rangle_a = \mathrm{Re}\left[a_0 e^{i\omega t}\chi_{BA}(\omega)\right]. \tag{A.1.26}$$

The admittance can also be derived from the relaxation function given in Equation A.1.23 (theorem 2 in [73]):

$$\chi_{BA}(\omega) = \Phi_{BA}(0) - i\omega\int_0^{\infty} \Phi_{BA}(t) e^{-i\omega t}\mathrm{d}t. \tag{A.1.27}$$

From the Kubo response function in Equation A.1.17 and the invariance of the trace with cyclic permutations, $\phi_{BA}(t)$ rewrites

$$\phi_{BA}(t) = \frac{1}{i\hbar}\mathrm{Tr}\left(\left[\rho_0, A\right] B(t)\right), \tag{A.1.28}$$

where $B(t)$ is the time dependent operator in the Heisenberg representation and $A = A(0)$. We consider the following identity [73]:

$$\begin{aligned}\left[\rho_0, A\right] &= \rho_0 \int_0^{\beta} e^{\lambda H_0}\left[A, H_0\right] e^{-\lambda H_0}\mathrm{d}\lambda \\ &= i\hbar\rho_0 \int_0^{\beta} e^{\lambda H_0}\dot{A} e^{-\lambda H_0}\mathrm{d}\lambda,\end{aligned} \tag{A.1.29}$$

where $\beta = \frac{1}{k_B T}$ and $\dot{A}$ is the time derivative of A at $t = 0$ ($i\hbar\dot{A} = [A(t), H_0]_{t=0}$) and we find that

$$[\rho_0, A] = i\hbar \int_0^\beta \mathrm{d}\lambda \rho_0 \dot{A}(-i\hbar\lambda), \tag{A.1.30}$$

where $\dot{A}(-i\hbar\lambda)$ is a Heisenberg operator as in Equation A.1.1 with an imaginary time $t = -i\hbar\lambda$.

Using A.1.30 in Equation A.1.28 yields

$$\phi_{BA}(t) = \int_0^\beta \langle \dot{A}(-i\hbar\lambda) B(t) \rangle \mathrm{d}\lambda. \tag{A.1.31}$$

If we use the canonical correlation function of X and Y

$$\langle X; Y \rangle = \frac{1}{\beta} \int_0^\beta \mathrm{d}\lambda \mathrm{Tr}\left(\rho_0 e^{\lambda H_0} X e^{-\lambda H_0} Y\right) \tag{A.1.32}$$

introduced by Kubo in [74] and Equation A.1.30, we find that

$$\langle [A(0), B(t)] \rangle = i\hbar\beta \langle \dot{A}(0); B(t) \rangle \tag{A.1.33}$$

and, with the spectral function:

$$\xi_{BA}(t) = -\frac{i\beta}{2} \langle \dot{A}(0); B(t) \rangle. \tag{A.1.34}$$

Thus the response function and the admittance become

$$\phi_{BA}(t) = \beta \langle \dot{A}(0); B(t) \rangle \tag{A.1.35}$$

$$\chi_{BA}(\omega) = \beta \int_0^\infty \langle \dot{A}(0); B(t) \rangle e^{-i\omega t} \mathrm{d}t. \tag{A.1.36}$$

A.1.6 Correlation functions

A.1.6.1 Fourier transform

In this section, we choose the following convention for the Fourier transform and its reciprocal:

$$\hat{f}(\omega) = \int_{-\infty}^\infty f(t) e^{-i\omega t} \mathrm{d}t \tag{A.1.37}$$

$$f(t) = \frac{1}{2\pi} \int_{-\infty}^\infty f(\omega) e^{i\omega t} \mathrm{d}\omega, \tag{A.1.38}$$

where $\hat{f}$ is the Fourier transform of the function f.

A.1.6.2 Symmetric correlation function

The symmetrised correlation function of two quantum operators A and B is [74]:

$$\langle\{AB\}\rangle = \mathrm{Tr}\left[\frac{\rho_0}{2}\left(AB + BA\right)\right], \tag{A.1.39}$$

where ρ_0 is the density matrix of the system at thermodynamical equilibrium. A and B can be time and space dependent ($A = A(\boldsymbol{r}, t)$ and $B = B(\boldsymbol{r}, t)$). If $A \equiv B$, $\langle\{AB\}\rangle = \langle\{A^2\}\rangle$ is called the auto-correlation function and $\langle\{A^2\}\rangle \geq 0$ [74].

A.1.6.3 Properties of the correlation functions

If the system is at equilibrium, then $\langle\{AB\}\rangle$ is stationary and [74]

$$\langle\{A(0)B(t)\}\rangle = \langle\{A(t_0)B(t + t_0)\}\rangle. \tag{A.1.40}$$

$\langle\{AB\}\rangle$ depends only on the distance between the times t and t_0.

In general [74]

$$\langle\{AB\}\rangle = \langle\{BA\}\rangle, \tag{A.1.41}$$

and thus, with the stationary property

$$\langle\{A(0)B(t)\}\rangle = \langle\{B(0)A(-t)\}\rangle \tag{A.1.42}$$

$$\langle\{A(0)A(t)\}\rangle = \langle\{A(0)A(-t)\}\rangle. \tag{A.1.43}$$

$\langle\{A(0)A(t)\}\rangle$ is the symmetric auto-correlation function. Those properties also apply to the canonical correlation function introduced in Equation A.1.32.

A.1.6.4 Spectral density and correlation spectrum

The spectral density or power spectrum of $A(0)$ and $B(t)$ is the Fourier transform of the spectral function $\xi_{BA}(t) = -\frac{1}{2\hbar}\langle[A(0), B(t)]\rangle$ defined in Equation A.1.19:

$$\hat{\xi}_{BA}(\omega) = \int_{-\infty}^{\infty} \xi_{BA}(t) e^{-i\omega t} \mathrm{d}t. \tag{A.1.44}$$

If we use the canonical or the symmetric correlation functions, we find that the correlation spectra are[1] [74]

$$G^c_{BA}(\omega) = \int_{-\infty}^{\infty} \langle A(0); B(t)\rangle e^{-i\omega t} \mathrm{d}t \tag{A.1.45}$$

$$G^s_{BA}(\omega) = \int_{-\infty}^{\infty} \langle \{A(0)B(t)\}\rangle e^{-i\omega t} \mathrm{d}t, \tag{A.1.46}$$

where $G^c_{BA}(\omega)$ is the canonical correlation spectrum and $G^s_{BA}(\omega)$ the symmetric correlation spectrum of $A(0)$ and $B(t)$.

The Fourier transform of the canonical and symmetric correlation functions are:

$$\langle A(\omega); B(\omega')\rangle = 2\pi\delta(\omega + \omega')G^c_{BA}(\omega) \tag{A.1.47}$$

$$\langle \{A(\omega)B(\omega')\}\rangle = 2\pi\delta(\omega + \omega')G^s_{BA}(\omega). \tag{A.1.48}$$

A.1.6.5 Relationship between $G^c_{BA}(\omega)$ and $G^s_{BA}(\omega)$

If A and B are two quantum operators, which do not commute in general ($\langle A(0)B(t)\rangle \neq \langle B(t)A(0)\rangle$), we have [74]

$$\int_{-\infty}^{\infty} \langle A(0)B(t)\rangle e^{-i\omega t} \mathrm{d}t = e^{\beta\hbar\omega} \int_{-\infty}^{\infty} \langle B(t)A(0)\rangle e^{-i\omega t} \mathrm{d}t. \tag{A.1.49}$$

From Equation A.1.49, we find that

$$\hat{\xi}_{BA}(\omega) = -\frac{\omega}{2E_\beta(\omega)} G^s_{BA}(\omega), \tag{A.1.50}$$

where $E_\beta(\omega) = \frac{1}{2}\hbar\omega \coth\left(\frac{\beta\hbar\omega}{2}\right)$. If we use property A.1.42 on $\langle \dot{A}(0); B(t)\rangle$ in Equation A.1.34 and then take the Fourier transform, we find that

$$\hat{\xi}_{BA}(\omega) = -\frac{\beta\omega}{2} G^c_{BA}(\omega). \tag{A.1.51}$$

And finally Equation A.1.50 and Equation A.1.51 yield

$$G^c_{BA}(\omega) = \frac{1}{\beta E_\beta(\omega)} G^s_{BA}(\omega). \tag{A.1.52}$$

[1] here again, we use the convention given in Equation A.1.37 for the Fourier transform.

A.1.7 Fluctuation-dissipation theorem

The *fluctuation-dissipation* theorem is the relationship between the correlation spectra and the dissipation of the admittance. Equation A.1.50 for the symmetric correlation and Equation A.1.51 for the canonical correlation, are two formulations of the theorem. The latter can be used in two ways:

1. to predict the characteristics of the fluctuation or the noise intrinsic to the system from the response function, which is known ([75])

2. to predict the response function by observing the thermal fluctuations of the system ([76, 77]).

A classic example used to illustrate the theorem is the Brownian (stochastic) movement of a pollen particle in water. The pollen particle is brought into motion by the water molecules hitting it. The pollen particle, which is the receptor of the motion, moves randomly and is fluctuating (Brownian motion). If now the pollen particle becomes motor, it transmits its motion to the surrounding water molecules, generating friction. Thus we see that collisions between the pollen and the water molecules create either a fluctuating driving force if the pollen is receptor or a dissipative frictional force if the pollen is motor. Both forces have the same origin and are related by the *fluctuation-dissipation* theorem.

A.2 Inelastic chapter

A.2.1 Background signal of LET with Sample C

A.2.1.1 Incident neutron energy of 2.48 meV

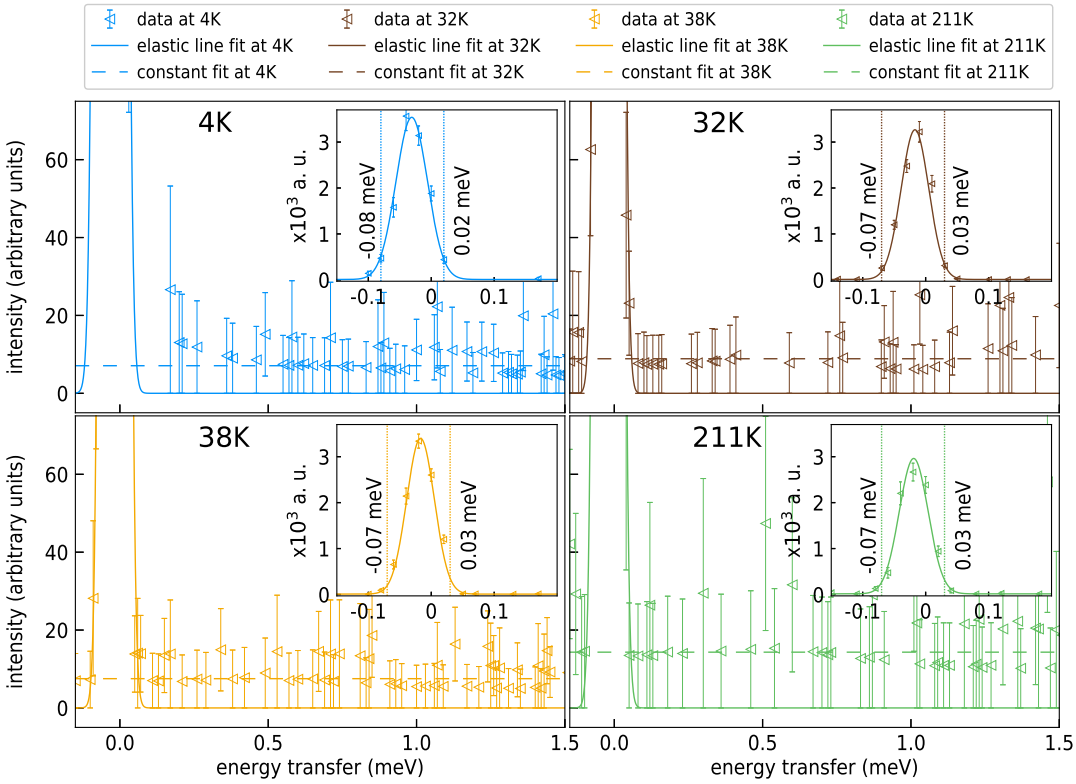

A.2.1.2 Incident neutron energy of 4.35 meV

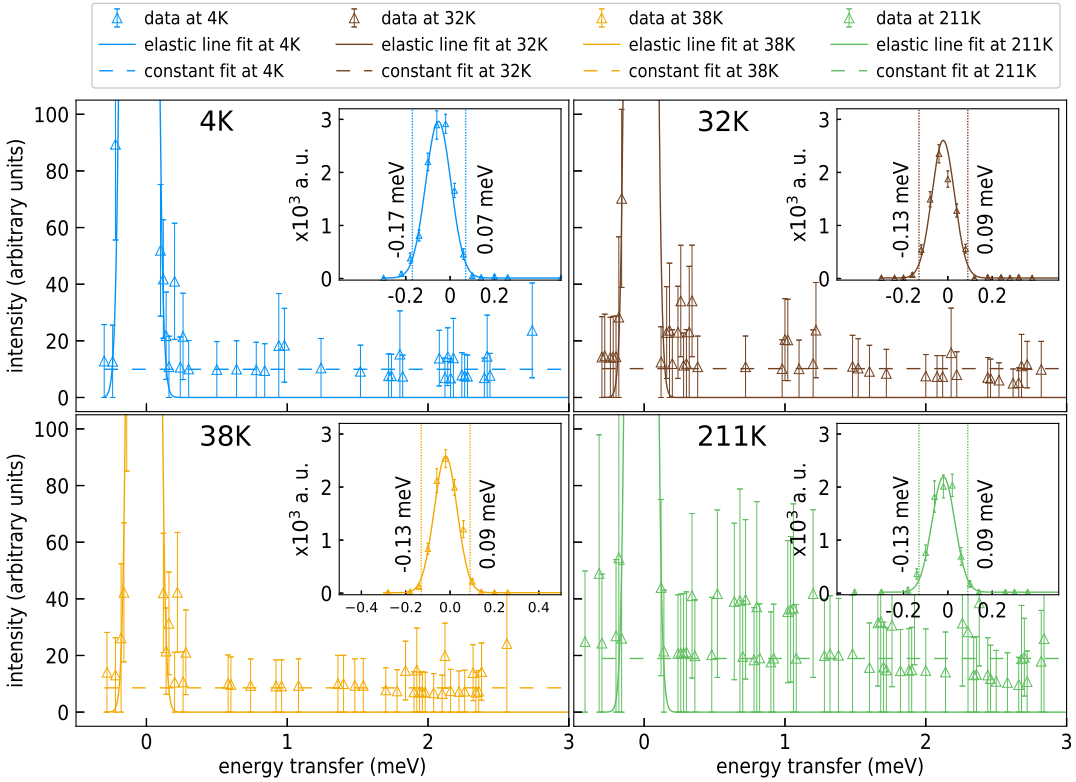

A.2.1.3 Incident neutron energy of 9.5 meV

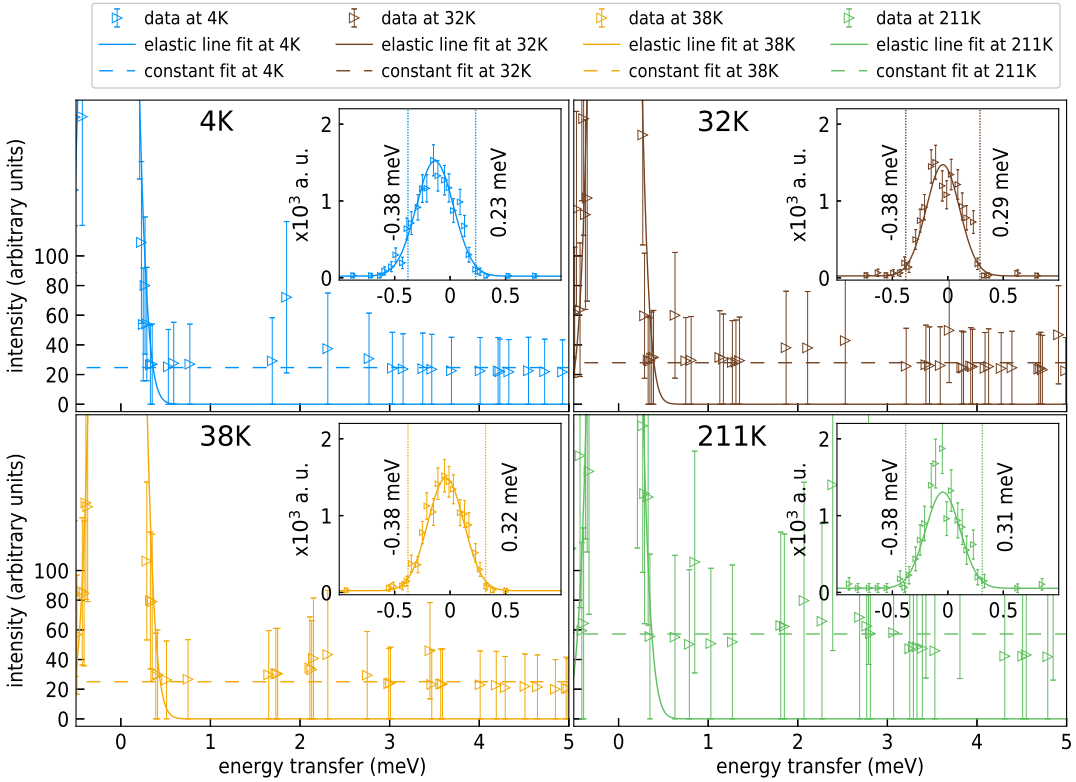

A.2.2 Measurements summary

A.2.2.1 Measurements of Sample A

Exhaustive list of measured positions in r.l.u. and temperatures in Samples A. All the signals were measured with Panda and fitted with an over-damped harmonic oscillator (ODHO) function.

SAMPLE A					
5K	(0 0 2)	(0 0 2.05)	13.8K	(0 0 2.2)	(0 0 2.25)
	(0 0 2.1)	(0 0 2.158)		(0 0 2.3)	(0 0 2.4)
	(0 0 2.2)	(0 0 2.25)		(0.025 0 2.158)	(0.05 0 2.158)
	(0 0 2.3)	(0 0 2.4)	30K	(0 0 2.156)	
	(0.025 0 2.158)	(0.05 0 2.158)	50K	(0 0 2.156)	
13K	(0 0 2.157)		100K	(0 0 2.156)	
13.8K	(0 0 2)	(0 0 2.05)	200K	(0 0 2.156)	
	(0 0 2.1)	(0 0 2.151)			

A.2.2.2 Measurements of Sample B

Exhaustive list of measured positions in r.l.u. and temperatures in Sample B. *d*, *o* or *so* near the *hkl*-positions indicates whether the data is fitted with a damped harmonic oscillator (DHO), an ODHO or a soft over-damped harmonic oscillator (SODHO) function. The symbols □ and ○ indicate which instrument we used (□ for Panda and ○ for 4F2).

SAMPLE B (d: DHO fit function, o: ODHO fit function)					
5K□	(0 0 2): d	(0 0 2.094): d	22.4K○	(0.025 0 2): d	(0.05 0 2): d
5.2K○	(0 0 2): d	(0 0 2.05): d		(0.1 0 2): o	
	(0 0 2.092): d	(0 0 2.15): d	25K□	(0 0 2): so	(0 0 2.095): d
	(0 0 2.2): d	(0 0 2.25): d	29K□	(0 0 2): d	(0 0 2.108): d
	(0 0 2.3): d	(0 0 2.4): o	32K□	(0 0 2): o	(0 0 2.11): o
	(0.025 0 2): d	(0.05 0 2): d	34.1K○	(0 0 2): o	(0 0 2.05): o
	(0.1 0 2): o			(0 0 2.109): o	(0 0 2.15): o
12K□	(0 0 2): d	(0 0 2.094): d		(0 0 2.2): o	(0 0 2.25): o
15K□	(0 0 2): d	(0 0 2.094): d		(0 0 2.3): o	(0 0 2.4): o
19K□	(0 0 2): d	(0 0 2.087): d		(0.025 0 2.109): o	(0.05 0 2.109): o
22K□	(0 0 2): d	(0 0 2.088): d		(0.1 0 2.109): o	
22.4K○	(0 0 2): d	(0 0 2.05): d	35K□	(0 0 2): o	(0 0 2.111): o
	(0 0 2.102): d	(0 0 2.15): d	50K□	(0 0 2): o	(0 0 2.111): o
	(0 0 2.2): d	(0 0 2.25): d	120K□	(0 0 2): o	
	(0 0 2.3): o	(0 0 2.4): o			

A.2.2.3 Measurements of Sample C with 4F2

Exhaustive list of measured positions in r.l.u. and temperatures in Sample C with 4F2 instrument. *d* or *o* near the *hkl*-positions indicates whether the data is fitted with a DHO or an ODHO function.

SAMPLE C (d: DHO fit function, o: ODHO fit function)					
5.1K	(0 0 2.093): d		32K	(0.025 0 2): d	(0.05 0 2): d
18.6K	(0 0 2.093): d			(0.1 0 2): o	
24.3K	(0 0 2.093): d		34.8K	(0 0 2.093): o	
32K	(0 0 2): d	(0 0 2.05): d	38K	(0 0 2.093): o	(0.025 0 2.093): o
	(0 0 2.093): d	(0 0 2.1): d		(0.05 0 2.093): o	(0.1 0 2.093): o
	(0 0 2.15): o	(0 0 2.2): o	42.2K	(0 0 2.093): o	
	(0 0 2.25): o	(0 0 2.3): o	50.3K	(0 0 2.093): o	
	(0 0 2.35): o	(0 0 2.4): o	100.3K	(0 0 2.093): o	

A.2.2.4 Measurements of Sample C with LET

Exhaustive list of measured positions in r.l.u. and temperatures in Sample C with LET instrument and for incident neutrons energy of 1.6 meV and 2.48 meV. *d* or *o* near the *hkl*-positions indicates whether the data is fitted with a DHO or an ODHO function, with the left character referring to the 1.6meV data and the right character referring to the 2.48meV data. ∅ indicates an unsuccessful fit.

SAMPLE C: 1.6 **and** 2.48 meV (d: DHO fit function, o: ODHO fit function, ∅: no fit)					
4K	(0 0 2): ∅,d	(0 0 1.95): ∅,d	32K	(0 0 1.7): o,o	(0 0 1.65): o,o
	(0 0 1.91): ∅,d	(0 0 1.85): ∅,d		(0 0 1.6): ∅,o	
	(0 0 1.8): ∅,d	(0 0 1.75): ∅,d	38K	(0 0 2): ∅,o	(0 0 1.95): ∅,o
	(0 0 1.7): ∅,d			(0 0 1.891): o,o	(0 0 1.85): o,o
32K	(0 0 2): ∅,d	(0 0 1.95): d,d		(0 0 1.8): o,o	(0 0 1.75): o,o
	(0 0 1.891): d,d	(0 0 1.85): d,o		(0 0 1.7): o,o	(0 0 1.65): o,o
	(0 0 1.8): d,o	(0 0 1.75): o,o		(0 0 1.6): o,o	

Exhaustive list of measured positions in r.l.u. and temperatures in Sample C with LET instrument and for incident neutrons energy of 4.35 meV. *d* or *o* near the *hkl*-positions indicates whether the data is fitted with a DHO or an ODHO function and ∅ indicates an unsuccessful fit.

SAMPLE C: 4.35 meV (d: DHO fit function, o: ODHO fit function, ∅: no fit)					
4K	(0 0 2): d	(0 0 2.05): d	32K	(0.1 0 2): ∅	(0.1 0 2.109): o
	(0 0 2.09): d	(0 0 2.15): d	38K	(0 0 2): o	(0 0 2.05): o
	(0 0 2.2): d	(0 0 2.25): d		(0 0 2.109): o	(0 0 2.15): o
	(0 0 2.3): d	(0 0 2.35): d		(0 0 2.2): o	(0 0 2.25): o
	(0 0 2.4): d			(0 0 2.3): o	(0 0 2.35): o
	(0.02 0 2): d	(0.02 0 2.09): d		(0 0 2.4): o	
	(0.025 0 2): d	(0.025 0 2.09): d		(0.02 0 2): o	(0.02 0 2.109): o
	(0.04 0 2): d	(0.04 0 2.09): d		(0.025 0 2): o	(0.025 0 2.109): o
	(0.05 0 2): d	(0.05 0 2.09): d		(0.04 0 2): o	(0.04 0 2.109): o
	(0.06 0 2): d	(0.06 0 2.09): d		(0.05 0 2): o	(0.05 0 2.109): o
	(0.08 0 2): d	(0.08 0 2.09): o		(0.06 0 2): o	(0.06 0 2.109): o
	(0.1 0 2): d	(0.1 0 2.09): ∅		(0.08 0 2): o	(0.08 0 2.109): o
32K	(0 0 2): d	(0 0 2.05): o		(0.1 0 2): o	(0.1 0 2.109): o
	(0 0 2.109): o	(0 0 2.15): o	211K	(0 0 2): o	(0 0 2.05): o
	(0 0 2.2): o	(0 0 2.25): o		(0 0 2.109): o	(0 0 2.15): ∅
	(0 0 2.3): o	(0 0 2.35): o		(0 0 2.2): ∅	(0 0 2.25): ∅
	(0 0 2.4): o			(0 0 2.3): ∅	(0 0 2.35): ∅
	(0.02 0 2): o	(0.02 0 2.109): o		(0 0 2.4): ∅	
	(0.025 0 2): o	(0.025 0 2.109): o		(0.02 0 2): o	(0.02 0 2.109): ∅
	(0.04 0 2): o	(0.04 0 2.109): o		(0.025 0 2): o	(0.025 0 2.109): ∅
	(0.05 0 2): o	(0.05 0 2.109): o		(0.04 0 2): o	(0.04 0 2.109): ∅
	(0.06 0 2): o	(0.06 0 2.109): o		(0.05 0 2): o	(0.05 0 2.109): ∅
	(0.08 0 2): o	(0.08 0 2.109): o			

A.2.3 Fit of the additional data measured with Sample C

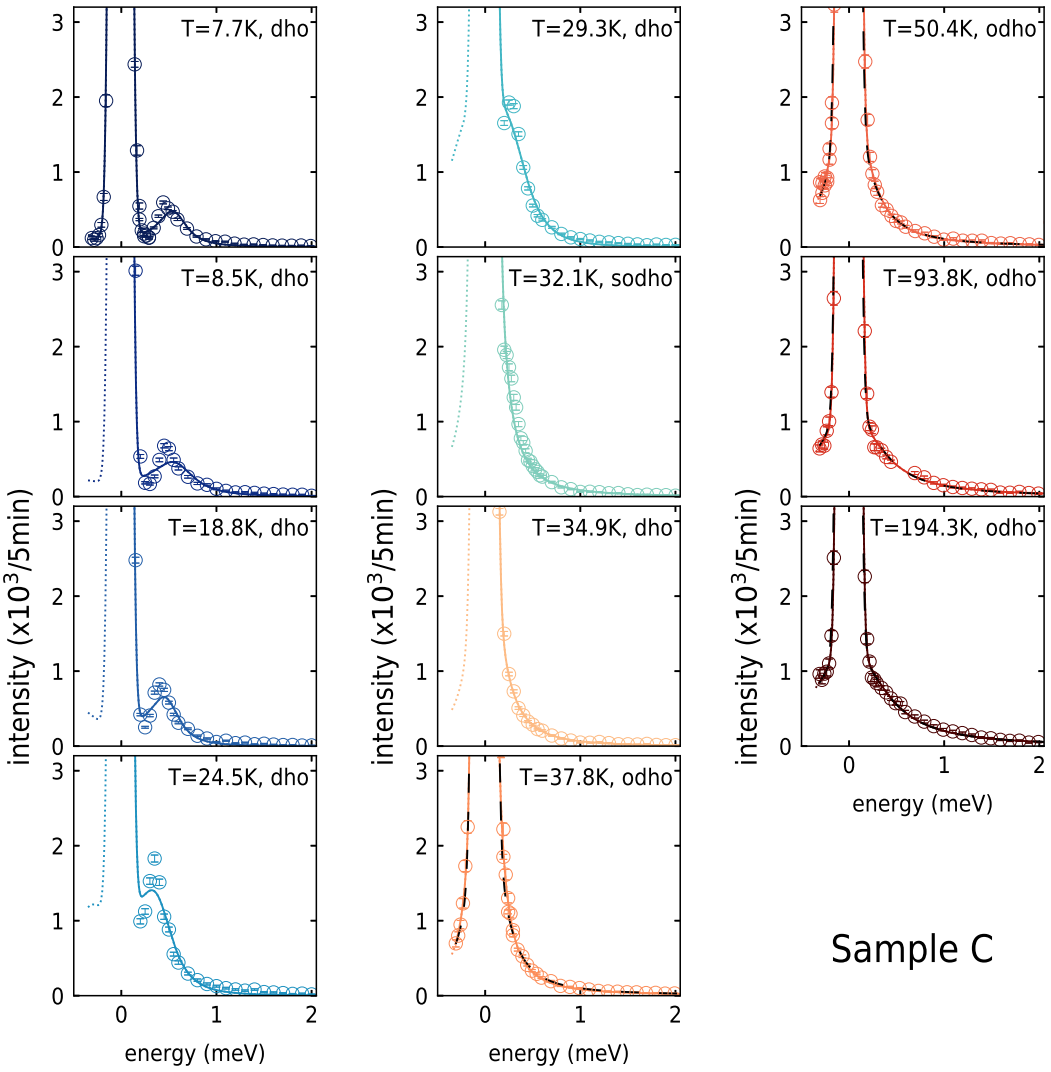

A.2.4 h-dependence of the magnetic excitations

A.2.4.1 Sample B at the ferromagnetic (FM) position

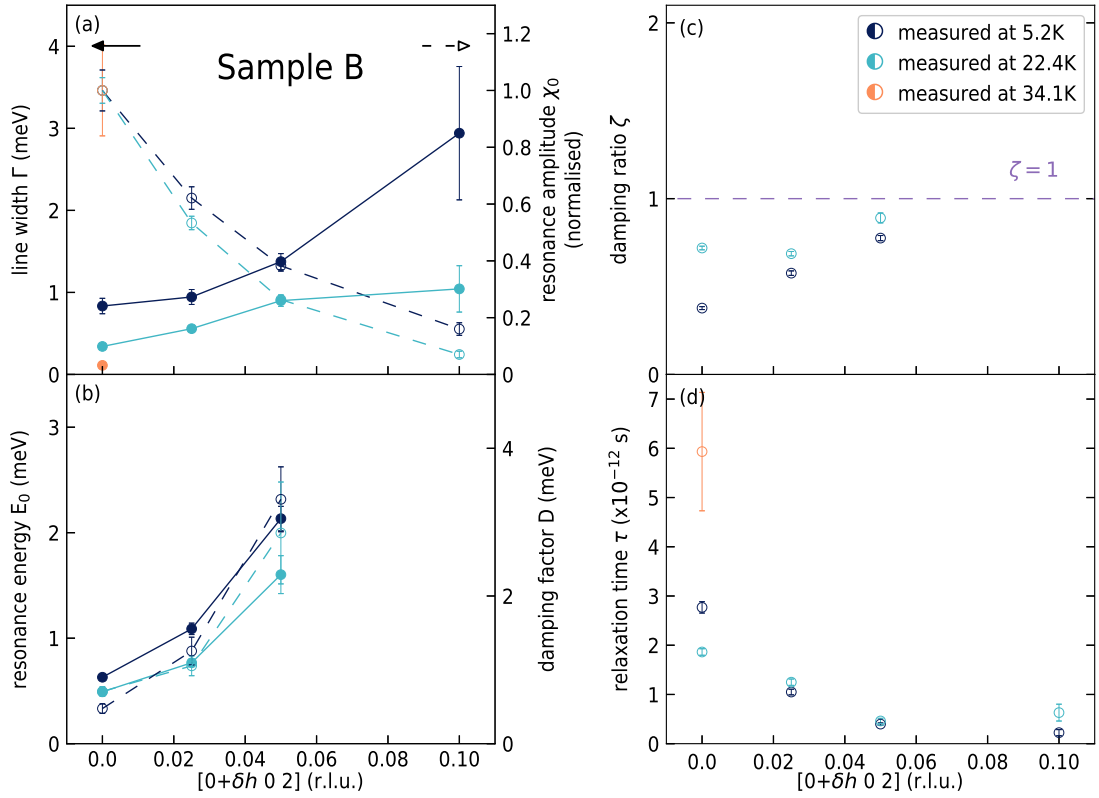

A.2.4.2 Sample C at the FM position

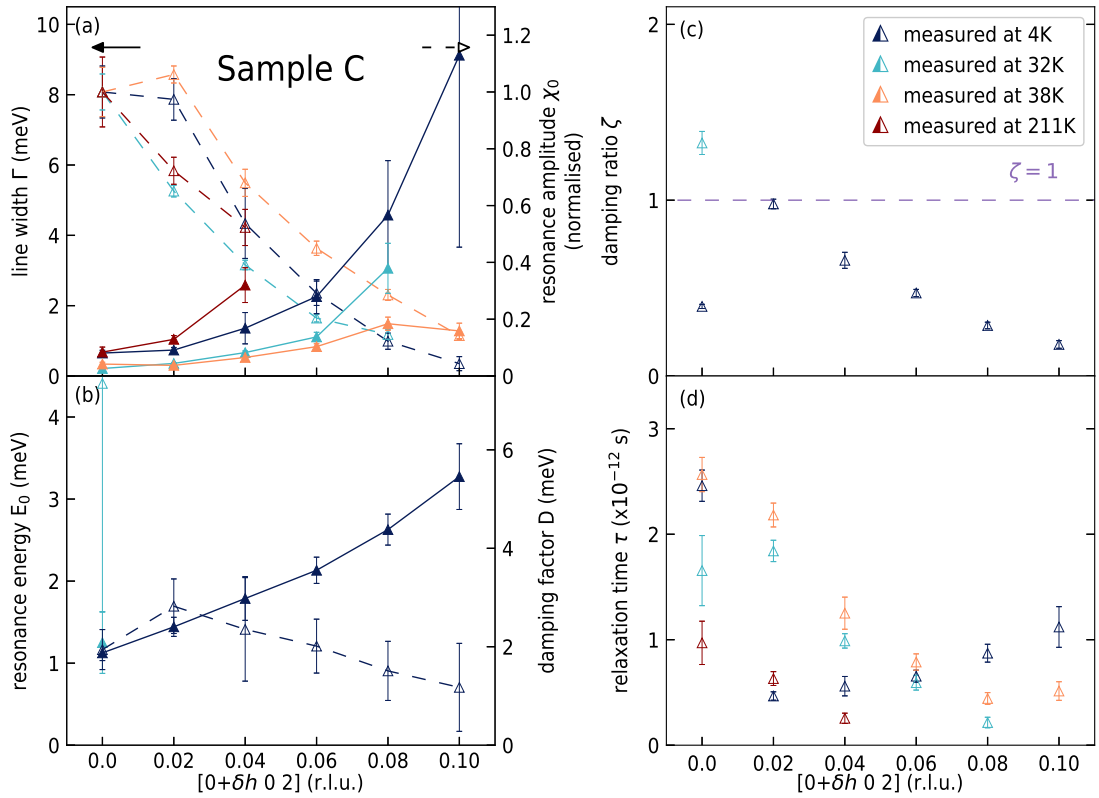

A.2.4.3 Sample A at the spin density wave (SDW) position

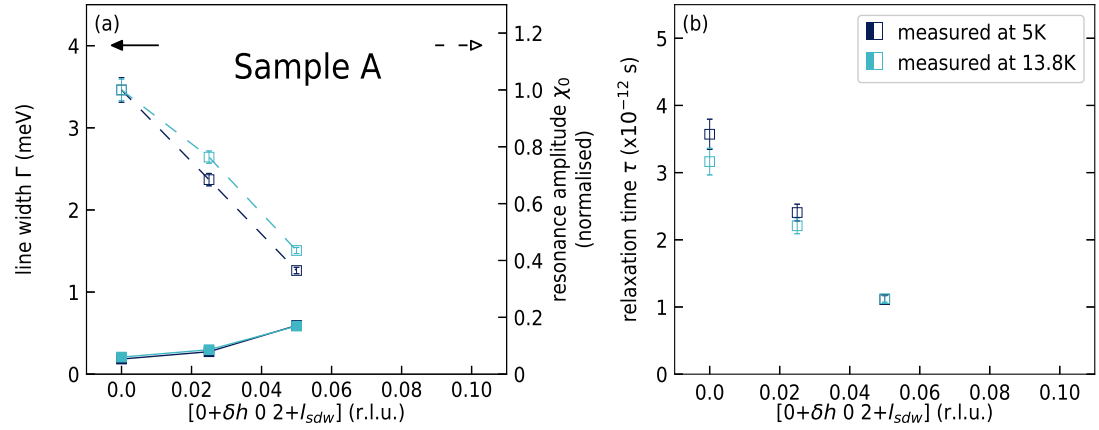

A.2.4.4 Sample B at the SDW position